

# On the interaction between tides and stratification in the Rhine Region of Freshwater Influence

Gerben J. de Boer





On the interaction between tides  
and stratification in the Rhine Region of  
Freshwater Influence





# On the interaction between tides and stratification in the Rhine Region of Freshwater Influence

PROEFSCHRIFT

ter verkrijging van de graad van doctor  
aan de Technische Universiteit Delft,  
op gezag van de Rector Magnificus prof.dr.ir. J.T. Fokkema,  
voorzitter van het College voor Promoties,  
in het openbaar te verdedigen op woensdag 14 januari 2009 om 12.30 uur

door

Gerben Jaring DE BOER  
civiel ingenieur  
geboren te Amsterdam

Dit manuscript is goedgekeurd door de promotor:

Prof.dr.ir. G.S. Stelling

Copromotor:

Dr. J.D. Pietrzak

Samenstelling promotiecommissie:

Rector Magnificus

voorzitter

Prof.dr.ir. G.S. Stelling

Technische Universiteit Delft, promotor

Dr. J.D. Pietrzak

Technische Universiteit Delft, copromotor

Dr.ir. J.C. Winterwerp

Technische Universiteit Delft

Prof.dr.ir. A.W. Heemink

Technische Universiteit Delft

Prof.dr.ir. H. Ridderinkhof

Koninklijk NIOZ, Texel en Universiteit Utrecht

Prof. J.H. Simpson BA (Oxon) PhD DSc (Liv)

University of Wales, Bangor, Verenigd Koninkrijk

Prof.dr. H. Burchard

Baltic Sea Research Inst. Warnemünde, Duitsland

Prof.dr.ir. M.J.F. Stive

Technische Universiteit Delft (reservelid)

The project has been funded by the Dutch Organization for Scientific Research (NWO) in the ALW programme within the framework of LOICZ-NL (ALW project number 014.27.006) with principal investigator Prof.dr.ir. H. Ridderinkhof.

Cover: [front]: TESO ferries on Texel, [back]: Rhine ROFI area as seen from space shuttle mission STS61A (credit: Image Science and Analysis Laboratory, NASA-Johnson Space Center. "The Gateway to Astronaut Photography of Earth." <http://eol.jsc.nasa.gov/>, image file: STS61A-201-57).

Copyright © 2008 by G.J. de Boer

Typeset by MiK<sub>T</sub>E<sub>X</sub>.

Printed by PrintPartners Ipskamp, the Netherlands.

ISBN 978-90-9023848-7

well-mixed or not well-mixed, that is the question  
whether 'tis weaker in the neap to alter  
the tidal currents of rotating systems  
or to take arms against a sea of freshness  
and by entraining end them. Homogenous;  
always; And by well-mixed to say we end  
the layers and the stratification  
that plumes are prone to, this ultimately  
happens every spring. Homogenous;  
well-mixed, albeit shortly. Ay, there's the rub  
for in due time more mechanisms act along  
when spring tides, strong winds passed away,  
that give us thoughts: more interactions  
strongly contribute when stratified:  
What does straining do in coastal shelves and seas,  
the residuals' effect, the estuaries' pulses,  
the fronts of upwelled water, inertia's delay  
the proximity of the boun'dries and the rays  
of spring-time sunlight on the upper lay'r,  
when winter periods might their quietus make  
with a single storm. What did Ekman say,  
on twist and turn on a spinning Earth,  
but that the tidal boun'dry layers,  
two opp'site phasors with two different heights  
that upward veer, puzzle the mind,  
and make us keen to learn the math they need,  
and to probe others we do not know of.  
These systems do make puzzlers of us all  
and thus the basic nature of the shelves  
is studied over with the methods of thought,  
with satellites and numerical tools.  
With this approach, their currents turn clear,  
reveal some of their secrets.



# Abstract

The Rhine ROFI (Region of Freshwater Influence) is a complex three-dimensional body of low salinity water in the North Sea. In this thesis the interaction between the semi-diurnal tide and the stratification field under the influence of the rotation of the Earth is investigated. The objective is to gain a further understanding of the complex interactions governed by both tidal mixing and tidal straining.

Previous studies, by Simpson and co-workers, identified that the Rhine ROFI is governed by two time scales in the stratification signal. First, the dominant cross shore density gradients in the Rhine ROFI compete with tidal/wind mixing to establish stratification. During neap periods with low mixing energy a large area becomes stratified, whereas during spring-tides the ROFI is well-mixed. During these well-mixed conditions the tidal currents are rectilinear alongshore, whereas under stratified conditions the tidal currents exhibit ellipses that rotate anti-cyclonically at the surface and cyclonically at the bottom, resulting in strong cross shore exchange flows. These interact with the dominant cross-shore density gradients through differential advection, a process referred to as tidal straining by Simpson, to generate a semi-diurnal cycle of stratification. This is the second time scale. We analyzed these processes further with an idealized 3D numerical model, remote sensing images and physical balance equations, notably potential energy anomaly budgets.

The main body of this thesis deals with tidal straining. Therefore a thorough analysis of tidal straining was performed first, starting with Prandles classic theory on the vertical profile of tidal flows. We show that his barotropic model already allows for a quantitative understanding of the aforementioned on-set in ellipse properties, as a function of the bulk eddy viscosity only. In addition, neap and spring tide simulations with an idealized 3D numerical model show that the two time scales can be reproduced successfully. Hence, the numerical model can be applied with confidence to further our ROFI research.

Our objectives have been achieved by adding two simple, yet powerful concepts to the Rhine ROFI body of literature. First, upwelling induced by tidal straining was identified as a new key mechanism operating in the Rhine ROFI. Due to continuity requirements imposed by the proximity of the coast, the aforementioned opposite cross shore surface currents and bottom currents should lead to coastal upwelling. The upwelling mechanism is detected using a 6-day unclouded series of KNMI NOAA-SST-imagery in May 1990 with about 2 images per tide. The

ROFI is much warmer than the surrounding water, exhibits a distinct diurnal solar heating response and is clearly delineated by large spatial temperature gradients at the edges. This indicates that the whole ROFI area is stratified, an essential requirement for upwelling to occur. On three consecutive middays a marked 5-10 km wide and 100 km alongshore band of cold upwelling water is visible along the coastline, while in the morning and afternoon this upwelling band is not present. The timing of this upwelling indicates that it is caused by tidal straining.

The existence of the upwelling mechanism was supported by simulations with the 3D numerical model of the idealized river plume. After adding temperature effects, the numerical model shows the same semi-diurnal band of cold upwelling water. We believe its presence shows for the first time the large spatial scale involved with the tidal straining mechanism of Simpson & Souza (1995). The upwelling mechanism has a large impact on for instance the advection and dispersal of nutrients in the coastal zone.

In addition to the cross-shore tidal straining mechanism and the associated upwelling, the SST images also display a bulge of warmer water moving alongshore, independent of the cross shore straining. The movement of this bulge does not fit the cross-shore tidal straining paradigm. Therefore, a framework was subsequently developed that combines the observed tidal straining paradigm with the observed alongshore movements. This forms the second simple, yet powerful contribution to meet our objectives.

For this framework the full potential energy anomaly equation suitable for the analysis of 3D numerical models is first derived. The ten terms that dominate the evolution of stratification in the Rhine ROFI are selected. These principal terms are the cross-shore and alongshore straining and cross-shore and along shore advection of horizontal density gradients. In addition, non-linear shear dispersion terms representing correlations between density and velocity perturbations over the vertical control horizontal exchange in the cross-shore and alongshore directions. Moreover, in the vertical direction one term describes the effect of vertical mixing on the density profile, while the other term is related to vertical advection, which we refer to elsewhere as upwelling and downwelling.

These ten terms are examined using the neap tide simulation of the Rhine ROFI that was used to analyze tidal upwelling before. Analysis of the model results using the potential energy anomaly equation allows us to present a detailed overview of the spatial distribution of the terms affecting the evolution of stratification. The results corroborate the important role that cross-shore tidal straining is known to play in the downstream coastal current region of the plume. In addition, the roles of alongshore advection, as well as alongshore and cross-shore straining are also of importance in the Rhine ROFI, in particular in the region of the bulge near the river mouth. The term ASIPS (advection and strain induced periodic stratification) is introduced in order to identify the joint action of these terms. ASIPS is shown to be a natural extension of the SIPS concept introduced by Simpson *et al.* (1990), but also forms the key subset of the terms

in the potential energy anomaly approach. Near the edges of the river plume shear dispersion and upwelling and downwelling terms also play a significant role, indicating that a different physical balance is dominant than in the ROFI interior. Additionally, near the river mouth advection of fresh water lenses plays an important role. The results for the Rhine ROFI show that the potential energy anomaly equation and ASIPS constitute powerful tools to analyse the mechanisms contributing to mixing and stratification in coastal seas and estuaries.





## Samenvatting

De Rijnpluim is een complex drie-dimensionaal volume van water met een laag zoutgehalte in de Noordzee. In dit proefschrift wordt de interactie tussen het dubbeldaags getij en de aanwezige gelaagdheid onderzocht. Het doel is om tot een beter begrip te komen van de complexe interacties die bepaald worden door zowel getij-geïnduceerde menging als door getijde-schering.

In voorgaande studies door Simpson en anderen is vastgesteld dat de Rijnpluim wat betreft de gelaagdheid onderhevig is aan twee tijdschalen. Ten eerste is er competitie tussen de dominante kustdwarse dichtheidsgradiënt die gelaagdheid bewerkstelligt en de menging door getij en wind die de gelaagdheid juist afbreekt. Tijdens periodes van doodtij die gekenmerkt worden door een lage mengingsenergie treedt er gelaagdheid op in een groot gebied, terwijl tijdens periodes van springtij de Rijnpluim vertikaal goed doormengd is. Tijdens deze doormengde toestand zijn de getijdestromingen louter evenwijdig aan de kust, terwijl tijdens gelaagde toestand de getij-geïnduceerde stromingen getijellipsen gaan vertonen, welke anti-cyclonisch draaien in de oppervlaktelaag, en cyclonisch in de bodemlaag. Dit resulteert in sterke kustdwarse uitwisselingsstromingen, die een relatieve verplaatsing van de onder- en bovenlaag ten opzichte van elkaar oplevert. Deze kustdwarse getijde-schering staat bekend als *tidal straining*. Door de dominante aanwezigheid van een kustdwarse dichtheidsgradiënt leidt deze kustdwarse getijde-schering tot een dubbeldaagse cyclus in de gelaagdheid, de tweede tijdschaal. Wij hebben deze processen verder geanalyseerd met behulp van een 3D numeriek model, met satelliet beelden en met fysische balansvergelijkingen, in het bijzonder die van de anomalie van de potentiële energie.

De bulk van dit proefschrift gaat over tidal straining. Daarom is er eerst een grondige analyse van dit fenomeen uitgevoerd, met als basis de klassieke theorie van Prandle over het verticale profiel van getijdestromen. We laten zien dat het met dit barotrope model al mogelijk is om de opwekking van de bovengenoemde getij-ellipsen kwantitatief inzichtelijk te maken, als een functie van de diepte gemiddelde eddy viscositeit. Daarnaast is het mogelijk om de twee tijdschalen te reproduceren met een geïdealiseerd 3D numeriek model met doodtij en springtij forcering. Zodoende kan het numerieke model met vertrouwen toegepast worden voor verder onderzoek aan de Rijnpluim.

Aan onze doelstelling is voldaan door twee simpele, maar krachtige concepten aan de bestaande literatuur over de Rijnpluim toe te voegen. Ten eerste is opwelling door getijde-schering door ons als een kenmerkend mechanisme geïdentificeerd. Door de eis die de nabijheid van de kust

oplegt aan de stromingen - er mag over de diepte gemiddeld geen kustdwarse stroming optreden - moeten de tegengestelde stromingen van het wateroppervlak en de bodemlaag leiden tot een opgaande dan wel neergaande waterbeweging nabij de kust. Dit opwellingsmechanisme is waargenomen in een 6-daagse onbewolkte serie KNMI NOAA beelden van de oppervlakte-watertemperatuur uit mei 1990 met 2 beelden per getij. Hierin is de Rijnpluim is veel warmer dan het omringende water, laat een geprononceerde dagelijkse opwarming zien als gevolg van de zonne-instraling en is duidelijk omlijnd door grote ruimtelijke temperatuur gradiënten. Dit geeft aan dat de hele Rijnpluim gelaagd is, een essentiële vereiste voor het optreden van opwelling. Op drie opeenvolgende middagen is een geprononceerde 5 - 10 km brede en 100 km lange strook van koud opwellend water langs de kust te zien, terwijl die strook in de ochtend en avond niet aanwezig is. Het tijdstip waarop deze opwellingsstrook optreedt, geeft aan dat deze veroorzaakt wordt door getijde-schering.

Het optreden van het opwellingsmechanisme wordt bevestigd door de simulaties die uitgevoerd zijn met het 3D numerieke model van de rivierpluim. Na het toevoegen van temperatuur als proces, laat het numerieke model ook deze koude opwellende strook zien. Wij geloven dat de waarneming van het optreden hiervan voor het eerst de grote ruimtelijke schaal laat zien van het getijde-scheringsmechanisme van Simpson & Souza (1995). Het opwellingsmechanisme heeft een grote impact op bijvoorbeeld de advectie en dispersie van nutriënten in de kustzone.

Naast het optreden van kustdwarse getijde-schering en de daarmee gepaard gaande opwelling, laten de beelden van de oppervlakte-watertemperatuur ook een bel warm water zien die zich evenwijdig aan de kust verplaatst, onafhankelijk van de kustdwarse getijde-schering. De beweging van deze bel strookt niet met het paradigma van kustdwarse getijde-schering. Daarom werd er vervolgens een raamwerk ontwikkeld dat de waargenomen kustdwarse getijde-schering combineert met de waargenomen kustlangse bewegingen. Dit raamwerk vormt de tweede simpele, maar krachtige bijdrage waarmee aan onze doelstelling wordt voldaan.

Voor dit raamwerk wordt eerst de vergelijking van de anomalie van de potentiële energie afgeleid die zich leent voor het analyseren van 3D numerieke modellen. De tien termen die hierin overheersen in de ontwikkeling van de gelaagdheid in de Rijnpluim worden geselecteerd. Deze dominante termen zijn de kustdwarse en de kustlangse advectie en schering van horizontale dichtheidsgradiënten. Daarnaast beheersen niet-lineaire scherings-dispersietermen de horizontale uitwisseling in zowel kustdwarse als kustlangse richting. Deze termen stellen correlaties voor tussen dichtheids- en snelheidsperturbaties over de vertikaal. Bovendien beschrijft in verticale richting de ene term het effect van verticale menging op het dichtheidsprofiel, terwijl de andere term gerelateerd is aan verticale advectie, waar we elders naar refereren als opwelling.

De tien termen worden onderzocht aan de hand van de doortijdsimulatie van de Rijnpluim die eerder gebruikt was om getijgedreven opwelling te analyseren. Een analyse van de modelresultaten met de vergelijking van de anomalie van de potentiële energie maakt het ons mogelijk een gedetailleerde overzichtskaart van de ruimtelijke verdeling te presenteren van de termen die de

gelaagdheid beïnvloeden. De resultaten versterken het bekende gegeven dat de kustdwarse schering een belangrijke rol speelt in het benedenstroomse gebied van de rivierpluim. Daarnaast zijn de rollen van kustlangse advectie, alsmede die van kustlangse en kustdwarse schering, van groot belang in de Rijnpluim, vooral in het gebied van de zoetwaterbel nabij de riviermonding. Het begrip ASIPS (Advectie- en Scheringsgeïnduceerde Periodieke Stratificatie) wordt gintroduceerd om het gezamenlijke effect van deze termen te identificeren. We laten zien dat ASIPS op een natuurlijke wijze volgt uit het SIPS concept zoals dat door Simpson *et al.* (1990) gintroduceerd is, maar dat het anderzijds ook een belangrijke subset vormt van de termen uit de vergelijking van de anomalie van de potentiële energie. Nabij de randen van de rivierpluim spelen dispersie door schering en opwelling ook een significante rol, wat aangeeft dat in het binnengebied van de Rijnpluim een andere fysische balans dominant is. Verder speelt nabij de riviermonding de advectie van zoetwaterbellen een belangrijke rol. De resultaten voor de Rijnpluim laten zien dat de vergelijking van de anomalie van de potentiële energie en ASIPS krachtige gereedschappen zijn om de mechanismen te analyseren die aan menging en gelaagdheid in kustzeeën en estuaria bijdragen.



# Contents

<b>1</b>	<b>Introduction</b>	<b>1</b>
1.1	<i>The Rhine ROFI</i>	1
1.2	<i>Rationale for studying Rhine ROFI physics</i>	8
1.3	<i>Objective</i>	10
1.4	<i>Main findings</i>	10
1.5	<i>Outline of thesis</i>	12
<b>2</b>	<b>Literature study</b>	<b>13</b>
2.1	<i>Scales and scope</i>	13
2.2	<i>The North Sea: density and residual current field</i>	14
2.2.1	Depth averaged situation	14
2.2.2	3D situation	20
2.2.3	River plumes	25
2.3	<i>The North Sea: barotropic tidal field</i>	29
2.4	<i>Tidal mixing and straining</i>	31
2.4.1	Spring neap cycle due to tidal mixing	32
2.4.2	Spring neap effect of stratification on tidal current ellipses	32
2.4.3	Barotropic Ekman dynamics	33
2.4.4	Baroclinic Ekman dynamics	34
2.4.5	Semi-diurnal cycle due to tidal straining	38
2.4.6	Semi-diurnal effect of tidal current ellipses on stratification	38
2.5	<i>Synthesis 3D ROFI structure</i>	43
<b>3</b>	<b>Set-up of study</b>	<b>47</b>
3.1	<i>Introduction</i>	47
3.2	<i>Idealized numerical model</i>	47
3.2.1	Numerical modelling system DELFT3D-FLOW	48
3.2.2	An idealized rectangular tidal basin with tidal forcing	54
3.2.3	Turbulence modelling	57
3.3	<i>Remote sensing of SST</i>	63

<b>4</b>	<b>On the vertical structure of the Rhine ROFI</b>	<b>67</b>
4.1	<i>Introduction</i> . . . . .	68
4.2	<i>Model set-up</i> . . . . .	70
4.3	<i>Barotropic tidal currents</i> . . . . .	73
4.3.1	Comparison of analytic and numerical results . . . . .	73
4.4	<i>Baroclinic tidal currents</i> . . . . .	75
4.4.1	Plume characteristics . . . . .	75
4.4.2	Vertical profiles of ellipse properties . . . . .	82
4.4.3	Tidal straining . . . . .	82
4.4.4	Correlation ellipse and Richardson number . . . . .	88
4.4.5	Heaps' Model Revisited . . . . .	93
4.4.6	Spring Neap Tidal Cycle . . . . .	94
4.5	<i>Discussion</i> . . . . .	94
4.6	<i>Appendix: Equations tidal velocity profile</i> . . . . .	98
<b>5</b>	<b>SST observations of upwelling induced by tidal straining</b>	<b>101</b>
5.1	<i>Introduction</i> . . . . .	102
5.2	<i>Methods</i> . . . . .	106
5.2.1	SST imagery selection . . . . .	106
5.2.2	SST analyses . . . . .	108
5.2.3	Idealized numerical model . . . . .	110
5.3	<i>SST sequence</i> . . . . .	112
5.3.1	The bulge . . . . .	112
5.3.2	Downstream coastal buoyancy current . . . . .	113
5.3.3	Modeled downstream coastal buoyancy current . . . . .	117
5.3.4	Role of near shore mixing and offshore winds . . . . .	121
5.4	<i>Discussion</i> . . . . .	122
	Appendix: warm upwelling band in autumn . . . . .	126
<b>6</b>	<b>The potential energy anomaly equation and ASIPS</b>	<b>131</b>
6.1	<i>Introduction</i> . . . . .	132
6.2	<i>Derivation of the potential energy anomaly equation</i> . . . . .	135
6.2.1	Description of the terms in the $\varphi_t$ equation . . . . .	136
6.2.2	Method of analysis . . . . .	137
6.3	<i>Numerical model set-up and calculation of terms in <math>\varphi</math> equation</i> . . . . .	138
6.3.1	Description of terms in the Rhine ROFI test case . . . . .	139
6.4	<i>Results of the potential energy anomaly equation budget</i> . . . . .	139
6.4.1	Covariance distribution $\varphi_t$ and $\varphi_t$ predictors . . . . .	139
6.4.2	$\varphi_t$ terms in the bulge and downstream locations . . . . .	142
6.4.3	Synthesis of results . . . . .	148

---

6.4.4	Discussion . . . . .	151
6.5	<i>Conclusions</i> . . . . .	154
<b>7</b>	<b>Synthesis</b>	<b>155</b>
7.1	<i>Tidal mixing and straining</i> . . . . .	156
7.2	<i>Tidal upwelling</i> . . . . .	159
7.3	<i>Advection of stratification</i> . . . . .	160
7.4	<i>Potential energy anomaly analysis</i> . . . . .	161
7.5	<i>Dealing with tidal mixing and straining</i> . . . . .	161
7.6	<i>Concluding remarks</i> . . . . .	163
	<b>References</b>	<b>164</b>
	<b>List of Figures</b>	<b>175</b>
	<b>List of Tables</b>	<b>179</b>
	<b>List of Symbols</b>	<b>181</b>
	<b>Acknowledgements</b>	<b>183</b>
	<b>Curriculum Vitae</b>	<b>185</b>
	<b>List of author's publications</b>	<b>187</b>





# Chapter 1

## Introduction

### 1.1 The Rhine ROFI

The Rhine ROFI, Region of Freshwater Influence, is a complex three-dimensional (3D) body of low salinity water in the North Sea (Figs. 1.1, 1.2), an energetic tidal marine environment at 52°N. The term ROFI was introduced by Simpson *et al.* (1993); a formal definition is given by Simpson (1997) as “the region between the shelf sea regime and the estuary where the local input of buoyancy from a coastal source is comparable with, or exceeds, the seasonal input of buoyancy as heat which occurs all over the shelf”. The Rhine ROFI is maintained by the input of significant amounts of buoyancy as freshwater from the river Rhine, the second largest river in Europe after the Danube, with an average discharge of 2500 m<sup>3</sup>s<sup>-1</sup>. This Rhine inflow represents a huge source of buoyancy equivalent to peak summer heating over an area of 100 × 100 km<sup>2</sup> (Souza, 1994), a significant portion of the North Sea continental shelf. After debouching into the Southern Bight of the North Sea the fresh water turns anti-cyclonically, to the right on the Northern Hemisphere (NH), due to the rotation of the Earth, a feature shared with other river plumes throughout the world. The resulting ROFI generally extends 20-40 km from the coast, with an occasional outburst 50 km offshore, whereas it extends over 100 km downstream (Northward) from the river mouth. The complex 3D density structure in this 50 × 100 km<sup>2</sup> region is the subject of this thesis.

The most energetic driving force in the North Sea is the semi-diurnal tide (Zimmerman, 1986). The semi-diurnal tide interacts with the 3D density field through a number of ways, involving the rotation of the Earth, the coastal boundary, residual currents, the bed friction and the density field itself as important moderators. These interactions are challenging and complex due their combination of shelf sea, estuarine and river plume features. In this thesis the interaction between the stratification field of the Rhine ROFI in rotating frame of reference and the semi-diurnal tide in particular is investigated. We extend the physical concepts known to govern these interactions as introduced by Simpson and co-workers. They identified that the Rhine ROFI is governed by two times scales, one fortnightly, and another semi-diurnal (Simpson *et al.*, 1993) and that these two time scales are dictated by tidal/wind mixing and tidal straining respectively. Stratification is the key parameter in both time scales.

The fortnightly time scale is related to the aspects that the ROFI shares with the dominant

seasonal stratification pattern in the central North Sea shelf. Both the central North Sea and the Rhine ROFI are intermittently well-mixed or stratified due to tidal/wind stirring. However, the competing stratifying influences as well as the resulting time scales are different. On the shelf the dominant balance of the hydrodynamics is governed by a competition between the stratifying influence of solar heating and the mixing influence of tidal/wind stirring. This results in a thermally stratified shelf in the summer, whereas in the winter the shelf is well-mixed. In the

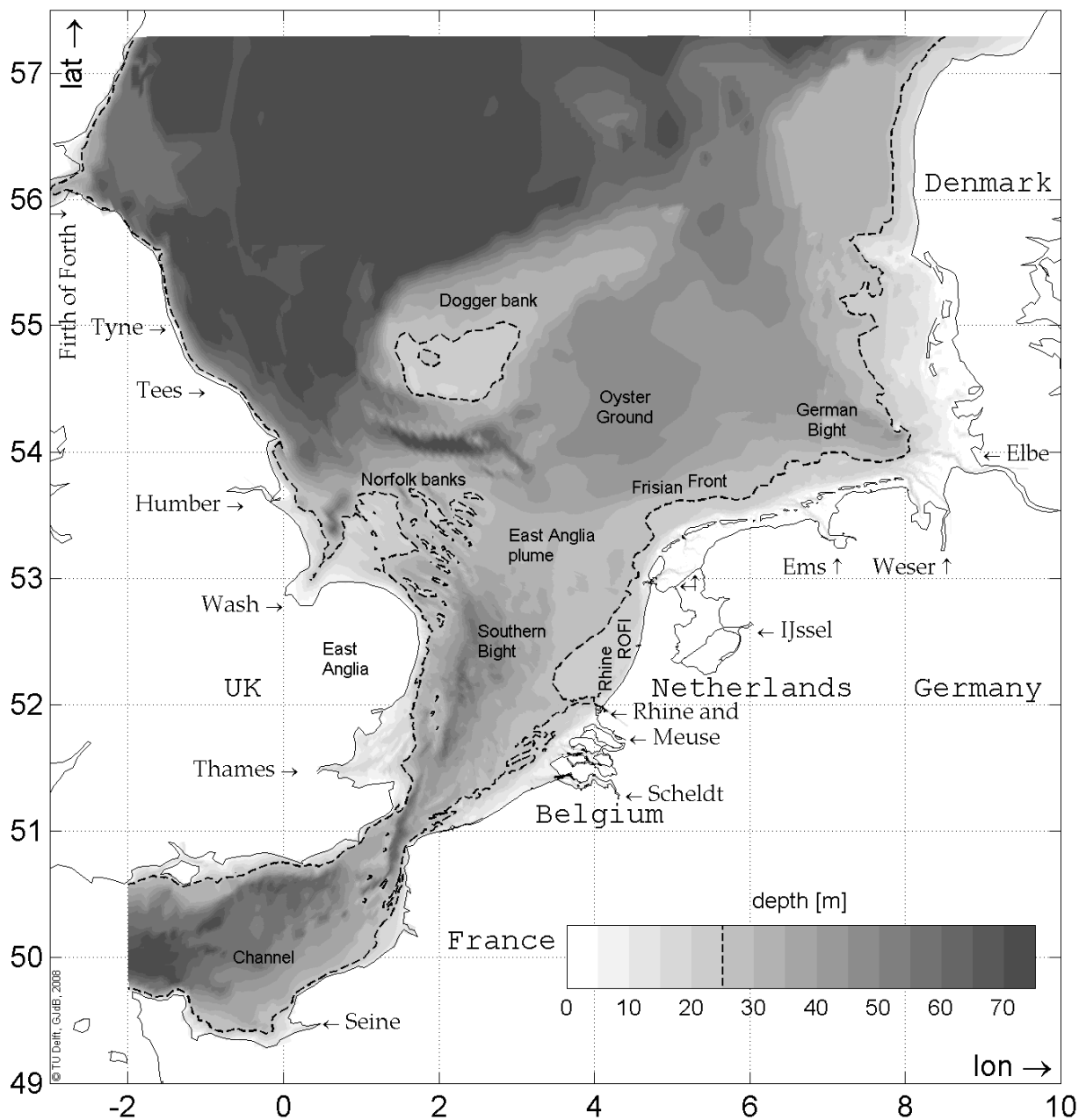


**Figure 1.1:** Overview of the Southern North Sea with names of regions and dominant rivers. The Rhine ROFI is located in the Dutch coastal zone on the Eastern margin of the Southern Bight.

Rhine ROFI the basic balance is between the stratifying influence of buoyancy input from the river and the destratifying influence of tidal/wind stirring. The Rhine ROFI is basically well-

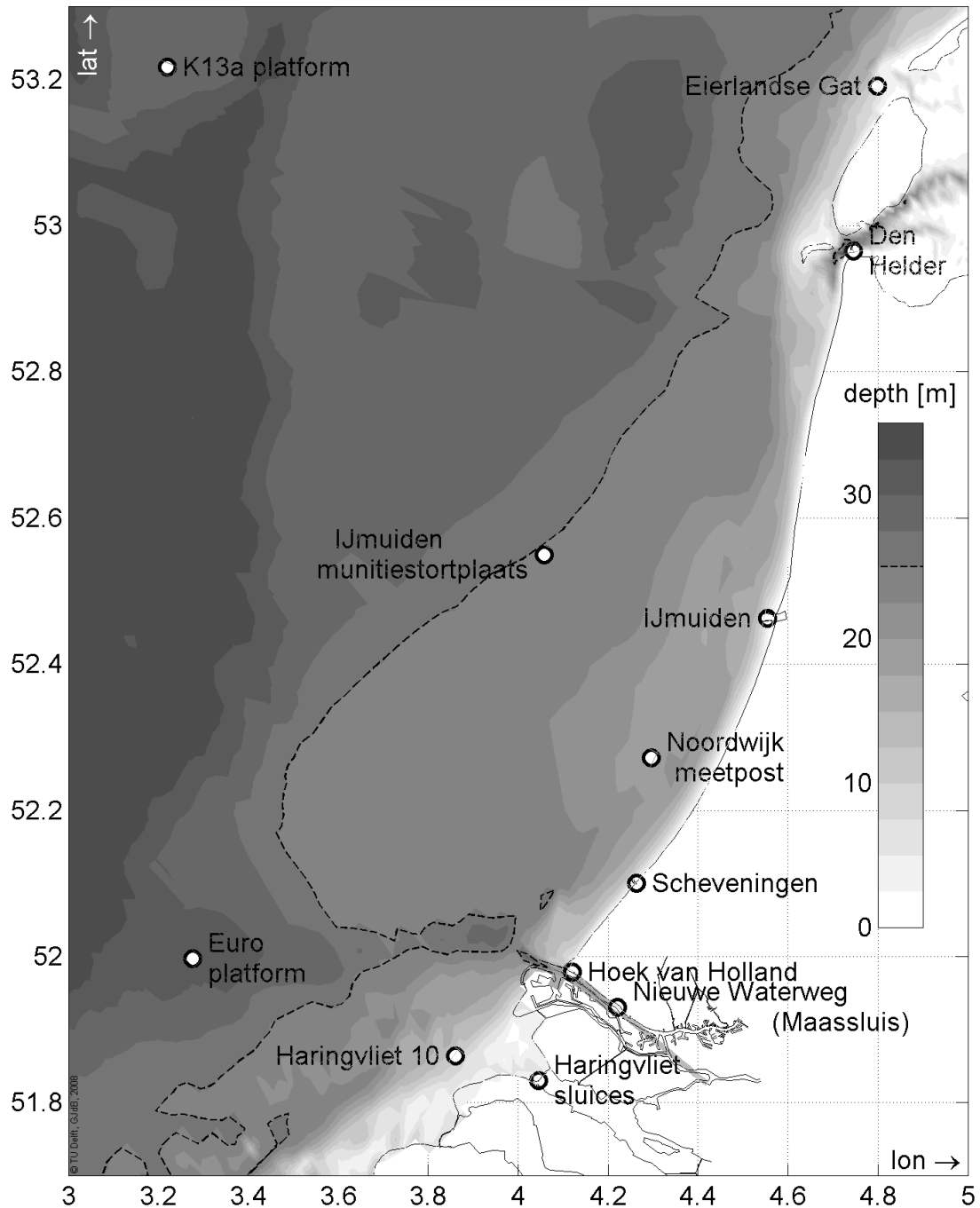


**Figure 1.2:** Overview of the Rhine ROFI with the main observation stations in detail. The Rhine water debouches in Hoek van Holland and Haringvlietsluizen buiten (sluices). The ROFI stretches alongshore to Den Helder. The deep lobe between Europlatform and Hoek van Holland is the deepened approach channel of Port of Rotterdam.

mixed during periods with increased stirring power such as spring-tides and storms, whereas it tends to show haline stratification during low energetic periods such as neap tides (Fig. 1.3). This succession in transitions between well-mixed and stratified conditions due to variations in tidal mixing levels over the spring neap cycle is the first dominant time scale of the ROFI.

In contrast, the semi-diurnal time scale is related to the interactions between the 3D density structure and the tidal velocity shear. During well-mixed conditions there is no systematic interaction between the alongshore Kelvin wave velocities and the dominant cross-shore density gradient (Fig. 1.4). However, during periods of stratification, the tidal current patterns are

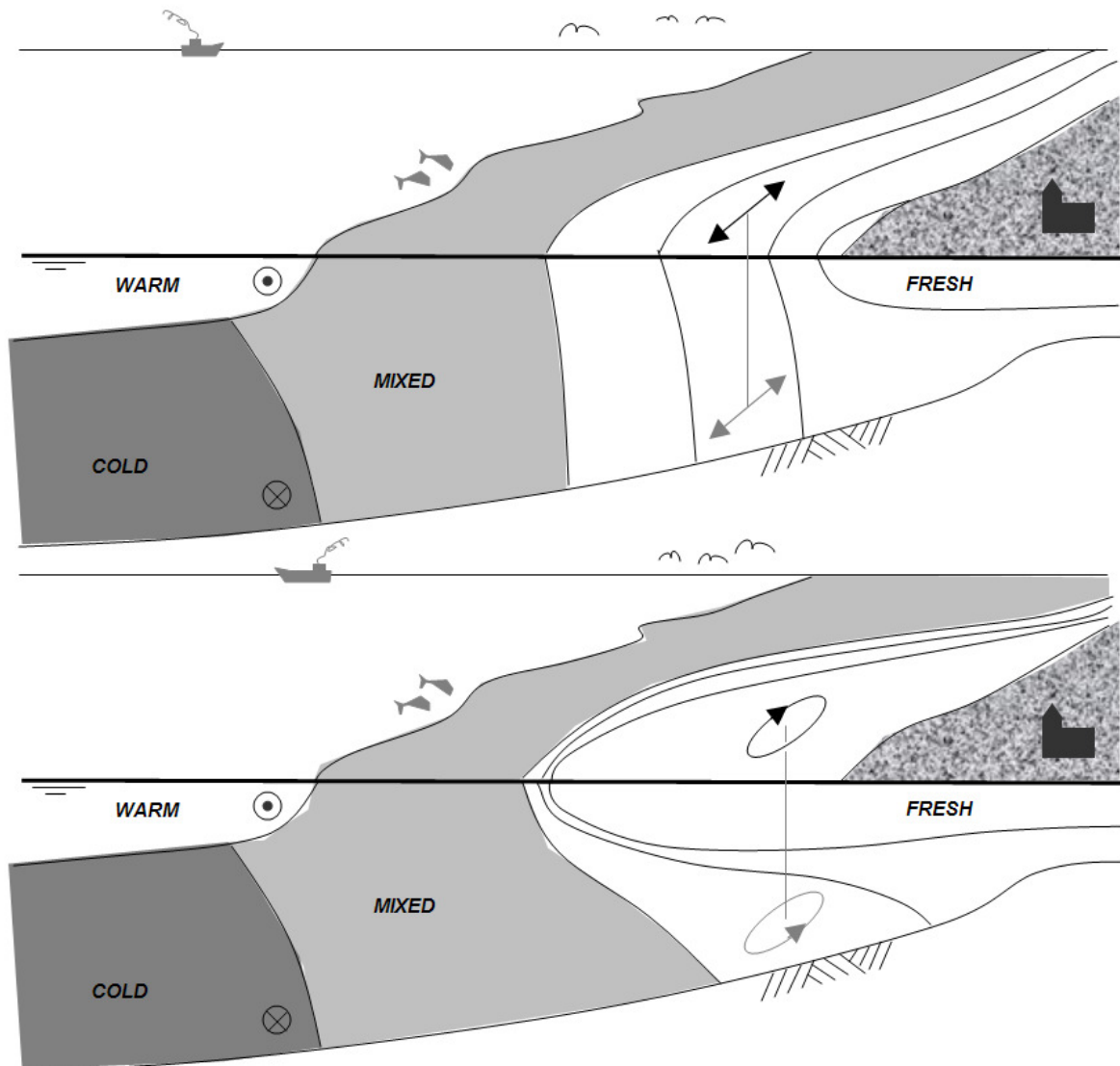


**Figure 1.3:** (top) The Rhine ROFI during well-mixed conditions and (bottom) the Rhine ROFI during stratified conditions (after Simpson *et al.* (1990)). The central North Sea (left) has a dominant seasonal thermal stratification cycle whereas the Rhine ROFI (right) has a dominant fortnightly haline stratification cycle.

---

significantly altered. Whereas the cross-shore tidal velocities are zero in the well-mixed state, during periods of stratification a significant cross shore velocity difference up to  $70 \text{ cm s}^{-1}$  emerges over the vertical (Figs. 1.3, 1.4, 1.5). This cross-shore tidal velocity shear controls a systematic interaction between the tide and the 3D density field (Fig. 1.4) first identified by Simpson & Souza (1995). The cross-shore surface currents alternately advect fresher coastal waters offshore and onshore, a process that has been labelled tidal straining by Simpson *et al.* (1990). This interaction causes a semi-diurnal Strain Induced Periodic Stratification signal in the Rhine ROFI (SIPS, Simpson *et al.* (1990)). The rotation of the Earth is responsible for the origin of the cross shore velocity shear during periods of stratification and hence for SIPS. This means that Coriolis effects not only directly control the very existence of the ROFI due to the onset of a coastal current, but also indirectly control the existence the tidal straining signal within the ROFI, the second time scale of the ROFI.

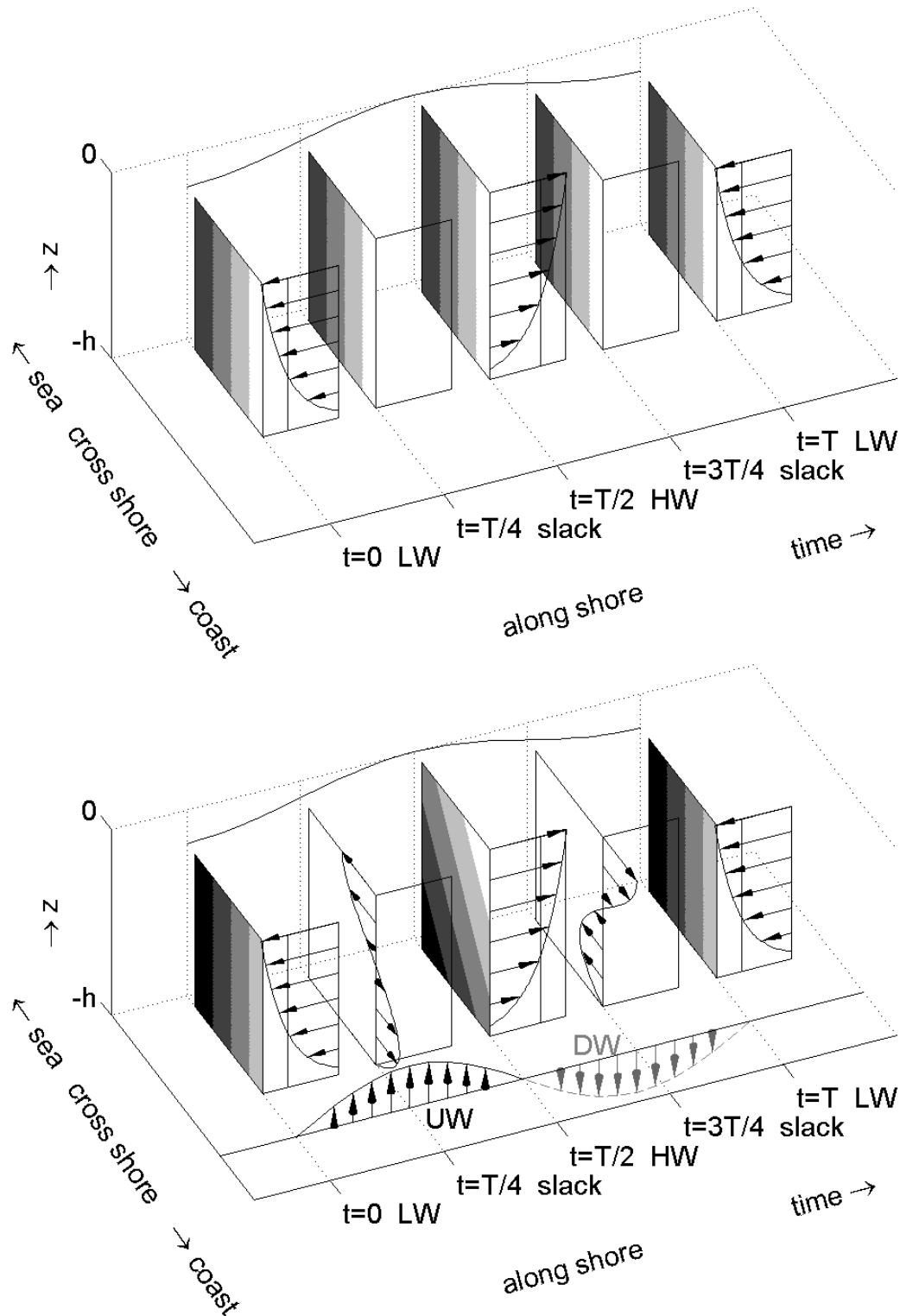


**Figure 1.4:** (top) During well-mixed conditions there is no systematic interaction between the alongshore ebb and flood velocities and the average cross shore density gradients. Only occasional fresh water lenses are known to be displaced with the tidal excursion due to alongshore advection (Van Alphen *et al.*, 1988; De Ruijter *et al.*, 1997). (bottom) Tidal straining (Simpson *et al.*, 1990) in the Rhine ROFI during stratified conditions is due to the systematic interaction of the cross shore velocity shear with the average cross shore density gradients (Simpson & Souza, 1995). The cross shore currents should lead to upwelling (UW) and downwelling (DW) as described in Chapter 5.

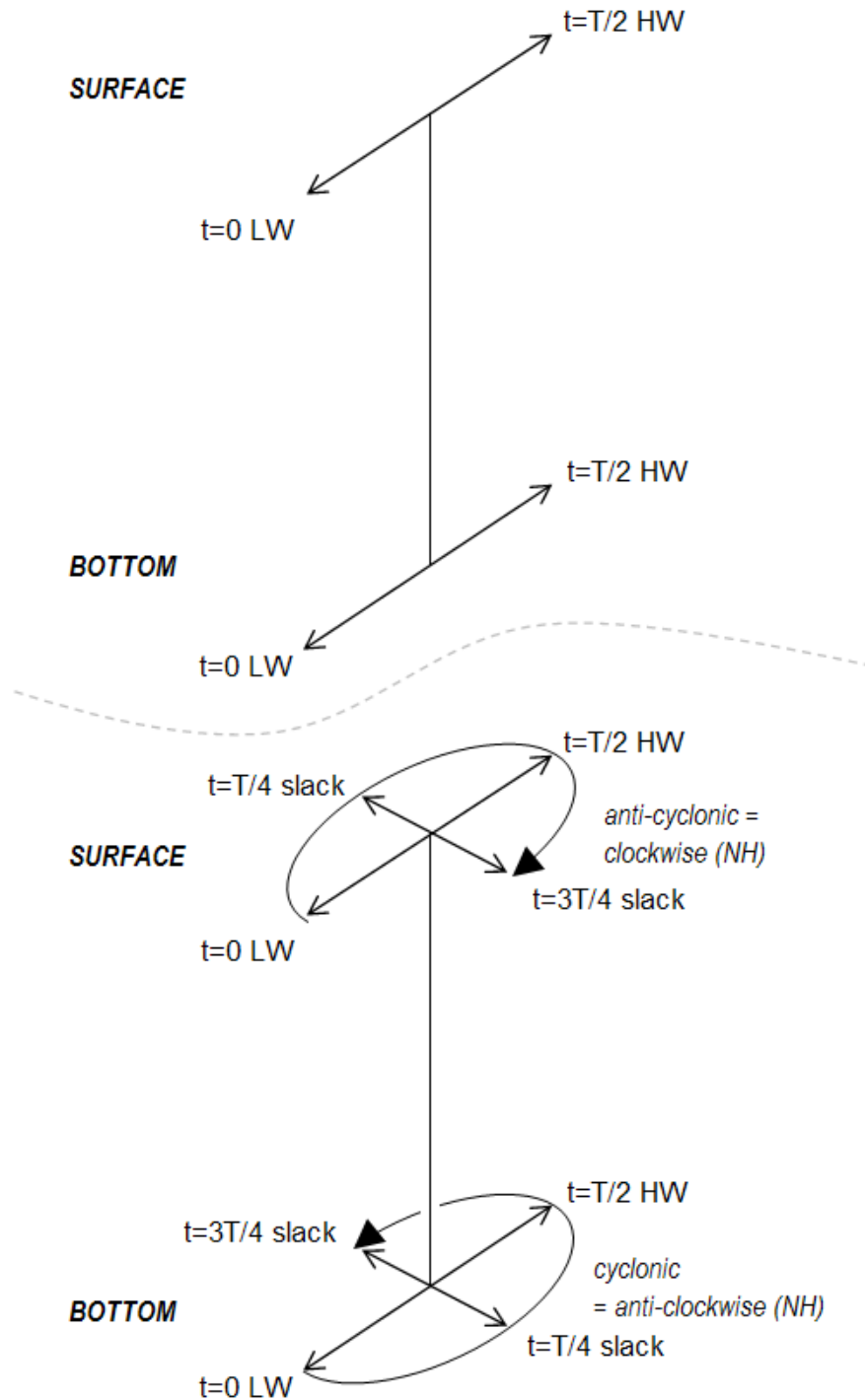


**Figure 1.5:** (top) The vertical variation of horizontal tidal velocities in the Rhine ROFI during well-mixed conditions and (bottom) during stratified conditions as distilled from measurements by Simpson *et al.* (1993) and Visser *et al.* (1994). During well-mixed conditions the ebb and flood currents are rectilinear alongshore over the entire water depth. In the stratified case the surface velocity vectors exhibit increased cyclonic ellipticity, which corresponds to anti-clockwise in a top view on the Northern hemisphere. In contrast, the bottom current vector exhibits increased anti-cyclonic rotation.

## 1.2 Rationale for studying Rhine ROFI physics

The interaction between the semi-diurnal tide and the stratification field has a pronounced effect on the advection and dispersal of dissolved and suspended contaminants, nutrients, sediments, as well as biological substances and detritus. This is illustrated by the patchy spreading of ocean colour on a satellite image of the Southern Bight (Fig. 1.6). Measurements in the Rhine ROFI have for instance shown that the water column stability influences chlorophyll sinking rates to a large degree (Joordens *et al.*, 2001; Peperzak *et al.*, 2003).

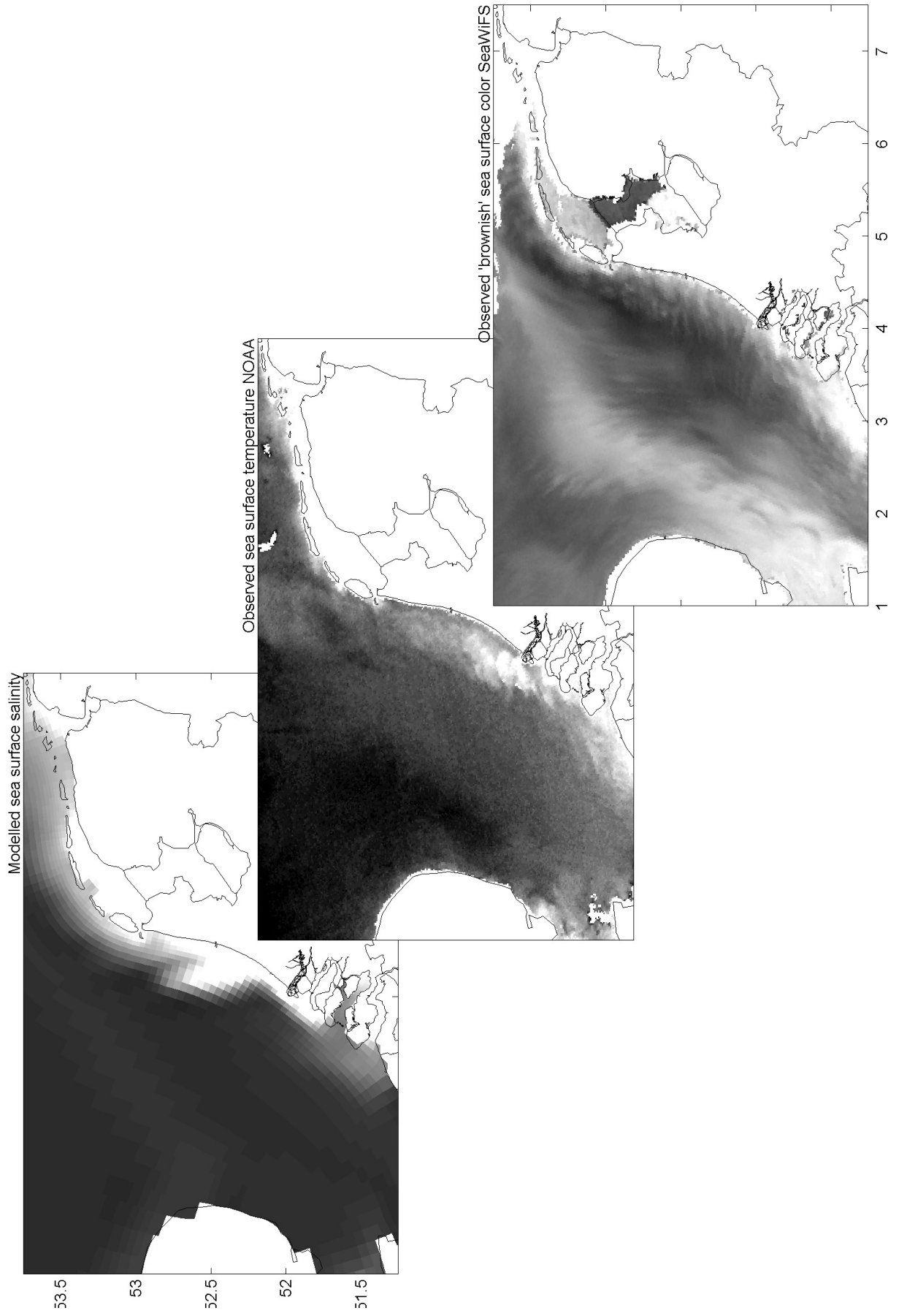
Contaminants were traditionally land-derived or originated from ship accidents and hull cleanings at open sea. Fortunately, decades of national and European environmental legislation are responsible for a huge improvement in the water quality in the North Sea through reduction of pollutant (OSPAR Commission, 2007a) and to a lesser extent also nutrient levels (OSPAR Commission, 2007b). However, contaminants have accumulated in the sea bed attached to fine sediments, thereby acting as secondary sources today (Klamer *et al.*, 1990). The practices from the past continue to affect present day water quality as a historical burden. Additionally, currently planned large-scale infrastructural works can cause a change in the fine sediment concentrations as large as the background levels. In the Dutch economical zone these include the construction of artificial islands, large scale sand mining, offshore wind farms and offshore gas drillings. These developments may significantly affect the ecosystem, for instance due to deterioration of the light climate, thereby affecting primary production, or by impeding the filter capacity of biota.

Both the cause and the consequences of changes in the concentrations of dissolved substances, either beneficial or detrimental, are of paramount importance due to the dense population concentrations surrounding the North Sea. The Netherlands and Belgium are among the most densely populated counties in the world. To assess the effect of changes in sources and sinks of dissolved substances, one has to determine their advection and dispersal behaviour properly. Moreover, after the recent national implementations of the EU Water Framework Directive and the Bird and Habitat Directives, the EU member states are even obliged to make detailed quantitative assessments of consequences of changes in advection and dispersal patterns in the coastal North Sea margins (12 km). A similar EU directive for the marginal seas is in

---

**Figure 1.6 (on the next page):** Three synoptic views on the North Sea. (left) Snap shot of modelled surface salinity 1998 Jan 1st (model of Roelvink *et al.* (2001)). (centre) Remote sensing image 1998 May 14th 1998 14:13 of Sea Surface Temperature by the NOAA-AVHRR satellite. (right) Remote sensing image 1998 Feb 14th 12:59 of ocean colour in the 555 nm band, representing total suspended matter, by SeaWiFS satellite (credit: SeaWiFS Project (code 970.2) & DAAC (code 902), Goddard Space Flight Center, MD, USA, sponsored by NASA's Mission to Planet Earth Program - <http://seawifs.gsfc.nasa.gov>, LAC data received by Dundee HRPT station - [www.sat.dundee.ac.uk](http://www.sat.dundee.ac.uk)).





preparation. Therefore a thorough understanding of the underlying physics is required.

### 1.3 Objective

The objective of this thesis is to gain a further understanding of the complex flow-density interactions governed by both tidal mixing and tidal straining in the Rhine ROFI.

### 1.4 Main findings

The main body of this thesis deals with tidal straining. Therefore a thorough analysis of tidal straining is first performed in **Chapter 4**, which starts with the classic theory on the vertical profile of tidal flows by Prandle (1982a,b). An attempt is made to understand the transition between well-mixed and stratified conditions as a function of the bulk eddy viscosity only. It is shown that a large, but realistic reduction of the bulk eddy viscosity in Prandle's model immediately results in a significant increase of vertical structure, although not as large as observed (Fig. 4.17). Visser *et al.* (1994) successfully adopted a two layer system, with a varying degree of coupling between the two layers as the parameter to capture the ellipse properties of the system in a quantitative manner. However, the basic model of Prandle also allows for a quantitative understanding of the on-set in ellipse properties. These analytical models provide a powerful and essential tool for insight into the ROFI system. However, for a proper description of the vertical variation of the ellipse properties, details of the vertical mixing profile have to be taken into account. A 3D numerical model can provide for this. Therefore an idealized model has been set-up to study the ROFI under the influence of the semi-diurnal tide.

To investigate the dominant fort-nightly time scale, separate neap and spring situations as well as a few full spring-neap cycles are simulated. Given the numerical settings, the system was well-mixed during the spring condition, whereas during neap tide it was stratified. Moreover, the modelled full spring-neap cycle exhibits the succeeding transitions from well-mixed to stratified and back (Fig. 4.16). The second, semi-diurnal time scale is also reproduced. During neap tides a station 12 km offshore in the downstream coastal current exhibited the characteristic tidal straining behaviour (Fig. 4.10). After the successful reproduction of both the spring-neap tidal mixing cycle and the semi-diurnal tidal straining cycle, the numerical model can be applied with confidence to further ROFI research. In Chapter 5 and 6 two simple, yet powerful new concepts are added to the Rhine ROFI body of literature using this model.

In **Chapter 5** upwelling induced by tidal straining is identified as a new key mechanism operating in the Rhine ROFI. We believe its presence shows for the first time the large spatial scale involved with the tidal straining mechanism of Simpson & Souza (1995). The upwelling mechanism has a large impact on for instance the advection and dispersal of nutrients.

When the ROFI is stratified, strong semi-diurnal cross-shore currents are observed (Figs. 1.3, 1.4, 1.5). Due to continuity requirements imposed by the proximity of the coast, the offshore-directed surface currents and onshore-directed bottom currents should lead to coastal upwelling. Due to the small vertical velocities involved, direct measurement is not possible. However, when the surface and bottom water have different properties such as a distinct temperature contrast, a narrow band of upwelled water, as well as its semi-diurnal time scale should be detectable with surface sensors. Fortunately, the very stratification that is indirectly responsible for the existence of upwelling, can also create temperature differences between the surface and bottom waters. Due to excess solar heating, surface waters in a stratified plume in early summer are generally significantly warmer than the surrounding or underlying ambient waters.

The upwelling mechanism is detected using a 6-day unclouded series of SST-imagery in May 1990 with about 2 images per tide. The ROFI is much warmer than the surrounding water, exhibits a distinct diurnal solar heating response and is clearly delineated by large spatial temperature gradients at the edges. This indicates that the whole ROFI area is stratified. On three consecutive middays a marked 5-10 km wide and 100 km alongshore band of cold upwelling is visible along the coastline, while in the morning and afternoon this upwelling band is not present (Figs. 5.3, 5.5, 5.6). The timing of this upwelling indicates that it is caused by tidal straining. The existence of the upwelling mechanism was supported with a simulation with the 3D numerical model of the idealized river plume previously validated in Chapter 4 (Figs. 5.8, 5.10). After adding temperature effects, the numerical model shows the same semi-diurnal band of cold upwelling.

In addition to the cross-shore tidal straining mechanism and the associated upwelling, the SST images also display a bulge of warmer water moving alongshore, independently of the cross shore straining (Fig. 5.3). The movement of this bulge does not fit the cross-shore tidal straining paradigm. Therefore, in Chapter 6 a framework is developed that combines the observed tidal straining paradigm with the observed alongshore movements.

In **Chapter 6** the full potential energy anomaly equation suitable for the analysis of three-dimensional numerical models is first derived. The ten terms that dominate the evolution of stratification in the Rhine ROFI are selected. These principal terms are the cross-shore and alongshore straining and cross-shore and along shore advection of horizontal density gradients. In addition non-linear shear dispersion terms representing correlations between density and velocity perturbations over the vertical control horizontal exchange and mixing in the cross-shore and alongshore directions. Moreover, in the vertical direction two terms dominate the vertical exchange processes. One term describes the effect of vertical mixing on the density profile, the other term is related to vertical advection, which we refer to elsewhere as up and down welling.

These ten terms are examined using the neap tide simulation of the Rhine ROFI that was validated in Chapter 4 and applied to tidal upwelling in Chapter 5. It is shown how the potential

energy anomaly equation can be used to analyse the physical processes affecting stratification. Analysis of the model results using the potential energy anomaly equation allows us to present a detailed overview of the spatial distribution of the terms affecting the evolution of stratification in the Rhine ROFI (Fig. 6.8). The results corroborate the important role that cross-shore tidal straining is known to play in the downstream coastal current region of the plume. In addition, the roles of alongshore advection, as well as alongshore and cross-shore straining are also of importance in the Rhine ROFI, in particular in the region of the bulge near the river mouth. The term ASIPS (advection and strain induced periodic stratification) is introduced as an extension of SIPS introduced by Simpson *et al.* (1990), in order to identify the joint action of these terms (Fig. 6.7). ASIPS is shown to be a natural extension of SIPS, but also forms the key subset of the terms in the potential energy anomaly approach. Near the edges of the river plume the shear dispersion and up and down welling terms also play a significant role, indicating that a different physical balance is dominant in the ROFI interior. Additionally, near the river mouth advection of fresh water lenses plays an important role.

The results for the Rhine ROFI show that the potential energy anomaly equation and ASIPS constitute powerful tools to analyse the mechanisms contributing to mixing and stratification in coastal seas and estuaries.

## 1.5 Outline of thesis

In Chapter 2 a literature survey is performed describing the interaction between the currents and the salinity distribution, the topic of this thesis. First the tidal and residual current system of the entire Southern North Sea is dealt with, before the existing knowledge on tidal mixing and tidal straining in the Rhine ROFI itself is described. Chapter 3 deals with the research approach. First the set-up of an idealised numerical model schematization resembling the Rhine ROFI is introduced. The tidal boundary conditions are derived using a simplified depth-averaged Kelvin wave model with spatially varying linearized friction. Subsequently, attention is paid to validation of the vertical turbulence model, and background details are given on the SST satellite imagery we employ. Chapter 4, 5 and 6 contain the main research items as outlined in detail in the previous section. In Chapter 4 our idealized model of the Rhine ROFI is validated against analytical models of residual and tidal velocity profiles and is shown to reproduce the two time scales known to govern the ROFI. In Chapter 5 upwelling induced by tidal straining is explored using SST imagery and the numerical model. In Chapter 6 tidal advection and straining (ASIPS) are identified as the key suite of processes required to describe intra-tidal variations of potential energy anomaly in the interior of the ROFI. Furthermore, application of the full potential energy anomaly equation to model results is shown to be a powerful new diagnostic tool for coastal ocean modelling in general. In Chapter 7 we synthesize and discuss the results of our analyses.

## Chapter 2

### Literature study

#### 2.1 Scales and scope

The physics governing tidal mixing and tidal straining in the Rhine ROFI, the topic of this thesis, encompasses a wide range of spatial and temporal scales, despite the limitation imposed by use of the predicate tidal. Studying the flow-density interactions at all relevant scales is beyond the scope of this thesis. With respect to temporal scales we focus on intra-tidal interactions but we do not consider processes faster than order 1 hour. With respect to horizontal spatial scales we consider the entire  $50 \times 100 \text{ km}^2$  ROFI (Fig. 2.1), but we do not consider structures finer than order 1 km. However, with respect to vertical scales we consider continuous variations of properties over the vertical. Although the Rhine ROFI can be characterized as a shallow water system with a water depth of only 20 m, within this relatively thin layer of water, vertical variations of both the density and horizontal velocity profiles are of paramount importance, and fully determine the basic nature of the ROFI.

Despite this limitation of spatial and temporal scales in this thesis, we realize that the tidal scales cannot always be separated from larger and smaller scales in a straightforward manner; they interact with the other scales to a high degree. At one side of the spectrum, the semi-diurnal tide in the Rhine ROFI is determined by the amphidromic system that covers the entire North Sea. Moreover, the density structure of the Rhine ROFI is governed by the residual current structure and water mass division that covers the entire North Sea. These important aspects are dealt with in a literature survey in sections 2.2 and 2.3. Wind and wave components are not the subject of this thesis; there is a vast literature on these subjects which we do not address here.

The topic of this thesis, the behaviour of the interactions between the tide and the 3D density field, has been studied extensively. Therefore in section 2.3 we perform a thorough literature survey of the governing concepts as introduced by Simpson and co-workers, before we extend these concepts in the main body of this thesis. The two main time scales of the Rhine ROFI as determined by tidal mixing and tidal straining are treated in detail, with the mathematical descriptions in Appendix 4.6.

## 2.2 The North Sea: density and residual current field

### 2.2.1 Depth averaged situation

The average density field upon which the semi-diurnal tide acts is determined by the residual current pattern that covers the entire Southern Bight of the North Sea. The North Sea has been classified into different hydrographical regions (Fig. 2.2). The riverine sources and lateral boundaries that are responsible for replenishing North Sea water are reflected in the water type names in this classification. The water mass classification shows that only Channel water (A3) and riverine continental coastal waters (A4) waters are relevant for the Rhine ROFI. The Rhine is the biggest river contributing to continental coastal water, so water type A4 is de facto the Rhine ROFI, diluted with water of Channel origin (A3). The water mass classification of the Southern North Sea is clearly reflected in remote sensing images of temperature and ocean colour, both of which are shown and compared in Pietrzak *et al.* (2008b) (see also Fig. 1.6). Their monthly SST images are enclosed here in Figs. 3.8, 3.9 and 3.10 for one year (1998).

The water type distribution is governed by the mean/residual circulation pattern of the North Sea, induced by the prevailing winds, the tide and by the density field itself. The tidally induced residual flows are largest along the coastal regions where the Kelvin wave amplitudes are largest and are directed in the same direction as the propagation of the Kelvin wave (Nihoul & Runday,

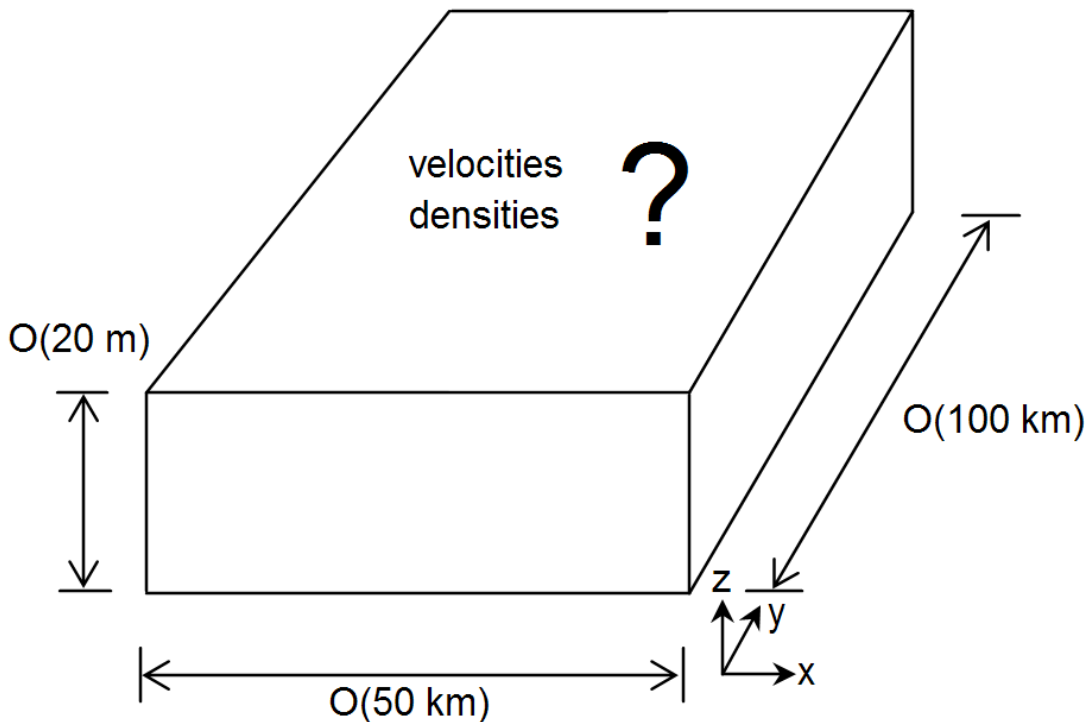


**Figure 2.1:** The topic of this thesis is the interaction between the tidal velocities and the 3D density structure in the Rhine ROFI. The study covers the entire  $50 \times 100 \text{ km}^2$  ROFI.



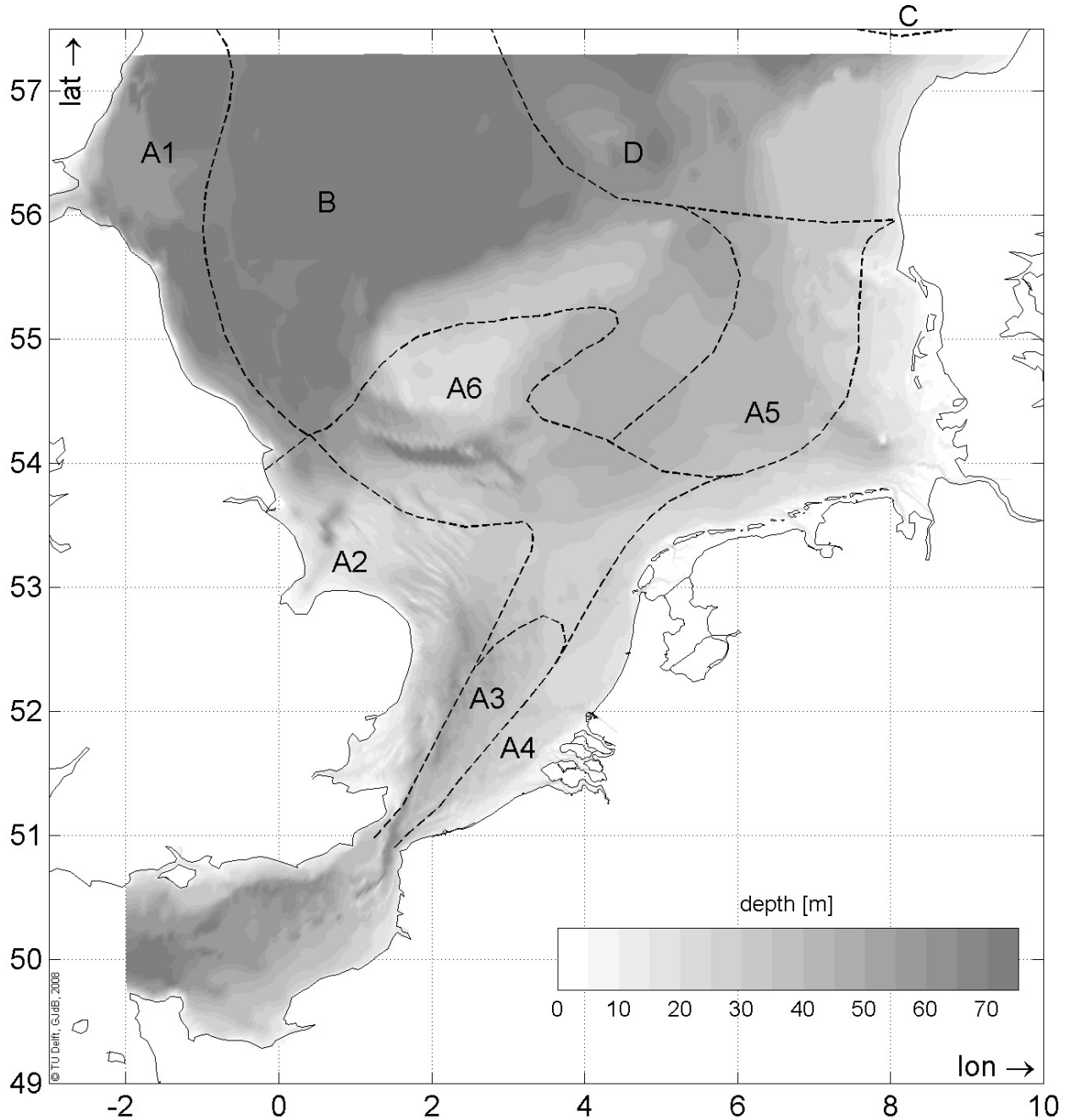


**Figure 2.2:** Classification of the different North Sea water masses [after Lee (1980) Fig. 14.13] who compiled this figure based upon data of Dietrich (1950) and Laevastu (1963). The water mass classification is based upon nearly a century of measured water properties such as salinity and radio-active isotopes, residual current data and numerical modeling work (Otto *et al.*, 1990). The water types are A1 (Scottish coastal water), A2 (English coastal water), A3 (Channel water), A4 (continental coastal water), A5 and A6 are transitional areas between A4 and B (Northern North Sea water), D is transitional water to C (Skagerrak and the Norwegian Rinne).

1975; Prandle, 1978; Tee, 1979, 1980; Prandle, 1984; Ye & Garvine, 1998). A second source for residuals in the Southern Bight is the wind. The average WSW direction of the wind, the predominant cyclonic rotation of the wind fields in combination with the bottom slope of the North Sea are responsible for a cyclonic residual current (Otto *et al.*, 1990). These tidal and wind driven residual currents are responsible for a net transport through the Channel northwards through the Rhine ROFI with an average velocity of a few  $\text{cm s}^{-1}$  (Fig. 2.3).

For a long time these wind and tide generated 2D cyclonic circulation patterns were considered to be representative for the North Sea (Zimmerman, 1978). This assumption made transport studies like those of Prandle (1984), van Pagee (1986) and de Ruijter (1987) possible (Fig. 2.3). The third source for residual flows, baroclinic flows, was considered negligible as a forcing mechanism for the Southern North Sea. Indeed the transport through Dover Strait is not much affected by density differences (Prandle, 1978). However, closer to the coast where lower densities due to river runoff prevail, the cyclonic circulation pattern is significantly enhanced by density effects. This holds especially for the Rhine ROFI.

Describing the paramount density driven residuals in the Southern North Sea requires a detailed knowledge of the prevailing density fields, which are governed by both salinity and temperature differences. Temperature is important in the central North Sea where salinity differences

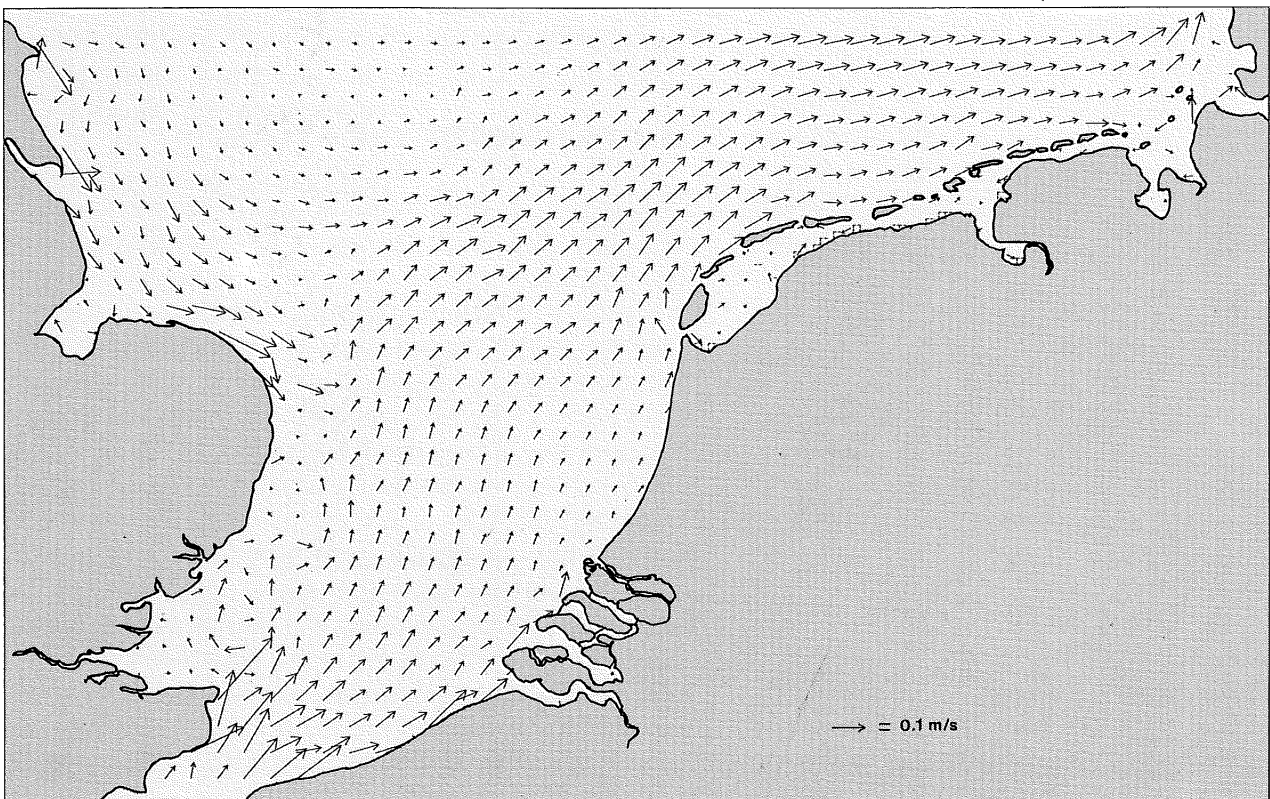


**Figure 2.3:** Depth averaged residual current field for a  $4.5 \text{ ms}^{-1}$  SW wind field [De Ruijter *et al.* (1987) Fig. 7].



are small. In contrast, haline differences prevail near the coast where they dwarf temperature effects. These temperature and salinity variations are reflected in the water mass classification in Fig. 2.2.

Temperatures patterns show a pronounced seasonal cycle. In the winter the Channel water temperature drops to 7 to 9 °C, while the coastal waters are colder due to colder river runoff. In contrast, in the summer time the Channel water is relatively cool with 16 to 17 °C, because the coastal waters are warmer at about 18 °C due to warmer land runoff and more shallow depth (Pietrzak *et al.*, 2008). However, density differences in the Rhine ROFI are governed by the salinity structure and not by temperature (De Kok *et al.*, 2001). Pronounced temperature patterns do occur, but mainly as a response to haline stratification. Therefore these temperatures do not significantly affect the flow structure. In chapter 5 it is shown that these temperature anomalies can conveniently be used to diagnose the salinity structure, by considering them as a non-conservative tracer.

The salinity structure of the North Sea was first mapped in the ICES atlases, and determines the prevailing water mass classification. Near the coast the water is relatively fresh (below 30 PSU) from where the salinities increase further offshore, reaching a maximum of over 34.5 halfway the Southern Bight in the Channel water mass (A3). At its southernmost tip in the Strait of Dover, the lower salinities in the continental coastal water mass (A4) originate almost entirely from the Rhine, and to a lesser extent from the much smaller Scheldt (Lacroix *et al.*, 2004). The depth and time averaged salinity structure in the Rhine ROFI region is fairly well known from cruise observations (Van Alphen *et al.*, 1988; Van der Giessen *et al.*, 1990; De Ruijter *et al.*, 1992; Simpson *et al.*, 1993; De Ruijter *et al.*, 1997; Suijlen & Duin, 2002). The average density gradients are predominantly cross shore, while in the alongshore direction the time averaged density field is approximately uniform (Suijlen & Duin, 2002) (Fig. 2.4). It should be stressed that the instantaneous density field is much more complicated due to for instance baroclinic instabilities and fresh water lenses.

The density structure in the Rhine ROFI is the result of the prevailing alongshore currents, which are mostly governed by the local density field. The dominant cross shore salinity gradient, in combination with Earth rotation, is responsible for this alongshore residual flow called a coastal current <sup>1</sup>. Residuals of 10 cms<sup>-1</sup> have been measured in the surface layer (De Ruijter *et al.*, 1992). Due to these residual currents the Rhine plume can maintain its cross shore density structure for hundreds of kilometres, thus forming the continental coastal water mass. The mutual reinforcement of the alongshore residual currents and the cross-shore density gradients makes the narrow coastal current a persistent system. The basic governing 2D current and density structure with coast-parallel isohalines in the Rhine ROFI region is sketched in Fig. 2.5.

---

1. *Kustrivier* in Dutch.

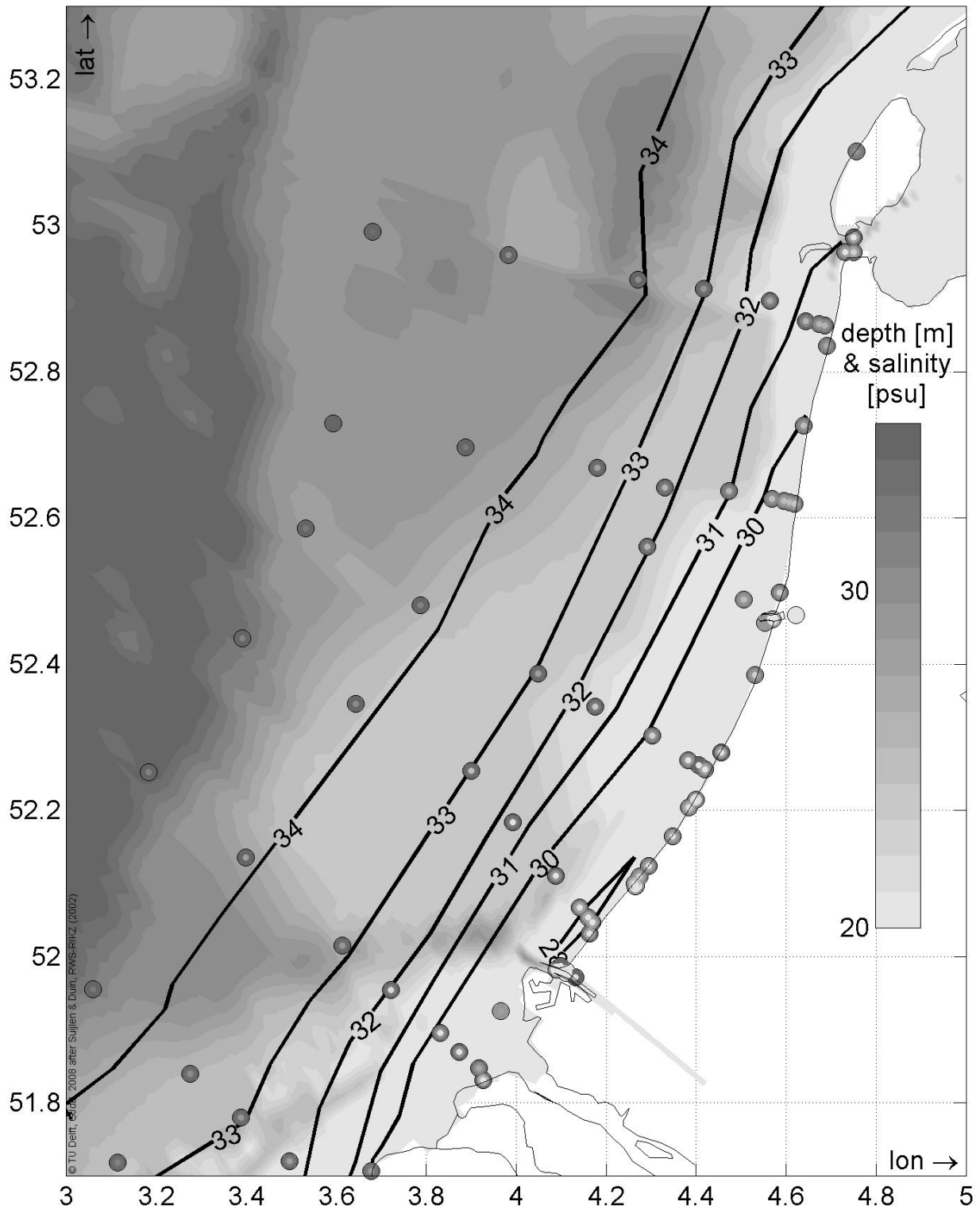


**Figure 2.4:** The average surface average salinity in the Rhine ROFI area based on 14 years of bi-weekly surface samples at the locations indicated with filled dots. [after Suijlen & Duin (2002) chart 2]. The colors in each dot indicate the long-term salinity values of the measurements at that location. The outer ring represents the maximum value, the middle ring the average value and the inner ring the minimum value.

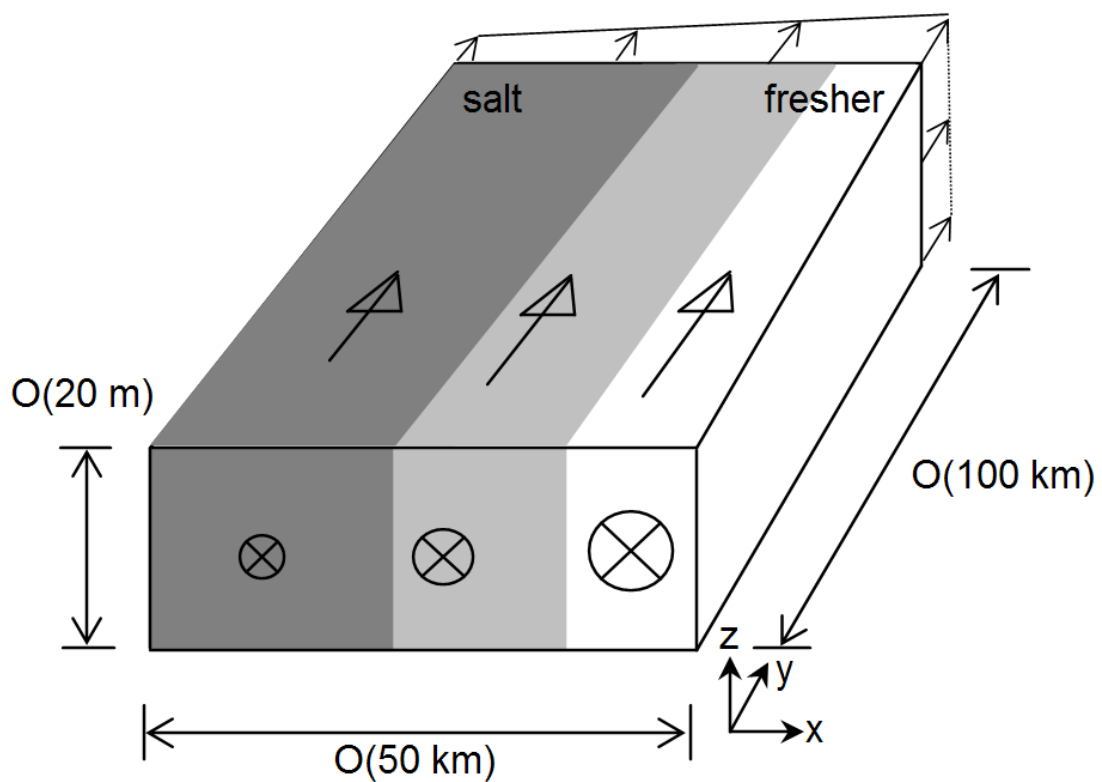


**Figure 2.5:** Cartoon of the 2D density and residual current structure in the Rhine ROFI, characterized by a cross shore density gradient and an alongshore velocity with maximum values near the coast.

### 2.2.2 3D situation

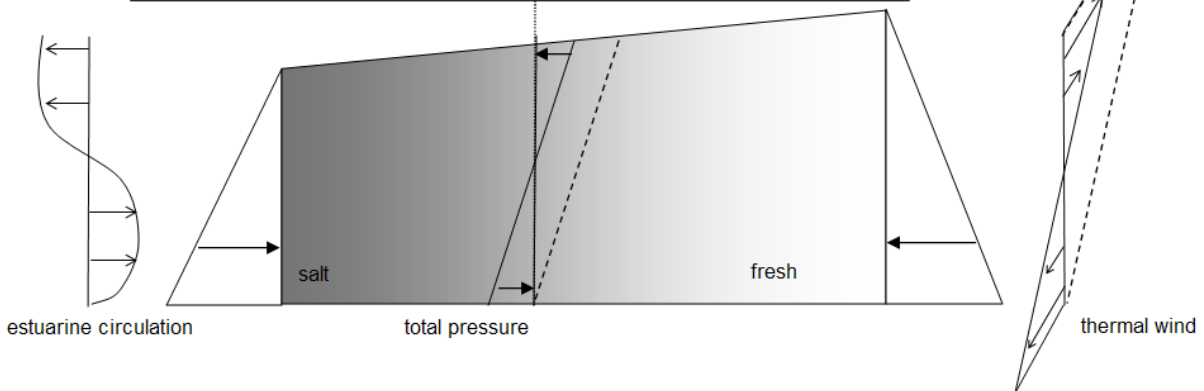
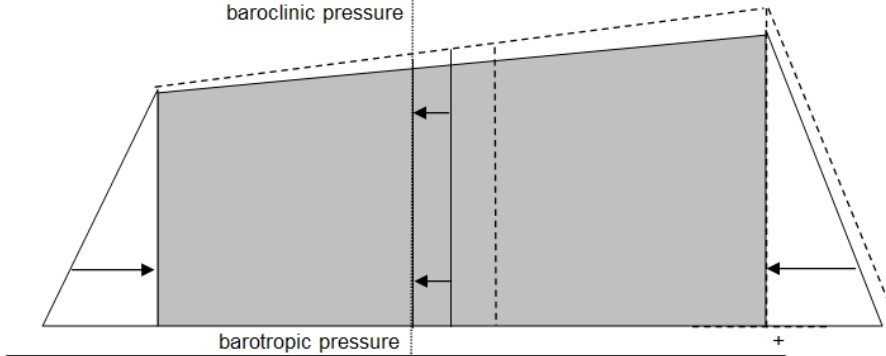
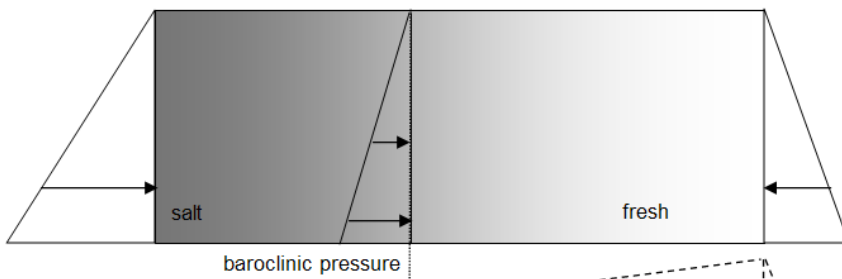
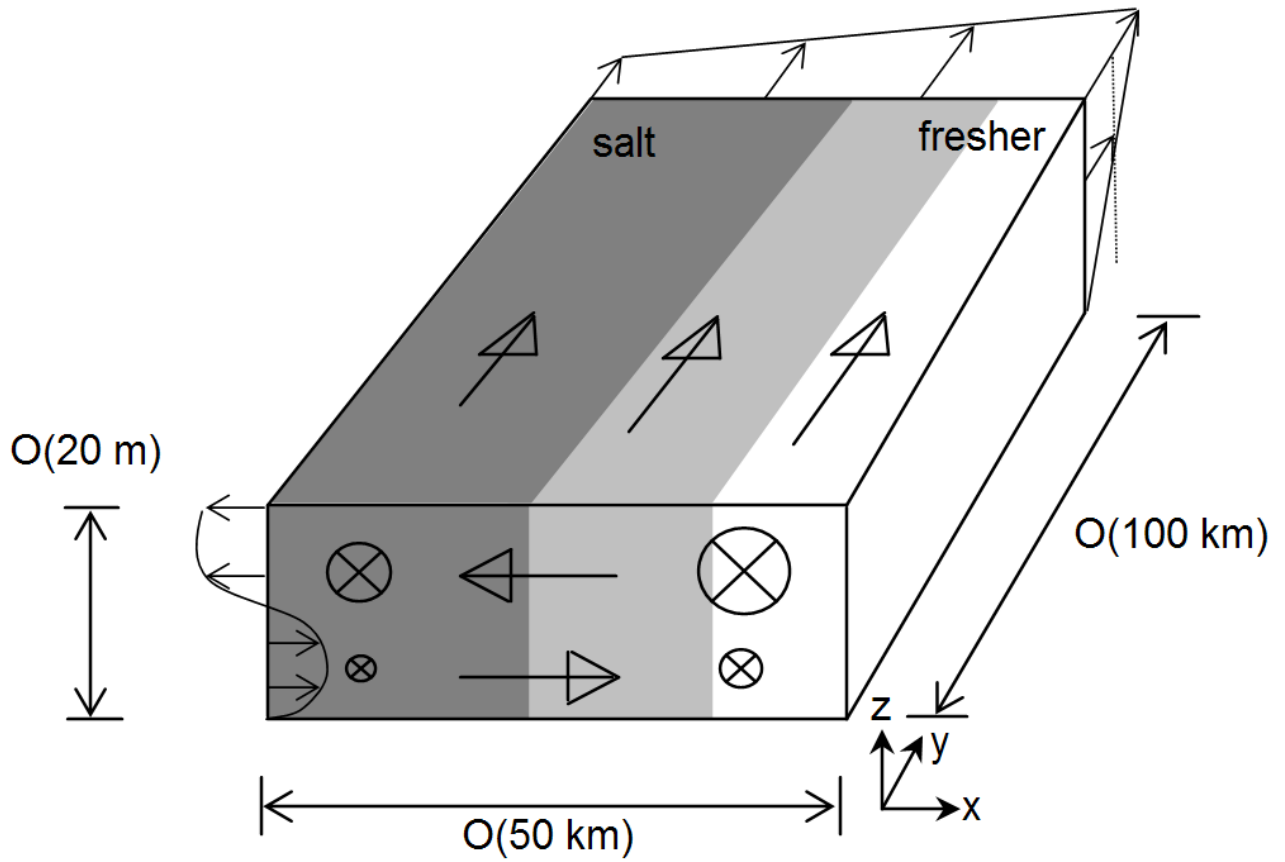
The depth-averaged water mass classification and residual current field described in the previous section also have an important vertical structure with respect to density and velocity. In the Rhine ROFI the density driven flow dominates over tidal and wind driven residuals. The description of the vertical velocity structure of a stationary density driven flow is given by Heaps (1972). In the alongshore direction a residual northward velocity shear is established that is basically in geostrophic balance with the cross shore baroclinic and barotropic pressure gradient (Fig. 2.6), known as ‘thermal wind balance’ from its origin in meteorology. However, because the Southern North Sea is a shallow frictional sea, there is a significant deviation from the basically frictionless thermal wind balance. In the cross shore direction there is also a gravitational (estuarine) exchange current comparable to the salt wedge exchange current in an estuary. This exchange profile has been described separately by Officer (1976). The residual current pattern from Heaps (1972) is a combination of the alongshore geostrophic thermal wind flow and cross-shore the gravitational circulation (Fig. 2.6).

The horizontal density gradients in the Rhine ROFI are not uniform. On average the cross shore density gradients are one order of magnitude larger than the along shore density gradients. For application of the Heaps profile only the cross shore horizontal density gradients can be taken into account. These cross shore density gradients diminish rapidly offshore. Because the horizontal density gradients determine the magnitude of the currents, the alongshore and cross shore currents tend to diminish as well offshore. By assuming an analytical expression for the offshore decay of the cross shore density gradient, one can construct a simple 3D picture of the governing 3D residual velocity field (Visser, 1993) (Fig. 2.7).

Measurements have corroborated the validity of the Heaps profile in the Rhine ROFI. Van der Giessen *et al.* (1990) show 2.5 to 3.5  $\text{cms}^{-1}$  onshore near bottom velocities, indicative of the estuarine circulation component, while in the surface layer typical velocities of 7 to

---

**Figure 2.6 (on the next page): (top)** Cartoon of the 3D density and current structure in the Rhine ROFI. Further to the 2D case shown in Fig. 2.5 the alongshore velocity varies almost linearly over the depth. In addition there is a current profile in the cross shore plane typical for density-induced exchange flows. **(bottom)** Cross shore force balance in thermal wind case. The sum of the barotropic and baroclinic pressure leads to an offshore force on the near-surface layers and an onshore force on the near-bed layer. A barotropic pressure gradient (dotted line) would result in a depth averaged offset of the alongshore velocity. In a frictionless case the cross-shore pressure gradient would be balanced only by the Coriolis force generated by an alongshore velocity profile with constant shear. This limit case is called ‘thermal wind’. In contrast, when friction is dominant, the cross-shore pressure gradient would be balanced only by the non-uniform velocity shear generated by the the cross shore exchange current. This limit case is called the ‘estuarine/gravitational circulation’. Heaps (1972) described the joint action of the alongshore thermal wind and cross-shore estuarine circulation velocity profiles.



$11 \text{ cms}^{-1}$  occur with a strong northward component, indicative of the thermal wind component. However, they also show that winds have a large effect on the residual currents. Simpson (1997) shows the occurrence of the Heaps (1972) profile with more detail over the vertical.

Similar to the residual current structure, the density structure is not homogenous over the vertical either. Stratification often occurs in the Rhine ROFI. Van Alphen *et al.* (1988), for instance, display the average stratification based on 20 cruise surveys (Fig. 2.8). A nearshore band of about 10 to 30 km wide in the continental water mass is generally stratified. Alongshore the stratified area can extend over 100 km. In line with the results of Lacroix *et al.* (2004) the stratification also extends far south. The presence of stratification is also visible in the sea surface temperature. Otto *et al.* (1990) show fronts observed from satellite infra-red images (Fig. 2.9). Alongshore fronts are visible from Belgium Northwards all the way along the continental coastal water. These data are in line with the extent of stratification sketched by of Van Alphen *et al.* (1988) and Pietrzak *et al.* (2008a).

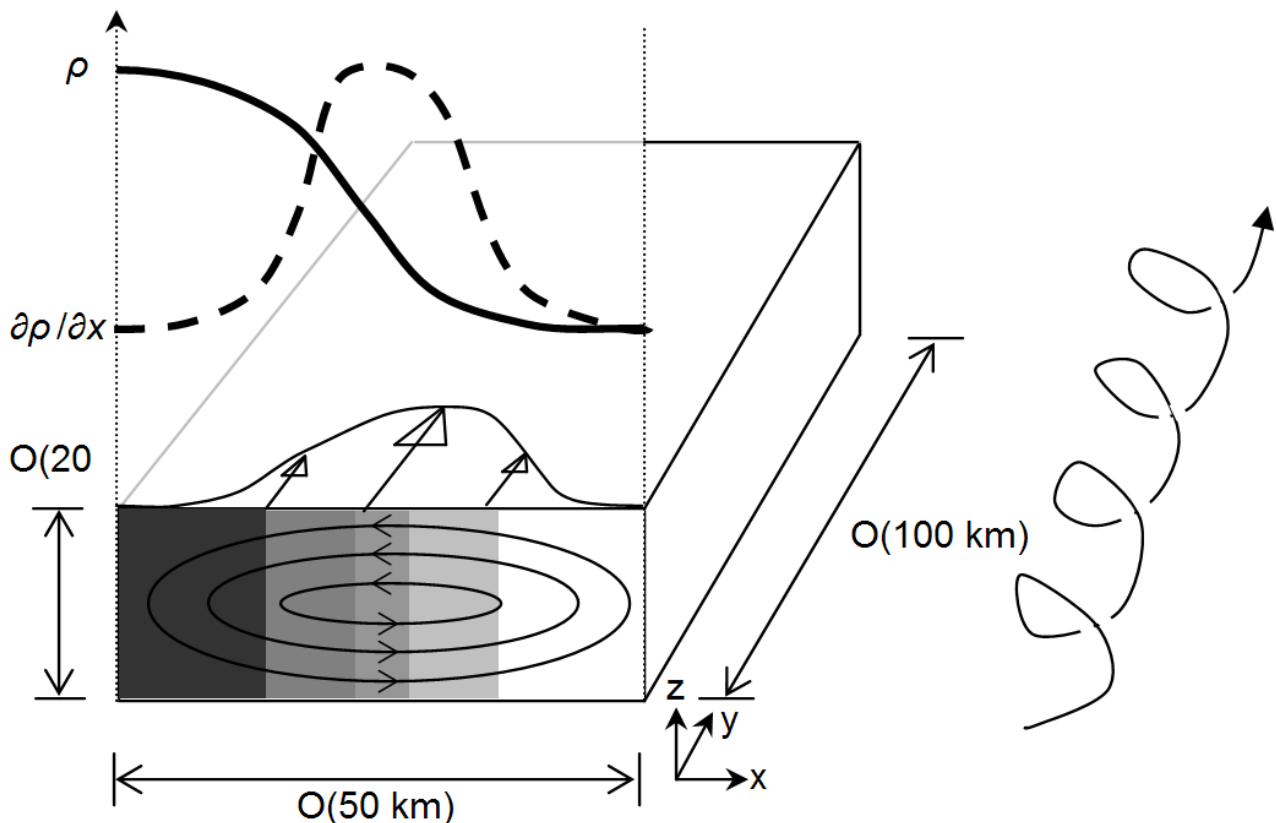


**Figure 2.7:** Cartoon of the 3D residual current structure after Visser (1993). The density  $\rho$  is assumed to vary with the shape of an S-curve such that the associated crossshore density gradient  $\frac{\partial \rho}{\partial x}$  exhibits a Gaussian curve. This results in a crossshore Gaussian distribution of both the alongshore ‘thermal wind’ velocity and of the crossshore exchange current. Visser (1993) showed that a non-buoyant particle would follow an helical path in this 3D velocity field.

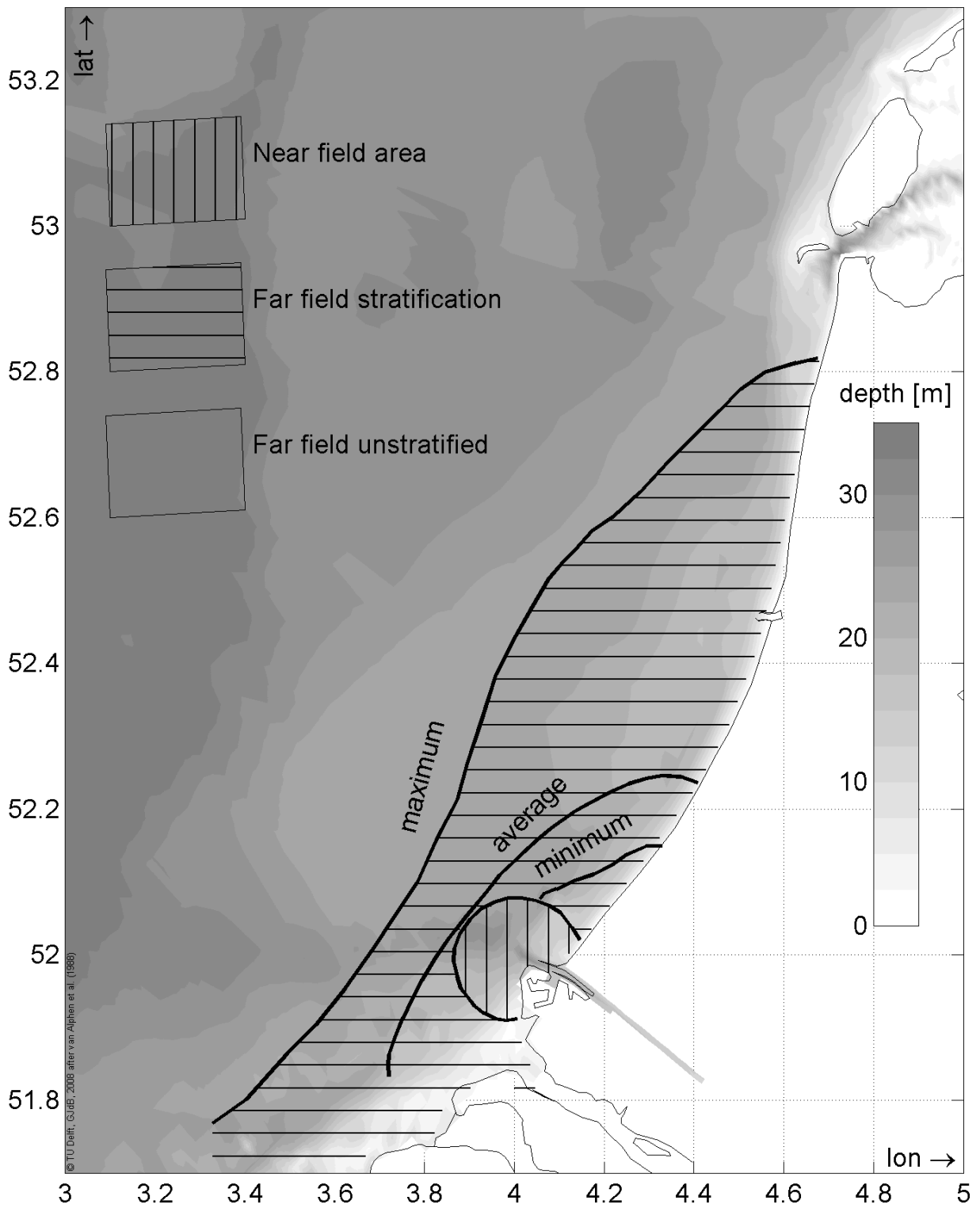
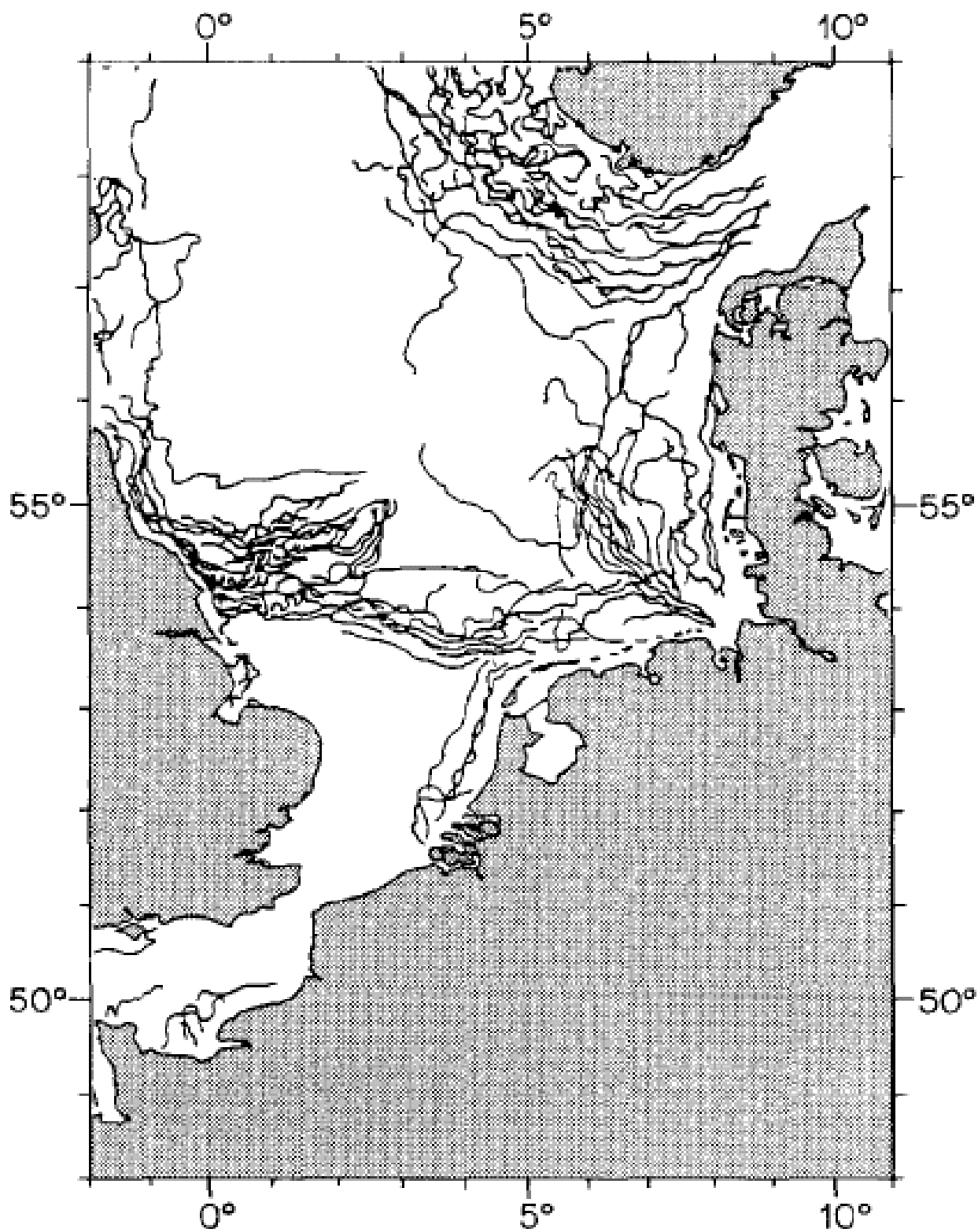


Figure 2.8: Extent of stratification in the Rhine ROFI area [after Van Alphen *et al.* (1988) Fig. 14].



**Figure 2.9:** Position of fronts as observed from infrared satellite imagery [Otto *et al.* (1990) Fig. 3.6, after Harding (pers.com.)].



### 2.2.3 River plumes

In the previous section the average currents of the Rhine ROFI were described by assuming a cross shore density gradient only. In the alongshore direction the Rhine ROFI was assumed homogenous. However, for the instantaneous salinity distribution this is far from true most of the time. Significant along-shore gradients can occur in certain positions and under certain conditions due to river discharge lenses, meanders and baroclinic instabilities (De Kok, 1996). Consequently, the Rhine ROFI is expected to look more like Fig. 2.10. Due to the anisotropy of this density field, the residual currents are not likely to be as simple as in Fig. 2.5. The most important source for anisotropy is the river mouth itself. At the location where the fresh water debouches into the marine environment, an anti-cyclonically rotating bulge of less saline water is formed. After a cyclonic turn this bulge feeds into a coastal current in the direction of the Kelvin wave. The system of bulge and the coastal current is known as river plume, the basic anatomy of which is sketched in Fig. 2.11.

The basic current structure at a position in the river plume is still expected to obey the vertical

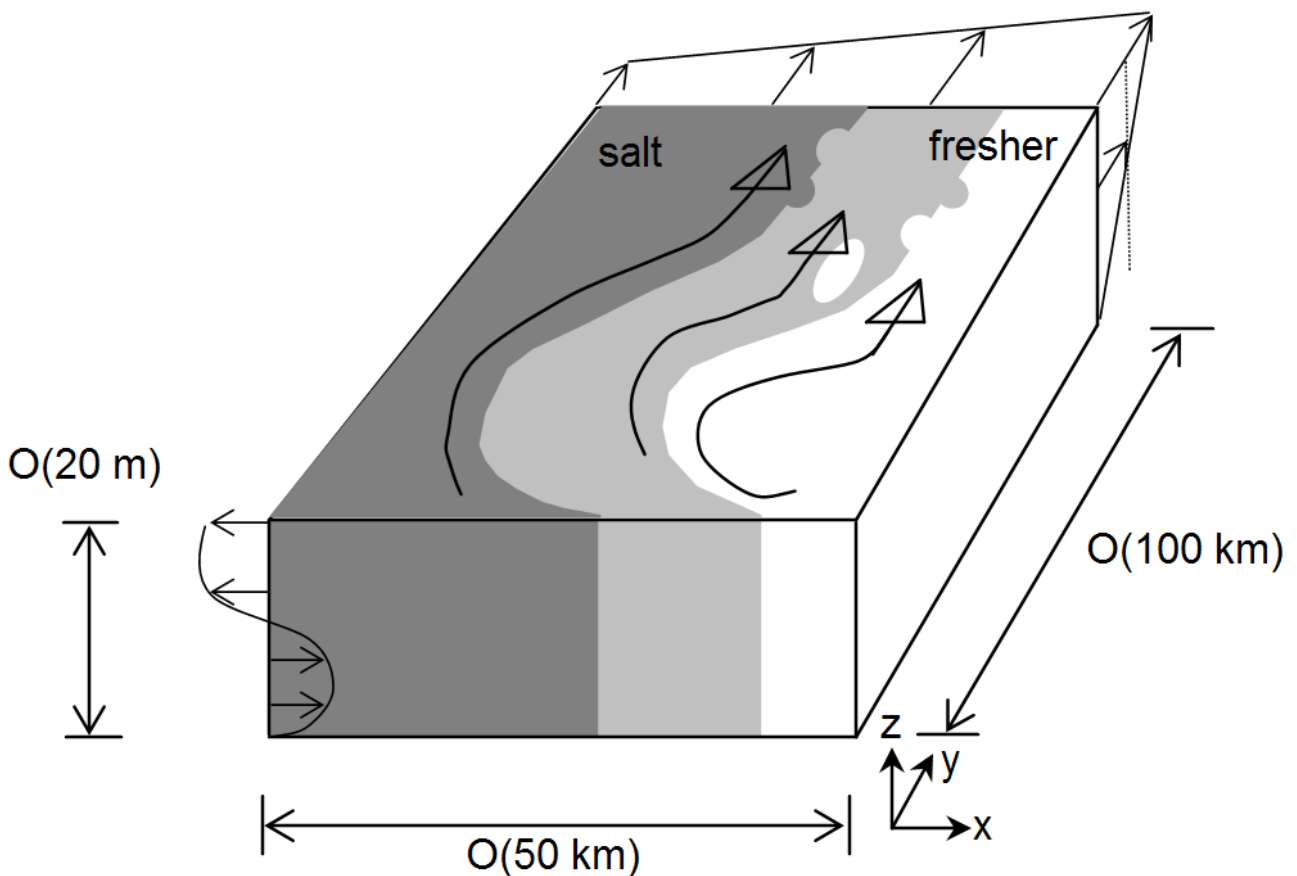


**Figure 2.10:** Cartoon of the density structure of the Rhine ROFI. The principles of the velocity profile sketched in Fig. 2.6 still hold when the thermal wind velocities are redefined in an isohaline plane rather than in the alongshore plane.

profile of Heaps (1972). However, rather than using alongshore and cross shore components (Fig. 2.5), the currents should be defined in a coordinate system aligned with the isopycnals (Fig. 2.10). Near the surface an along-isopycnal current is present, whereas in the bottom layer there is a cross-isopycnal current (Fig. 2.11). Near the bottom there is a cyclonic inward spiralling flow, whereas near the surface there is an anti-cyclonic outward spiraling. In addition, whereas Heaps assumed a spatially uniform density field, hence a spatially uniform current pattern, the salinity structure of a river plume is more dynamic.

Numerous factors influencing the behavior of river plumes have been studied. Mestres *et al.* (2007) give a succinct overview of the variety of modeling efforts. Shao & Boicourt (1986) were the first to model estuarine river plumes with a 3D numerical model, in contrast to previous analytic plume studies such as Kao (1981). The effect of wind on river plumes was modeled soon after that by Chao (1988) for a wide estuary. Their work was extended onto the shelf by for instance Kourafalou *et al.* (1996a), Xing & Davies (1999), Garcia Berdéal *et al.* (2002)

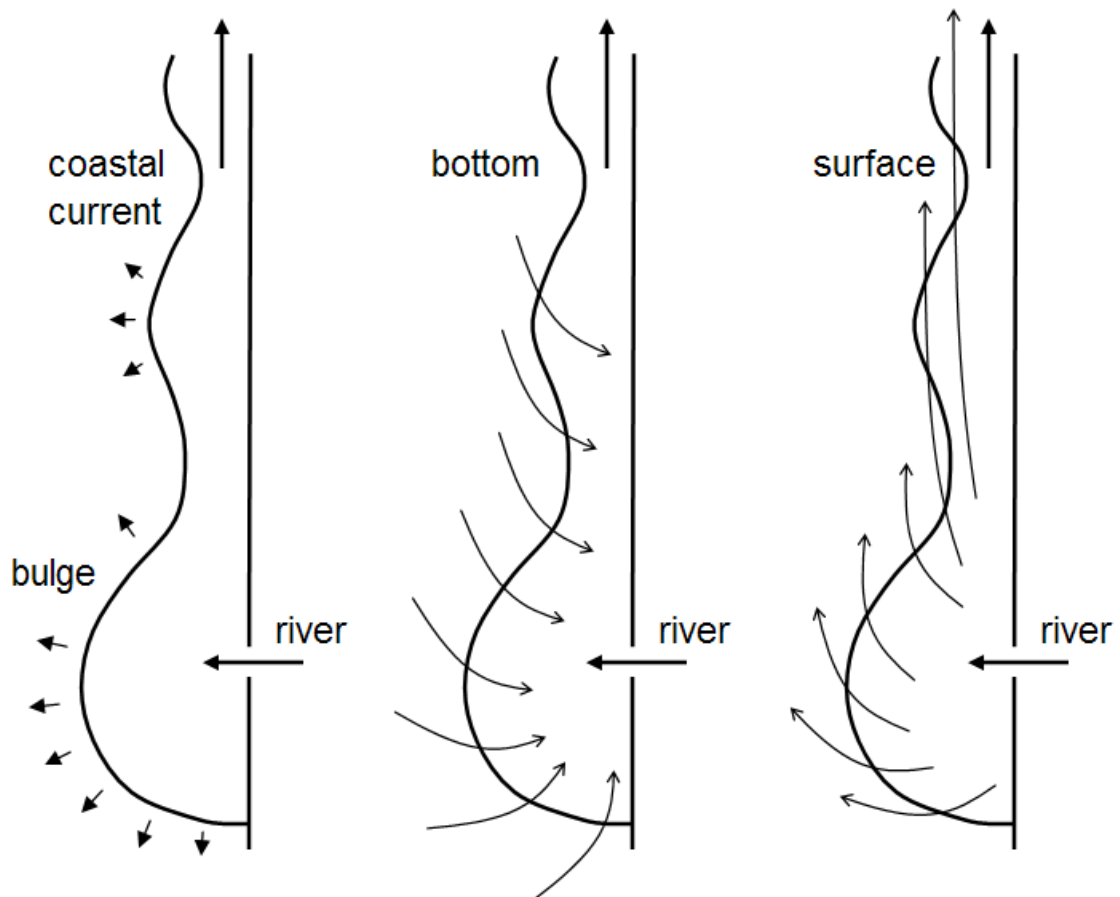


**Figure 2.11:** Sketch defining river plume. Near the seabed there is an inward (about cross shore) velocity component, near the water surface there is an outward (about cross shore) velocity component. In the surface layer the velocities have a strong along-isopycnal component, whereas in the bottom layer there is a dominant cross-isopycnal velocity component.

and Fong & Geyer (2001). These studies all affirm the conclusion of Chao (1988) that the plume response to the wind can be described by Ekman drift, even when the area is shallow and frictional. During upwelling favorable alongshore wind, the plume is advected offshore and thins (Fig. 2.12). The cross shore current shear, the increased plume surface area and the thinning make the plume prone to mix up, with most intense mixing occurring at the seawards plume front (Fong & Geyer, 2001). In contrast, during downwelling favorable, alongshore wind, the coastal jet is strengthened, leading to alongshore acceleration of the plume. In chapter 5 the response of the Rhine plume to wind is also shown to be in approximate Ekman balance.

3D numerical models are a tool commonly employed for river plume studies. Here the tuning parameters are of key importance. For instance, the advection scheme adopted has a profound effect on the evolution of the plumes, as shown by Hyatt & Signell (2000). Moreover, Davies & Xing (1999) show that the choice of the vertical turbulence model and background

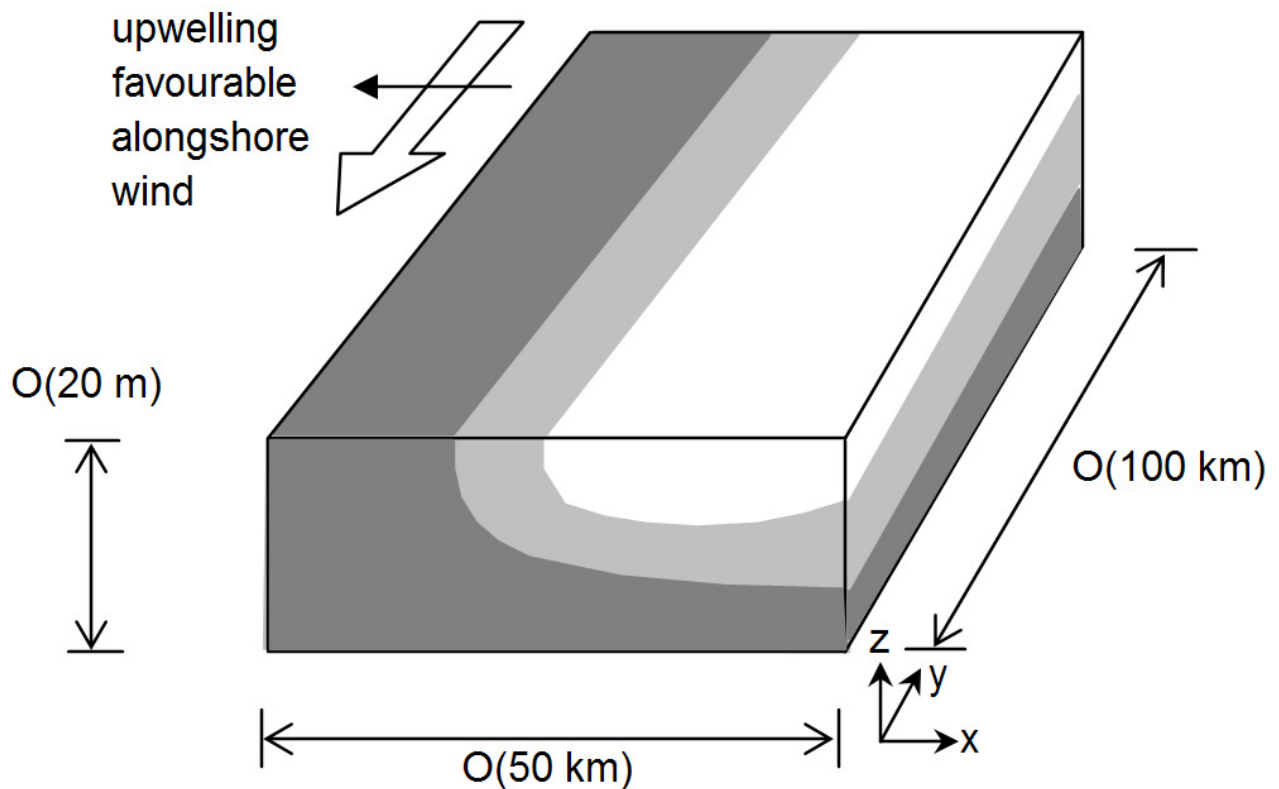


**Figure 2.12:** Cartoon of the effect of alongshore upwelling favorable wind. The upper plume layer responds in approximate Ekman balance moving offshore with alongshore winds (NH). The offshore movement causes thinning, a growing surface area and an enhanced stratification which together cause increased mixing. The alongshore velocities diminish. For southerly winds the effect is opposite, leading to a near coast well-mixed plume near the coast, accelerating alongshore (following Fong & Geyer (2001)).

mixing rate determine the alongshore and cross shore extent of the plume. However, they also show that topographic effects can be more important. A bathymetry deepening offshore, limits the offshore extent and meandering of the plume. Numerous other studies have also focused on the effect of geometrical and bathymetric features (e.g. Garvine (2001)). The effect of discharge variations has been studied in detail. Nof & Pichevin (2001) show that when only fresh water is modeled, the plume bulge is growing forever, while hardly any coastal current is formed. They called this ‘the momentum paradox’, as in reality bulges do not grow forever. Fong & Geyer (2002) show that either wind or an ambient alongshore current are required to let the river discharge eventually match the discharge of the coastal current to get a stable bulge. In this thesis we do not elaborate on the effect of all these parameters, as we focus on the key effect of the tides only. Although bathymetric effects are important, we employ a rectangular tidal sea with a constant river discharge and a flat bottom, to facilitate our interpretation of the governing baroclinic physics.

The effect of tides on river plumes has not received much attention. Authors who studied the effect of tides focused on the near field close to the estuary. Chao (1990) for instance found two counter-rotating eddies offshore of the river mouth which affect the river plume bulge. However, he used cross shore shelf tides, so that his theories are not applicable to the Rhine ROFI which has alongshore tides (see section 2.3). Blanton *et al.* (1997) showed that ebb tidal advection of fresh water turns abruptly south with the shelf current when leaving the estuary. In the Rhine ROFI a similar near field effect of tides has been described by Van Alphen *et al.* (1988) (their Fig. 6), Ruddick *et al.* (1994) and (De Ruijter *et al.* (1997), their Fig. 8). Frontal formation and strong downwelling are reported just outside the river mouth. In chapter 6 the trajectories of fresh water lenses are further discussed, employing Potential Energy Anomaly arguments. However, no study has focused on the larger scale effect of tides on river plumes on the shelf. On the widely studied river plumes on the deep USA east and west shelves tidal affects can often be neglected, but for the shallow Rhine ROFI the tides are always of paramount importance.

The dynamically most energetic forcing in the North Sea is the semi-diurnal tide (Zimmerman, 1986). In the North Sea the semi-diurnal M2 and S2 tides dominate. Inclusion of the tide to the aforementioned residual flows involves a dramatic change of the vertical mixing of salinity and momentum in the plume. A drawback of residual current models often employed for river plume studies is that there is hardly any generation of turbulence in the model. That means that the effective mixing in the model reverts almost all the time to the background mixing imposed in the turbulence model. For instance Garcia Berdéal *et al.* (2002) note that “holding both vertical mixing coefficients at a constant value of  $10^{-4}$  and  $10^{-3} \text{ m}^2\text{s}^{-1}$  instead of using the closure scheme (with imposed background values  $10^{-4}$  and  $10^{-3} \text{ m}^2\text{s}^{-1}$ ) yielded virtually identical runs”. The inclusion of the tide in river plume simulations can therefore be said to be a prerequisite for realistic mixing. Therefore, in the next sections the tide in the Southern North Sea is investigated, before tidal mixing is discussed in section 2.3.

### 2.3 The North Sea: barotropic tidal field

The tides in the Rhine ROFI are determined by the geometry of the entire North Sea, and the Southern Bight in particular. The most energetic components are the semi-diurnal M2 tide (amplitude order 1 m) and the smaller S2 tide (order 10 cm)<sup>2</sup>. The first co-tidal M2 map of the North Sea, based solely on observations, was published by Proudman & Doodson (1924) (Fig. 2.13). The M2 tide is generated by the co-oscillation of this (sub-) basin with the Atlantic Ocean, and further amplified internally. The resulting tidal wave propagates cyclonically along the edges of the Southern Bight, such that in the Rhine ROFI it has the character of a Kelvin wave propagating northward along the Dutch coast. The conceptual behavior of such a coastally trapped wave was first elaborated by Taylor (1921) for a semi-enclosed rectangle. This study shows the main characteristics: a set of amphidromic systems along the main axis of the basin with the elevation amplitude increasing exponentially towards the coasts. Between the two opposing coasts there is a point with no tidal elevation, the amphidromic point. The depth-averaged velocities describe ellipses near corners where the Kelvin wave is deflected inducing Poincaré waves. However, the velocities are coast-parallel along all straight parts of the coastline, where they can be described with degenerated ellipses. The latter is the case for the entire Rhine ROFI. In the propagating Kelvin wave the velocities are in phase with the elevations. Maximum velocities occur at high water, although friction introduces a small phase shift.

In the Rhine ROFI the co-tidal phase lines are more or less normal to the coast, with the tidal elevation lines almost coast-parallel. The Kelvin wave propagates along the straight Dutch coast from South to North with almost no amplitude decay on its path, but with a fair cross shore tilting in line with the large external Rossby radius. The chart shows amplitudes ranging from 60 to 90 cm. The S2 tide behaves similarly, albeit with smaller amplitudes ranging from 10 to 20 cm. The vertically averaged velocities vary between 0.5 and 1.0 ms<sup>-1</sup> (De Kok, 1996) while within the ROFI area surface currents have speeds ranging between 0.7 and 1.1 of ms<sup>-1</sup> over the spring-neap cycle (Van Alphen *et al.*, 1988; Van der Giessen *et al.*, 1990). The basic behavior of the tidal Kelvin wave in the average density field of the Rhine ROFI is sketched in Fig. 2.14.

The interaction between the major axis of the Kelvin wave velocities and the average density field was the first studied interaction between the tide and the density field. Due to the proximity of the coast, the tidal velocities are alongshore over the entire water depth. Because the average density gradients are cross shore, there is no first order systematic interaction between the Kelvin wave and the average density structure (Fig. 2.15). However, near the mouth of the Rhine, fresh water lenses may be present (Van Alphen *et al.*, 1988; De Ruijter *et al.*, 1992; Simpson *et al.*, 1993; De Ruijter *et al.*, 1992, 1997; De Boer *et al.*, 2007; Pietrzak *et al.*,

---

2. For the North Sea 300 years of tidal water levels recordings are available (IPCC, 2001). The Dutch Ministry of public Works makes water level recordings available on the Internet for Rhine ROFI stations Hook of Holland from 1900 and at Katwijk from 1737 ([www.waterbase.nl](http://www.waterbase.nl)).

2008b,a). The interaction of the tide with these lenses consists of an alternate tidal advection in North and South direction with the tidal excursion (Van Alphen *et al.*, 1988; De Ruijter *et al.*, 1997).

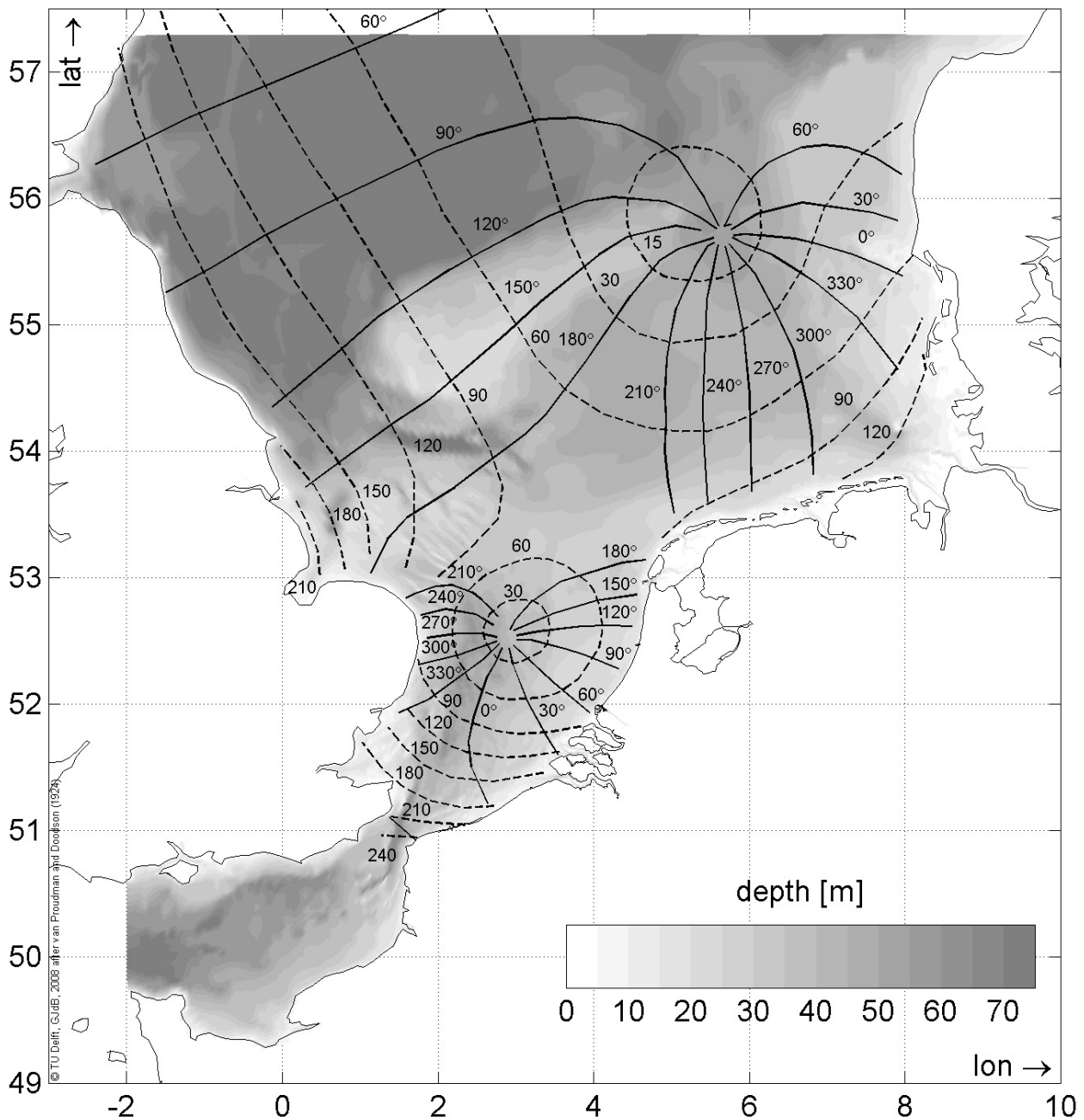


**Figure 2.13:** The first compilation of the amphidromic system of the North Sea, based on observational data only [after (Proudman & Doodson, 1924) Fig. 11].



## 2.4 Tidal mixing and straining

In the previous sections the density structure and tide in the Rhine ROFI were discussed. The subject of this thesis is the interaction between those two fields. The basic interaction, along-shore advection of fresh water lenses with the tidal excursion, is already understood since Van Alphen (1988). Significant steps forward in our understanding of the tide-density interactions in the Rhine ROFI were made in the early 1990s with extensive EU-sponsored field measuring campaigns in the PROFILE project (Huthnance, 1997) and later that decade during the PROVESS project (Howarth *et al.*, 2002). Simpson and co-authors (Simpson *et al.*, 1993; Visser *et al.*, 1994; Simpson & Souza, 1995; Souza & James, 1996; Souza & Simpson, 1996, 1997; Simpson, 1997; Souza & Simpson, 1997; Joordens *et al.*, 2001; Fisher *et al.*, 2002; Souza *et al.*, 2008) describe the results as the basic mixing-stratifying-straining processes that take place in the Rhine ROFI. In the Rhine ROFI the buoyancy input competes with wind, wave and tidal mixing to establish stratification. Tidal current profiles are significantly affected by this stratification, as well as residual current profiles. Simpson *et al.* (1993) detected two distinct time scales in the water column structure: a spring-neap cycle imposed by tidal/wind mixing and a semi-diurnal cycle imposed by tidal straining. These two interactions are discussed in detail in this section.

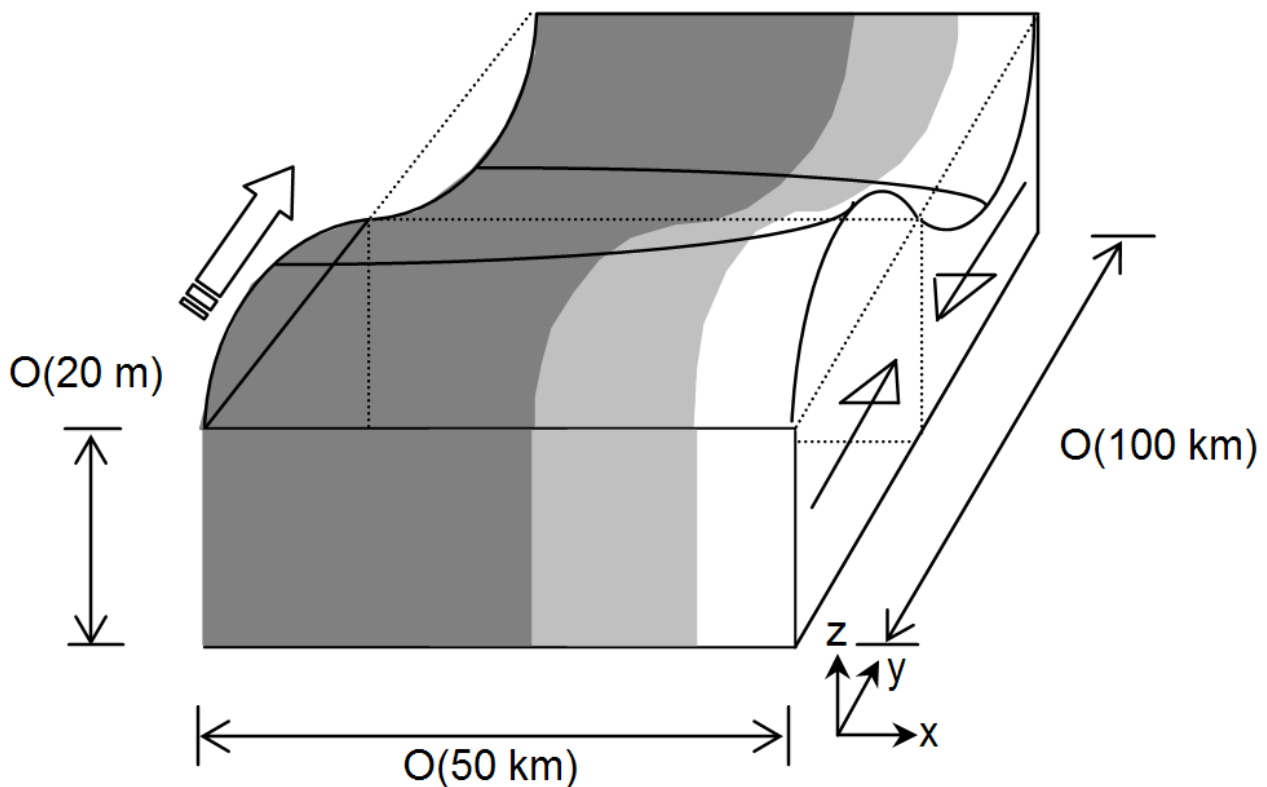


**Figure 2.14:** Cartoon of the Kelvin wave, propagating with the coast on the right hand side on the Northern Hemisphere. Lower left: flood, upper right: ebb. At slack the velocities are zero.

### 2.4.1 Spring neap cycle due to tidal mixing

In the observations of Simpson *et al.* (1993) spring tides in combination with wind mixing brought about periods of complete vertical homogeneity resulting in a well-mixed plume. In contrast, during neap tides and low energetic winds, the region was observed to re-stratify due to relaxation of the cross-shore density gradients under the influence of gravity. This resulted in a stratified plume. However, the state of the Rhine ROFI system not only switches at regular intervals due to changes in the mixing level with the spring-neap cycle, but also at irregular intervals due to storm mixing events and river buoyancy input variations.

### 2.4.2 Spring neap effect of stratification on tidal current ellipses

The stratified and well-mixed periods as observed by Simpson *et al.* (1993) were accompanied by a second phenomenon. Visser *et al.* (1994) employed an HF radar station and observed that, during stratified periods, the Rhine ROFI suddenly exhibited tidal current ellipses at the surface, whereas during well-mixed conditions there were no tidal currents ellipses, as in

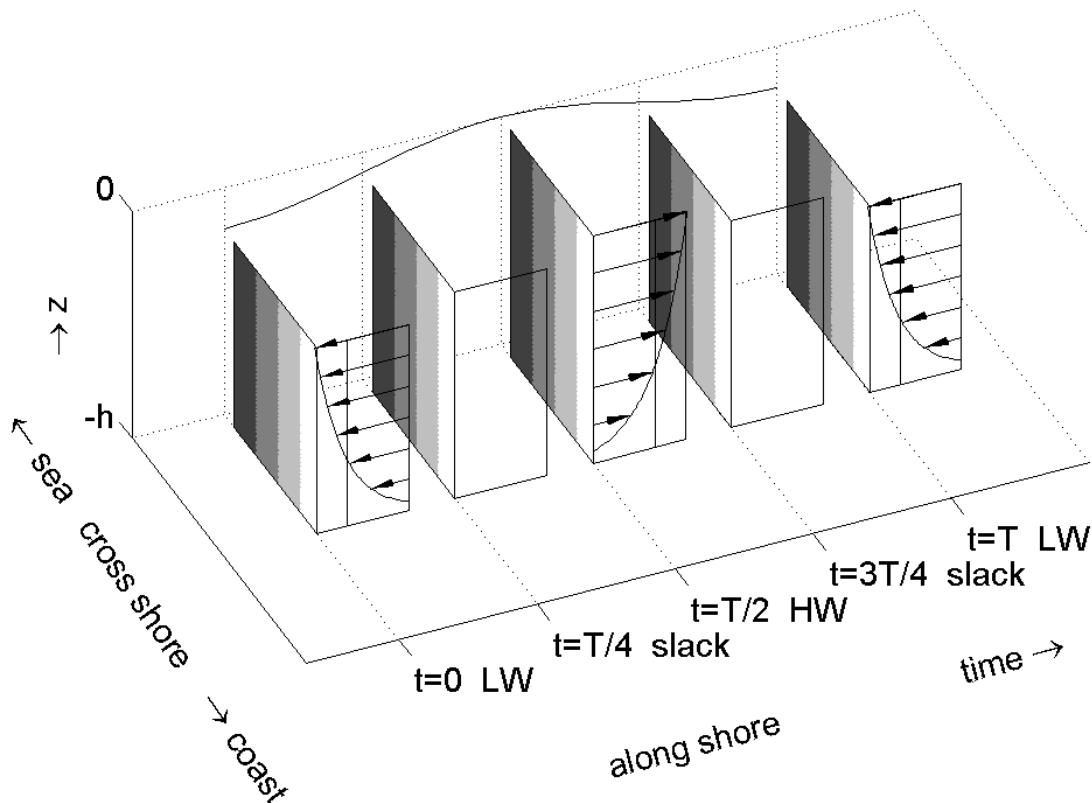


**Figure 2.15:** Cartoon of a well-mixed condition in the Rhine ROFI. There is no systematic interaction between the alongshore ebb and flood velocities and the average cross shore density gradients. Only occasional fresh water lenses will be displaced with the tidal excursion due to alongshore advection (Van Alphen *et al.*, 1988; De Ruijter *et al.*, 1997).



the case of barotropic tides along a straight coast in the model of Taylor (1921) (Fig. 2.16). In addition, an in-situ device employed during the same campaign showed that the bottom layer exhibits the onset of current ellipses at the same time as the surface layer, albeit with an opposite sense of rotation. The resulting total response of the Rhine ROFI is sketched in Fig. 2.17. The existence of counter rotating ellipses in the surface and bottom layer implies a strong cross shore exchange current. The onset of tidal ellipses during periods of stratification can readily be explained with Ekman dynamics (Visser *et al.*, 1994; Souza & Simpson, 1996). Therefore a recapitulation of Ekman dynamics for barotropic waters is given below, before we proceed with the baroclinic case that serves to explain the on-set and existence of tidal ellipses in the Rhine ROFI.

### 2.4.3 Barotropic Ekman dynamics

It is well known that tidal currents in shallow water exhibit a marked vertical structure (Sverdrup, 1927; Prandle, 1982a,b; Soulsby, 1983, 1990; Yasuda, 1987; Maas & Van Haren, 1987). In order to facilitate the investigation of this vertical structure, Prandle (1982a,b) derived analytic solutions to the linear shallow water equations, assuming a vertically uniform eddy viscosity. He decomposed the tidal current vectors, that can be described with an elliptical path as they rotate in the horizontal plane, into two circular phasors, one rotating anti-clockwise and one clockwise, following Godin (1972) and Gonella (1972). These two phasors are conveniently uncoupled in a mathematical sense. This allows one to solve the momentum equations of the two phasors separately, whereas the  $u$  and  $v$  momentum equations cannot be solved separately because they are inextricably linked through the Coriolis parameter  $f$ . Using this simple model, properties such as the semi-major axes, ellipticity, inclination and phase and their variation from surface to bed, may be investigated. The full equations of the model of Prandle are enclosed in Appendix 4.6.

In addition to facilitating the understanding and mathematical handling of tidal currents, this decomposition turns out to be very powerful in the context of the rotation of the Earth. The decomposition into counter rotating phasors can be given a geophysical interpretation when using an anti-cyclonic and cyclonic rather than clockwise and anti-clockwise interpretation. The component of the tide that rotates in the same direction as the planetary rotation (cyclonic <sup>3</sup>), is not as strongly affected by bottom friction and has a thinner Ekman bottom boundary layer than the component that rotates against the direction of planetary rotation (anti-cyclonic <sup>4</sup>). The near-bottom velocity therefore has a tendency to rotate in the same direction as the planetary rotation, whereas the surface velocities tend to rotate in opposite direction. These analytical models of Prandle have been used successfully to explain quantitatively the observed vertical variations in the structure of barotropic tidal current profiles in homogenous waters.

3.  $\propto 1/\sqrt{\omega + f}$  where  $\omega$  is the radial frequency and  $f$  is the Coriolis parameter.

4.  $\propto 1/\sqrt{\omega - f}$

For the Rhine ROFI a special case of the model of Prandle (1982a,b) holds, both during well-mixed and during stratified conditions. The proximity of the coastal wall imposes a zero depth-averaged cross-shore current at all times. In the model of Prandle this can only be obtained by requiring equal amplitudes of the depth-averaged counter-rotating phasors. In contrast, far offshore the two counter-rotating phasors can have independent amplitudes, as for example in the Celtic Sea (Simpson & Tinker, 2007) and in the central North Sea (Maas & Van Haren, 1987) (Fig. 2.18).

Although the proximity of the coast requires that the instantaneous depth averaged velocity is zero, variations of the cross shore velocity over the water depth can still occur. A cross shore velocity profile shape that obeys the presence of the coastal wall is an exchange current where any flux in the upper layer is compensated by an opposite flux in the bottom layer. Usually strong cross shore exchange currents are prevented by vertical mixing though. The cross shore current amplitude is therefore negligible, although its small value can have significant implications, such as determining the orientation of sand ridges (Hulscher, 1996). However, the onset of the strong ellipticity veering observed during stratified conditions can be explained by starting from this barotropic case.

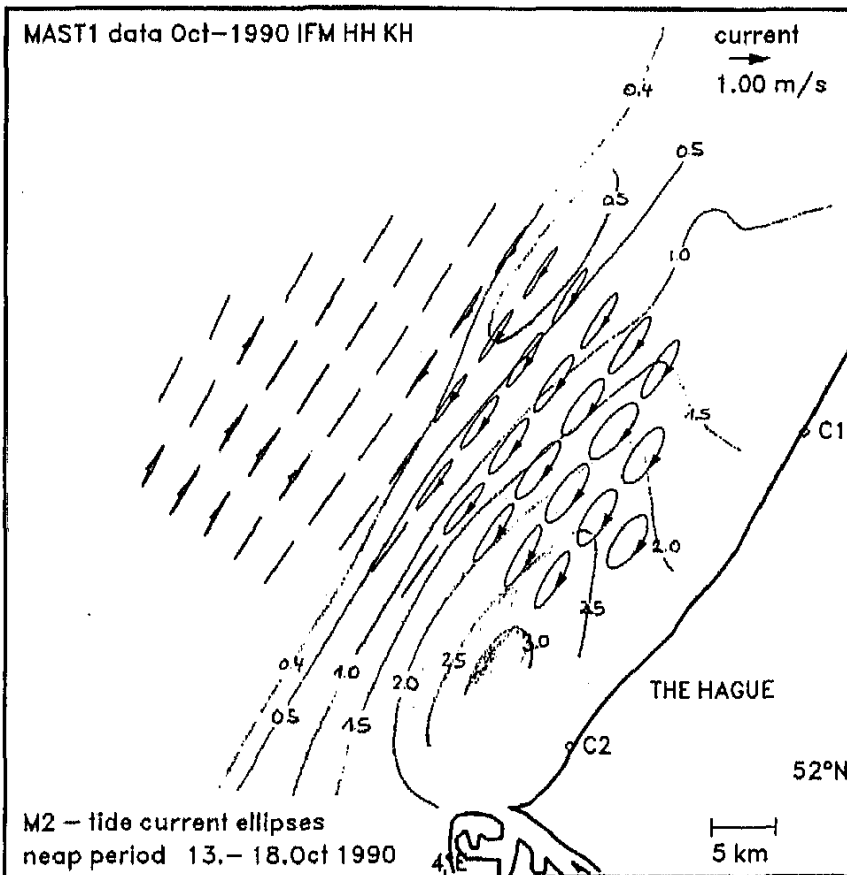
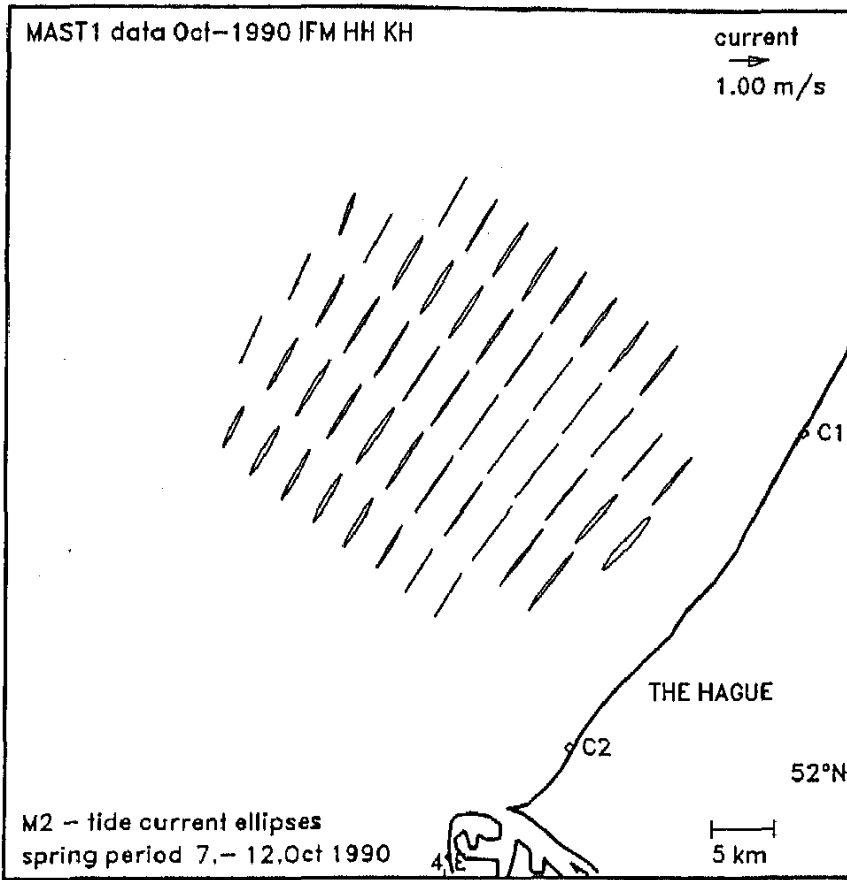
#### 2.4.4 Baroclinic Ekman dynamics

Since stratification leads to a reduction in the vertical redistribution of turbulence levels, the assumptions of the vertically uniform or linearly varying eddy viscosity by Prandle (1982a,b) are inadequate for stratified seas. Stratification alters the vertical structure of the mixing and thereby of tidal currents (see for example Sverdrup (1927); Maas & Van Haren (1987)). Stratification causes a partial decoupling of the velocity profiles below and above the pycnocline. This allows bottom friction to induce a stronger velocity component rotating in the same direction as the Earth in the bottom layer in comparison with the well-mixed case. At the same time it allows the surface layer to respond more independently to the Coriolis force, which results in a stronger velocity component rotating opposite to the direction of rotation of the Earth. Consequently, barotropic current profile models such as those of Prandle (1982a,b) have only limited validity in stratified areas. However, in some cases it is possible to schematize the eddy viscosity profile with a layered approach. When assigning constant or linearly-varying eddy viscosity values to different layers, separate solutions per layer can be constructed and linked at the interfaces. This has been done for the central North Sea by Maas & Van Haren (1987).

During stratified conditions the coupling between surface layers and bottom layers becomes

---

**Figure 2.16 (on the next page): (top)** Near-surface tidal ellipses distilled from a time series of HF radar measurements during spring tide at strong winds and **(bottom)** during neap tides with low energetic winds. The isolines indicate stratification levels. [Visser *et al.* (1994) Fig. 4].



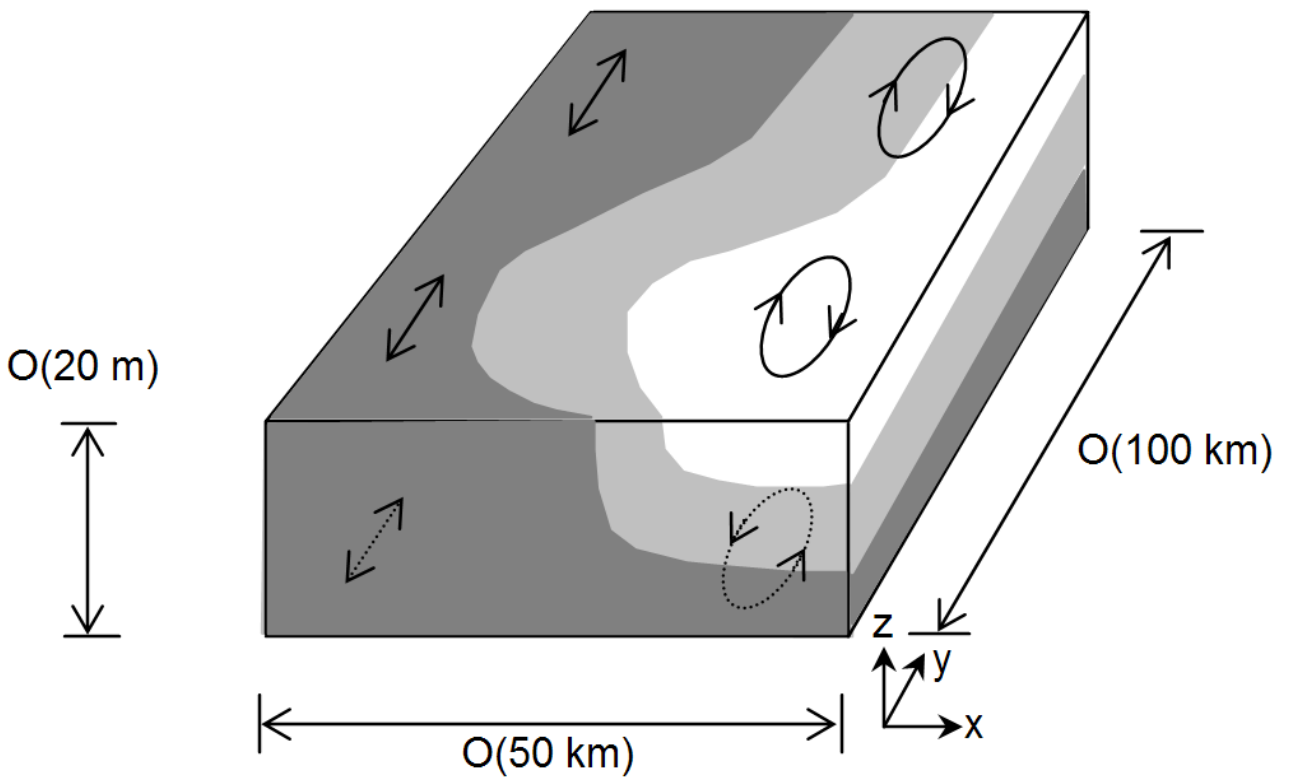
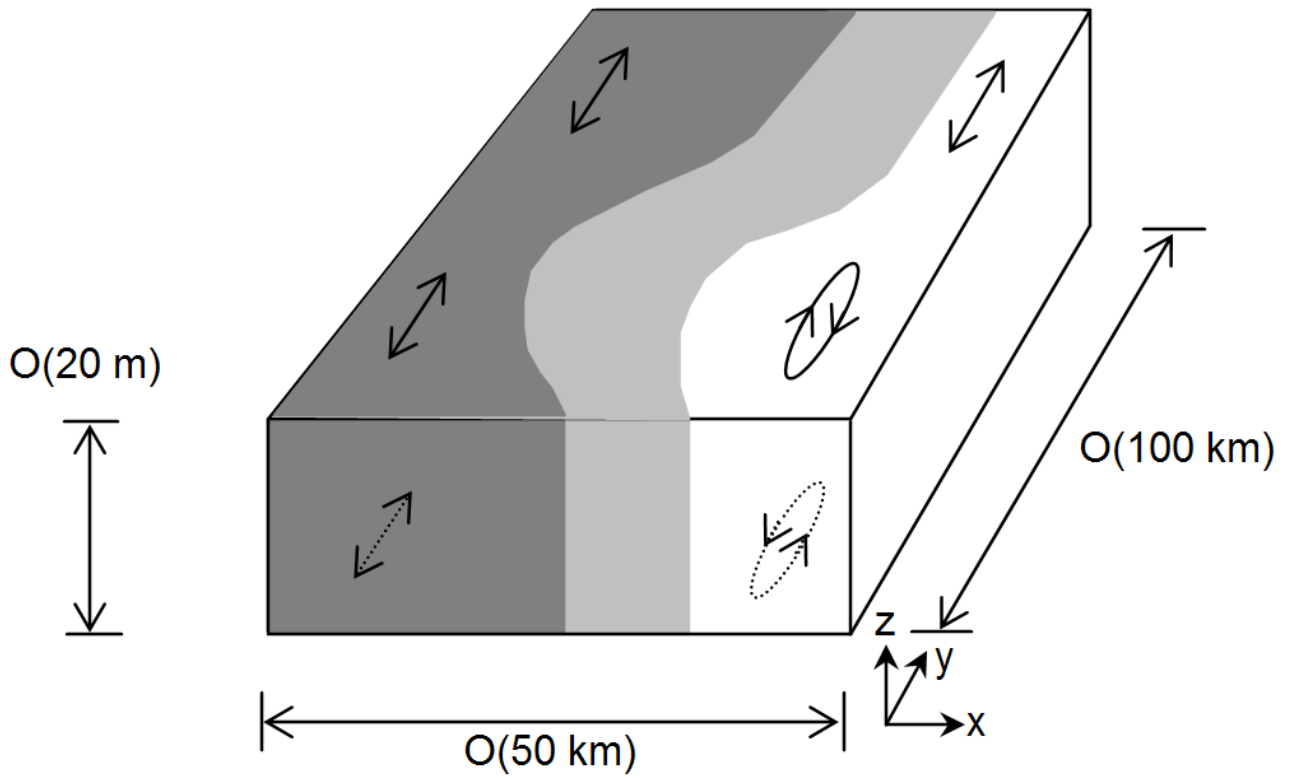
weaker due to reduced mixing such that the surface and bottom layers can start to respond independently. In the limit case a fully decoupled two layer system arises as studied by De Kok (1996). The decoupling permits the bottom currents to adopt the sense of rotation of the Earth (cyclonic). However, due to the presence of a coastal boundary, the depth-averaged cross-shore tidal transport must still be zero at all times, as shown in Fig. 2.18, also during stratified conditions. Hence, any cross shore component in the bottom layer will immediately generate an opposite current in the surface layers such that the net cross-shore discharges in the surface and bottom layer cancel. Visser *et al.* (1994) and Simpson *et al.* (1996) successfully described these semi-diurnal exchange currents in the Rhine ROFI during stratified periods with counter-rotating surface and bottom ellipses.

An alternative explanation to the onset of ellipses is obtained by starting our reasoning from the surface layers rather than from the bottom layer. In the Northern Hemisphere (NH) Coriolis tends to redirect all velocities to the right. The Coriolis force varies linearly with the velocity magnitude. Due to the logarithmic shape of the velocity profile, Coriolis has a larger effect on the faster surface velocities than on the slower bottom velocities. In addition, due to the coastal wall requiring a zero depth averaged cross shore velocity, the surface and bottom velocities cannot both be redirected in the same direction. Hence, the cross shore component of the larger surface velocities forces the bottom velocities in the opposite direction. During well-mixed conditions this phenomenon is constrained by vertical mixing of momentum, limiting the velocity difference between surface and bottom layers. During stratified conditions the system does allow for a velocity difference. Therefore, the bottom current will immediately be deflected in the opposite direction. This explanation is similar in nature to the outward deflection of the surface velocity vector in river bends. There the centrifugal force is responsible for the outward deflection, while in the Rhine ROFI it is the Coriolis force.

Thus, stratification results in bottom currents that rotate cyclonically (anti-clockwise on the NH), and surface currents that rotate anti-cyclonically (clockwise in NH) (Fig. 2.19). The observed cross-shore velocity shear in this situation can be up to  $70 \text{ cm s}^{-1}$  over the water depth (Simpson *et al.*, 1993; Visser *et al.*, 1994). This cross shore velocity shear is responsible for a

---

**Figure 2.17 (on the next page): (top)** Cartoon of the density and velocity structure of the Rhine ROFI during well-mixed conditions. The surface and bottom velocities are alongshore, except for the near field close to the river mouth where small cross shore velocities are present, leading to small ellipticities. **(bottom)** Cartoon of the density and velocity structure of the Rhine ROFI during stratified conditions based on observations by a HF radar and vertical profiles by (Visser *et al.*, 1994). The main tidal surface and bottom velocities are alongshore, but between ebb and flood strong cross shore exchange currents are present. The surface amplitude of these cross shore currents is up to 40% of the alongshore velocities. This situation can be described with counter rotating surface and bottom ellipses.



semi-diurnal modulation of stratification as described in the next section.

#### 2.4.5 Semi-diurnal cycle due to tidal straining

The second time scale found by Simpson *et al.* (1993) is a semi-diurnal variation in the cross-shore velocity field as described above, in combination with a semi-diurnal variation of the stratification field. These quantities both exhibit a pronounced tidally varying oscillation during periods when the ROFI is stratified in a tidally averaged sense, as governed by the first time scale. In contrast, during periods when the ROFI is well-mixed in a tidally averaged sense, both these semi-diurnal signals are absent (Figs. 2.20 and 2.21). The coincidence of the two semi-diurnal signals is not accidental. There is a causal link between the semi-diurnal stratification signal and semi-diurnal cross-shore velocity signal, which was identified by Simpson & Souza (1995) as tidal straining. They showed that the cross-shore velocity signal dictates the semi-diurnal stratification signal. This process is described in the next subsection.

#### 2.4.6 Semi-diurnal effect of tidal current ellipses on stratification

The aforementioned cross shore velocity shear during periods of stratification is responsible for the second time scale observed in the water column stability, through a process called tidal straining. Tidal straining is the effect of differential advection by a vertical velocity shear acting on a horizontal density gradient. Van Aken (1986) was the first to study effects of horizontal differential advection on stratification, as proposed by De Ruijter (1983). He showed that an excess residual surface current can advect fresher surface water over a slower and denser bottom layer. This results in the onset of stratification. Subsequently, the subtle haline stratified surface layer can be heated faster by solar radiation than the bottom layer, resulting in a further decrease of the surface density. This, he showed, can lead to the onset of seasonal thermal stratification just North of the Rhine ROFI.

The effect of differential advection on stratification was further explored as a dynamic process by Simpson *et al.* (1990). They derived the concept of tidal straining for estuarine-like sites. Here the reversing tidal velocity shear interacts with the horizontal density gradient as shown in Fig. 2.22. During ebb, the faster surface currents advect fresher river water over more saline bottom waters. This results in a stratified estuary. However, during flood the faster surface currents advect the fresher surface water back upstream into the estuary, until the water column is well-mixed again. This way, Simpson *et al.* (1990) elegantly show how differential advection by a tidal velocity shear acting upon a horizontal density gradient can be used to explain the oscillation of the stability of the water column. They demonstrated how tidal straining contributed to the semi-diurnal episodes of haline stratification observed within Liverpool Bay in the Irish Sea. In this way they demonstrated that Strain Induced Periodic Stratification (SIPS) was a dominant process in estuaries and coastal seas with large horizontal gradients of density.

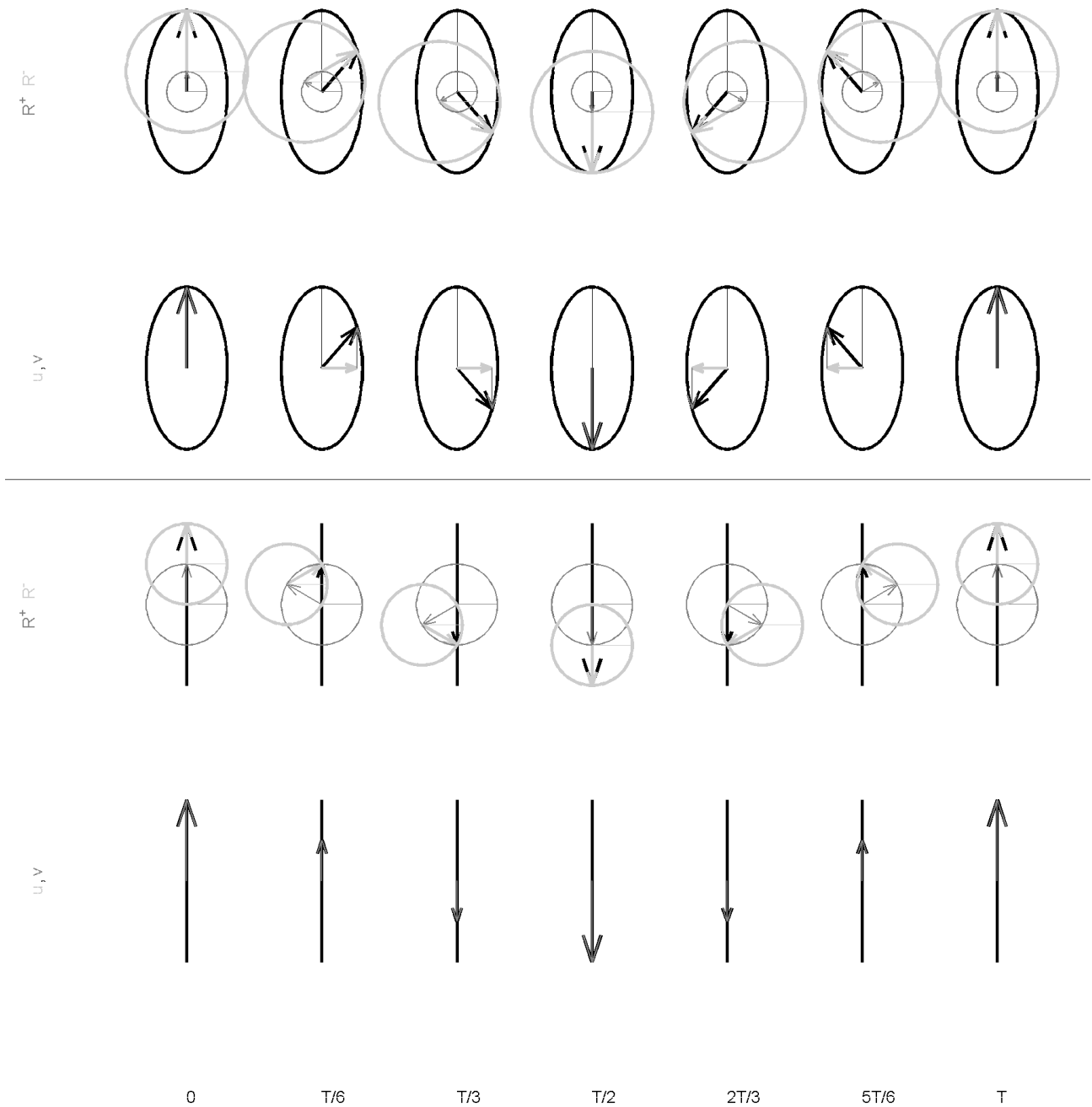


**Figure 2.18: (top)** Example of the decomposition of a time-series of a harmonic depth-averaged velocity vector  $(u, v)$  (row 2) describing an elongated ellipse (black) into two counter-rotating phasors  $R^+$  and  $R^-$  (row 1). **(bottom)** Example of the decomposition of a time-series of a harmonic depth-averaged velocity vector  $(u = 0, v)$  (row 4) describing a degenerated ellipse (black) into two counter-rotating phasors  $R^+$  and  $R^-$  (row 3) as in the Rhine ROFI. The phasors  $R^+$  and  $R^-$  must have the same amplitude to have a zero velocity cross-shore component  $u$  at all times. Consequently, the velocity component  $v$  has an amplitude of twice the phasor amplitude  $v = 2|R^+| = 2|R^-|$ .

In Liverpool Bay the main tidal shear is in the same direction as the density gradient. This allowed ready application of the tidal straining paradigm to this semi-enclosed sea. Simpson & Souza (1995) applied the same concept to the Rhine ROFI where the situation is more complicated, however. Here the tide has the nature of a propagating Kelvin wave, where the main tidal currents are alongshore, whereas the main density gradient is cross shore. Simpson & Souza (1995) were the first to realize that tidal straining in the Rhine ROFI consists of the episodic cross-shore velocity shear interacting with the average cross-shore density gradients. As such they were able to explain the semidiurnal oscillations in stratification by applying the tidal straining concept in the cross-shore direction only. The tidal straining mechanism in the Rhine ROFI works as follows.

In the Rhine ROFI the tide has the character of a propagating Kelvin wave with maximum flood velocities at HW and maximum ebb velocities at LW, neglecting the small phase shift due to friction. In well-mixed conditions the tidal currents are zero at slack water (Fig. 2.15).

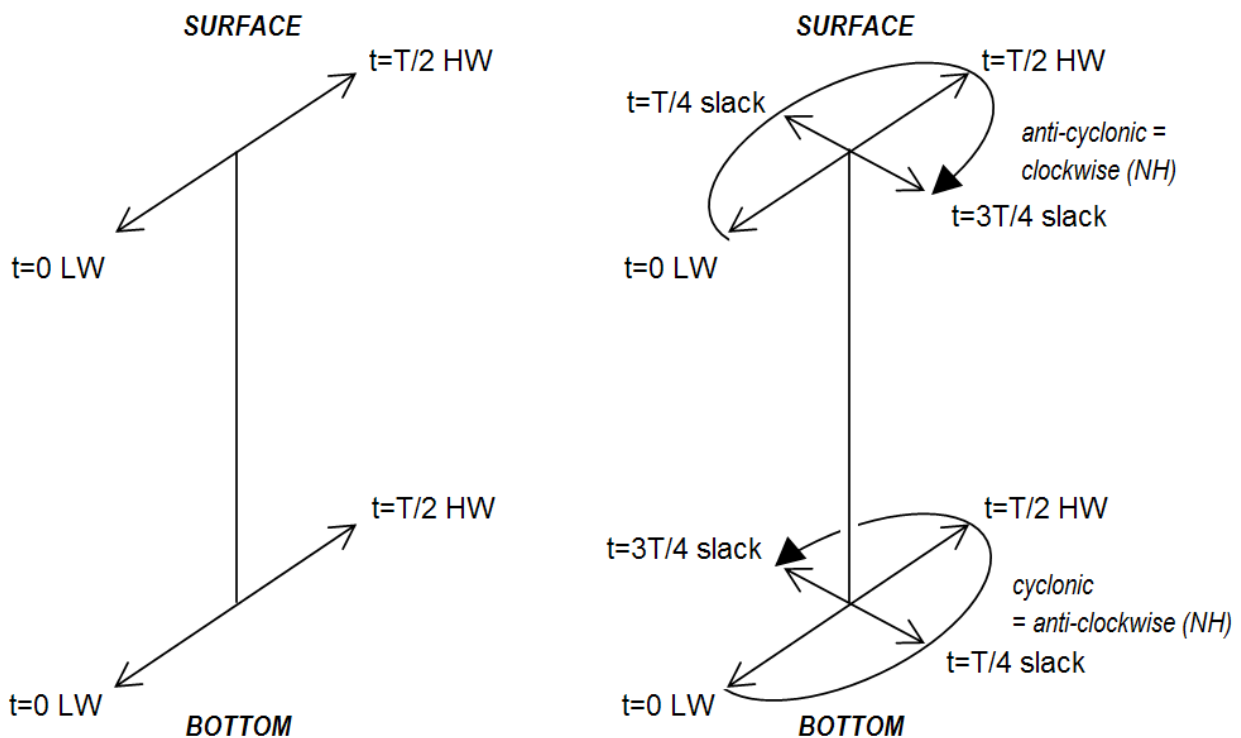


**Figure 2.19:** The vertical variation of horizontal tidal velocities in the Rhine ROFI during well-mixed conditions (left) and stratified conditions (right) as distilled from measurements by Simpson *et al.* (1993) and Visser *et al.* (1994). During well-mixed conditions the ebb and flood currents are rectilinear alongshore over the entire water depth. In the stratified case the surface velocity vectors exhibit increased cyclonic ellipticity, which corresponds to anti-clockwise rotation in a top view on the Northern Hemisphere. In contrast, the bottom current vector exhibits increased anti-cyclonic rotation.



However, during stratified conditions, from LW to HW the anti-cyclonic surface currents are directed offshore instead of dropping to zero (Figs. 2.19 and 2.23). In this configuration, they advect fresher coastal water offshore. At the same time the opposed onshore bottom currents advect saltier offshore waters onshore. Hence the plume is maximally stratified at HW when the cross-shore exchange current drops to zero to reverse. From HW to LW the surface currents are directed onshore and advect the fresher surface water back towards the shore. Meanwhile, the offshore bottom currents advect the saltier waters back offshore. Accordingly, the plume is closest to well-mixed again at LW.

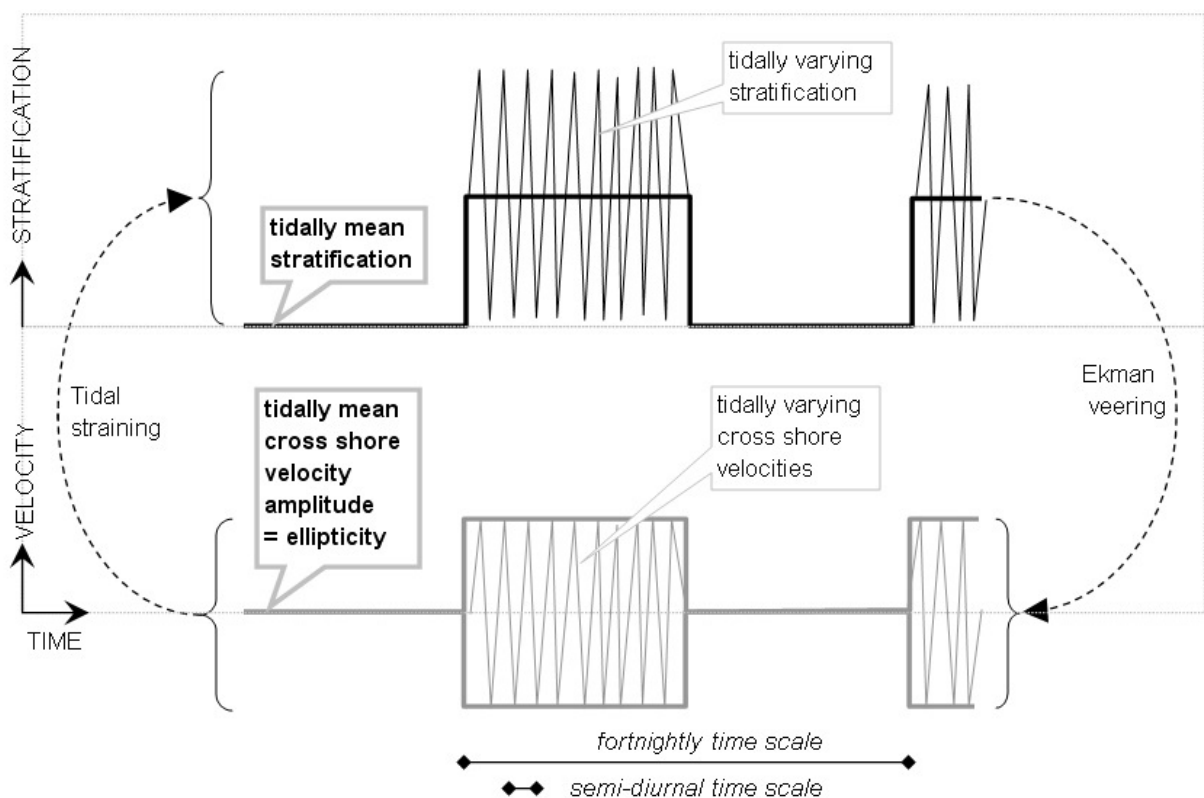
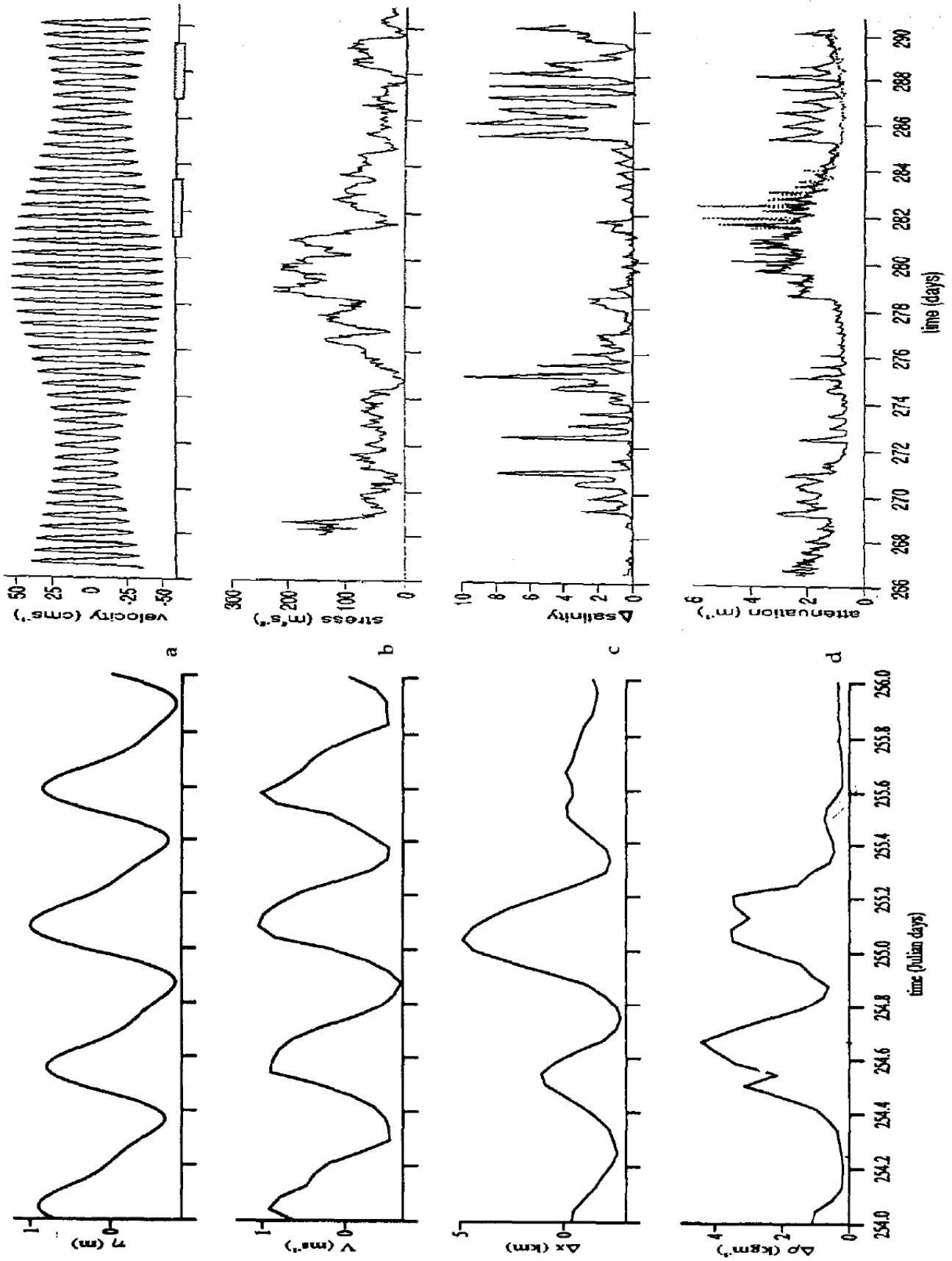


**Figure 2.20:** Cartoon of a synthetic time-series of the two quantities which show a fortnightly and a semi-diurnal variation, distilled from measurements shown in Fig. 2.21.

**Figure 2.21 (on the next page):** (left, bottom) Measured time-series in September 1992 showing semi-diurnal timescale of stratification [Simpson & Souza (1995) Fig. 2]. The upper line depicts the water level, the second line the velocity, the third line the relative cross shore displacement of the surface layer (as time integral of the cross shore velocity shear) and the fourth line the density difference. (right, top) Measured time-series in September and October 1990 showing fortnightly timescale of stratification [Simpson *et al.* (1993) Fig. 4]. The first line depicts the velocity, the second line the mixing stress due to waves and tides, the third line the stratification, and the fourth line the light attenuation.



The amplitude of the resulting semi-diurnal modification of stratification may be so strong with respect to the mean stratification, that the system can switch from well-mixed to stratified within one tidal cycle, with the tidally mean stratification being half the maximum stratification. Through this process the tidally averaged and the tidally varying stratification are inextricably linked (Simpson & Souza, 1995).

## 2.5 Synthesis 3D ROFI structure

For a first order level of understanding, the current structure in the Rhine ROFI can be considered as a superposition of a residual component and a tidal component. The residual current exhibits alongshore velocities increasing with depth (thermal wind) superimposed on a cross shore exchange current (estuarine circulation) (Fig. 2.6). The tide exhibits only alongshore velocities during well-mixed conditions, while during stratified neap conditions it also exhibits strong semi-diurnal cross shore exchange currents. The variation over the vertical and during the tidal cycle can therefore be visualized as a superposition of Fig. 2.10 plus Fig. 2.17<sub>top</sub> during well-mixed conditions and Fig. 2.10 plus Fig. 2.17<sub>bottom</sub> during stratified conditions.

This approach to obtain a first order understanding has been adopted by Simpson *et al.* (1991). They described the evolution of the velocity as a superposition of an estuarine exchange current and a tidal profile, using simple analytical formulations for both. The data set of De Ruijter *et al.* (1992) (Fig. 2.24) can readily be explained with this conceptual model.

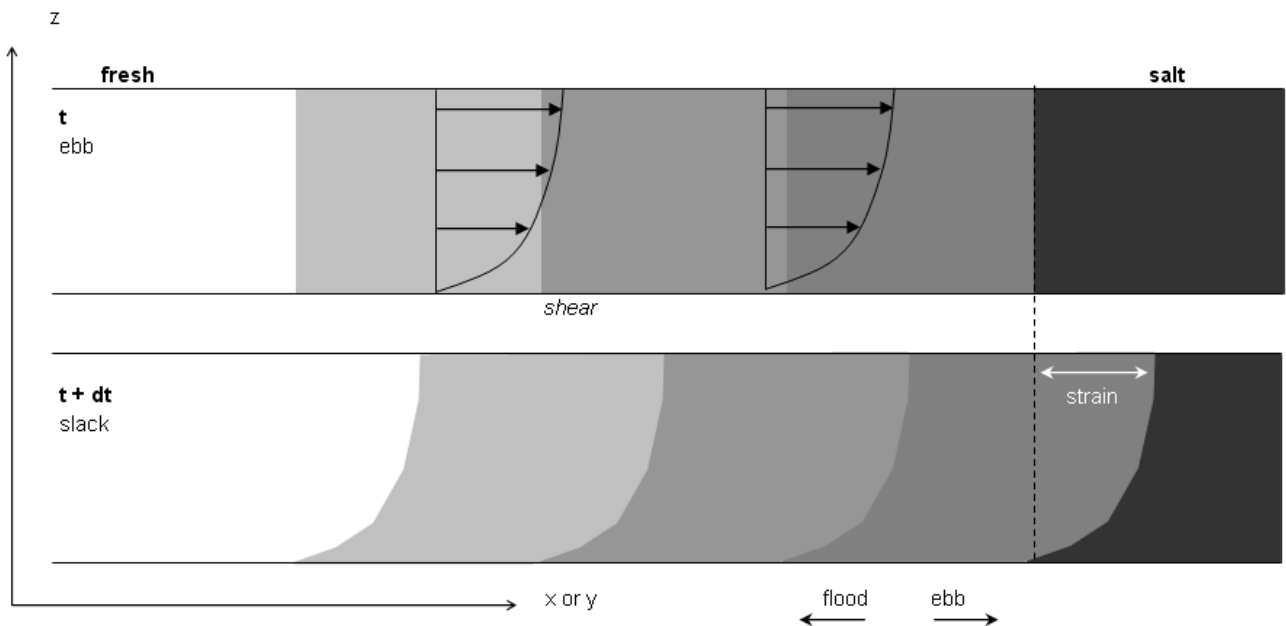


**Figure 2.22:** Cartoon of tidal straining principle (after Simpson *et al.* (1990)). A vertical velocity shear acts on a horizontal density gradient to induce stratification.

First, the data show that the near bottom current has a shoreward drift. This is the estuarine or gravitational circulation component in the model of Heaps (1972) due to the cross shore density gradient. Second, the surface current exhibits an alongshore residual velocity. This is the geostrophic Coriolis induced (thermal wind) component of the model of Heaps (1972). Third, both surface and bottom currents follow counter rotating tidal ellipses superimposed on these residual currents.

This basic conceptual model provides a strong concept for the understanding of the basic processes. However, for predictive purposes it suffers from limitations. Foremost, the model cannot deal with non-linear interactions between the residual and tidal components, notably tidal straining. In addition, the residual current is very likely to be modulated by stratification as well. Therefore in this thesis the interaction between 3D tidal currents and the 3D density currents is further explored.

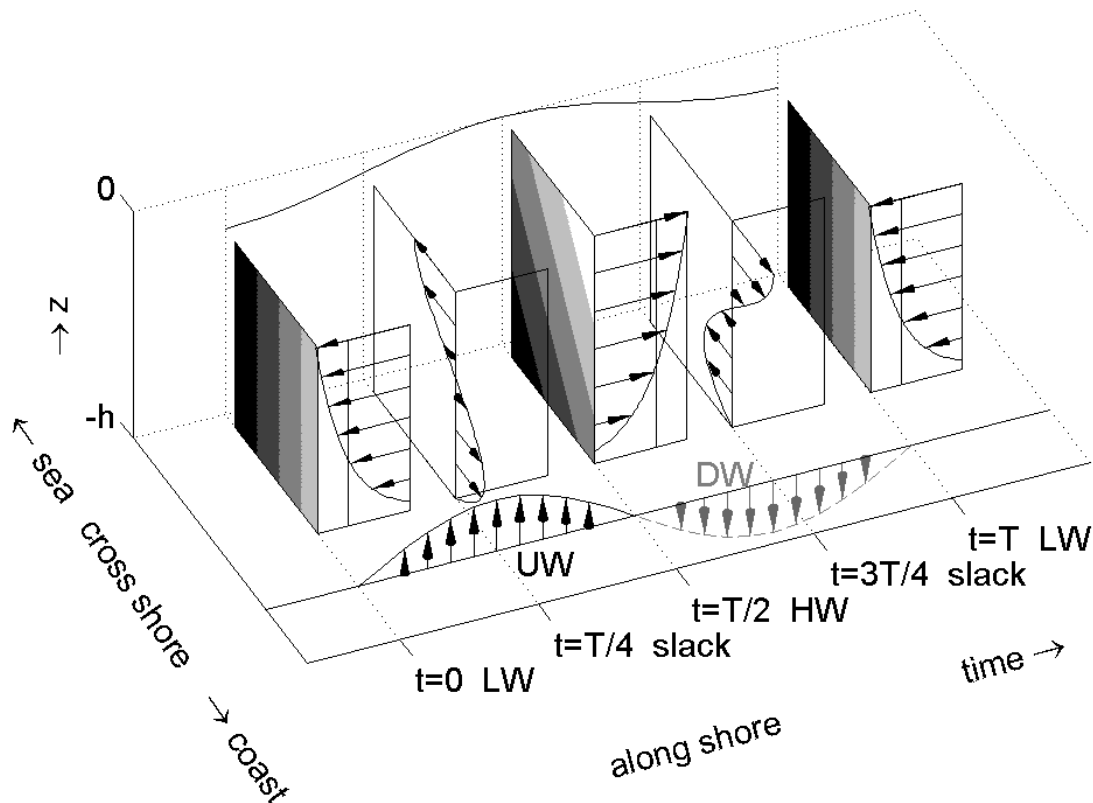


**Figure 2.23:** Cartoon of a stratified condition in the Rhine ROFI. Tidal straining (Simpson *et al.*, 1990) in the Rhine ROFI consist of the systematic interaction of the cross shore velocity shear with the average cross shore density gradients (Simpson & Souza, 1995). The cross shore currents should lead to up welling (UW) and downwelling (DW) due to the presence of the coast.

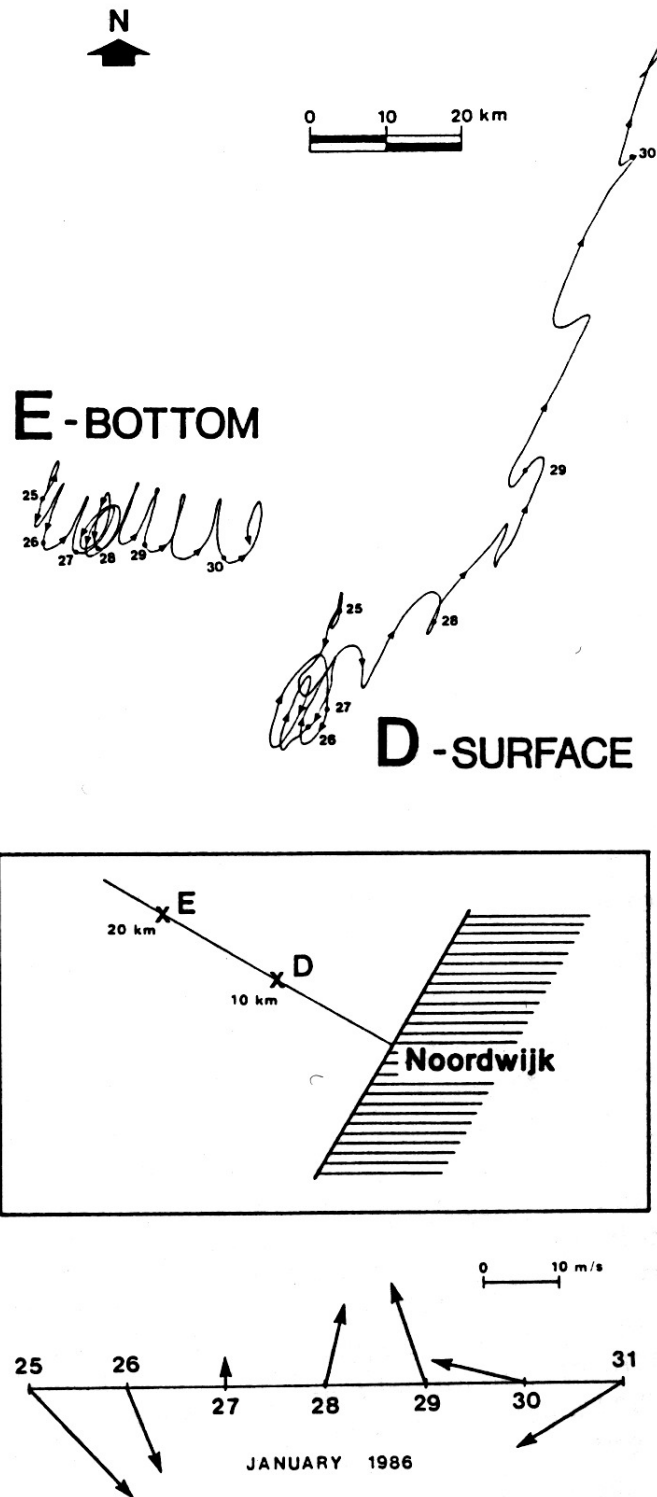


**Figure 2.24:** Observations of progressive vectors diagrams of velocities measured at a fixed mooring [Van der Giessen *et al.* (1990) Fig. 14]. The bottom exhibits a shoreward drift, while the surface velocities show a strong alongshore drift in line with Heaps (1972). Both layers have tidal effects superimposed on them.



## Chapter 3

### Set-up of study

#### 3.1 Introduction

This chapter deals with the research methods. In the past the processes in the Rhine ROFI have been studied with in situ measurements from fixed moorings and during cruises. Also spatially powerful coherent surface measurements of the velocities over a larger area were obtained with HF radar (Visser *et al.*, 1994). In addition 1D vertical models (Simpson & Souza, 1995), 2D  $x$ - $z$  cross shore slice models (Souza & Simpson, 1996) and parametric 3D models (Luyten, 1996) have been adopted. However, all these methods only allow for limited spatial coverage in at least some aspect. In this thesis we endeavour to obtain a further understanding of the Rhine ROFI by employing two methods hitherto not fully exploited in Rhine ROFI studies. These are first an idealized but full 3D numerical model and secondly remote sensing images of Sea Surface Temperature (SST). These methods would enable us to develop an increased level of insight, based on spatially more coherent interpretations. This would allow for a further understanding of tidal mixing and tidal straining in the ROFI system. In section 3.2 the numerical modelling system is introduced and in section 3.3 the necessary background details are given on SST satellite imagery.

#### 3.2 Idealized numerical model

In this study we employ a non-linear 3D numerical model for an idealized domain as our main tool. Although nowadays engineering models of the Rhine ROFI with a high level of detail are available, e.g. Roelvink *et al.* (2001), we employ a different strategy. Using a simple idealized numerical model, we plan to capture only the essential physics of the Rhine ROFI. The characteristics of the ROFI system are determined by three components: a buoyant source, the rotation of the Earth and the semi-diurnal Kelvin wave. We construct a simple rectangular coastal sea to study the consequences of these three ingredients in isolation only, without being diverted by an overload of details due to for instance bathymetric variations. In this approach we do not limit ourselves with respect to physical descriptions; we only limit ourselves with respect to the complexity and amount of detail in spatial and temporal forcings. The set-up of this idealized 3D numerical model of the Rhine ROFI is discussed in this section.

The modelling system DELFT3D-FLOW in which we built our idealized Rhine ROFI is introduced in section 3.2.1 by summarizing the equations that it solves. The basic features of the rectangular tidal basin set-up are discussed in section 3.2.2. The most important, yet most difficult aspect of the set-up of our numerical modelling effort was to represent the tidal velocities properly. This work, which has been performed in close collaboration with Walter Jacobs while working on his MSc. thesis (Jacobs, 2004), is discussed in this section. The tidal boundary conditions are derived using a simplified depth-averaged Kelvin wave model with spatially varying linearized friction. The vertical turbulence model is validated in section 3.2.3. Further details, regarding the river discharge and spin-up times, can be found in section 4.2.

### 3.2.1 Numerical modelling system delft3d-flow

*The governing equations in  $\sigma$ -coordinates*

The modelling system used is the three-dimensional FLOW module of DELFT3D. We employ the vertical  $\sigma$ -grid transformation (Phillips, 1958) which is defined by

$$\tilde{x} = x; \tilde{y} = y; \sigma = \frac{z - \eta(\tilde{x}, \tilde{y})}{H(\tilde{x}, \tilde{y})}; \tilde{z} = z; \tilde{t} = t \quad (3.1)$$

where  $H$  is the water depth, given by  $H = \eta + h$ ,  $\eta$  is the free surface,  $h$  is the location of the bed. The  $\sigma$ -grid ‘breathes’ vertically with the barotropic water level changes and bottom level changes between 0 at the surface and -1 at the bed. After transformation to a  $\sigma$ -grid the gradients in all directions read

$$\frac{\partial}{\partial x} = \frac{\partial}{\partial \tilde{x}} + \frac{\partial \sigma}{\partial \tilde{x}} \frac{\partial}{\partial \sigma}; \quad \frac{\partial}{\partial y} = \frac{\partial}{\partial \tilde{y}} + \frac{\partial \sigma}{\partial \tilde{y}} \frac{\partial}{\partial \sigma}; \quad \frac{\partial}{\partial z} = \frac{1}{H} \frac{\partial}{\partial \sigma}; \quad \frac{\partial}{\partial t} = \frac{\partial}{\partial \tilde{t}} + \frac{\partial \sigma}{\partial \tilde{t}} \frac{\partial}{\partial \sigma} \quad (3.2)$$

The transformed vertical velocity  $\omega_k$  relative to the vertical movement of the  $\sigma$ -planes located at  $z_k$  is defined as

$$\omega_k \equiv H \frac{D\sigma_k}{D\tilde{t}} = w_k - \frac{Dz_k}{D\tilde{t}} = w_k - \frac{\partial z_k}{\partial \tilde{t}} - u_k \frac{\partial z_k}{\partial \tilde{x}} - v_k \frac{\partial z_k}{\partial \tilde{y}} \quad (3.3)$$

The horizontal momentum equations in  $x$ ,  $y$ , and  $\sigma$ -space per  $\sigma$ -layer  $k$  read, after simplifying the horizontal eddy viscosity terms, neglecting molecular viscosity and dropping the tildes of Eq. 3.1, and substitution of Eq. 3.3

$$\begin{aligned} \frac{Du_k}{Dt} &= \frac{\partial u_k}{\partial t} + u_k \frac{\partial u_k}{\partial x} + v_k \frac{\partial u_k}{\partial y} + \frac{\omega}{H} \frac{\partial u_k}{\partial \sigma} \\ &= -\frac{1}{\rho_0} \left( \frac{\partial p_k}{\partial x} + \frac{\partial \sigma}{\partial x} \frac{\partial p_k}{\partial \sigma} \right) + f v_k + E_H \Delta u_k + \frac{1}{H^2} \frac{\partial}{\partial \sigma} \left( E_z \frac{\partial u_k}{\partial \sigma} \right) \end{aligned} \quad (3.4)$$



$$\begin{aligned}
\frac{Dv_k}{Dt} &= \frac{\partial v_k}{\partial t} + u_k \frac{\partial v_k}{\partial x} + v_k \frac{\partial v_k}{\partial y} + \frac{\omega}{H} \frac{\partial v_k}{\partial \sigma} \\
&= -\frac{1}{\rho_0} \left( \frac{\partial p_k}{\partial y} + \frac{\partial \sigma}{\partial y} \frac{\partial p_k}{\partial \sigma} \right) - f u_k + E_H \Delta v_k + \frac{1}{H^2} \frac{\partial}{\partial \sigma} \left( E_z \frac{\partial v_k}{\partial \sigma} \right)
\end{aligned} \tag{3.5}$$

where  $E_H$  and  $E_z$  are the turbulent eddy viscosity in horizontal and vertical direction respectively,  $\Delta \bullet = (\partial^2 \bullet / \partial x^2 + \partial^2 \bullet / \partial y^2)$  the Laplace operator and  $\rho_0$  a representative density ( $\sim 1000 \text{ kgm}^{-3}$ ). Note that, unlike the other terms, the viscosity terms are not transformed according to Eq. 3.2 to keep the numerical implementation definite. The pressure is given by

$$p(x, y, z) = p_a + gH \int_{\sigma^*=\sigma}^0 \rho(x, y, \sigma^*, t) d\sigma^* = g \int_{z^*=z}^{\eta} \rho(x, y, z^*, t) dz^* \tag{3.6}$$

where  $p_a$  is the atmospheric pressure. Note that the density is taken constant  $\rho_0$  in the momentum Eqs. 3.4 and 3.5, but is allowed to vary vertically in the horizontal pressure gradient Eq. 3.6 according to the Boussinesq approximation. The hydrostatic assumption is applied such that the vertical momentum equation reads:

$$\frac{\partial p}{\partial \sigma} = -\rho g H \tag{3.7}$$

The horizontal pressure gradients follow by application of the Leibniz rule

$$\begin{aligned}
\frac{\partial p_k(x, z^*)}{\partial x} &= g \frac{\partial}{\partial x} \int_{z^*=z}^{\eta(x)} \rho(x, z^*) dz^* = g \int_{z^*=z}^{\eta(x)} \frac{\partial}{\partial x} \rho(x, z^*) dz^* + g \rho(\eta) \frac{\partial \eta}{\partial x} \\
\frac{\partial p_k(y, z^*)}{\partial y} &= g \frac{\partial}{\partial y} \int_{z^*=z}^{\eta(y)} \rho(y, z^*) dz^* = g \int_{z^*=z}^{\eta(y)} \frac{\partial}{\partial y} \rho(y, z^*) dz^* + g \rho(\eta) \frac{\partial \eta}{\partial y}
\end{aligned} \tag{3.8}$$

The pressure gradient terms in Eqs. 3.4 and 3.5 are not obtained by substitution of Eq. 3.8. Straightforward substitution and subsequent discretization would lead to artificial flow and associated mixing due to stratification near bottom slopes. This is a well-known problem of application of  $\sigma$ -planes. In DELT3D-FLOW this problem is minimized by the method of Stelling & Van Kester (1994). First they solve the transport equation for temperature and salinity (Eqs.3.11) in such a way that, despite of  $\sigma$ -planes, the anisotropy of pure horizontal diffusion along the cartesian horizontal axes and vertical diffusion is taken into account such that the solution is strictly positive, and allows steady state solutions that are strictly stratified. This is obtained by the application of a limiter to horizontal gradients. Secondly, the very

same gradients are applied, via application of the chain-rule to the equation of state, to the computation of the density gradients in the momentum equations (Eq. 3.8). This yields consistency between the transport equation and the momentum equations, i.e. if salinity gradients are zero in the transport equation, then the density gradients in the momentum equations are zero as well. Further explanation and computational examples are given by Stelling & Van Kester (1994).

The depth averaged continuity equation reads

$$\frac{\partial \eta}{\partial t} + \frac{\partial HU}{\partial x} + \frac{\partial HV}{\partial y} = 0 \quad (3.9)$$

where  $U = \int_{-1}^0 u d\sigma$  and  $V = \int_{-1}^0 v d\sigma$ . The vertical velocities  $w/\omega$  at the interfaces are dependent variables and can be determined with the continuity equation after solving the state vector  $(u, v, p, \eta)$  and using  $\omega = 0$  at the free surface and likewise at the bed

$$\frac{\partial u}{\partial x} + \frac{\partial v}{\partial y} + \frac{\partial w}{\partial z} = 0 \quad (3.10)$$

The advection-diffusion equation for a dissolved substance  $c$  (temperature, salinity) in  $\sigma$ -coordinates reads

$$\begin{aligned} \frac{Dc_k}{Dt} &= \frac{\partial c_k}{\partial t} + \frac{\partial u_k c_k}{\partial x} + \frac{\partial v_k c_k}{\partial y} + \frac{\omega}{H} \frac{\partial c_k}{\partial \sigma} \\ &= \frac{\partial}{\partial x} E_H \frac{\partial c}{\partial x} + \frac{\partial}{\partial y} E_H \frac{\partial c}{\partial y} + \frac{1}{H^2} \frac{\partial}{\partial \sigma} \left( \frac{E_z}{\sigma_c} \frac{\partial c}{\partial \sigma} \right) + Q_k \end{aligned} \quad (3.11)$$

where the Prandtl-Schmidt number  $\sigma_c$  is 700 for salinity, 6.7 for temperature and  $Q$  are the sources/sinks per unit volume. The density  $\rho$  is calculated with the state equation of Eckart (1958) after calculating the advection-diffusion of the set of constituents  $c = (T, S)$  with temperature  $T$  and salinity  $S$ . As already mentioned above, for the horizontal diffusive fluxes in Eq. 3.11 the  $\sigma$ -transformation is taken into account implicitly and at the numerical level rather than by explicit and analytic transformation (Stelling & Van Kester, 1994).

The  $k - \varepsilon$  equations in  $\sigma$ -coordinates, after neglecting the horizontal mixing terms, read

$$\begin{aligned} \frac{Dk}{Dt} &= \frac{\partial k}{\partial t} + u \frac{\partial k}{\partial x} + v \frac{\partial k}{\partial y} + \frac{\omega}{H} \frac{\partial k}{\partial \sigma} \\ &= \frac{1}{H^2} \frac{\partial}{\partial \sigma_k} \left( \frac{E_z}{\sigma_k} \frac{\partial k}{\partial \sigma} \right) + P_k + B_k - \varepsilon \end{aligned} \quad (3.12)$$

$$\begin{aligned}
\frac{D\varepsilon}{Dt} &= \frac{\partial\varepsilon}{\partial t} + u\frac{\partial\varepsilon}{\partial x} + v\frac{\partial\varepsilon}{\partial y} + \frac{\omega}{H}\frac{\partial\varepsilon}{\partial\sigma} \\
&= \frac{1}{H^2}\frac{\partial}{\partial\sigma_k}\left(\frac{E_z}{\sigma_\varepsilon}\frac{\partial\varepsilon}{\partial\sigma}\right) + \left[ \underbrace{c_{1\varepsilon}\frac{\varepsilon}{k}P_k}_{P_\varepsilon} + \underbrace{c_{1\varepsilon}\frac{\varepsilon}{k}(1-c_{3\varepsilon})B_k}_{B_\varepsilon} - c_{2\varepsilon}\frac{\varepsilon^2}{k} \right]
\end{aligned} \tag{3.13}$$

where  $P_k$  is production and  $B_k$  is buoyancy flux. Eqs. 3.12 and 3.13 determine the vertical eddy viscosity  $E_z$  through the Kolmogorov-Prandtl expression

$$E_z = c_\mu k^{3/2} / \varepsilon \tag{3.14}$$

with empirical coefficients

$$c_\mu = 0.09 \quad c_{1\varepsilon} = 1.44 \quad c_{2\varepsilon} = 1.92 \quad \sigma_\varepsilon = 1.3 \quad \sigma_k = 1 \quad c_{3\varepsilon} = \begin{cases} 1 & B_k < 0 \\ 0 & B_k > 0 \end{cases} \tag{3.15}$$

The coefficient  $c_{3\varepsilon}$  switches off the buoyancy flux for stable stratification.

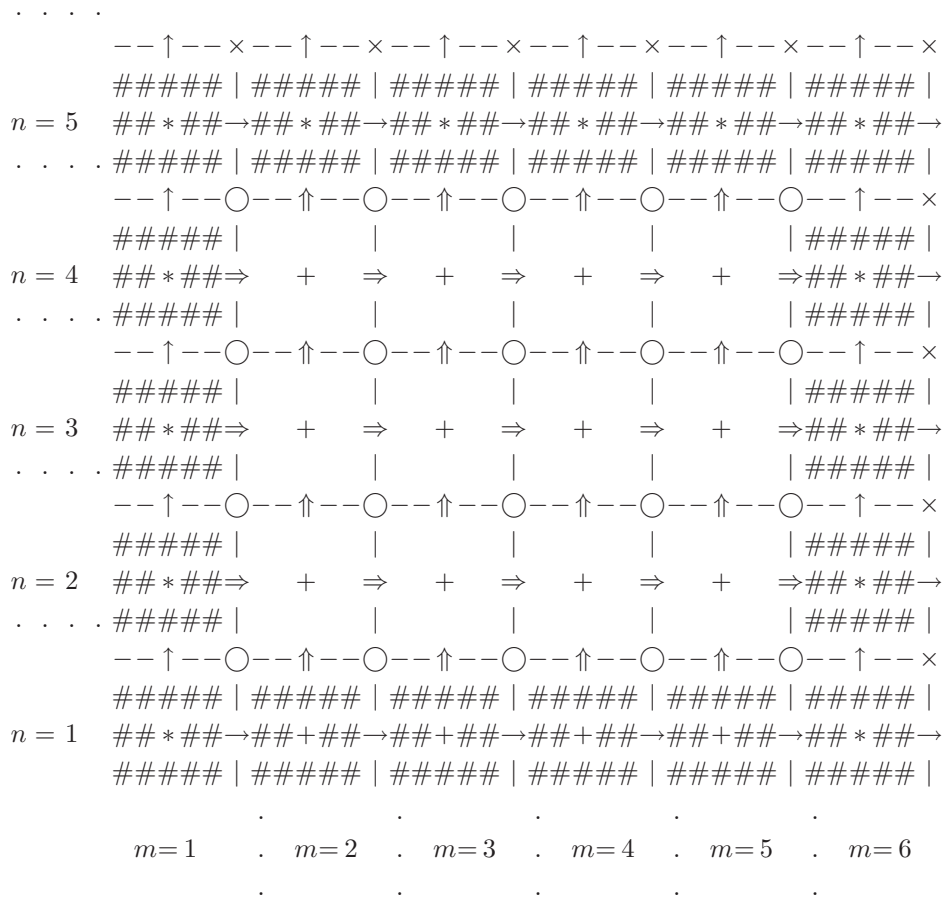
### Discretizations

The horizontal grid on which the above equations are discretised is an Arakawa-C grid (Arakawa & Lamb, 1977) where the velocity and water level points are staggered in space (Fig. 3.1). This grid has intuitive control volumes for mass (volume) where the velocities are located at and perpendicular to the faces, while the pressure (water level), temperature and salinity are located in the centres of the control volumes.

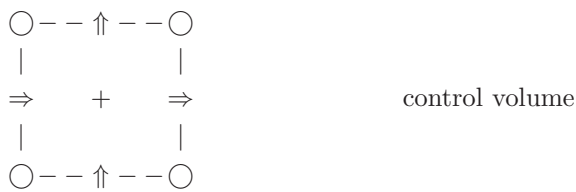
The system of equations is solved through time with the ADI method (Alternate Direction Implicit) to allow for a speedup of solving the system of equations (Stelling, 1984). In ADI each time step is subdivided into two stages at each half time steps. In the first stage one grid direction is calculated implicit, while the other direction is calculated explicit. In the second stage the implicit and explicit directions are swapped.

Although DELFT3D-FLOW allows for curvi-linear grids, we only employed orthogonal grids. For the horizontal momentum advection terms a third-order implicit upwind scheme is used in one ADI stage and with an explicit central difference scheme in the other ADI stage called the Cyclic method (Van Eijkeren *et al.*, 1993; Stelling & Leendertse, 1991). The momentum equations are discretised in non-conservative form. The horizontal constituent advection terms use the same method, albeit with a different stencil. The vertical momentum and constituent equations are solved fully implicitly to guarantee stability with the large time steps optimal for the horizontal

direction. A second-order central scheme is used (Stelling, 1984; Stelling & Van Kester, 1994; Delft Hydraulics, 2006). A mass conservative Forrester filtering process is used in the vertical to prevent non-physical oscillations, and especially overshoot of the salinities below the pycnocline. In addition, the filter mixes up immediately any unstable reverse stratification that would lead to convection. In the horizontal direction also a Forrester filter is applied. For the exact notation of the discretization of all terms in for each ADI stage the reader is referred to Broomans (2003) and TriWaq (1999).



$\bigcirc \quad \times$  corner points (active, dummy)  
 $+$   $*$  centre ( $\eta$ ) points (active, dummy)  
 $\Rightarrow \quad \rightarrow$   $u$ -velocity points (active, dummy)  
 $\Uparrow \quad \uparrow$   $v$ -velocity points (active, dummy)  
 $\#$  dummy area of grid



$\Uparrow \quad \dots \quad \bigcirc$   
 $|$   
 $+$   $\Rightarrow$  points with same matrix index

**Figure 3.1:** The DELFT3D-FLOW horizontal staggered Arakawa-C grid.

### 3.2.2 An idealized rectangular tidal basin with tidal forcing

#### Domain

The idealized numerical model is chosen to encompass the  $50 \times 100 \text{ km}^2$  core of the Rhine ROFI (Fig. 2.1). The inner high resolution part of the domain is 65 km in cross shore width by 105 km in alongshore length, see Fig. 3.2. Here the grid consists of  $130 \times 210$  grid cells with a grid size of 500 m. On the Northern and Western side of the inner domain an additional margin of 25 cells was added to minimize boundary effects. The grid size of these cells increased with a factor 1.2 per cell from the  $130 \times 210$  inner domain towards the boundaries. In this way the open boundaries could be located as far away as possible, while still satisfying the numerical constraint of a maximum 20% grid size variation.

A coastal wall is located on the Eastern side of the domain with a river discharge located 30 km to the North of the Southern boundary. The river has a constant discharge of  $2500 \text{ m}^3\text{s}^{-1}$  located at the head of the estuary. The estuary consists of a uniform one grid cell wide, 45 km long channel. The width of the river discharge at the mouth is 500 m. The depth decreased linearly

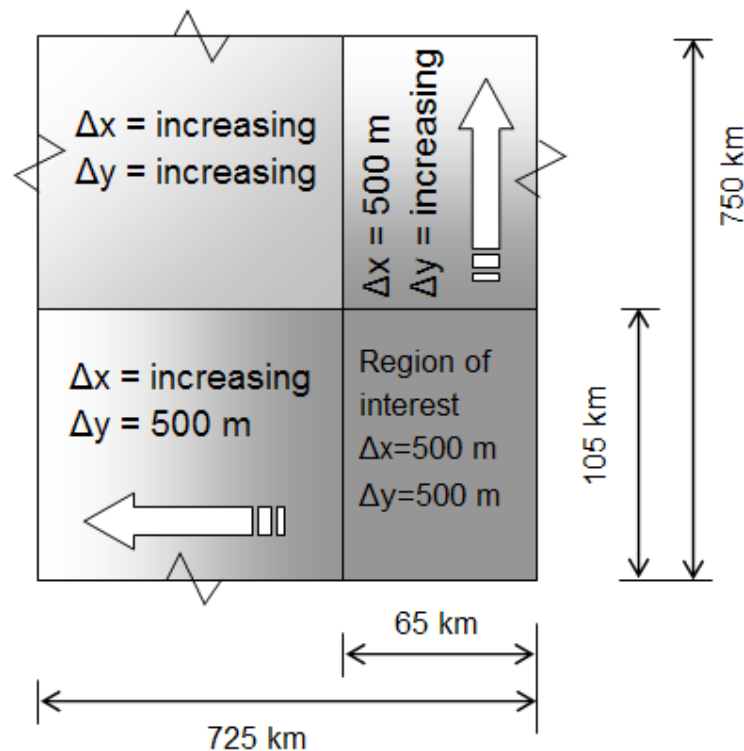


**Figure 3.2:** Plan view of the numerical model grid. The northern and eastern boundaries are located far away using a gradually increasing cell size from the inner  $65 \times 105 \text{ km}^2$  domain outwards. At the South boundary a water level boundary condition (BC) is imposed, the West and North boundaries are of the Riemann type. See also Fig. 4.1.

from 20 m at the mouth to 5 m at the head, where a 0 PSU fresh water source was located. This lay-out allowed for a stable salt wedge to develop. This was found to be important for a correct two-layer velocity profile and momentum exchange at the mouth of the estuary. The river has a 90° bend to avoid large numbers of inactive grid points. The other three boundaries are open. The model is initialised with a salinity of 34.5 PSU, which is the long term average for the North Sea found by van Suijlen & Duin (2002). The model is located at the position of the Rhine outflow, i.e. at a latitude of 52 °N. Coriolis is constant throughout the domain. For further details refer to chapter 4.

### *Tide*

The tide is imposed at the downstream Southern boundary of the model by specifying the harmonic semi-diurnal 12 hour S2 component for the water level for every single grid cell separately (Fig. 3.2). Although the M2 component is in fact the main component, we employ only an S2 signal with a period of exactly 12 hour for easy time keeping. The imposed water level disturbances at the Southern boundary propagate northward into the model domain as a Kelvin wave. The Eastern boundary is closed and behaves as a coastal wall supporting the Kelvin wave. Due to the relatively large size of the grid cells - the depth of the grid cells is much smaller than the horizontal dimension - this boundary can be modelled as free-slip.

At the West and North boundary the Riemann boundary type is imposed (Fig. 3.2). For a one dimensional wave propagation phenomenon this type allows the outgoing Riemann invariant to propagate undisturbed out of the model domain. By specifying a zero incoming Riemann invariant this boundary becomes weakly-reflective. In a two-dimensional case weak reflections can occur due to components that are not strictly normal to the boundary. These disturbances are small though, because the Kelvin wave propagates in fact parallel to the coast, perpendicular to the boundary. To avoid any disturbances the boundaries are located hundreds of kilometres away from the area of interest.

The water levels prescribing the incoming Kelvin wave are calculated for each grid cell separately from simplified depth-averaged shallow water equations neglecting the advective acceleration terms, an approach we started in Jacobs (2004). The cross shore velocity component in  $x$ -direction is set to zero in line with the definition of a Kelvin wave (Taylor, 1921). The resulting equations read:

$$\frac{\partial \eta}{\partial t} + H \frac{\partial V}{\partial y} = 0 \quad (3.16)$$

for continuity and (see Fig. 3.3)

$$fV + g \frac{\partial \eta}{\partial x} = 0 \quad (3.17)$$

for cross shore momentum balance and

$$\frac{\partial V}{\partial t} + g \frac{\partial \eta}{\partial y} - F_y = 0 \quad (3.18)$$

for alongshore momentum balance, where  $V$  is the depth averaged velocity component in alongshore  $y$ -direction,  $f$  is the Coriolis parameter,  $t$  is time,  $g$  is the gravitational acceleration and  $F$  represents the bottom friction. For bottom friction a linearized formulation is employed to allow for an analytic solution. The linearized friction coefficient  $\lambda_{lin}$  is determined by equating the energy loss over one tidal cycle with the one calculated with quadratic bottom friction coefficient  $\lambda_{quad}$  using as formulation for the bottom friction  $\tau_{quad}$  (Battjes, 1998)  $\tau_b = \lambda_{quad} V |V| \equiv \lambda_{lin} V$ :

$$\int_0^T \tau_{lin} V dt \equiv \int_0^T \tau_{quad} V dt \Leftrightarrow \int_0^T \lambda_{lin} V^2 dt \equiv \int_0^T \lambda_{quad} |V| V^2 dt \quad (3.19)$$

This results in the following bottom friction coefficient

$$\lambda_{lin} = \frac{8}{3\pi} \rho C_f \hat{V} \quad (3.20)$$

where  $\hat{V}$  is the time and depth averaged velocity and  $C_f$  is a friction factor. Defining an alongshore friction coefficient  $\kappa$  as

$$\kappa = \tau_{lin,y} / \rho h V = \frac{8}{3\pi} C_f \hat{V} / h \quad (3.21)$$

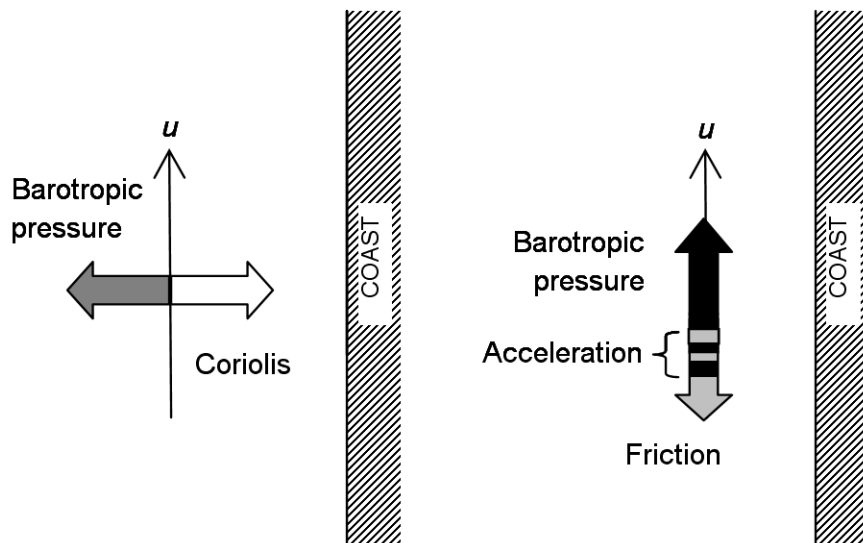


**Figure 3.3:** Sketch of the cross shore and alongshore force balance in a Kelvin wave along a straight coastline.



the final alongshore momentum balance Eq. 3.18 reads

$$\frac{\partial V}{\partial t} + g \frac{\partial \eta}{\partial y} + \kappa V = 0 \quad (3.22)$$

The set of equations Eqs. 3.16, 3.17 and 3.22 is solved assuming a harmonic solution

$$\eta = \eta_0 e^{(-k_x x - k_y y + i\omega t)} \quad (3.23)$$

where  $k$  are the wave numbers,  $\omega$  is the frequency of the harmonic constituent considered,  $i$  is the imaginary unit and  $\eta_0$  is the water level amplitude at the origin. Substitution yields

$$k_x = \frac{f}{c_0} \frac{1}{\sqrt{1 - (i\kappa/\omega)}}, k_y = i \frac{\omega}{c_0} \sqrt{1 - (i\kappa/\omega)} \quad (3.24)$$

with the frictionless wave speed  $c_0 = \sqrt{gH}$ . In the limit case of no bottom friction, there is no alongshore variation and the cross shore variation reduces to  $\eta = \eta_0 e^{-(x/R_0) + i\omega t}$  with the external Rossby radius  $R_0 = c_0/f$ . Note that the cross shore variation is a function of the alongshore friction. This implies that although we only have to impose the tide at the cross shore Southern boundary of our model, we do have to take into account alongshore friction. An iteration procedure is performed per grid point until the amplitude of the velocity  $\hat{V}$  and the friction coefficient  $\kappa = f(\hat{V})$  are in agreement, resulting in a spatially variable field of  $\kappa = f(\hat{V})$ . The resulting amplitudes and phases of the water level are shown in Fig. 3.4.

### 3.2.3 Turbulence modelling

The vertical mixing is resolved with a standard  $k - \varepsilon$  model, including a buoyancy destruction term, the development of which has been described in Uittenbogaard *et al.* (1994), Van Kester *et al.* (1994), Delft Hydraulics (2006) and Stelling (1995). A special feature is that  $k$  and  $\varepsilon$  are not calculated in the cell centres as other scalars, but on the vertical faces. A background eddy viscosity of  $10^{-4} \text{ m}^2\text{s}^{-1}$  is adopted, which is small compared to the tidally induced eddy viscosity (order  $10^{-2} \text{ m}^2\text{s}^{-1}$ ). The reason for this to avoid the onset of too strong stratification in the model, due to the neglect of mixing generated by internal wave breaking (Uittenbogaard & Imberger, 1993). In this section the  $k - \varepsilon$  model of DELFT3D-FLOW is validated against field measurements of dissipation. Because turbulence models are usually validated on derived quantities as velocities and Reynolds stresses, dissipation measurements provide an excellent opportunity to validate “the models more directly and fundamentally at the ‘intermediate level’ by comparing measurable aspects of the turbulence with model simulations” (Simpson *et al.*, 1996).

Rippeth *et al.* (2001) report high-resolution profile measurements that were performed in the Irish Sea. Data were collected at (53°28.4'N, 3°39.2'W) in Liverpool Bay during two tidal cycles on 5-6 July 1999. The following data were collected. Dissipation rates ( $\varepsilon$ ) were measured with the free-falling FLY4 probe that measures the microstructure of the velocity shear. For details on the FLY4 probe refer to Simpson *et al.* (1996) and Dewey *et al.* (1987). Temperature and conductivity (i.e. salinity) were measured at 20 Hz with sensors mounted on the FLY4 probe. The flow structure of the water column was observed using an RDI 600-KhZ ADCP employed on the seabed. The raw data are shown in Fig. 3.5. These data are made available on the GOTM website ([www.gotm.net](http://www.gotm.net)) as part of a test bank for GOTM. We express our gratitude to the GOTM team and the authors of Rippeth *et al.* (2001) for providing the data.

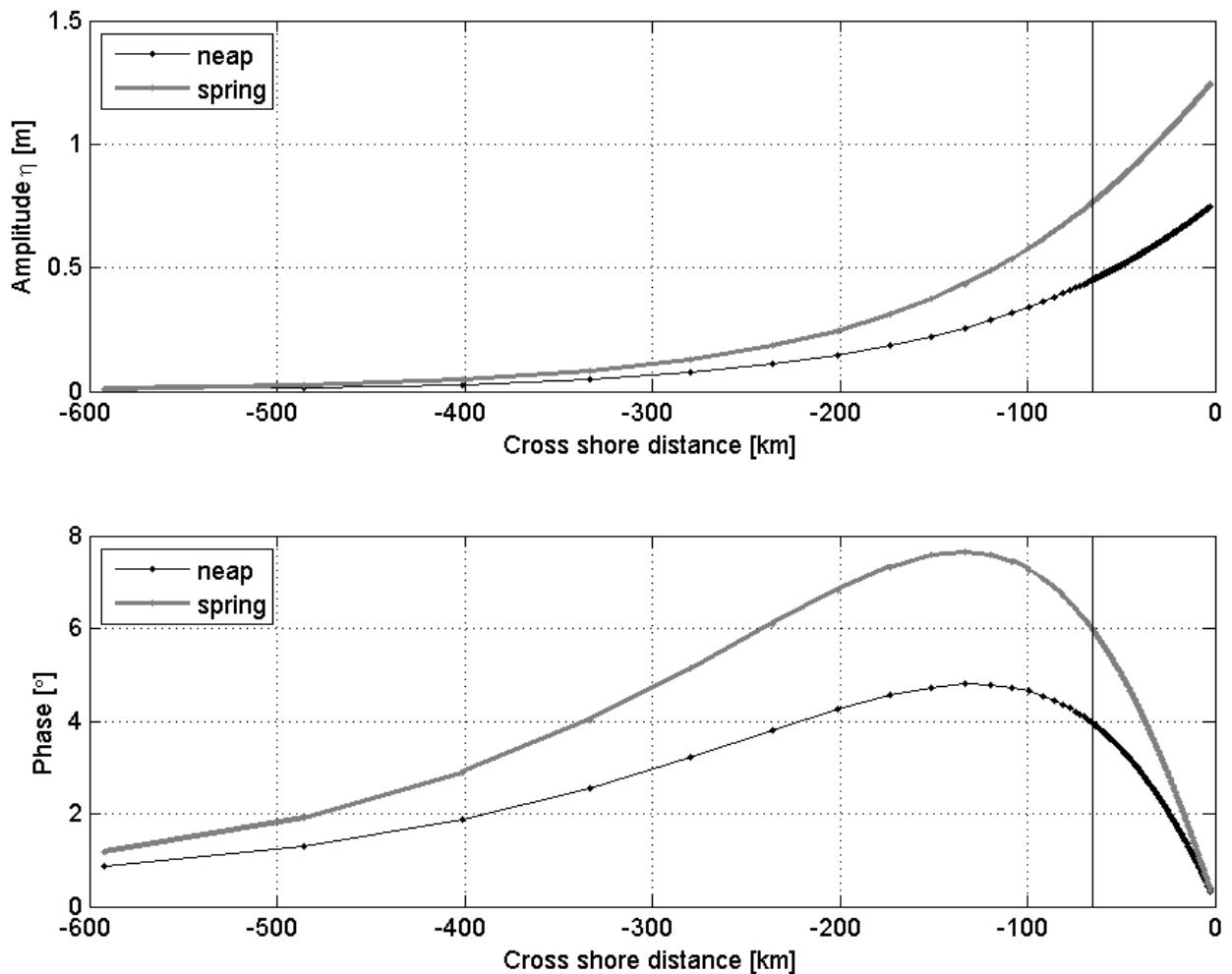


**Figure 3.4:** Tide at Southern boundary of idealized model, the area right of the vertical line indicates the region of interest with constant 500 m grid resolution. The representative neap and spring tide as used in chapters 4, 5 and 6 have an amplitude of 75 and 125 cm respectively at the coast. The dots represent the cell centres where the water levels are imposed.

The settings of the numerical model are:

- 50  $\sigma$ -layers are used, this number is from Simpson *et al.* (2002). The top and bottom of the water column do not contain data due to the missing raw data near the bottom and free water surface. Therefore these data are filled in by extrapolating with the nearest neighbour real value. A second simulation is performed with 16 layers, the same number as used in our simulations of the Rhine ROFI in Chapters 4, 5 and 6.
- Boundary data are binned to 30 minutes bins. Every bin time step is interpolated between the previous and subsequent raw data time step.
- An integration time step of 60 seconds is used.
- A spin-up period of 10 hr (adopted from Simpson *et al.* (2002)).
- The bottom roughness length of  $2.5 \times 10^{-3}$  m is adopted from Simpson *et al.* (2002).
- The data were smoothed with a  $3 \times 3$  stencil, using 3 time steps and 3  $\sigma$ -layers. The binned, smoothened data set is shown in Fig. 3.5.
- $5 \times 5$  grid cells with  $\Delta x = 100$  m.
- Horizontal gradients are neglected.
- At the West boundary water levels are imposed.
- At the East boundary the 3D (boundary normal)  $u$ -velocity profile is imposed, for the (along-boundary)  $v$ -velocity a zero boundary-normal gradient is chosen.
- At the North and South boundary the 3D (boundary normal)  $v$ -velocity profiles are imposed, for the (along-boundary)  $u$ -velocity a zero boundary-normal gradient is chosen.
- Temperature and salinity are initialised with vertically homogenous profiles of  $14.7^\circ$  and 33.2 PSU respectively.
- Wind (momentum) fluxes are ignored.
- Turbulence is initialized zero. At the inflow boundary the turbulence parameters are estimated with a simplified 1D vertical model (Uittenbogaard, pers. com.).
- The only  $k - \varepsilon$  parameter that can be changed in the official release executable of DELFT3D is the background viscosity. This value is set to the value  $10^{-4} \text{ m}^2\text{s}^{-1}$  that is commonly used to prevent artificial decoupling due to the buoyancy term in the turbulence model (Uittenbogaard & Imberger, 1993). Because the velocity, salinity and temperature are almost fully governed by the boundary conditions, this value only matters for  $k$  and  $\varepsilon$ .

The model results are shown in Figs. 3.6 and 3.7. The model is able to reproduce the main characteristics of the measured dissipation profiles. In the bottom layer a quarter diurnal pattern dominates, in phase with velocity amplitude. In the upper layer the pattern has a semi-diurnal nature, governed by the periodic stratification. The bottom layers are much better reproduced with the model with 50 layers, the simulations with 16 layers underestimate  $k$  and the dissipation near the bed. However, in the upper two-thirds of the water column the results are identical. We can therefore conclude that the interaction between tidal shear and stratification, which occurs in the upper water layers, can be reproduced sufficiently well with 16 layers.

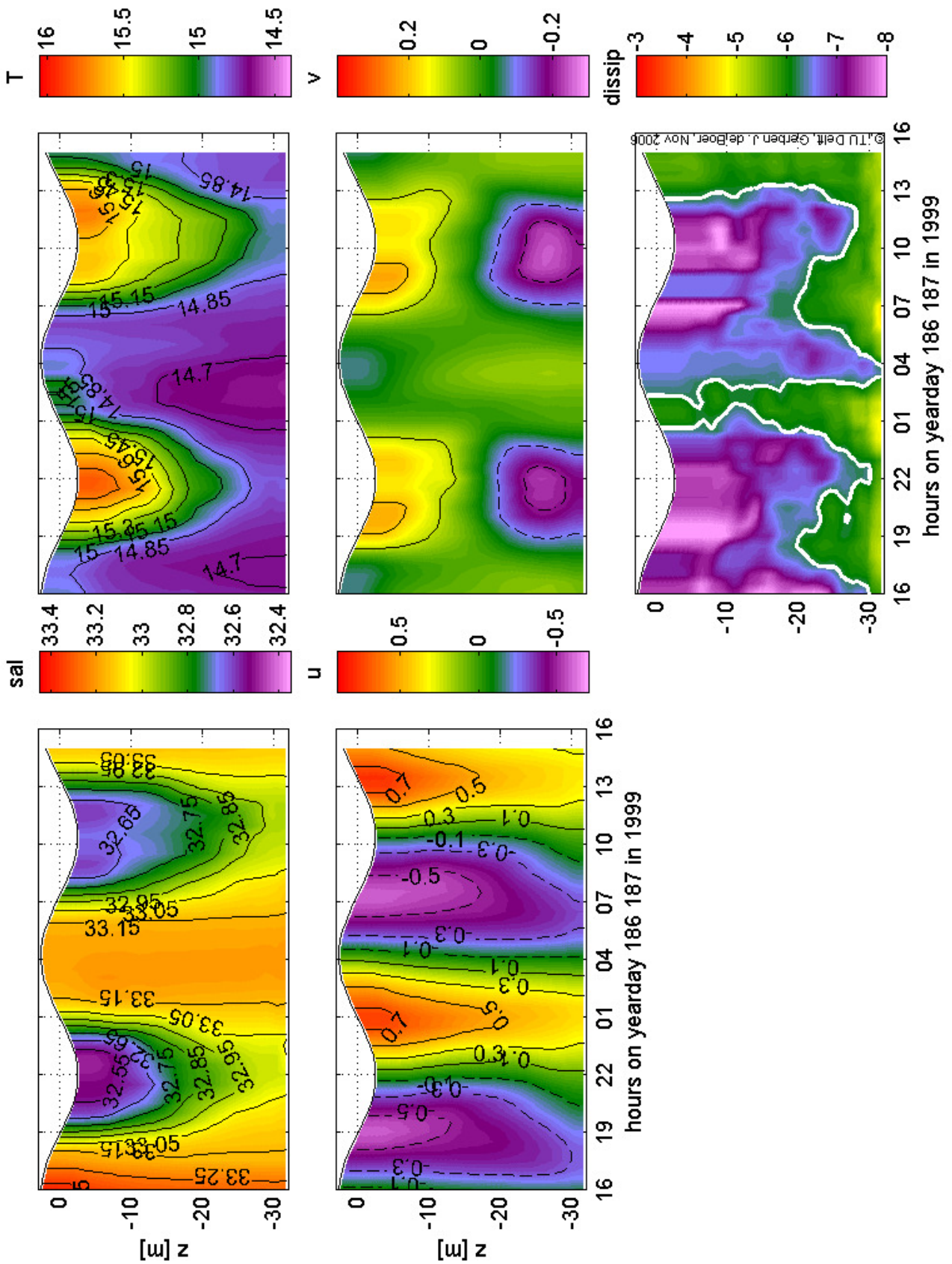


**Figure 3.5:** Measured temperature, salinity, velocities and dissipation of Rippeth *et al.* (2001) binned to 50  $\sigma$ -layers and 30 minute temporal bins.



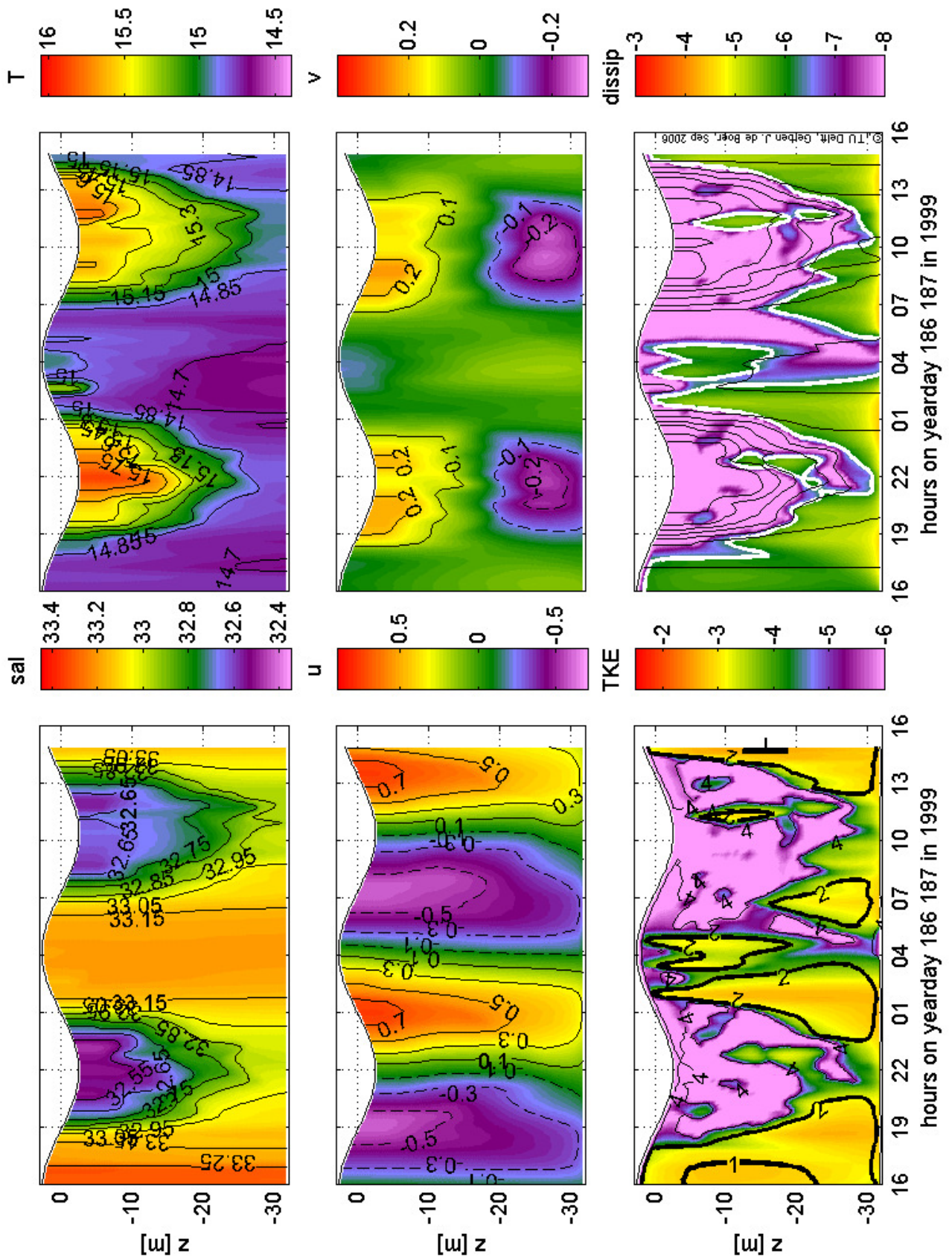


Figure 3.6: Modelled situation of Fig. 3.5 with 50  $\sigma$ -layers (same number of layers as Burchard (2002)).





### 3.3 Remote sensing of SST

Since 1990 KNMI, the Dutch met office, collects NOAA AVHRR imagery at the raw data resolution of 1 km, processes it to SST and maps it for the North Sea (Roozekrans & Prangma, 1992; Roozekrans, 1997). The 1 km resolution is just sufficient to capture coastal ROFI features that have an internal Rossby Radius up to 10 km. We received the full 1990 - 2005 archive from KNMI containing over 3000 images.

SST data from the polar orbiting NOAA-AVHRR satellites were obtained from the Royal KNMI, who operate an HRPT receiving station and could thus provide for 1.1 km LAC resolution. The data were supplied as readily processed L3 data. For details on the processing see (Roozekrans & Prangma, 1992). Despite the fact that this processing line might not provide for the latest state-of-the-art processing algorithms, the accuracy of the data is sufficient for this study purpose. Relevant details of the processing are repeated here.

The SST L3 data are binned on a rectangular polar stereographic projection centred at (0 °W; 52°N) with a resolution of 1 km per pixel. The data cover roughly the region [0 - 8 °E; 54.7 - 55.3 °N]. In order to reduce data storage, immediately after receiving the data were cropped to the North Sea and then automatically processed using a navigation algorithm with a spatial accuracy of 20 km. After stereographic projection the data were manually geo referenced (shifted) using distinctive Ground Control Points on the Dutch coastline. The vegetation index image (using channel 1 and 2) was used for this, as in this image the coastline is generally best visible. After this manual correction the accuracy has increased 1 to 2 km. However, due to the fact that the data were not geo-referenced until after projection, the images are slightly distorted and can not always be shifted to fit the whole coastline. Images on which the Dutch coastline was not visible at all, could not be geo-referenced and were discarded by KNMI. Not unfortunate, our SST data set therefore shows a strong bias towards unclouded pixels in the Rhine ROFI region (Figs. 3.8, 3.9 and 3.10).

The NOAA satellites record and store reflectance data at 1024 levels with a resolution of 0.1 °K. The SST values are determined with a zenith-dependable linear split-window technique using channels 4 and 5 and coefficients from the Rutherford Appleton Laboratory. Comparison with field data in various studies shows that the bulk temperature (defined at 1 m below the surface) can be determined with an accuracy of more than 0.5 °K. Cloud edges were determined using an 8 step test in which sometimes, as a side-effect, the strong gradients present on the margins of a stratified plume subject to solar heating are flagged off as clouds.

The (annual) variation of the SST in the Southern North Sea is discussed in Pietrzak *et al.* (2008b) and Pietrzak *et al.* (2008a). Note that the temperature pattern correlates well with the water mass classification (Fig. 2.2).

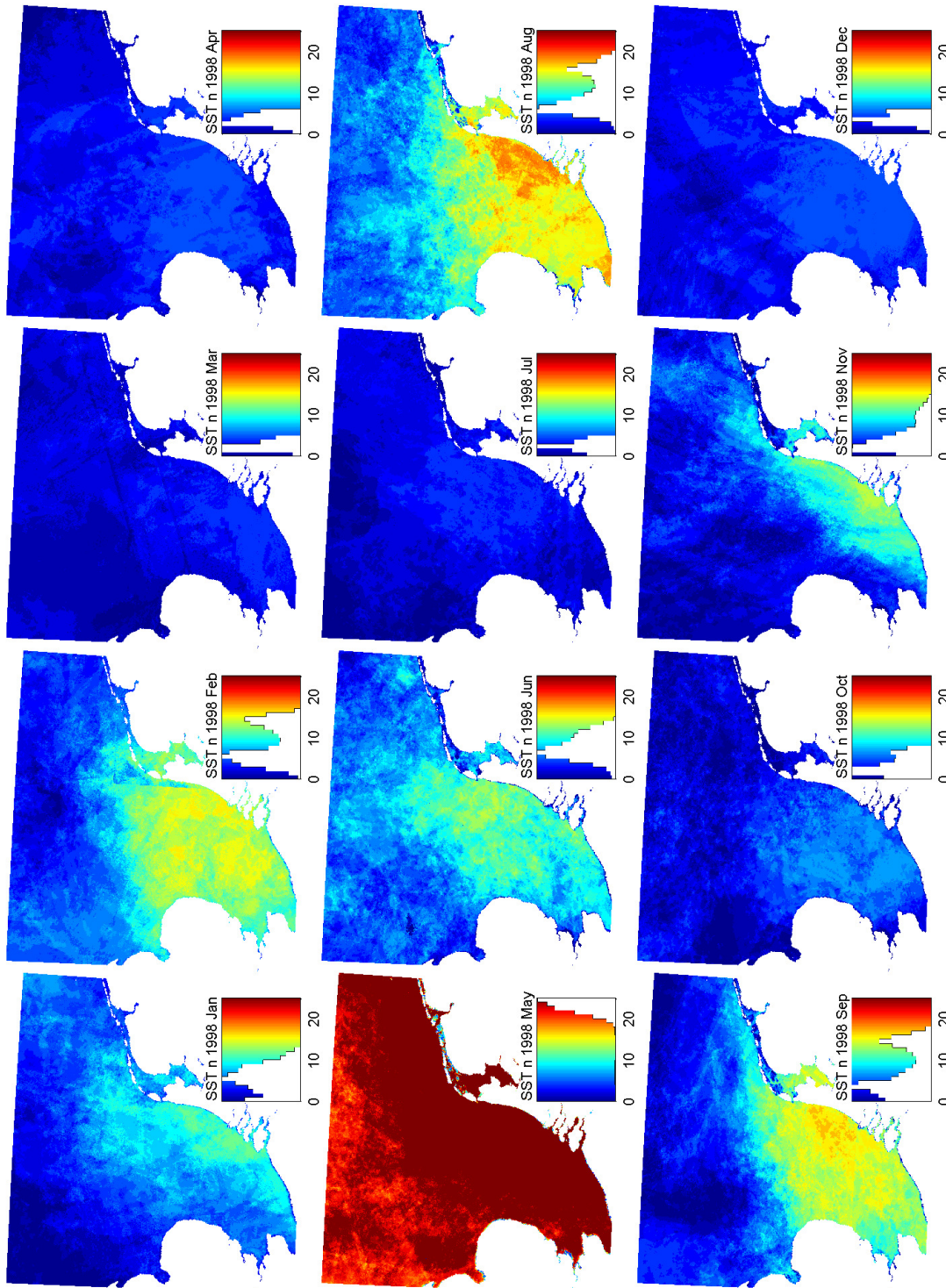


**Figure 3.8:** Monthly number of SST pixels available in 1998 binned per month. Note the strong bias of images in the Rhine ROFI due to the selection process of KNMI. Also note that most months contain insufficient images for proper statistical analyses, only May contains enough images over the whole domain, while Feb., Aug. en Sep. show a more than average number of pixels in the Rhine ROFI sub-region. Moreover, if a large number of images are present, they come in clusters with up to 6 images per day, an example of which in May 1990 is shown in Fig. 5.3.



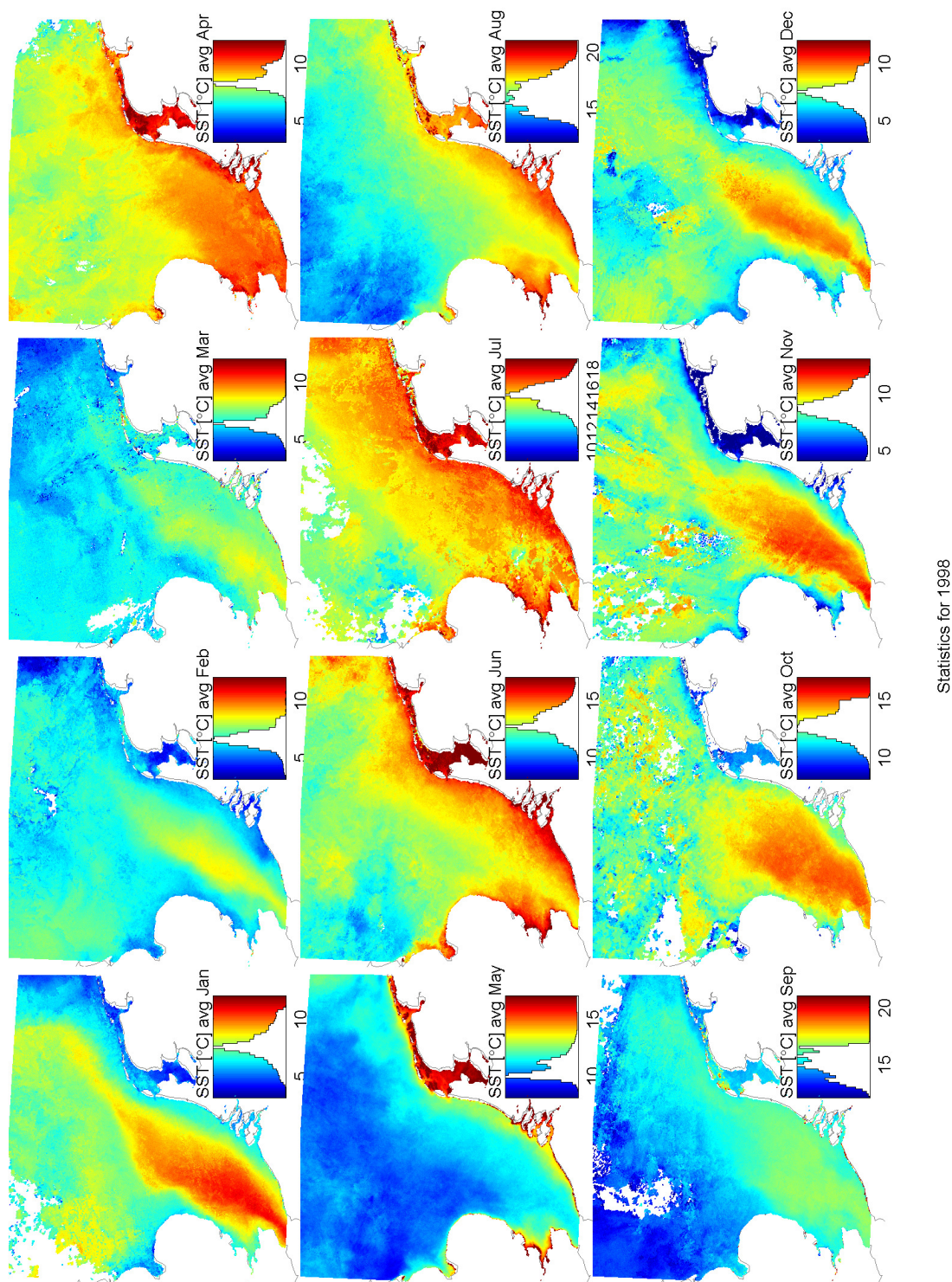


**Figure 3.9:** Monthly mean SST in 1998 binned per month. Note the annual cycle of the North Sea temperatures. Note that in the winter (Oct. - Feb.) the Channel water mass is relatively warmer than the Rhine ROFI water due to cold land run-off. In contrast, in the summer (Apr. - Aug.) the Rhine ROFI water is warmer than the Channel water mass due to warmer land run-off, and due to excess heating of the stratified ROFI waters. During the transition in Mar. and Sep. the two water masses cannot clearly be delineated.



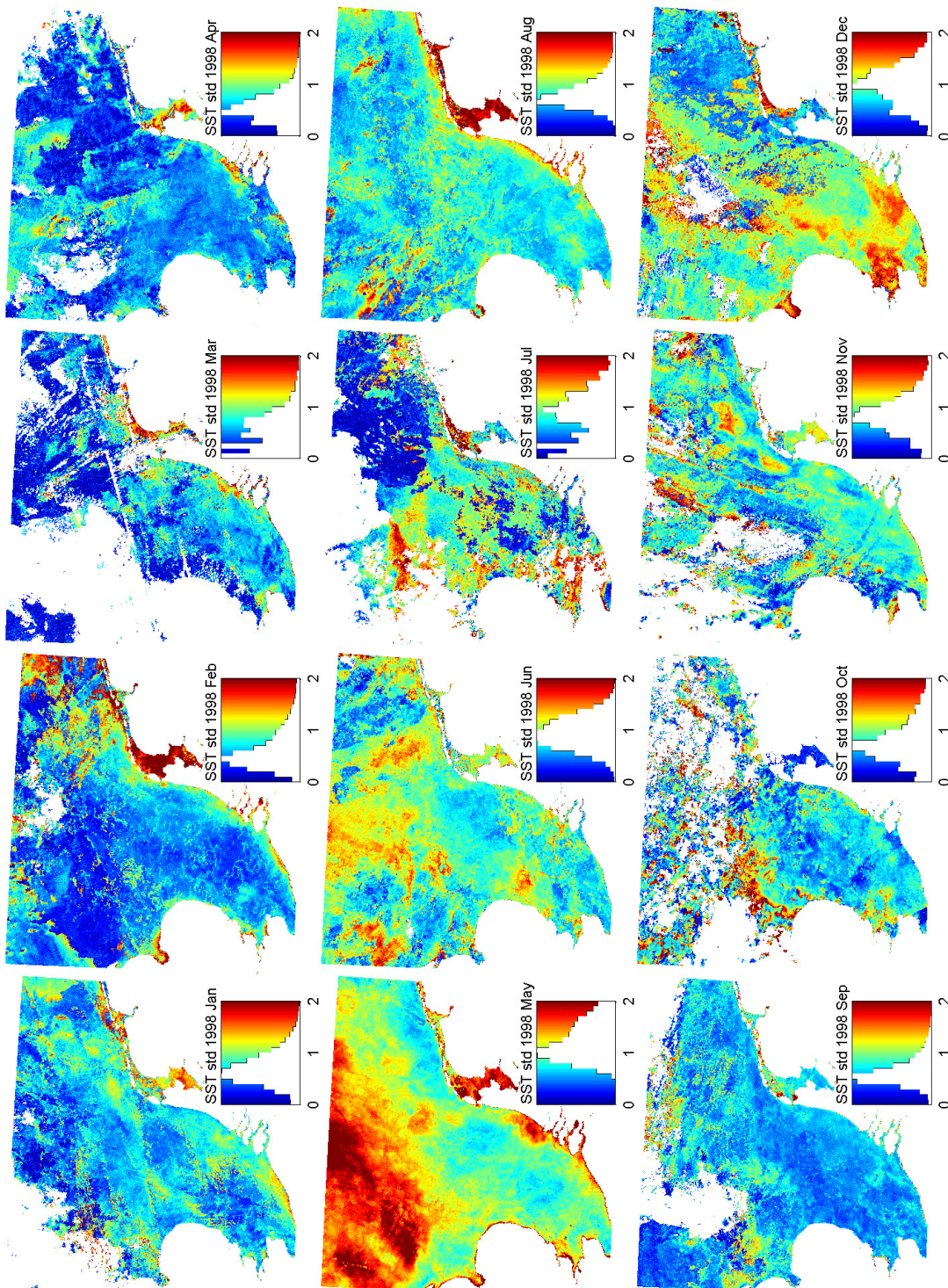


**Figure 3.10:** Monthly standard deviation SST in 1998 binned per month. Note that the SST only has significance in those areas where enough pixel data are available, i.e. in May. Three distinct regions with large SST variations are present. In the central North Sea the seasonal stratification allows for distinct diurnal-variations. The shallow Wadden Sea and shallow Lake IJssel also show large variations. The third region is the Rhine ROFI, the topic of this thesis. In chapter 5 the SST variations in this region are exploited.

## Chapter 4

### On the vertical structure of the Rhine ROFI

This chapter has been published as :

de Boer, G.J., Pietrzak, J.D., & Winterwerp, J.C. 2006. *On the vertical structure of the Rhine region of freshwater influence*. *Ocean Dynamics*, **56**(3-4), (special issue PECS 2004), 198–216. doi:10.1007/s10236-005-0042-1.

#### **Abstract**

An idealised three dimensional numerical model of the Rhine ROFI was set up in order to explore the effect of stratification on the vertical structure of the tidal currents. Prandles dynamic Ekman layer model, in the case of zero depth averaged cross shore velocities, was first used to validate the response of the numerical model in the case of barotropic tidal flow. Prandles model predicted rectilinear tidal currents with an ellipse veering of up to 2%. Then the behaviour of the Rhine ROFI in response to both a neap and a spring tide was investigated. For the given numerical specifications the Rhine plume region was well mixed over the vertical on spring tide and stratified on neap tide. During spring conditions rectilinear tidal surface currents were found along the Dutch coast. In contrast, during neap conditions significant cross shore currents and tidal straining were observed. Prandles model predicted ellipse veering of 50% and was found to be a good indicator of ellipticity magnitude as a function of bulk vertical eddy viscosity. The modelled tidal ellipses showed that surface currents rotated anti-cyclonically whereas bottom currents rotated cyclonically. This caused a semi-diurnal cross shore velocity shearing which was 90° out of phase with the alongshore currents. This cross shore shear subsequently acted on the horizontal density gradient in the plume thereby causing a semi-diurnal stratification pattern with maximum stratification around high water. The same behaviour was exhibited in simulations of a complete spring neap tidal cycle. This showed a pattern of recurring stratification on neaps and destratification on springs in accordance with observations collected from field campaigns in the 90s. In order to understand the increase in ellipticities to 30% during neaps as well as the precise shape of the vertical ellipse structure, stratification has to be taken into account. Here a full three dimensional numerical model was employed and was found to represent the effect of decoupling of the upper and lower layers due to a reduction of mixing at the pycnocline.

## 4.1 Introduction

River plumes occur wherever significant amounts of buoyancy, due to freshwater from rivers, flow out into coastal seas and oceans. Under the influence of the Earth's rotation the out flowing estuarine waters tend to turn to the right on leaving the river mouth (in the Northern Hemisphere) forming narrow coastal currents. River plumes can maintain their cross-shelf structure for hundreds of kilometres, e.g. Chao (1987), Chao (1988), Chao (1990), Fong & Geyer (2001), Fong & Geyer (2002), Kourafalou *et al.* (1996a), Kourafalou *et al.* (1996b), Rasmussen *et al.* (1999), McClimans *et al.* (2000), Pietrzak & Bolding (1999), Pietrzak *et al.* (2002), Yankovsky *et al.* (2001) and Garcia Berdéal *et al.* (2002). Consequently they are extremely important in determining the transfer of matter and the fate of pollutants in coastal seas. The term, region of fresh water influence (ROFI) was introduced by Simpson *et al.* (1993) as a generalisation of the river plume terminology. He did this in order to specifically take into account effects of vertical mixing and tidal straining (Simpson *et al.*, 1990). Simpson (1997) describes the physical processes occurring in a ROFI and the competition between buoyancy and stirring.

The Rhine - Meuse River system has an annual mean discharge of  $2500 \text{ m}^3\text{s}^{-1}$ . It acts as a source of buoyancy into the shallow and high tidal energy North Sea forming a fairly large ROFI. The Rhine ROFI is on average concentrated within a 20 km wide coastal strip, while occasionally it extends a distance of almost 40 km offshore (De Kok, 1996; De Ruijter *et al.*, 1997; Van Alphen *et al.*, 1988). The tides in the Southern bight of the North Sea are dominated by the M2 tide, with a significant S2 component. The tide has the character of a progressive Kelvin wave with vertically averaged velocities between  $0.5$  and  $1.0 \text{ ms}^{-1}$  (De Kok, 1996) while within the ROFI area surface currents have speeds ranging between  $0.7$  and  $1.1 \text{ ms}^{-1}$  over the spring-neap cycle (Van der Giessen *et al.*, 1990).

It is well known that tidal currents in shallow water exhibit a marked vertical structure. In order to investigate this vertical structure Prandle (1982a,b) derived analytic solutions to the linear shallow water equations, assuming a vertically uniform eddy viscosity. Tidal current vectors describe an elliptical path as they rotate in the horizontal plane. An ellipse can be resolved into two circular motions, one rotating anti-cyclonically and the other rotating cyclonically, (respectively, clockwise and anticlockwise in the N. Hemisphere). Using this simple model, properties such as the semi-major axes, ellipticity, inclination and phase and how they vary from the surface to the bed, may be investigated. These analytical models have been used to explain the observed vertical variations in the structure of a tidal current in homogenous waters. The component of the tide that rotates in the same direction as the planetary rotation is not as strongly affected by bottom friction and has a thinner bottom Ekman layer than a component that rotates against the direction of planetary rotation. Since stratification leads to a reduction in turbulence production, the assumption of a vertically uniform eddy viscosity is inadequate for stratified seas (Maas & Van Haren, 1987). Furthermore this alters the behaviour



of the tidal ellipses and hence alters the vertical structure of the tidal currents (Visser *et al.*, 1994; Van Alphen *et al.*, 1988).

Simpson *et al.* (1993) presented data which was collected in the Rhine ROFI in Sept. and Oct. 1990 and provided evidence of both semi-monthly and semi-diurnal time scales in the water column structure associated with the spring and neap surveys. The spring survey was augmented by wind which led to a well mixed water column everywhere except near the mouth of the Rhine. In contrast during the neap survey, which was accompanied by weak winds, stratification was observed. In their study the average Rhine River discharge was  $2000 \text{ m}^3\text{s}^{-1}$ . The data they used were from hydrographic surveys, HF radar measuring surface currents and moorings. They found that the vertical structure of tidal currents could vary in a systematic fashion due to stratification and de-stratification events. They also found that during well mixed conditions the tidal currents were rectilinear and directed parallel to the coast. In contrast during stratified conditions the tidal currents contained significant cross shore components. The phases of the cross shore currents at the surface and bed show a difference of  $180^\circ$ . Visser *et al.* (1994) and Simpson & Souza (1995) reported observations of semi-diurnal tidal ellipse profiles within the Rhine plume using the same data set. Notably, they found a slow variation of the properties of the semi-diurnal tidal current ellipse in the Rhine ROFI. The surface currents rotated anti-cyclonically and near bed currents rotated cyclonically. Visser *et al.* (1994) used a simple two-layer model and found that stratification caused a reduction in the mixing, thereby decoupling the upper and lower layers. Simpson & Souza (1995) also found evidence for the change in polarisation of the tidal ellipses due to the stratification.

In addition to the switching behaviour observed in the tidal ellipses during the spring-neap tidal cycle, tidal straining also generates fluctuations in the vertical stability at the semi-diurnal tidal frequency. Stability was found to be maximal at high water. Tidal straining (Simpson *et al.*, 1990) refers to the influence of differential advection arising from the vertical shear in the tidal flow and which interacts with the horizontal density gradient to generate fluctuations in the vertical stratification at the tidal frequency. For example, in an estuary the gravitational circulation arising from the longitudinal density gradient is acted upon by the vertical shear in the tidal current. Consequently, during the ebb higher seaward velocities at the surface move the lighter water seaward faster than the slower moving denser waters near the bed, thereby increasing the stratification in the estuary. Conversely on the flood the reverse happens and the effect of vertical shear is to reduce the stratification. In the Rhine ROFI when the water column is stratified the tidal currents exhibit a marked cross shore structure, with cross shore currents showing a  $180^\circ$  phase difference between the surface and bed. This marked increase in cross shore shear in the vertical flow structure gives rise to tidal straining and periodic semi-diurnal stratification. Upon returning to well mixed conditions the tidal ellipses return to rectilinear form and the periodic semi-diurnal stratification also ceases. Data collected from a number of ROFIs and estuarine systems has found evidence for the tidal straining mechanism. Examples

include Liverpool Bay (Simpson *et al.*, 1990), The Rhine ROFI (Fisher *et al.*, 2002), and the York Estuary, (Simpson *et al.*, 2005).

Simpson & Souza (1995) studied the semi-diurnal switching of stratification in the Rhine ROFI and concluded that this semi-diurnal variation resulted from cross shore tidal straining. Souza & Simpson (1997) also included data from a survey in Sept. 1992 which further demonstrated the role of tidal straining. Simpson (1997) discussed the physical processes in the ROFI regime, commenting on the importance of tidal straining in ROFI systems.

Results from a one dimensional point source model confirmed the crucial role of cross shore tidal straining in the Rhine ROFI. This was further supported by the results of Souza & James (1996) who used a two-dimensional cross shore vertical slice model. Ruddick *et al.* (1995) employed a three dimensional model and could reproduce the qualitative differences observed in the vertical structure of the tidal currents due to stratification. However, they looked at tidally averaged properties, and did not investigate the influence of stratification on the tidal ellipses. Luyten (1996) also used a three dimensional model in which they assumed a cross shore horizontal density gradient which was constant over depth and time (their model did not include advection or diffusion of momentum). They also demonstrated the importance of stratification on the development of cross shore flow and the role of tidal straining on the semi-diurnal variability in stratification.

In this paper we investigate the influence of stratification on the rotary components of the tidal current vectors in the River Rhine Plume. In order to achieve this objective we use a numerical model and consider two different scenarios, in the first case a stratified neap plume and in the second case a well mixed spring plume is investigated. In both cases an idealised rectangular basin, with a constant depth of 20 m and a constant discharge of  $2500 \text{ m}^3\text{s}^{-1}$  (the long-term average of the combined Rhine-Meuse system) is specified to explore the two scenarios. Additionally, a sequence of three spring neap tidal cycles were explored. The conditions are chosen to correspond to those explored by Visser *et al.* (1994). In section 2 we describe the numerical model set up. In section 3 barotropic tidal results from the numerical model are compared with the analytical solutions of Prandle (1982a,b). In section 4 we describe the baroclinic behaviour of the plume. Section 5 concludes with a discussion.

## 4.2 Model set-up

The numerical model used in this study is the FLOW module of DELFT3D. It is a three-dimensional, curvilinear, primitive equation model, for a description see Stelling (1984), Stelling & Van Kester (1994) and Lesser *et al.* (2004). A 20 m deep rectangular domain was used. The inner high resolution part of the domain is 65 km in cross shore width by 105 km in alongshore length, see Fig. 4.1. Here the grid consists of  $130 \times 210$  grid cells with a grid size

of 500 m. On the Northern and Western side of the inner domain an additional margin of 25 cells was added. The grid size of these cells increased with a factor 1.2 per cell from the  $130 \times 210$  inner domain towards the boundaries. In this way the open boundaries could be located as far away as possible, while still satisfying the numerical constraint of a maximum 20% grid size variation.

A coastal wall is located on the Eastern side of the domain with a river discharge located 30 km to the North of the Southern boundary. The river has a constant discharge of  $2500 \text{ m}^3\text{s}^{-1}$  located at the head of the estuary. The estuary consists of a uniform one grid cell wide, 45 km long channel. The width of the river discharge at the mouth is 500 m. The depth decreased linearly from 20 m at the mouth to 5 m at the head, where a 0 PSU fresh water source was located. This lay-out allowed for a stable salt wedge to develop. This was found to be important for a correct two-layer velocity profile and momentum exchange at the mouth of the estuary. The river has a  $90^\circ$  bend to avoid large numbers of inactive grid points. The other three boundaries are open. The model is initialised with a salinity of 34.5 PSU, which is the long term average for the North Sea found by van Suijlen & Duin (2002). The model is located at the position of the Rhine outflow, at a latitude of  $52^\circ$  North. Coriolis is constant throughout the domain.

The model has 16 equidistant  $\sigma$ -layers in the vertical, which, combined with the depth of 20 m and a water level variation of less than 1.25 m, always gives a resolution better than 1.33 m in the vertical in the entire domain. Vertical mixing of salt and momentum are resolved with the standard  $k$ - $\epsilon$  model, including a buoyancy destruction term (Stelling, 1995). A background viscosity and diffusivity of  $10^{-4} \text{ m}^2\text{s}^{-1}$  are imposed. Compared to the tidally induced eddy

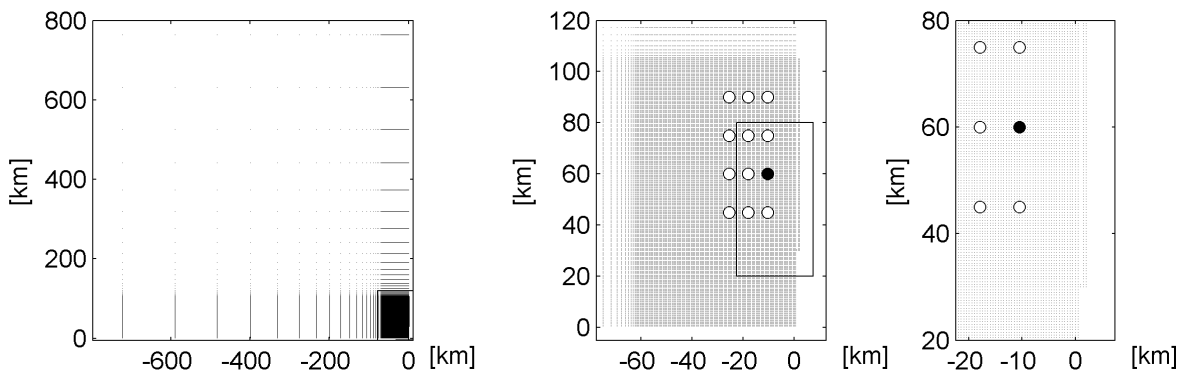


**Figure 4.1:** Schematic overview of the model grid: the middle panel shows the cell corners of the orthogonal equidistant  $65 \times 105$  km grid covering the plume region of interest with a resolution of 500 m. The white dots represent the locations where vertical ellipse profiles are plotted later on in the paper, the black dot marks the station where a time series is plotted. The left panel shows a 25 grid cell margin added to both the west and north side, with cell sizes increasing with the maximum allowed 20% per cell towards the boundary. The right panel zooms closer into the 1 cell wide river branch region debouching into the sea at the coastal wall 30 km from the Southern boundary. The river depth decreases from 20 m at the mouth to 5 m at the head where a 0 PSU discharge is located.

viscosity (order  $10^{-2} \text{ m}^2\text{s}^{-1}$ ) this background mixing is negligible. In the horizontal plane a constant low mixing of  $1 \text{ m}^2\text{s}^{-1}$  is applied. These values were selected based on a sensitivity analysis performed by Jacobs (2004).

The model is run with a time step of 120 seconds. The wave Courant number is smaller than 4, which is always stable with the Alternate Direction Implicit scheme used in DELFT3D. Velocities in the model do not exceed  $1 \text{ ms}^{-1}$ , giving an advection Courant number smaller than 0.25. This poses no severe constraints on the advection scheme used in DELFT3D. The advection scheme is a combination of a third-order upwind scheme in the horizontal direction and a second-order central scheme in the vertical (the Cyclic-method, Delft Hydraulics, 2006).

For reasons of simplicity the model was forced on the Southern boundary with water levels describing a Kelvin wave with a 12 hour (S2) period. The amplitudes and phases were specified at each grid cell. These values were calculated using an analytical 2D model for a Kelvin wave based on the simplified linear shallow water equations with the assumption of linear bottom friction (Jacobs, 2004). Characteristic values of the S2 spring and neap tide are shown in Table. 4.1. At the Western and Northern boundary the tidal elevation cannot be specified with this analytical model as the results from an analytical tidal model with linear bottom friction do not match the numerical results with quadratic friction at these boundaries. The Western boundary is therefore located more than three Rossby radii away from the coastal wall, so that a zero water level can be imposed there. For the Northern boundary a non-reflective Riemann-type boundary is used. This boundary is also located far away to allow small reflection (only one Riemann invariant is specified) to damp out before they will disturb the plume. Consequently the Northern and Western boundaries are located farther away than would be required to keep the plume, which has maximum cross shore and alongshore extents of 40 and 100 km respectively, inside the model domain.

The time scale of the plume was taken into account by allowing a separate spin-up of the plume for both the spring and the neap conditions. The model was first spun up barotropically for a period of 2.5 days. Then fresh water was released from the river and the model was allowed to spin up baroclinically for another 15 days. It took one day for the river discharge to reach the mouth of the estuary. Then the plume formed along the coast reaching a distance of 100 km downstream. At the end of the 15 days the plume demonstrated almost periodic behaviour. The same plume state returned after 12 hour (albeit not exactly as fresh water is still added to the plume system). After this baroclinic spin-up simulation, the model state was saved and used to initialise the final 24 hour simulation covering 2 tidal periods. During this 24 hour period model output is stored every 20 minutes. This model data was subsequently used for harmonic analysis and interpretation, see Table. 4.2. The spring and neap simulations were performed both with and without a fresh water source, yielding the four simulations which are the subject of this study.



	Neap	Spring
Water level amplitude imposed at South-West corner	0.75 m	1.25 m
Resulting amplitude in plume area	0.6 m	0.89 m
Resulting depth averaged velocity in plume area	0.43 ms <sup>-1</sup>	0.66 ms <sup>-1</sup>

**Table 4.1:** Overview of semi-diurnal tide imposed at boundaries during spring and neap simulations, and resulting characteristic hydrodynamic values in plume area.

Simulation	Duration	Storage and inspection frequency
Barotropic spin-up	2.5 days, 5 tides	Every 2 hour
Baroclinic spin-up plume	15 days, 30 tides	Every 2 hour
Final	1 day, 2 tides	Every 20 minutes

**Table 4.2:** Overview of time frame applied for spin-up simulations and final simulations.

## 4.3 Barotropic tidal currents

### 4.3.1 Comparison of analytic and numerical results

The analytic solution to the linear shallow water equations described in Prandle (1982a,b) is used to validate the numerical model results. It is worth noting that the time varying velocity vector was decomposed into the cyclonic and anti-cyclonic rotating phasors  $R^+$  and  $R^-$  and that the results are presented in terms of the major and minor ellipse axes, the ellipticity of the ellipse, the inclination and the relative phase difference, see Appendix 4.6 for details. Due to the proximity of the coastal wall in the Rhine ROFI, the instantaneous depth averaged cross shore velocities can be assumed to be zero. That is a cross shore velocity in the surface layer is compensated by a velocity in the reverse direction in the bottom layer. Consequently the depth averaged values of  $R^+$  and  $R^-$  should be equal. The total velocity for the Rhine ROFI area can therefore be modelled by  $R = R^+ + R^-$ , with  $\|R^+\| = \|R^-\|$ . Under barotropic conditions the two phasors have almost equal vertical profiles in the 20 m deep Rhine ROFI. Consequently ellipticities are small.

Figs. 4.2 and 4.3 show plots of the vertical profiles of the ellipse properties as obtained from the numerical model. Using the viscosity and velocity values listed in Table. 4.3, numerical results in close agreement with the profiles according to Prandle (1982a,b) were obtained. The eddy viscosity value required in the analytical model is about two thirds of the maximum eddy viscosity produced by the  $k-\epsilon$  scheme in the numerical model. The eddy viscosity formulation used by Prandle gives about two thirds of the average eddy viscosity calculated by the numerical model.

The numerical and analytical results show very good agreement. Only near the bed are any significant differences observed, which are probably due to differences in the eddy viscosity profiles. The numerical model has a parabolic eddy viscosity profile with a small eddy viscosity

near the bed, whereas the analytical model assumes a constant value. The mismatch near the bed agrees with the profiles which Prandle (1982a) obtained using linearly varying eddy viscosity. The same mismatch was found by Maas & Van Haren (1987). Both models show increased vertical structure near the bed. The numerical simulations therefore appear to correctly reproduce the essential features of the barotropic tide. Due to the rotation of the Earth the ellipticity is small and cross shore currents occur, (up to a few percent of the alongshore velocities) during both normal neap and spring conditions. While the numbers are large enough to be reproduced by a numerical model, they are small enough in an absolute sense that the barotropic tide may be considered to have a rectilinear nature.

Furthermore, there is a pronounced vertical structure. Approaching the bed, a decrease in the maximum velocity (major axis) of about 50% is observed (with depth averaged velocities of  $0.43 \text{ ms}^{-1}$  during neap, and  $0.66 \text{ ms}^{-1}$  during spring). The largest velocity gradient occurs in the near-bottom layer. However, the vertical phase veering and inclination veering are small. The velocities near the bed are only  $3^\circ$  ahead of the upper part of the water column and the major axis near the bed only turns a couple of degrees away from the coastal wall. Comparing the neap profiles to the spring profiles, a 50% increase in all ellipse properties is visible.

Figs. 4.2 and 4.3 show that the inclination and phase veering hardly vary with location in the basin. However, the major and minor axis, and the associated ellipticity do change throughout the basin. A substantial decay of  $0.05$  to  $0.10 \text{ ms}^{-1}$  over  $15 \text{ km}$  of the major axis is observed in the cross shore direction. This is due to the exponential decay of the S2 Kelvin wave away from the coastal wall. Note that the decay over the  $15 \text{ km}$  is quite large, despite the large of the Rossby radius ( $138 \text{ km}$ ). The spatial variation of the minor axis, and accordingly the ellipticity, is not straightforward.

	Numerical model DELFT3D:			Analytical model (Prandle, 1982a,b)	
	Depth averaged velocity	Maximum eddy viscosity $E_z$ in vertical	Depth and time averaged eddy viscosity $E_z$	Eddy viscosity required to match DELFT3D ellipse profiles.	Eddy viscosity with relation $E_z = \alpha \cdot U \cdot D$ (Prandle (1982b) with $k = 0.0012$ )
	$[\text{ms}^{-1}]$	$[\text{m}^2\text{s}^{-1}]$	$[\text{m}^2\text{s}^{-1}]$	$[\text{m}^2\text{s}^{-1}]$	$[\text{m}^2\text{s}^{-1}]$
Neap	0.43	0.036	0.0147	0.0275	0.010
Spring	0.66	0.060	0.0240	0.040	0.015

**Table 4.3:** Overview of vertical eddy viscosity values  $E_z$  obtained with numerical DELFT3D model and the eddy viscosity values required as input in the analytical model of Prandle to make the vertical profiles of the ellipse properties match.

## 4.4 Baroclinic tidal currents

### 4.4.1 Plume characteristics

Figs. 4.4 and 4.5 show the depth and time (over a tidal cycle) averaged values of salinity and salinity anomalies on the neap and spring tides respectively. Cross-sections of salinity are also shown at 15 to 60 km from the mouth of the estuary. These figures clearly highlight the stratification on neap tides and the well mixed behaviour of the plume on spring tides. This shows that for the selected numerical conditions and given discharge conditions, the increase in tidal amplitude on the spring tide is enough to mix the plume fully over the vertical. Furthermore, the main plume features are roughly in accordance with results in transects obtained in field surveys, see Van Alphen *et al.* (1988), Van der Giessen *et al.* (1990) and Joordens *et al.* (2001). These features concern a maximum surface trapped plume depth of 5 to 10 m located 5 to 10 km offshore during neap and a maximum offshore width of less saline water of 30 km during mixed spring conditions.

The residual current profiles at a number of stations are shown in Fig. 4.6 and Fig. 4.7 compared to the analytical model of Heaps (1972). While the alongshore currents in the model are roughly in accordance with Heaps (1972), the cross shore currents show substantial differences. The only neap stations to show a resemblance with Heaps' model are 18w, 38 to 45n, while on a spring tide the best matches are found at 18w, 15 to 30n. Coincidentally, these stations are all located in the vicinity of the station where Simpson (1997) showed an agreement between Heaps' model and residual currents. Their data were obtained from two weeks of ADCP data (mooring A or B in Simpson & Souza (1995), 30 km north, 10 km or 23 km west respectively).

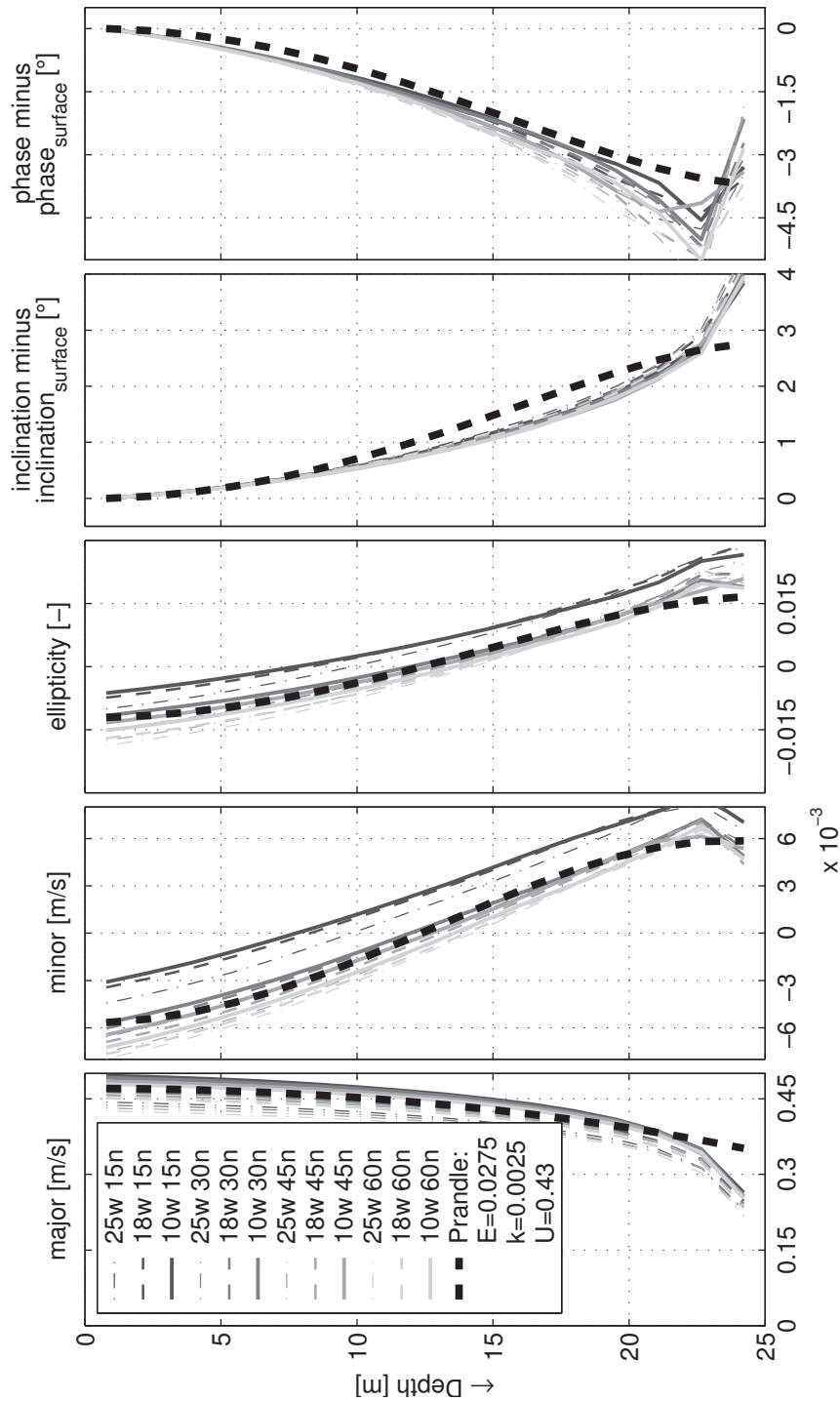


**Figure 4.2:** Vertical profiles of ellipse properties during neap tide (with representative depth averaged velocity  $U$  of  $0.45 \text{ ms}^{-1}$  in plume area). The grey tones refer to alongshore positions in the numerical model: 15n, 30n, 45n and 60n refer to kilometres north of the river mouth. The line types refer to cross shore positions in the numerical model: 10w, 17.5w and 25w refer to kilometres west (offshore) of the coastal wall (see the white dots Fig. 4.1 for locations). The thick dashed line is a best fit solution with the model of Prandle (1982a,b) obtained with a vertical eddy viscosity  $E_z = 0.028 \text{ m}^2\text{s}^{-1}$  (Table 3) (with  $k = 0.0025$ ).

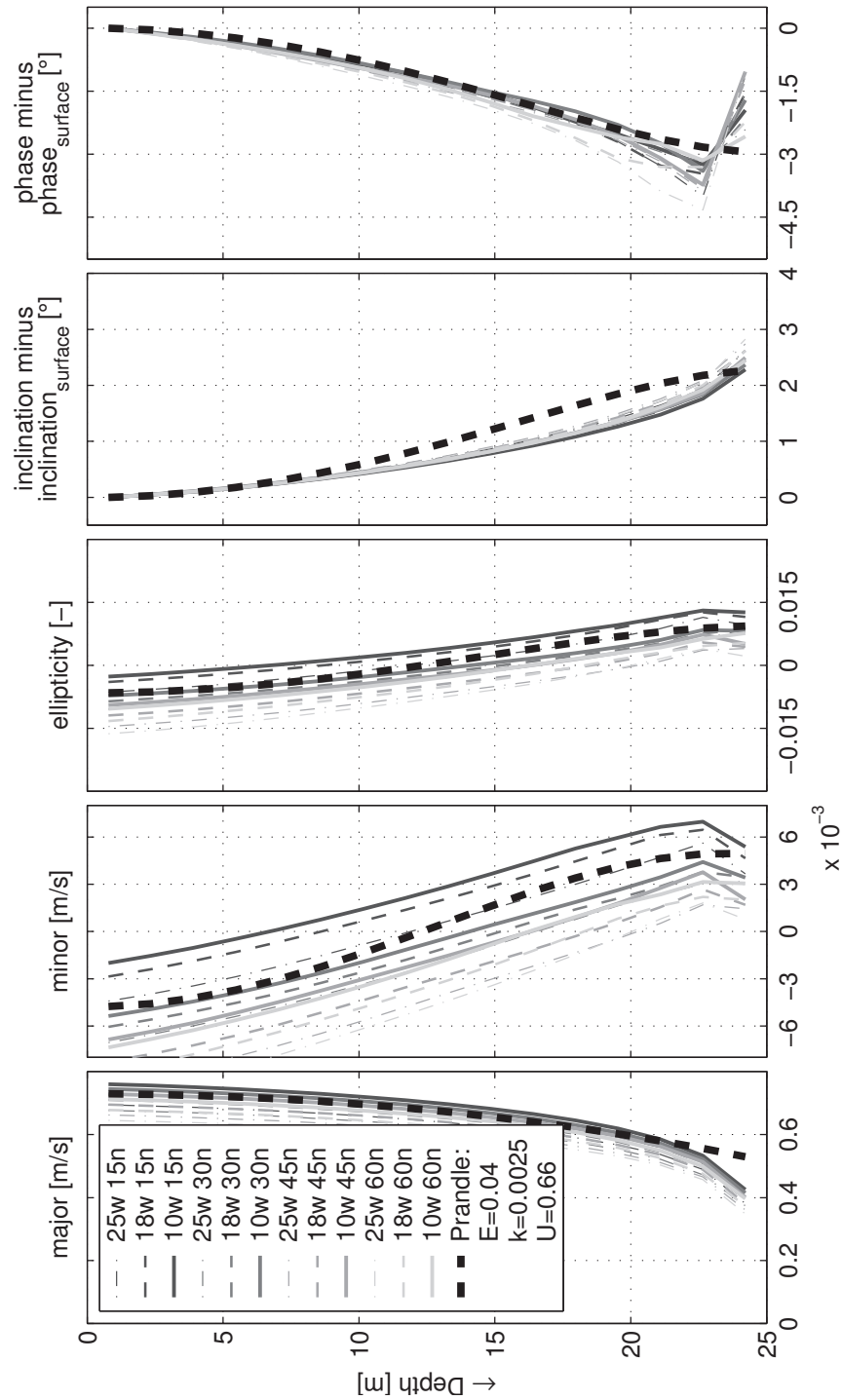


**Figure 4.3:** Vertical profiles of ellipse properties during spring tide (with representative depth averaged velocity  $U$  of  $0.6 \text{ ms}^{-1}$  in plume area). The same colour coding as in Fig. 4.2 is used. The thick dashed line is a best fit solution with the model of Prandle (1982a,b) obtained with a vertical eddy viscosity  $E_z = 0.04 \text{ m}^2\text{s}^{-1}$  (Table 3) (with  $k = 0.0025$ ).

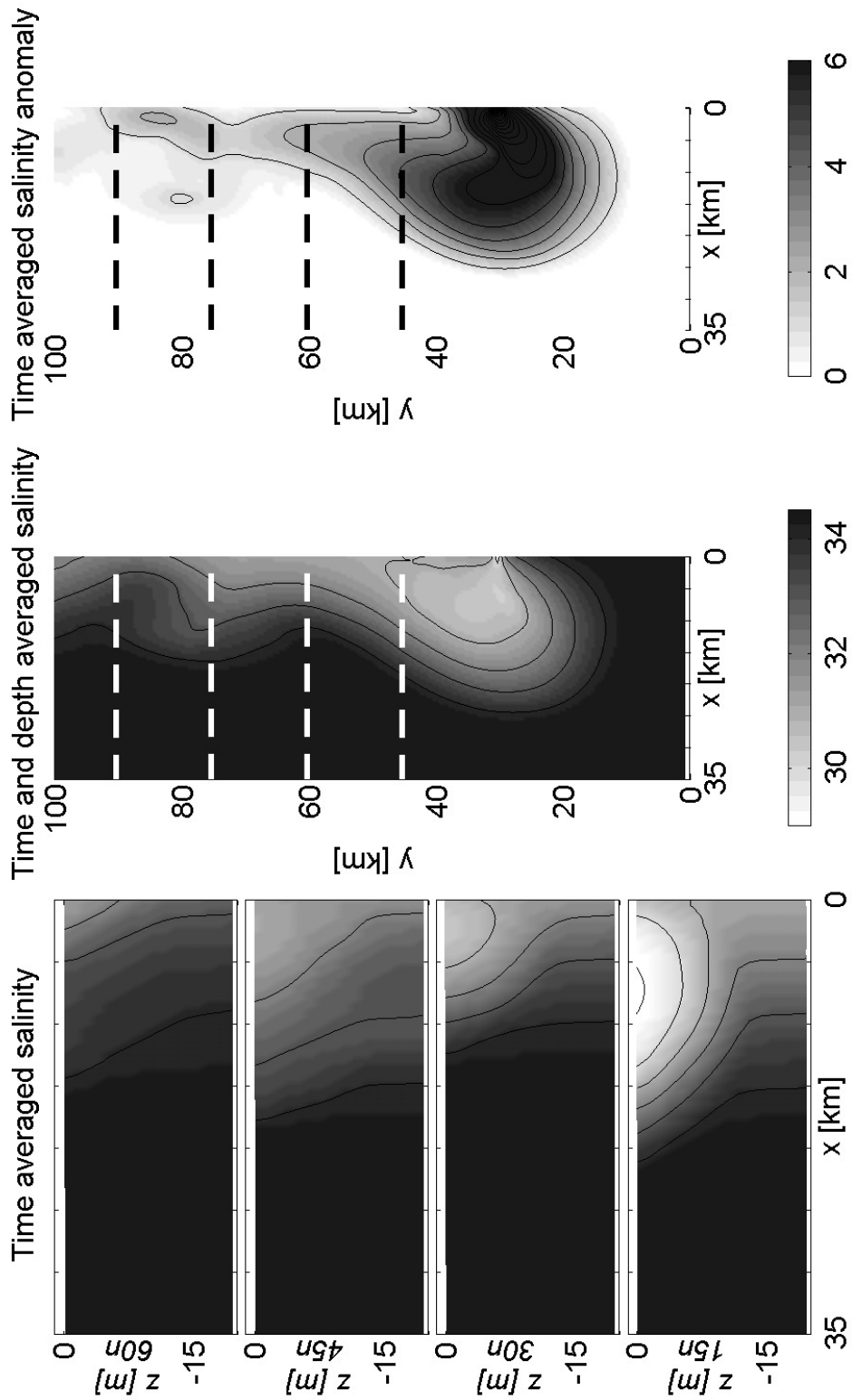


**Figure 4.4:** Time averaged values of salinity during neap simulations: the left panels show cross-sections located at 4 locations north of the river mouth (15, 30, 45 and 60 km) as shown by the dashed lines in the right panels. The middle panel show a plan view of the depth-averaged salinity, the right panel show the density anomaly. The five leftmost panels share the same grey tone colour coding.

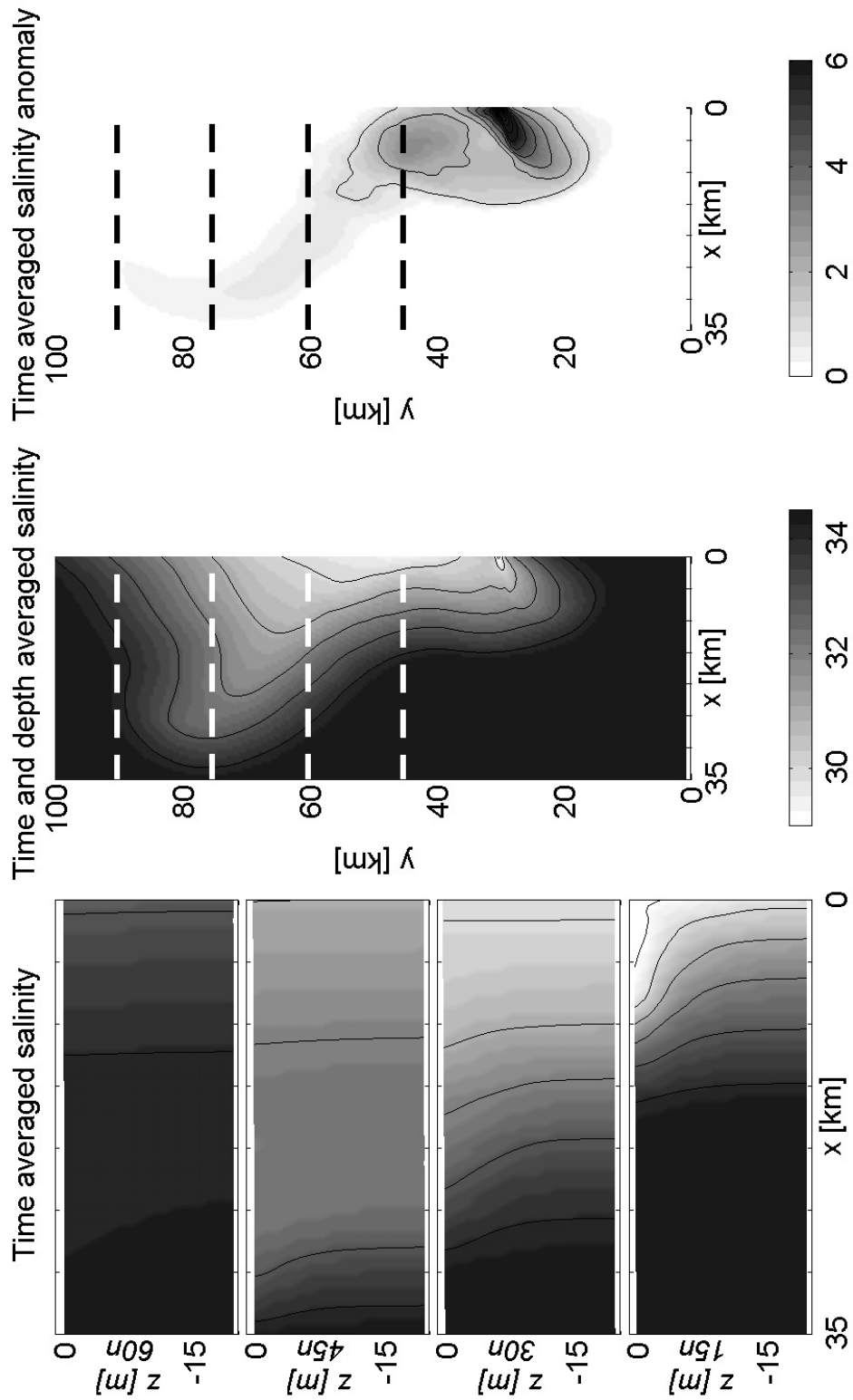


**Figure 4.5:** Time averaged values of salinity during spring simulations: the left panels show cross-sections located at 4 locations north of the river mouth (15, 30, 45 and 60 km) as shown by the dashed lines in the right panels. The middle panel show a plan view of the depth-averaged salinity, the right panel show the density anomaly. The five leftmost panels share the same grey tone colour coding.

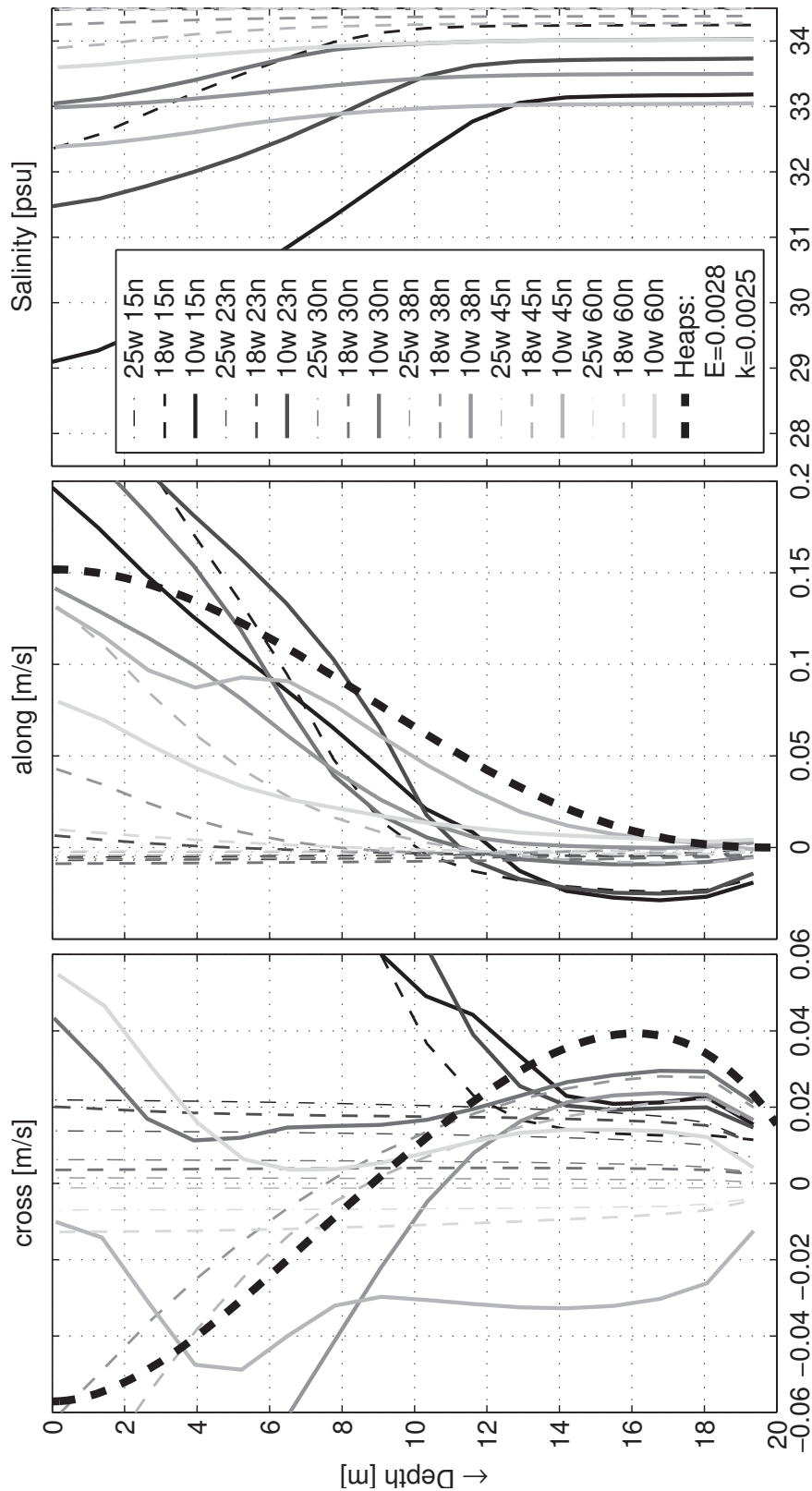


**Figure 4.6:** Vertical profiles of residual velocities and mean salinities during neap tide. The line types refer to cross shore positions as in Fig. 4.4, the grey tones refer to alongshore positions in the numerical model: 15n, 23n, 30n, 38n, 45n and 60n refer to kilometres north of the river mouth. The thick dashed line is the model of Heaps (1972) with a density gradient  $(\partial\rho/\partial x)/\rho$  of  $2 \times 10^{-7} \text{ m}^{-1}$  and a vertical eddy viscosity  $E_z = 0.0028 \text{ m}^2\text{s}^{-1}$  (Table 3) (with  $k = 0.0025$ ).



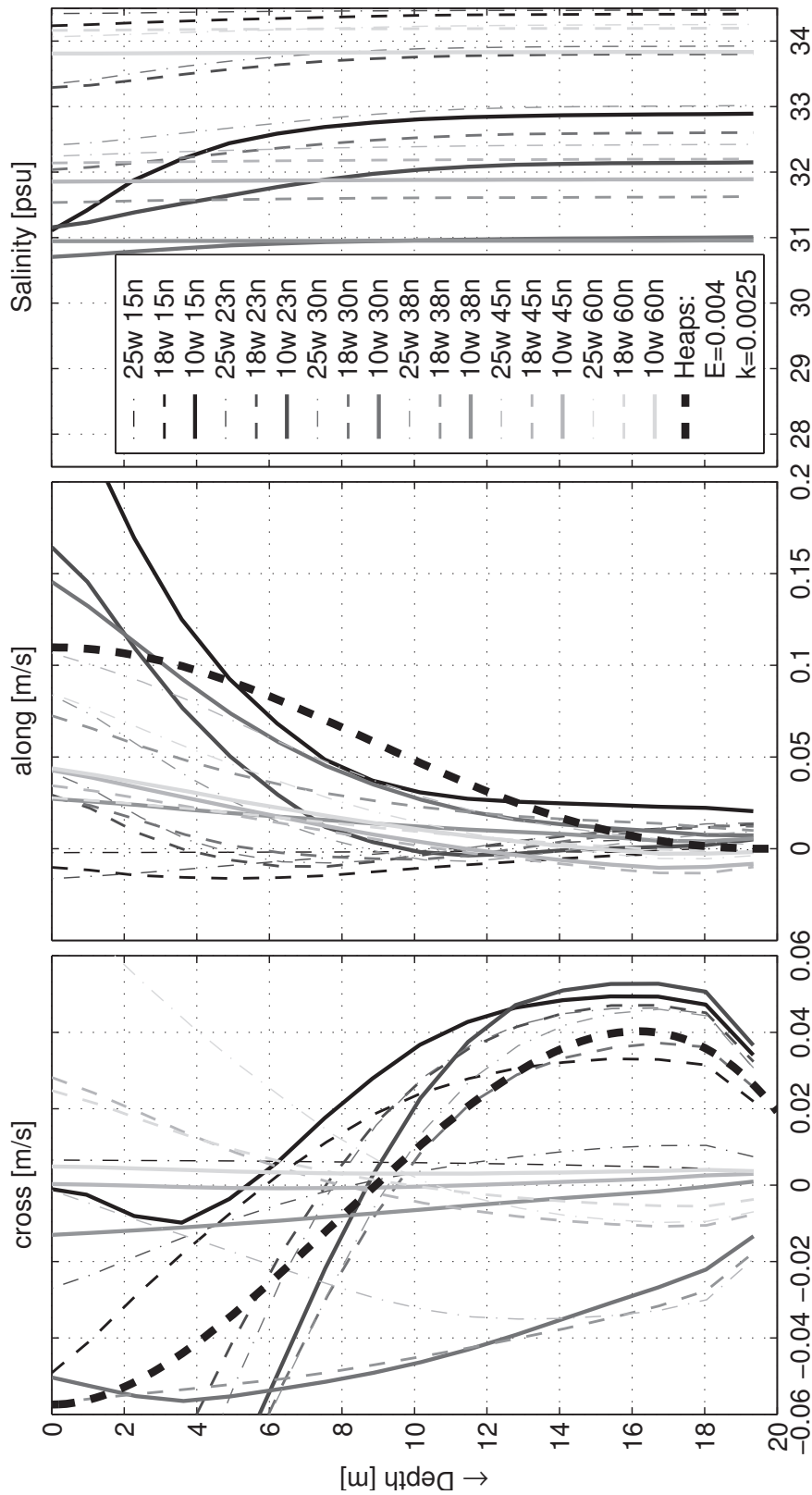


**Figure 4.7:** Vertical profiles of residual velocities and mean salinities during spring tide. The same colour coding as in Fig. 4.6 is used. The thick dashed line is the model of Heaps (1972) with a density gradient  $(\partial\rho/\partial x)/\rho$  of  $2 \times 10^{-7} \text{ m}^{-1}$  and a vertical eddy viscosity  $E_z = 0.0040 \text{ m}^2\text{s}^{-1}$  (Table 3) (with  $k = 0.0025$ ).

We can conclude though that the alongshore velocities are a factor three bigger than the cross shore velocities. The alongshore geostrophic balance is therefore considered to dominate over the effects of friction in the Rhine ROFI.

#### 4.4.2 Vertical profiles of ellipse properties

Figs. 4.8 and 4.9 show a marked effect of stratification on the vertical profiles of the ellipse properties for the neap tide and the spring tide. Prandle (1982a,b) solution with a tenfold reduced eddy viscosity is also shown. In the case of neap tides, the water column is stratified and the surface ellipses become strongly anti-cyclonic, while those in lower part of the water column remain cyclonic. During the well mixed spring tide the general pattern of the tidal ellipses is one of cyclonic rotation near the bed decreasing with height above the bed. Surface ellipses have a small anti-cyclonic rotation. The few stations that do show ellipses at spring tides are all located close to the coast in that part of the plume that is still stratified (Fig. 4.13). In all other stations the surface currents are predominantly rectilinear and directed parallel to the coast at spring tides. During neap tide large anti-cyclonic ellipticity is seen near the coast, where the stratification is strongest. Surface currents become increasingly anti-cyclonic (large and negative) as the coast is approached. It is clear from Figs. 4.2 and 4.8 that during neap tide and in comparison with the situation without a plume, maximum velocities (major axis) increase in the surface layer, from  $0.5 \text{ ms}^{-1}$  to  $0.6 \text{ ms}^{-1}$ . At the same time velocities in the bottom layer decrease from almost  $0.4$  to  $0.3 \text{ ms}^{-1}$ . Furthermore, ellipticity increases considerably. Cross shore currents of up to 30% of the major axis now occur in both surface and bottom layers, amounting to  $0.1 \text{ ms}^{-1}$  just below mid-depth and to  $0.20 \text{ ms}^{-1}$  in the surface layer. In addition the inclination veering of up to  $25^\circ$  is considerable. The phase veering also shows that the near bed layer is 1.5 hour ahead of the upper part of the water column. Only the station closest to the river mouth (10w, 15n) behaves differently, probably due to near field effects.

#### 4.4.3 Tidal straining

Figs. 4.10 and 4.11 show time series of vertical profiles of alongshore and cross shore velocity and salinity. The Richardson number, a measure for mixing, is also included in this latter plot. These time series are from a station located 9.5 km offshore and 29.5 km north of the river mouth, the same position as mooring A employed in the PROFILE project (Simpson & Souza (1995), Huthnance (1997)). A clear difference between the spring and neap tide is once more apparent. The two-layer behaviour of the plume on a neap tide is clear with counteracting surface and bottom currents. The alongshore currents attain their maximum value below the surface, which is in accordance with the major axis profiles in Fig. 4.8. Note also that the alongshore near bed currents are almost two hours ahead of the surface currents, and are in agreement with the  $40^\circ$  phase veering shown in Fig. 4.8. The surface currents lag somewhat behind the water levels.

The salinity during neap also exhibits a semi-diurnal signal. The semi-diurnal stratification of more than 1 PSU is in agreement with the data reported by Simpson *et al.* (1993). On the spring tide the reversing alongshore tidal currents without phase veering, weak cross shore currents and well mixed behaviour are obvious. Now the alongshore velocities are a little ahead of the water levels. Additionally a quarter diurnal variation of eddy viscosity is apparent in both scenarios. This scenario is common with semi-diurnal tides, albeit limited to the area below the pycnocline during neap conditions.

A semi-diurnal variation in the pattern of stratification is clearly visible in the neap simulations. It is not visible in the well mixed spring simulations. This variation in stratification is almost in phase with the water level. On a neap tide minimum stratification and stability (as indicated by the Richardson number) are observed in the Rhine ROFI directly after low water, whereas maximum stratification and stability occur directly after high water. This semi-diurnal stratification signal in the Rhine Plume is caused by the aforementioned cross-shore component of the shear acting on the density gradient normal to coast. The tidal ellipse properties observed in Fig. 4.8 provide the cross shore shear mechanism. From just after low water (minimum vertical stability) to directly after high water, cross shore surface currents are directed offshore, while the bottom currents are directed onshore. In this situation less saline coastal waters are transported over the underlying more saline bottom waters, while at the same time more saline offshore water is transported towards the coast by the onshore bottom currents. As a consequence, directly after high water, when the shearing is zero and reverses, maximum stratification is observed. Next, from directly after high water to directly after low water the shearing effect is opposite and acts to re-establish the mixed situation initially present at low water. The onshore surface currents advect the fresh surface layer back to the coast, while at the same time less saline coastal waters are transported offshore in the bottom layer. Consequently, when the shearing reverses and is zero again directly after low water, minimum stratification occurs. This tidal straining concept, which was introduced by Simpson & Souza (1995) and Simpson (1997) is remarkably well reproduced by our numerical model.

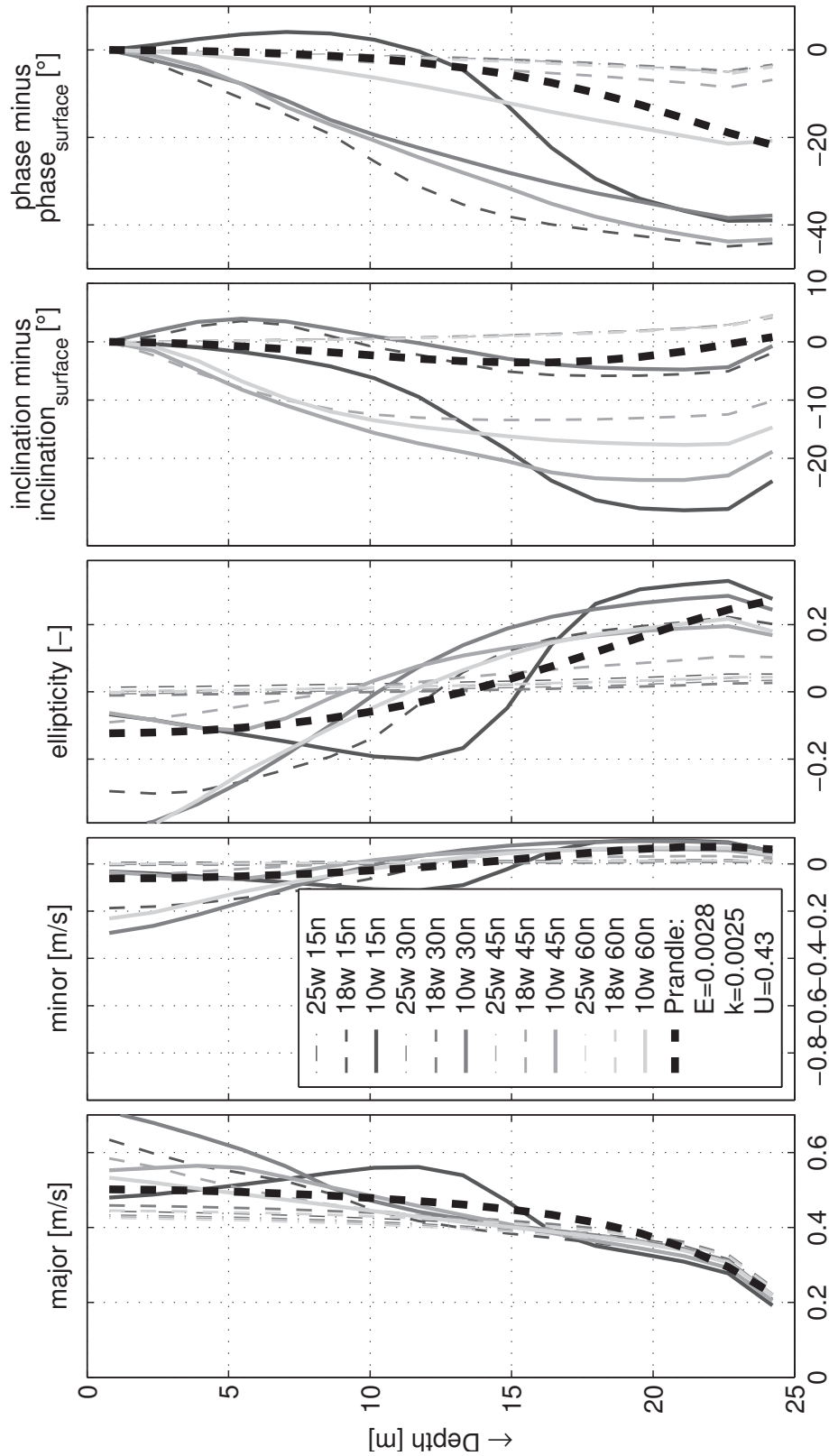


**Figure 4.8:** Vertical profiles of ellipse properties during neap tide including a background plume (with representative depth averaged velocity  $U = 0.45 \text{ ms}^{-1}$  in plume area). The same colour coding as in Fig. 4.4 is used. The thick dashed line is the solution with the model of Prandle (1982a,b) obtained with an arbitrary strongly decreased vertical eddy viscosity  $E_z = 0.0028 \text{ m}^2\text{s}^{-1}$ , a tenfold reduction with respect to Fig. 4.2.

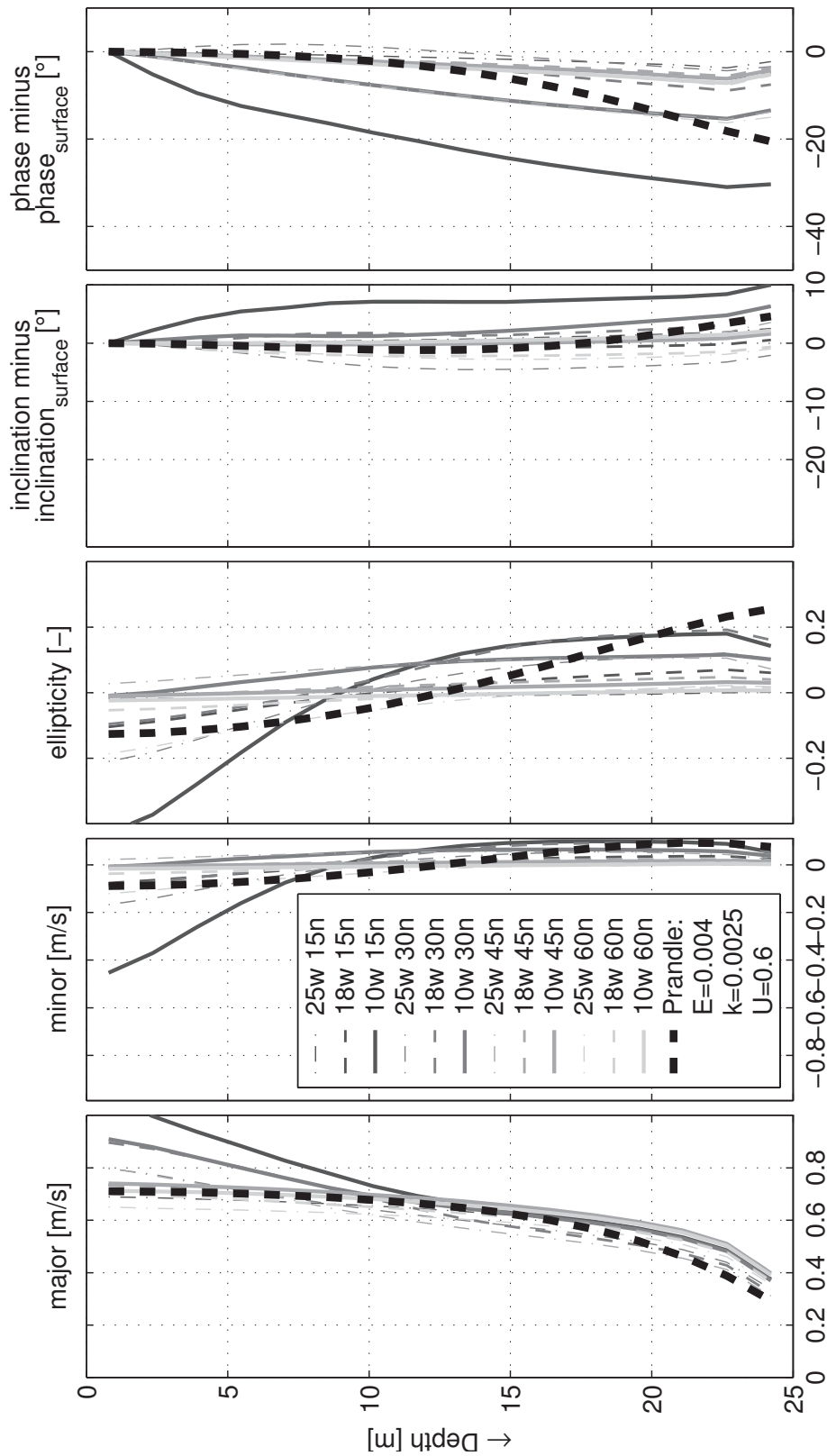


**Figure 4.9:** Vertical profiles of ellipse properties during spring tide including a background plume (representative depth averaged velocity  $U = 0.6 \text{ ms}^{-1}$  in plume area). The same colour coding as in Fig. 4.4 is used. The thick dashed line is the solution with the model of Prandle (1982a,b) obtained with an arbitrary strongly decreased vertical eddy viscosity  $E_z = 0.004 \text{ m}^2\text{s}^{-1}$ , a tenfold reduction with respect to Fig. 4.3.

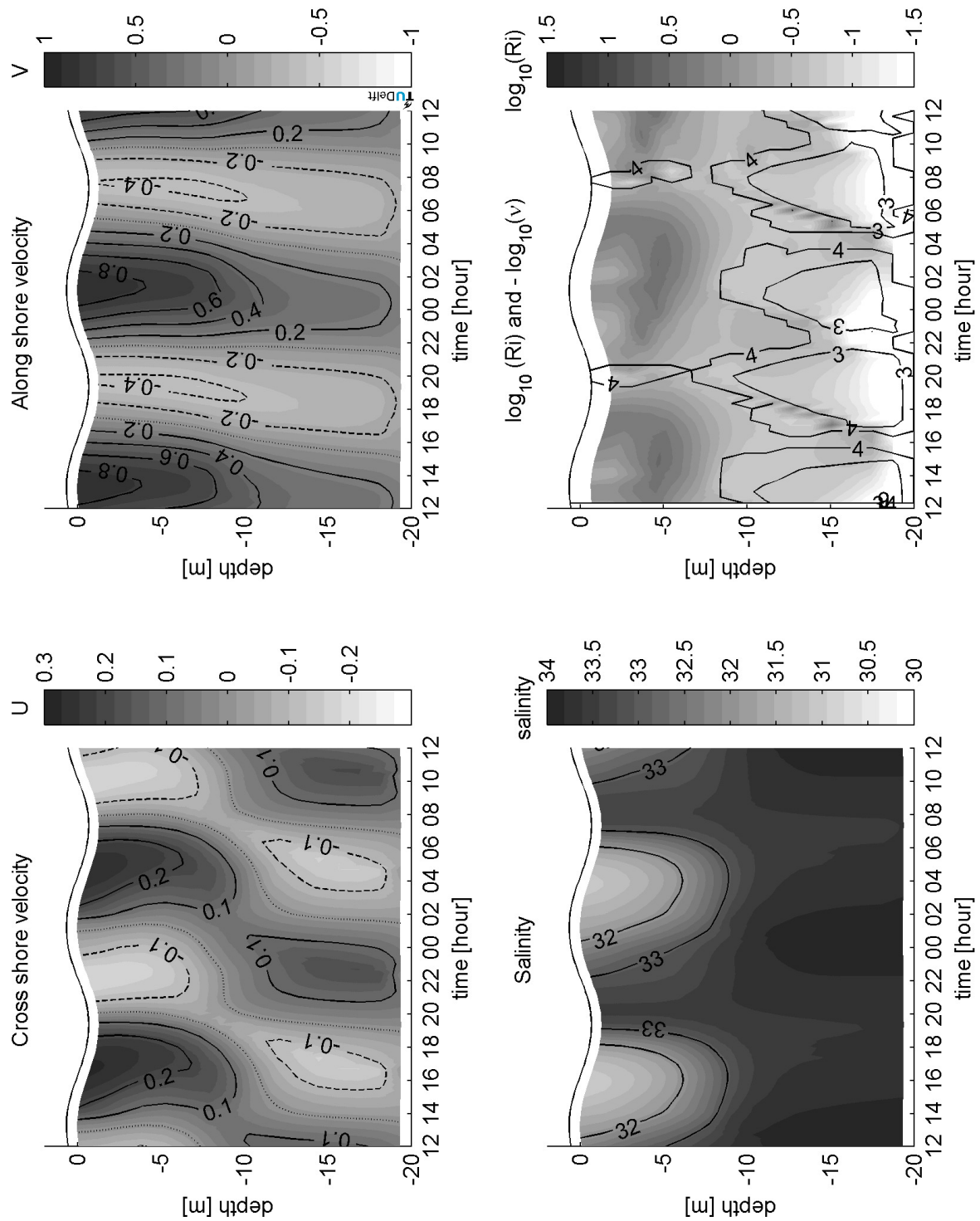


**Figure 4.10:** Time series of vertical profiles of velocity, salinity and eddy viscosity from neap tide simulation at station located 9.5 km offshore and 29.5 km North of the river mouth (10w, 30n in Figs. 4.2 - 4.9, see black dot in Fig. 4.1 for location).

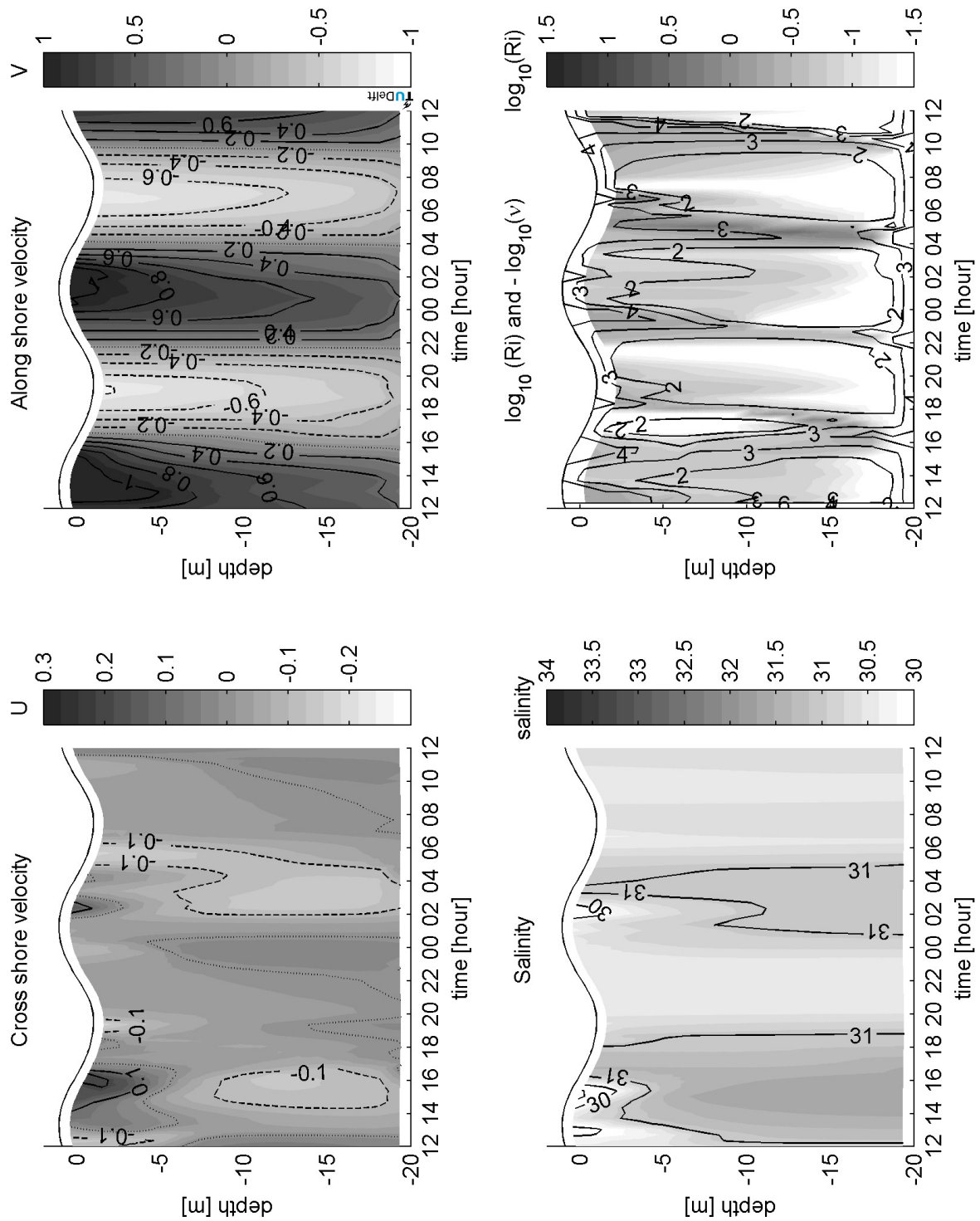


**Figure 4.11:** Time series of vertical profiles of velocity, salinity and eddy viscosity from spring tide simulation at station located 9.5 km offshore and 29.5 km North of the river mouth (10w, 30n in Figs. 4.2 - 4.9, see black dot in Fig. 4.1 for location).



In summary, the out of phase component of the cross shore velocity is the origin of the strong vertical shear. Maximum stratification occurs when the straining reverses, so surface offshore displacement relative to lower layers is maximal. The resulting straining displacement is almost in phase with the alongshore velocity and the surface elevation. The largest straining mechanism itself occurs at the time of mean water. This shear acts on the horizontal density gradient to induce vertical structure by the mechanism of tidal straining. Consequently a clear semi-diurnal change in the vertical salinity profile is observed that in phase with the water level.

#### 4.4.4 Correlation ellipse and Richardson number

The spatial distribution of the surface (layer 1) and near bottom layer (layer 10) tidal ellipses are shown in Figs. 4.12 and Fig. 4.13, for both neap and spring conditions respectively. In addition the spatial distribution of the time averaged Richardson number for layers 1 and 10 are shown. Per vertical the maximum Richardson number is chosen. The ellipse shapes, ellipticity values and locations results agree with the findings of the HF radar for the Dutch Coastal Zone reported in Visser *et al.* (1994). Both the model results and the data of Visser *et al.* (1994) show that during neap tide the ellipses obtain a strong minor axis component, whereas the ellipses are only slightly deformed during spring tide. Both also show that the surface currents are rotating anti-cyclonically (clockwise), whereas the bottom currents are rotating cyclonically (anti-clockwise).

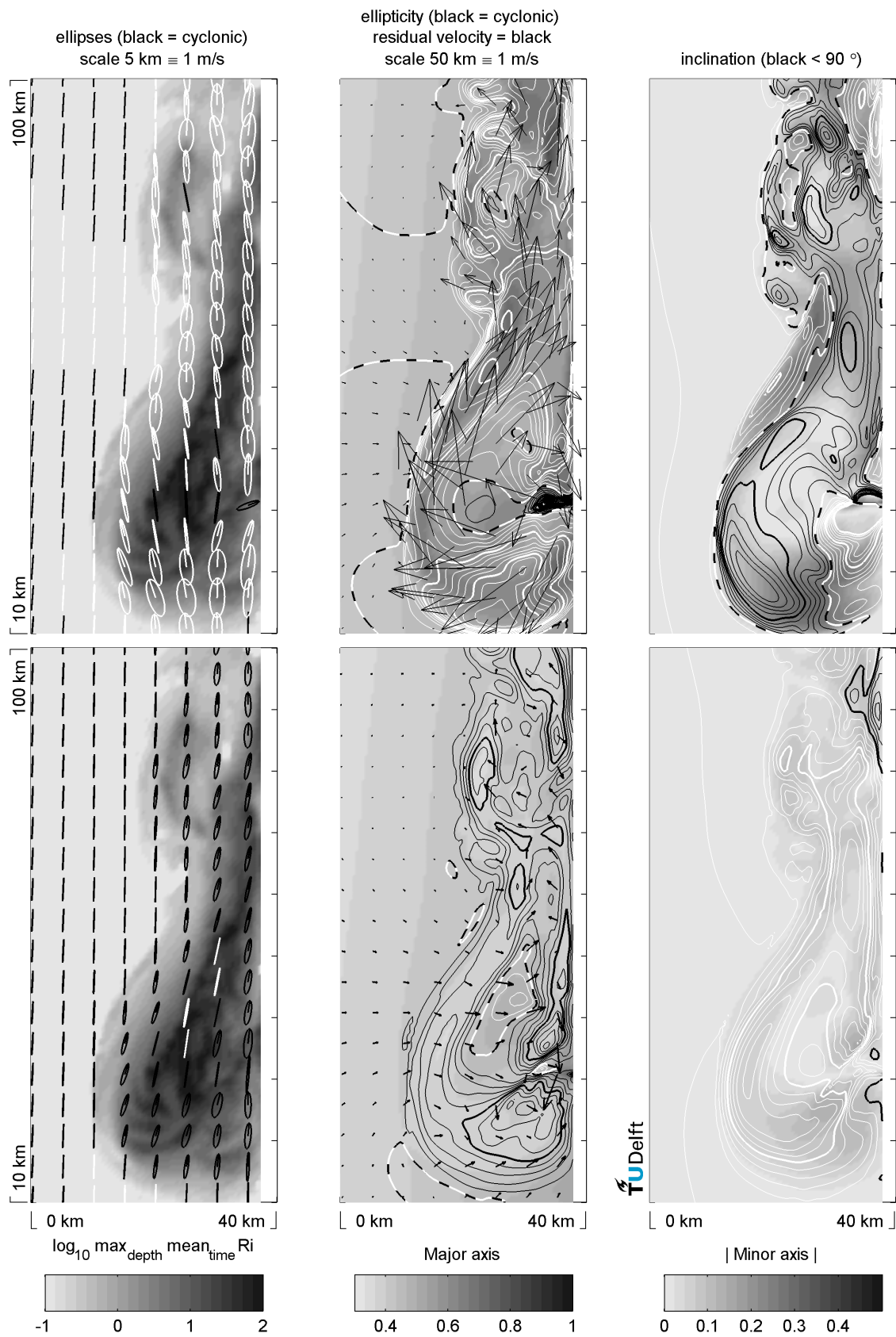
The models shows that pronounced ellipses occur only in the region of the plume. During spring tide the areas where pronounced ellipses occur has drastically diminished, although some areas with ellipses remain close to the mouth. The position of the surface ellipses coincides perfectly with the mean salinity associated with the plume just as in the neap run. Apparently spring velocities are sufficient to mix up the plume, thereby limiting the northward extension and preventing stratification, and, consequently resulting in degenerate ellipses. When we compare this to the data of Visser *et al.* we see that during spring tide ellipses should indeed be degenerate, except for small ellipticities close to the coast. The data of Visser *et al.* (1994) however cover only the area more than 10 km north of the plume, so we can make no conclusive statement about ellipses close to the river mouth. The fact that in the model in the area more than 20 km north of the river discharge point no ellipses occur is therefore in agreement with Visser *et al.* (1994).

Residual velocities are also shown in Figs. 4.12 and 4.13. Outside the plume surface residual velocities are zero, whereas residual surface velocities of order  $20 \text{ cms}^{-1}$  are observed within the plume (see also Figs. 4.6 and 4.7). This velocity pattern is in accordance with previous studies, for example, Fong & Geyer (2001), Fong & Geyer (2002); Garcia Berdéal *et al.* (2002); Kourafalou *et al.* (1996a). In the bottom layer frictional effects cause residual onshore velocities of  $5 \text{ cms}^{-1}$ . The same pattern exists during both neap and spring conditions, although residual surface velocities during spring are smaller and have a smaller alongshore extent.



---

**Figure 4.12 (on the next page):** Spatial distribution of ellipse, velocity and stability properties from neap tide simulation. The upper left panel show the ellipses in the surface layer (layer 1) on top of the Richardson number in grey tones (taken as average in time and maximum in the vertical). The lower left panel shows the ellipses in near-bottom layer 10 on top of the same Richardson number (layer 10 of 16 is the layer having the most pronounced near-bottom ellipse values below mid-depth). The middle panels show the residual velocities on top of the major axis in grey tones (with layer 1 in upper panel and layer 10 in lower panel). The ellipticity is shown in black (cyclonic) and white (anti-cyclonic) contours with thick contours at the  $-0.2$  and  $+0.2 \text{ ms}^{-1}$  intervals. The right panels show inclination contours on top of the absolute value of the minor axis in grey tones (with layer 1 in upper panel and layer 10 in lower panel). Thick contours are drawn at  $70, 80, 90, 100$  and  $110^\circ$  with angles smaller than  $90^\circ$  in black (directed offshore) and angles larger than  $90^\circ$  in white (directed onshore).



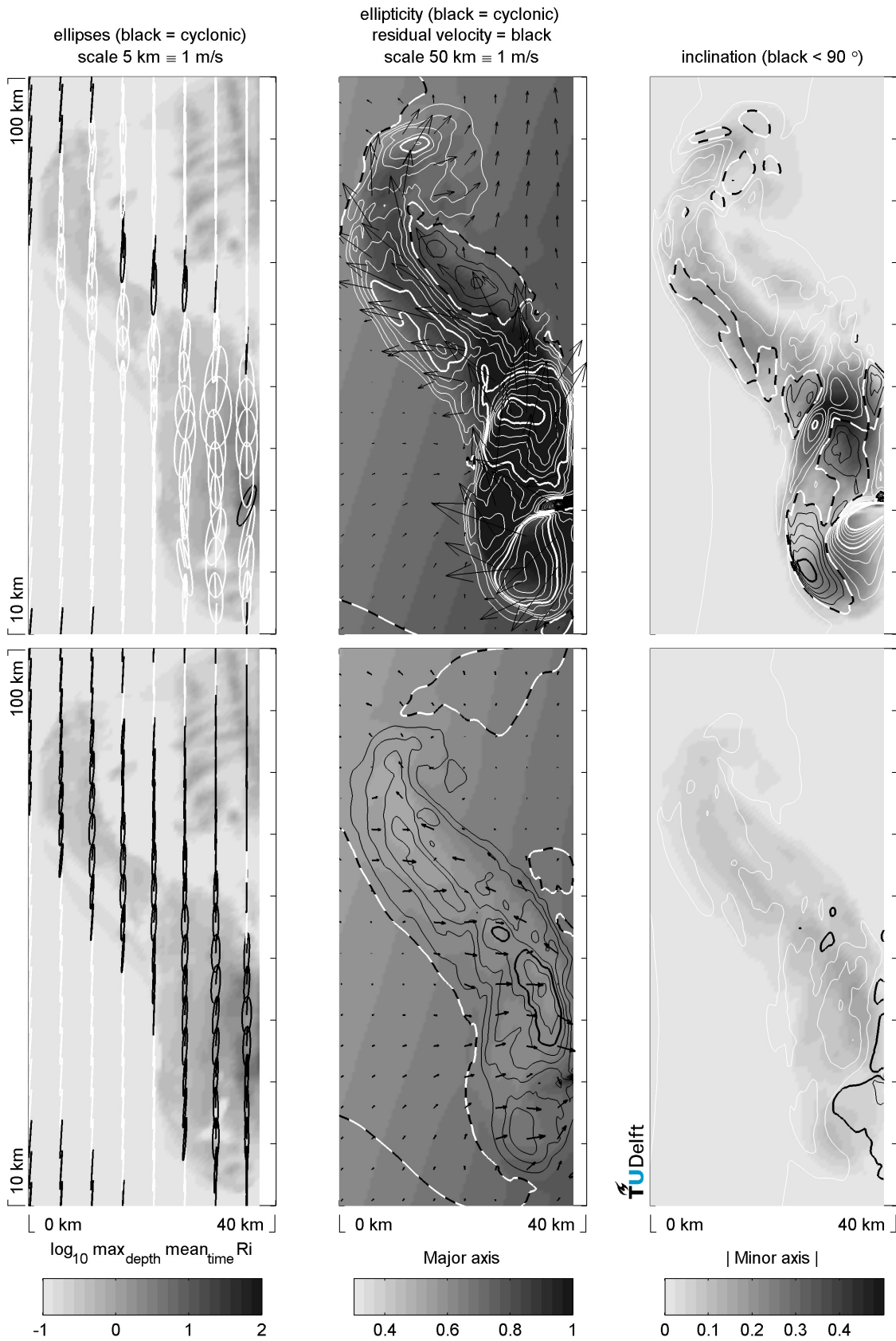


**Figure 4.13:** Spatial distribution of ellipse, velocity and stability properties from spring tide simulation. Same colour coding as in Fig. 4.12.

Fig. 4.14 shows the same relation between Richardson number and ellipticity as Fig. 5 of Souza & James (1996). This relation can be characterized as follows. Low ellipticities only occur at low Richardson numbers. When Richardson numbers increase at neap tide, ellipticities increase rapidly and then reach a maximum value. In the data this maximum ellipticity veering is about 0.6, whereas in the model ellipticity veering also saturates at about 0.6 (-0.35 in the surface layer and +0.25 in the bottom layer). Due to this saturation, the neap plume can be concluded to have reverted to a two layer system at Richardson numbers of 10. As Fig. 4.14 shows that there are no distinct regions showing just one type of dot, all areas in the plume area behave similarly. The whole plume area can therefore be considered to be stratified.

Fig. 4.15 shows that during spring tide stability is smaller (max Richardson number of  $10^3$  instead of  $10^4$  during neap). Unlike the neap conditions, no distinct saturation of ellipticity is observed at values of the Richardson number larger than 10. Apparently the spring plume does not consist of a large stratified patch. It is only in the region between 10 and 20 km north of the mouth that considerable ellipticities occur. The surface ellipticities exhibit ellipticity values of about 40%. On the other hand, in the bottom layer the ellipticity is up to 30%.

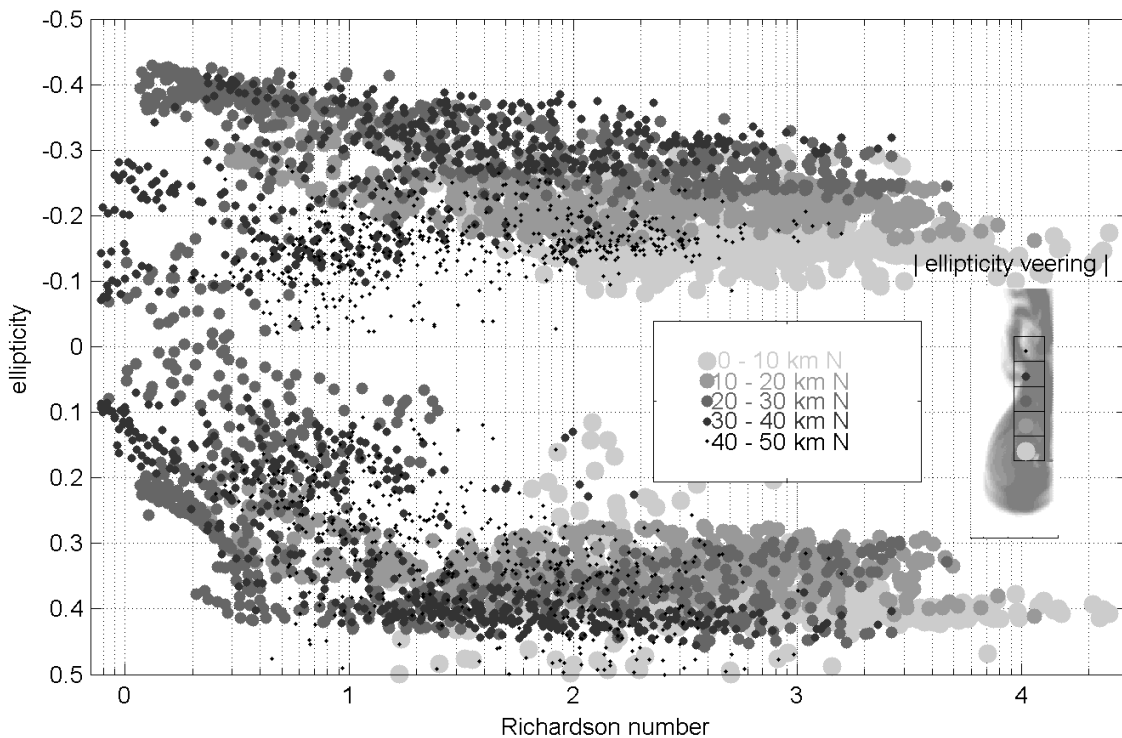


**Figure 4.14:** Relation between  $^{10}\log$  of Richardson number (mean in time, maximum in vertical) and minimum and maximum ellipticity per vertical during neap.

#### 4.4.5 Heaps' Model Revisited

Substantial differences to Heaps' model were noted above. Heaps (1972) attributed deviations from his theory in Liverpool Bay to residual movements of tidal origin, wave action and meteorological forcings. However, it should be noted that the density gradients are not parallel to the coast. Fig. 4.5 shows that at spring tide the isohalines are at an angle of up to  $30^\circ$  with the coast, yielding a significant contribution of the along isohaline flow to the cross shore residuals. Additionally tidal straining and tidal stirring might have a significant effect on the cross shore current distribution. To assess the relative effect of straining versus stirring, the data in Fig. 4.14 and Fig. 4.15 prove useful. It shows a scatter plot of the Richardson number (an indirect measure of tidal stirring) versus ellipticity (a direct measure of the tidal straining). At neaps large differences in stability occur at an almost constant strength of the tidal straining (ellipticity veering of 60%). At springs however, there is hardly any correlation between stability and ellipticity. Maximum stability is smaller, but all combinations of stability and ellipticity occur. The fact that at neaps all stations are subject to a similar degree of tidal straining, but that the cross shore residuals do show substantial differences, leads us to conclude that it appears unlikely that tidal straining is the mechanism causing the differences in the residual currents. Consequently, it is hypothesized that the tidal stirring is the mechanism leading to the differences. Interestingly the largest differences between Heaps' model and our results are

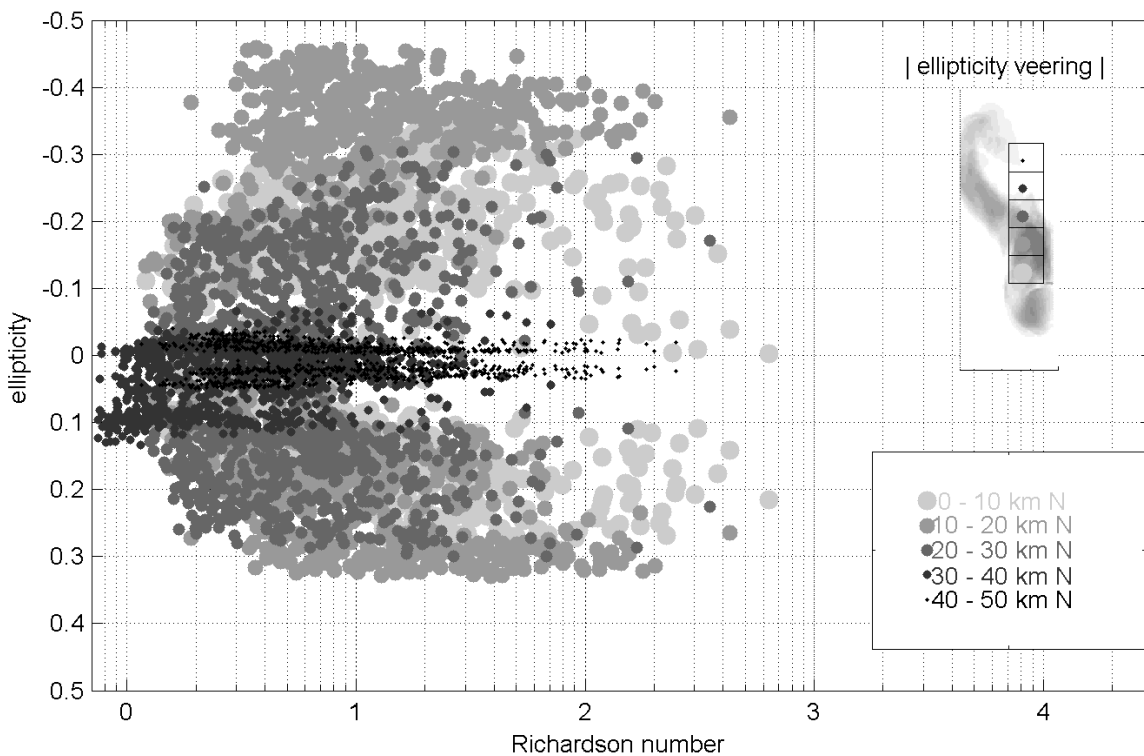


**Figure 4.15:** Relation between  $^{10}\log$  of Richardson number (mean in time, maximum in vertical) and minimum and maximum ellipticity per vertical ellipticity during spring.

indeed found at stations that exhibit significant mean stratification, and are thus prone to experiencing the largest damping of tidal stirring. This occurs in Fig. 4.6 at all but one station 10 km offshore and at 18w, 15n and in Fig. 4.7 at the station with the largest stratification, 10w, 15n. All these stations, and only these, show an extra point of inflection at the bottom of the stratified part of the water column. Above this level the residual current is again directed coastward. This double curvature bears resemblance to the three-layer behaviour in the residual currents present in the measurements of De Ruijter *et al.* (1992), 40 km north, 3 to 20 km west. Questions still remain as to the cause of the other differences with Heaps' model, especially the reversed profiles at spring tide, Fig. 4.7.

#### 4.4.6 Spring Neap Tidal Cycle

In order to assess whether the Rhine ROFI can switch between the spring and neap states described above, results from a full spring-neap simulation are presented in Fig. 4.16. Multiple full spring-neap cycles are included to assess with confidence the ability of the plume to revert to stratified conditions after a well-mixed spring state. To reduce simulation time a 9.5 day tidal modulation is assumed. A moving harmonic tidal analysis is applied to obtain ellipticity as a function of time. The 30 days time series in Fig. 4.16 shows that stratification and the associated increased ellipticity veering occur during neap tide only. The two distinct plume states can be defined as typical neap and spring tide states. The behaviour of the plume corresponds well with observational work from 1990 of Simpson *et al.* (1993). They found that spring tidal stirring, reinforced by strong winds, brought about almost complete vertical homogeneity. After the following neaps, and a period of light winds, the water column was observed to have re-stratified. Souza & Simpson (1996) also show a correlation in time between ellipticity and stratification during observations in 1992. Due to the presence of irregular wind mixing events over the spring neap cycle they could not uniquely label the states as spring and neap. They actually found four periods of complete vertical homogeneity during a 10 day period (their Fig. 4). In addition to wind mixing, discharge variations might also cause an alteration from the typical spring and neap states. An excess discharge might lead to spring tide stratification, whereas a low discharge might cause the neaps to be well mixed. Additional observational corroboration of our model results is found in the Liverpool Bay ROFI. The time versus height plots of salinity shown by Simpson (1997) look identical to our Fig. 4.16, albeit with slightly longer homogeneity at springs.

### 4.5 Discussion

Rivers, discharging their typically fresher water into saltier coastal waters are an important source of momentum and buoyancy for coastal seas. Understanding the dynamics of ROFIs and the factors influencing their spreading is an important objective of coastal ocean research.



It is also of direct relevance to studies of sediment and pollutant transport. A key step in this direction was undertaken in the 90s with extensive field campaigns in the Rhine ROFI, see Huthnance (1997) for a summary. The results from these campaigns demonstrated the importance of stratification in altering the vertical structure of tidal currents. The numerical simulations presented here reproduced many of their key findings. However, it is clear that there is a complex interaction between the mixing, ellipticity veering and stratification.

The numerical model results for the spring tide showed that the Rhine outflow area was predominantly well mixed with rectilinear tidal currents along the Dutch coast. In contrast, during the neap tide a marked effect of stratification was observed in combination with significant cross shore currents. The surface currents rotated anti-cyclonically whereas bottom currents rotated

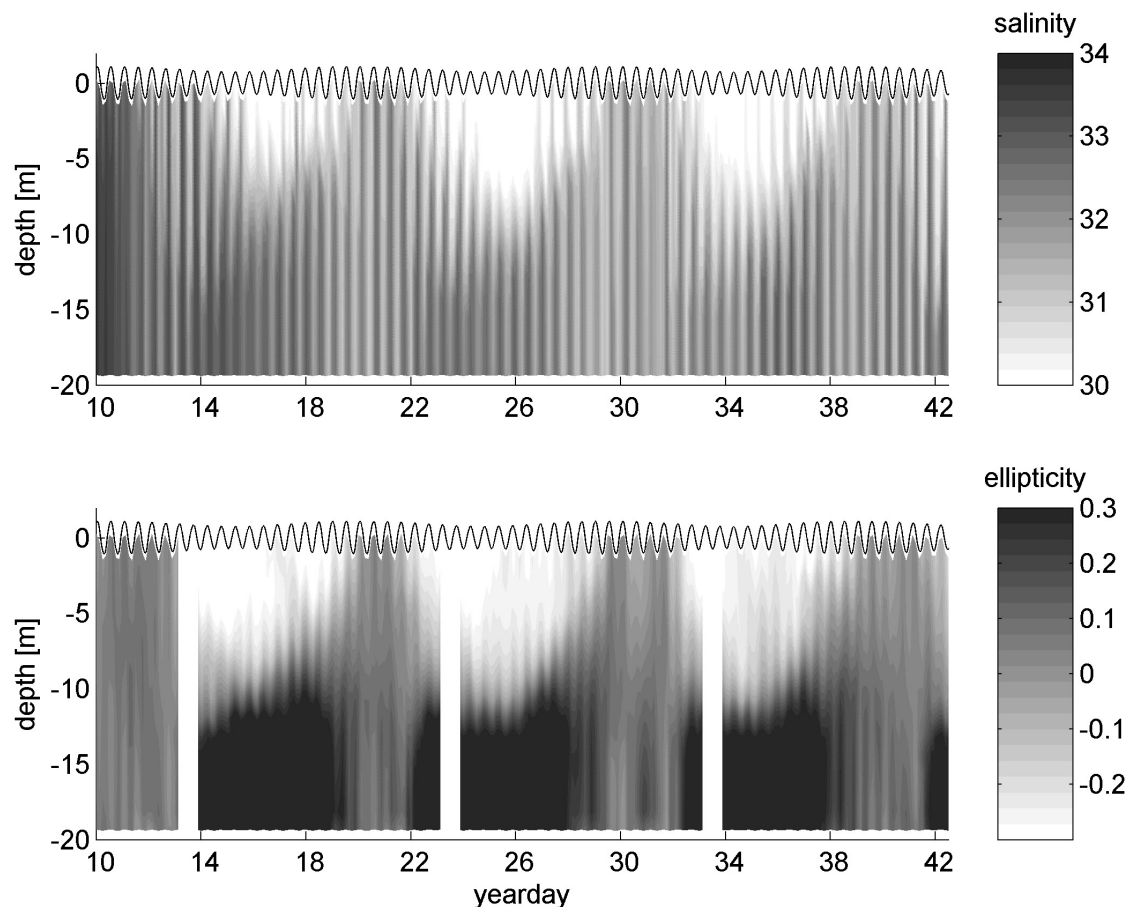


**Figure 4.16:** Vertical distribution of ellipticity and salinity during a number of spring neap cycles at a station 9.5 km offshore and 29.5 km North of the river mouth (10w, 30 n in Figs. 4.1 - 4.11, see black dot in Fig. 4.1 for location). The plume arrives at this station at yearday 11. A spring neap cycle of 9.5 days is adopted (combining a 12 hour and a 12 hour 40 min component) to reduce simulation time. The white bands in the ellipticity are due to the fact that the simulation had to be split up in 4 parts. At the start and end of each simulation the moving harmonic analysis could not be applied.



cyclonically. This caused a semi-diurnal cross shore velocity shear which was  $90^\circ$  out of phase with the alongshore currents. This cross shore shear was responsible for tidal straining which caused a semi-diurnal variation in the pattern of vertical stratification at a location 10 km offshore. Maximum stratification occurred around high water and the model results were in fair agreement with field data collected in the 90s. The spring neap tidal cycle simulations demonstrated a pattern of recurring stratification on neaps and destratification on springs in agreement with the observations of Simpson *et al.* (1993).

When all the barotropic and baroclinic simulations were ordered according to their maximum ellipticity veering, it was found that in simulations without a plume only a few percent ellipticity veering was observed. The tidal currents were rectilinear. Interestingly, during well mixed plume conditions on the spring tide, the ellipticity veering increased to almost 30%. This was attributed to a reduction in vertical eddy viscosity since some of the momentum in the tidal system had gone into mixing the plume over the vertical on the spring tidal conditions. Here results from Prandles model with a tenfold reduced eddy viscosity reproduced a quite similar veering of the ellipticity. This could be attributed to a decrease in the depth averaged vertical eddy viscosity. However, on stratified neap conditions, a markedly different response was observed with maximum ellipticity veering of up to almost 70%. In this case a tenfold reduction in eddy viscosity was not sufficient to attain the large ellipticity values seen in the numerical model, despite the considerable increase of veering of up to 40% in the analytical model.

In Fig. 4.17 ellipticity veering according to Prandle's solution is shown for all realistic eddy viscosity values at a depth of 20 m. This shows that with high eddy viscosities ellipticity is practically zero. This is the situation corresponding to the barotropic runs presented in section 3. In this case the anti-cyclonic boundary layer thickness is larger than the water depth, while the cyclonic boundary layer can develop fully. When eddy viscosity is reduced by an order of magnitude, ellipticities can increase up to 15% in the surface layer and 40% in the bottom layers. These values are sufficient to explain the increased ellipse properties during spring, as well as a large part of the increase during neaps. As a first approximation increased magnitudes of ellipticity veering can therefore simply be explained by a reduction of bulk eddy viscosity in the classical Ekman dynamics theory.

However, in order to explain the variation of the ellipse properties with depth as well as the ellipticity veering of up to 70% seen during neap tides one has to include information on the vertical structure of the eddy viscosity. During neap tides the plume reverts to a decoupled two layer system which does provide the additional explanation for the excess increase in ellipticity. A model for such a two layer system with a variable degree of coupling between the layers has already been given by Visser *et al.* (1994) and Simpson & Souza (1995). During neap tides the Richardson numbers reached values an order of magnitude larger than during springs. Ellipticity does not increase when the Richardson number increases above a value of 10. Note also that consequently the maximum value of the Richardson number in the vertical is not a

good measure for this stratification, since during spring no decoupling of bottom and surface layers is seen at values of 10. Conversely, when large ellipticities (30%) are observed over a large area, it can be concluded that the plume is stratified. This suggests that stratification in the Rhine outflow region can be detected with a HF radar system as employed in the 90s by Simpson *et al.* (1993).

The reason that a two layer system can explain increased ellipticities during neap in the Rhine plume has to do with the coincidental combination of the height of the Ekman boundary layers in combination with the bottom depth and the plume depth, see Visser *et al.* (1994) and Simpson & Souza (1995). It was found that the stratified plume covered the upper most 5 to 10 m of the water column. The bottom boundary layers are therefore confined to the remaining

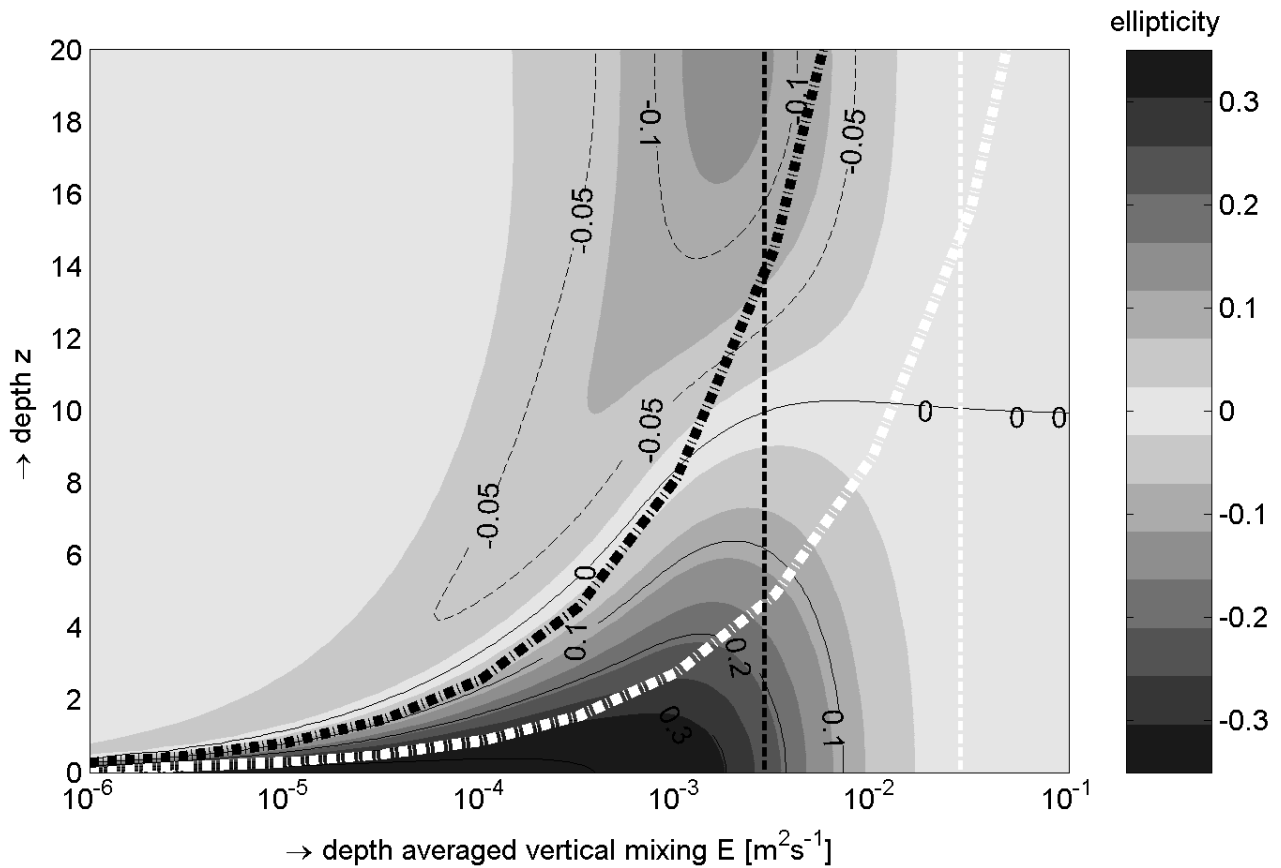


**Figure 4.17:** Ellipticity in grey tones for a depth of 20 m as a function of all realistic depth averaged eddy viscosity values (starting at molecular viscosity  $10^{-6} \text{ m}^2\text{s}^{-1}$ ) and depth during neap conditions ( $U = 0.43 \text{ ms}^{-1}$  with  $k = 0.0025\text{m}$ ). Dashed black isolines represent negative ellipticities, the solid black isolines positive ones. The eddy viscosity value  $0.028 \text{ m}^2\text{s}^{-1}$  (Fig. 4.4) is shown as a dashed vertical white line, the eddy viscosity value of  $0.0028 \text{ m}^2\text{s}^{-1}$  (the tenfold decrease in eddy viscosity shown in Fig. 8) is shown as a dashed vertical black line. The very thick dash-dotted white line is the boundary layer thickness for the cyclonic phasor  $R^+$ , the very thick dash-dotted black line the boundary layer for anti-cyclonic phasor  $R^-$  (defined by  $\delta^\pm = \sqrt{2E/\omega \pm f}$ ).

15 to 20 m of the water column. With realistic eddy viscosity values ( $<0.05 \text{ m}^2\text{s}^{-1}$ ) this height is sufficient to allow the cyclonic phasor to develop its full vertical structure. However, the anti-cyclonic boundary layer cannot fully develop with realistic eddy viscosity values. However, for a proper description of the ellipse profiles a two layer system has its limitations. Here the advantages of a three dimensional numerical model have been demonstrated. Much attention has been paid to the validation of the given numerical setup which has been shown to be an adequate tool to model the details of the vertical structure of tidal currents in the Rhine outflow region. This model will be used in future investigations of tidal straining as well as the effect of stratification on the distribution of suspended particulate matter in the Dutch Coastal Zone.

Residual currents and vertical structure in a stratified flow are controlled by river discharge (the amount of buoyancy forcing available) and the mixing processes that act to breakdown the stratification. In ROFIs variations in density occur, resulting in interfaces and fronts that are significantly influenced by the flow and mixing and which in turn significantly influence the flow and mixing. Understanding these ROFI systems is of vital importance. Numerical models have a key role to play and it is important to ensure that numerical models of river plume systems in a tidally dominated area can successfully reproduce the effects of stratification on tidal polarity. Then such models can be used with more confidence as tools with which to better understand the transport of freshwater, sediments, nutrients and pollutants.

## Acknowledgements

The project is funded by the Dutch Organization for Scientific Research (NWO) in the ALW programme within the framework of LOICZ-NL (ALW project number 014.27.006) whose support is gratefully acknowledged. We would like to thank the principal investigator, Dr. H. Ridderinkhof from Royal Netherlands Institute for Sea Research (NIOZ) for a number of discussions. We would also like to thank Prof. J.H. Simpson for a number of valuable discussions on our work. In addition we thank him for his detailed comments as a reviewer, which substantially improved the manuscript. Finally we are grateful to Walter Jacobs for the contribution he made during his MSc project.

## 4.6 Appendix: Equations tidal velocity profile

Prandle (1982a,b) obtained vertical velocity profiles and associated depth-variations of the tidal ellipse properties using the following simplified model.

$$\frac{\partial u}{\partial t} - fv = -g \frac{\partial \eta}{\partial x} + \frac{\partial}{\partial z} E_z \frac{\partial u}{\partial z} \quad (4.1)$$

$$\frac{\partial v}{\partial t} + fu = -g \frac{\partial \eta}{\partial y} + \frac{\partial}{\partial z} E_z \frac{\partial v}{\partial z} \quad (4.2)$$

$$z = 0 : \quad \frac{\partial u}{\partial z} = 0, \quad \frac{\partial v}{\partial z} = 0 \quad (4.3)$$

$$z = -D : \quad \frac{\partial u}{\partial z} = su, \quad \frac{\partial v}{\partial z} = sv \quad (4.4)$$

where  $x$  is the alongshore axis,  $y$  the cross shore axis,  $z$  the vertical axis,  $t$  time,  $u$  the alongshore velocity,  $v$  the cross shore velocity,  $f$  the Coriolis parameter,  $\eta$  the water level elevation and  $E_z$  the vertical eddy viscosity. The linearised bottom friction  $s$  is defined as  $s = 8kU/3\pi E$ , in which  $U$  is the depth averaged velocity and  $k$  is a friction factor introduced by Prandle (1982b). In this model vertical acceleration, convective and density terms are neglected. The equations are solved assuming zero frictional stress at the surface and applying a vertically constant value of the eddy viscosity  $E_z$ . The equations can be solved by rephrasing the current and pressure gradient vectors as the sum of two phasors  $R^\pm$  and  $G^\pm$  counter rotating in the complex plane as follows

$$R = R^+ + R^- = u + iv \quad (4.5)$$

$$G = G^+ + G^- = \frac{\partial \eta}{\partial x} + i \frac{\partial \eta}{\partial y} \quad (4.6)$$

where  $R^\pm$  (and analogously  $G^\pm$ ) are defined in the complex plane as

$$R^\pm = |R^\pm| \exp(i\phi_\pm) \exp(\pm i\omega t) \quad (4.7)$$

where  $\omega$  is the angular frequency and  $\phi$  is the phase in the complex plane. Substituting  $R^\pm$  into the equations of motion (Eqs. 4.1 and 4.2) yields:

$$i(f + \omega) R^+ = G^+ + \frac{\partial}{\partial z} E_z \frac{\partial R^+}{\partial z} \quad (4.8)$$

$$i(f - \omega) R^- = G^- + \frac{\partial}{\partial z} E_z \frac{\partial R^-}{\partial z} \quad (4.9)$$

By assuming a solution of the form  $R^\pm = [a \exp(-\alpha z) + b \exp(\alpha z) + c] \cdot \exp(\pm i\omega t)$ , and dividing by the expression for the depth-averaged current  $\langle u \rangle = \int_{-D}^0 u(z) dz$  (neglecting the integral over  $D \pm \eta$ ) we obtain the following solution

$$\frac{R^\pm}{\langle R^\pm \rangle} = \frac{\cosh(\alpha^\pm [z - D]) - [\cosh(\alpha^\pm D)] - \frac{\alpha^\pm}{s} \cdot [\sinh(\alpha^\pm D)]}{-[\cosh(\alpha^\pm D)] + \left(\frac{1}{\alpha^\pm D} - \frac{\alpha^\pm}{s}\right) \cdot [\sinh(\alpha^\pm D)]} \quad (4.10)$$

where  $\alpha^\pm = (1 + i) \sqrt{(f \pm \omega)/2E} \equiv 1/\delta^\pm$  is the inverse of the boundary layer height. From the solutions  $R^\pm$  the ellipse properties can be evaluated as follows:

$$\begin{aligned} A_{major} &= |R^+| + |R^-| && \text{Major axis} \\ A_{minor} &= |R^+| - |R^-| && \text{Minor axis, positive in } \exp(+i\omega t) \text{ direction} \\ \psi &= \frac{1}{2}(\phi_- + \phi_+) && \text{Inclination} \\ \phi &= \frac{1}{2}(\phi_- - \phi_+) && \text{Phase} \\ E &= \frac{A_{minor}}{A_{major}} = \frac{|R^+| - |R^-|}{|R^+| + |R^-|} && \text{Ellipticity, positive in } \exp(+i\omega t) \text{ direction} \end{aligned} \quad (4.11)$$

Note that the ellipticity used here differs from the eccentricity that is generally used in mathematics. Following Souza and Simpson (1996) the ellipticity is defined as the signed ratio of the minor axis to the major axis. The ellipticity is therefore zero for a degenerate ellipse, 1 for a cyclonic circular path and -1 for an anticyclonic circular path.

For comparison to numerical results, which yield the  $u$  and  $v$  velocity components, the ellipse properties can also be calculated as follows:

$$A_{major} = \frac{1}{2} |(a + d) + i(c - b)| + \frac{1}{2} |(a - d) + i(c + b)| \quad (4.12)$$

$$A_{minor} = \frac{1}{2} |(a + d) + i(c - b)| - \frac{1}{2} |(a - d) + i(c + b)| \quad (4.13)$$

$$\psi = \frac{1}{2} \arg\left(\frac{1}{2} [(a + d) + i(c - b)]\right) + \frac{1}{2} \arg\left(\frac{1}{2} [(a - d) + i(c + b)]\right) \quad (4.14)$$

$$\phi = \frac{1}{2} \arg\left(\frac{1}{2} [(a + d) + i(c - b)]\right) - \frac{1}{2} \arg\left(\frac{1}{2} [(a - d) + i(c + b)]\right) \quad (4.15)$$

when coefficients  $a$  to  $d$  are defined as in

$$u = a \cos(\omega t) + b \sin(\omega t) \quad (4.16)$$

$$v = c \cos(\omega t) + d \sin(\omega t) \quad (4.17)$$

## Chapter 5

### SST observations of upwelling induced by tidal straining

This chapter has been published as :

de Boer, G.J., Pietrzak, J.D., & Winterwerp, J.C. 2007. *SST observations of upwelling induced by tidal straining in the Rhine ROFI*. *Continental Shelf Research*, (special issue PECS 2006). doi:10.1016/j.csr.2007.06.011.

#### Abstract

In this paper SST imagery and a three-dimensional numerical model of a river plume were employed to detect upwelling induced by tidal straining in the Rhine ROFI (region of fresh water influence). Previous studies have shown that the Rhine ROFI in the North Sea exhibits strong cross-shore density gradients that compete with tidal and wind mixing to establish stratification. During neap periods with low mixing energy an area measuring 30km offshore by 100km alongshore becomes stratified. When the ROFI is stratified strong cross-shore currents are observed, with surface currents rotating anti-cyclonically and bottom currents rotating cyclonically. The crossshore currents interact with the cross-shore density gradients to produce a semi-diurnal cycle of stratification. Due to continuity requirements imposed by the proximity of the coast, the offshore-directed surface currents and onshore-directed bottom currents should lead to coastal upwelling.

A 6-day unclouded series of SST-imagery was found in May 1990 with about two images per tide. The ROFI is much warmer than the surrounding water, exhibits a distinct diurnal solar heating response and is clearly delineated by large spatial temperature gradients at the edges. This indicates that the whole ROFI area is stratified. On three consecutive middays, a marked 5-10km wide and 100km alongshore band of cold upwelling is visible along the coastline, while in the morning and afternoon this upwelling band is not present. The timing of this upwelling indicates that it is caused by tidal straining. This conclusion was supported with a simulation with a threedimensional numerical model of an idealized river plume showing the same semi-diurnal cold upwelling band. We believe these are the first SST images to show upwelling induced by tidal straining, as well as the large spatial scale of idal straining in the Rhine ROFI.

## 5.1 Introduction

Rivers release significant amounts of freshwater into coastal areas. Upon entering the open sea or ocean this buoyancy input turns anti-cyclonically under the influence of the rotation of the Earth and establishes a plume downstream. The importance of these buoyant coastal currents has led to many studies, see for example, Kourafalou *et al.* (1996a), Kourafalou *et al.* (1996b), Fong & Geyer (2001), Fong & Geyer (2002), McClimans *et al.* (2000), Pietrzak *et al.* (2002), Yankovsky & Chapman (1997), Garcia Berdéal *et al.* (2002), Hickey *et al.* (2005), Hetland (2005) and Horner-Devine *et al.* (2006). Simpson *et al.* (1993) introduced the name ROFI (region of freshwater influence) for such river plume areas. The freshwater significantly affects the current patterns in the ROFI, where it is one of the main agents governing the advection and dispersion of sediments, pollutants and biota. In order to understand primary production it is therefore of paramount importance that we increase our knowledge about ROFIs. Measurements in the Rhine ROFI have for instance shown that the water column stability influences chlorophyll sinking rates to a large degree (Joordens *et al.*, 2001; Peperzak *et al.*, 2003).

The Rhine ROFI (Fig. 5.1) is fed by the Rhine-Meuse system with an average combined discharge of  $2500 \text{ m}^3\text{s}^{-1}$ . The ROFI generally extends 20 - 40 km from the coast, with an occasional outburst 50 km offshore. Downstream from the river mouth the ROFI covers an area of over 100-120km (De Ruijter *et al.*, 1992; Van Alphen *et al.*, 1988; De Kok *et al.*, 2001). Here it joins with any fresh water that might come through the Texel inlet, which is significantly less than the Rhine discharge. The barotropic tide in the 20m deep Dutch coastal zone has the character of a propagating Kelvin wave with surface velocities ranging from 0.7 to  $1.1 \text{ ms}^{-1}$  (Van Alphen *et al.*, 1988). Significant steps forward in our understanding of the Rhine ROFI were made in the early 1990s during the Profile project, and later that decade during the PROVESS project. In both projects extensive field measuring campaigns were carried out, see Huthnance (1997) and Howarth *et al.* (2002), respectively, for overviews of the two projects. Simpson *et al.* (1993), Visser *et al.* (1994), Simpson & Souza (1995), Souza & Simpson (1996), Souza & Simpson (1997), Simpson (1997) and Fisher *et al.* (2002) describe the basic mixing-stratifying processes that take place in the Rhine ROFI. Here the buoyancy inputs compete with wind, wave and tidal mixing to establish stratification and the tidal and residual current profiles are significantly affected by water column stability.

Simpson *et al.* (1993) detected two distinct time scales in the water column structure. Spring tides in combination with wind mixing brought about periods of complete vertical homogeneity resulting in a well-mixed plume. In contrast, during neap tides and low winds, the region was observed to re-stratify due to relaxation of the cross-shore density gradients under the influence of gravity. This resulted in a stratified plume. The second time scale is a semi-diurnal variation during periods of stratification. It is only during these periods that significant semi-diurnal cross-shore exchange currents occur. Visser *et al.* (1994) further explored these semi-



diurnal exchange currents and described them successfully with counter-rotating surface and bottom ellipses. However, Simpson & Souza (1995) were the first to realize that when the mean state of the ROFI is stratified, these semi-diurnal exchange currents interact with the cross-shore density gradients according to the tidal straining theory of Simpson *et al.* (1990) to generate fluctuations in the vertical stability of the water column at the semi-diurnal frequency (Fig. 5.2).

The onset of the semi-diurnal fluctuations can readily be explained with Ekman dynamics (Visser *et al.*, 1994; Souza & Simpson, 1996). Following (Prandle, 1982a,b) tidal currents can be decomposed into two counter-rotating phasors. The component of the tide that rotates against the direction of the rotation of the Earth is affected more by bottom friction than the component that rotates in the same direction as the planetary rotation. The near-bottom velocity therefore has a tendency to rotate in the same direction as the planetary rotation. Studies on the properties of the tidal ellipses indicate substantial changes in the form of the tidal ellipses during periods of stratification (Visser *et al.*, 1994; Souza & Simpson, 1996). Stratification causes a decoupling of the layers above and below the pycnocline; consequently, near surface currents experience an increase in anti-cyclonic rotation in comparison with the well-mixed case. Additionally, given the presence of a coastal boundary, the net cross-shore tidal transport must be zero at all times. Hence as stratification leads to surface currents that rotate anticyclonically, compensating bottom currents must rotate cyclonically leading to the development of significant crossshore currents that act in the opposite direction. The observed cross-shore velocity shear in this situation can be up to  $70 \text{ cms}^{-1}$ , see Simpson *et al.* (1993) and Visser *et al.* (1994).

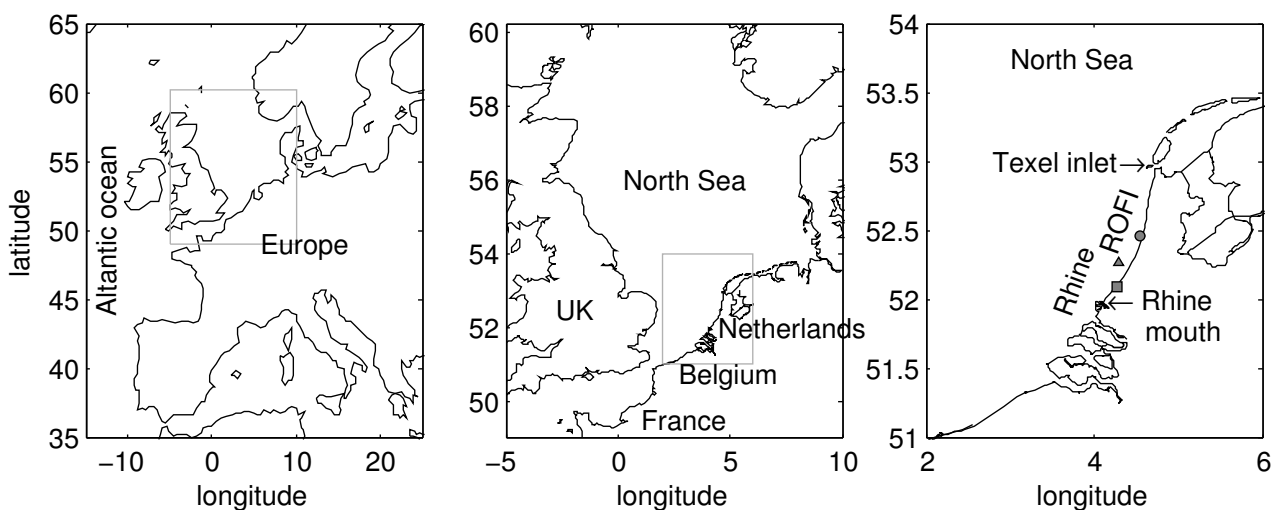


**Figure 5.1:** The location of the Rhine ROFI. The positions of three water level stations are marked in the right panel: IJmuiden (circle), Noordwijk meetpost (triangle) and Scheveningen (square). A sluice 15 km south of the Rhine mouth also debouches a fraction of the Rhine discharge during periods of high discharge.

This cross-shore tidal straining mechanism in the Rhine ROFI was then confirmed with one-, two- and threedimensional models. With a one-dimensional vertical model Simpson & Souza (1995) successfully reproduced a time series with semi-diurnal oscillations in stratification. Subsequently, Souza & James (1996) used a twodimensional cross-shore model to confirm tidal straining in the Rhine ROFI. More recently, De Boer *et al.* (2006) carried out a detailed three-dimensional numerical study of the Rhine ROFI in which they examined the properties of

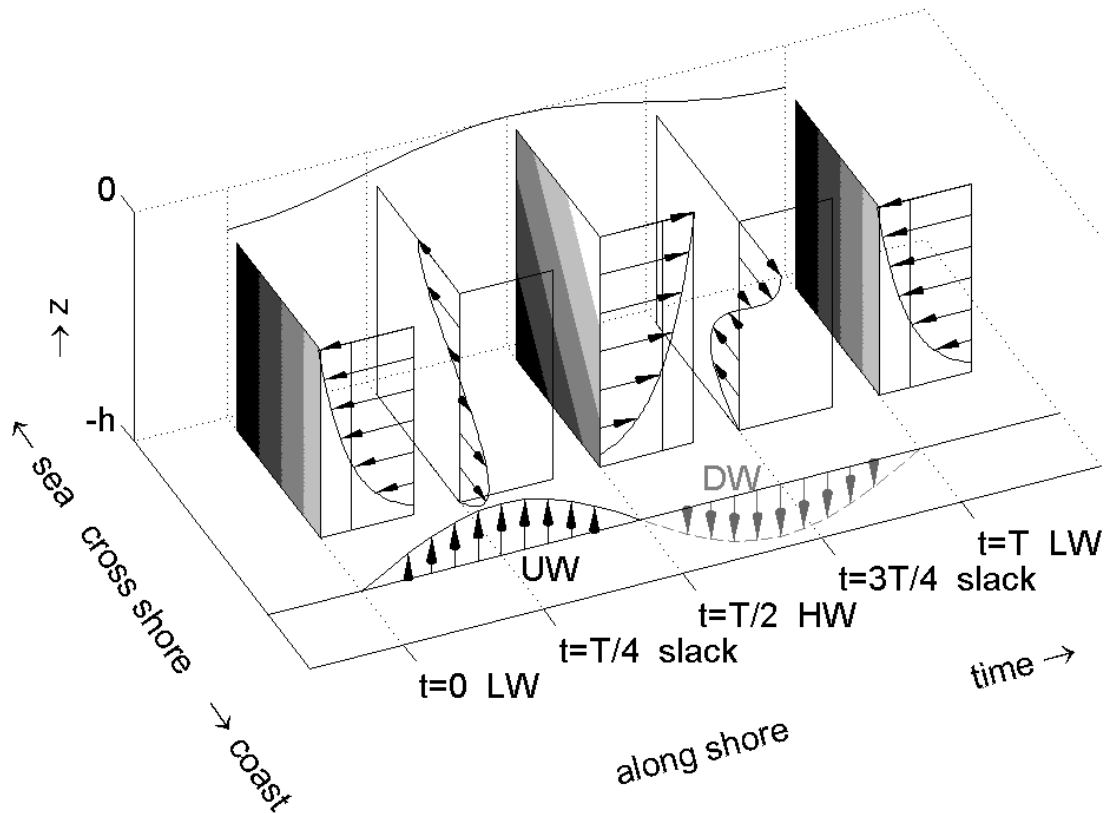


**Figure 5.2:** Conceptual sketch of tidal straining (Simpson *et al.*, 1990) during one tide cycle in the Rhine ROFI. The interaction between the cross-shore velocity shear (arrows) and the cross-shore density gradients (gray tones) was first recognized by Simpson & Souza (1995). The tide has the character of a propagating Kelvin wave with maximum flood velocities at HW. From LW to HW the anti-cyclonic surface currents are directed offshore, so that the plume is maximally stratified at HW. From HW to LW the surface currents are directed onshore, the plume is closest to wellmixed at LW. Due to continuity requirements imposed by the coastal wall there has to be upwelling (UW) from LW to HW, and downwelling (DW) from HW to LW. Slack is defined here at  $T/4$  and  $3T/4$  when the (depth averaged) alongshore currents are zero, the depth-averaged cross-shore currents are always zero.

the tidal ellipses as the system switched between well-mixed and stratified conditions. Their study, in line with that of Visser *et al.* (1994) and Simpson & Souza (1995), demonstrated the importance of the proximity of the coastal wall which couples the two rotary components by requiring that at any moment in time the depth averaged cross-shore velocity is zero; this has the consequence that the absolute values of the depth integrated phasors should be equal. Any cross-shore current caused by the preference of the bottom current to rotate cyclonically, is therefore immediately compensated by an opposite cross-shore surface current. Because the alongshore surface and bottom currents are almost fully in phase, this gives an anti-cyclonic rotation of the surface currents. De Boer *et al.* (2006) also demonstrated that this latter constraint leads to cross-shore currents even in the well-mixed case; however, they only become significant when stratification decouples the upper and lower layers of the water column.

In the Rhine ROFI the proximity of the coastal wall leads to an interesting situation. The landward progression onshore or offshore in the bottom layer is limited by the presence of the coast. Therefore, continuity requires a region of up- and downwelling to be present close to the coast. Because the cross-shore currents vary semi-diurnally, up- and downwelling is expected to take place on a semidiurnal time scale as well. In the case of a propagating Kelvin wave, tidal straining theory predicts offshore surface currents from LW to HW, and onshore surface currents from HW to LW (Fig. 5.2). Accordingly, upwelling takes place from LW to HW, and is strongest after one quarter of a tidal period ( $T$ ) at  $T/4$ , when the cross-shore currents are strongest. Conversely, downwelling takes place from HW to LW and is strongest at  $3T/4$ . The plume displacements are obtained by integrating the cross-shore surface currents in time. The plume is therefore located furthest offshore at HW. Similarly, the presence of upwelled water at the surface is obtained by integrating the vertical velocities over time. We can therefore expect upwelled deep water to be at the water surface from slack before HW to slack after HW. The band of upwelled water will be widest at HW. Consequently, if one considers that the Rhine ROFI extends over 100 km alongshore, a stratified plume would be expected to be subjected to up- and downwelling in a narrow 100 km long strip close to the coast.

Moreover, when the surface and bottom water have different properties such as a distinct temperature contrast, this narrow band of upwelled water, as well as its semidiurnal time scale should be detectable with surface sensors. Surface waters in a stratified plume in early summer are generally significantly warmer than the surrounding ambient waters. Tidal straining is therefore expected to be visible as a semi-diurnal appearance of a band of colder water. Because the phase delays associated with the Kelvin wave in the Rhine ROFI are small (Simpson, 1997), the cold band should appear simultaneously over the ROFI area. In stratified plumes during other periods of the year, or in well-mixed plumes, coastal upwelling is not expected to exhibit a distinct sea surface temperature (SST) signature. To our knowledge coastal upwelling driven by tidal straining has not been investigated before. In this paper, we present a unique sequence of AVHRR SST imagery with high temporal resolution. We use these images together with an

idealized river plume model to investigate upwelling induced by tidal straining. The numerical model described and validated in De Boer *et al.* (2006) is extended to include temperature effects. The model results are used to explain and corroborate the findings in the SST images which show the dominant role of cross-shore tidal straining in causing the observed coastal upwelling. In Section 2, our methods are described. First, the database of the SST imagery is discussed. Then the methods to extract information from these images are dealt with. Finally, the set-up of the numerical model is described. In Section 3, the temperature patterns are presented and we demonstrate that the cold water band, that appears around high water in this sequence of SST images, is due to upwelling induced by tidal straining. We end with a discussion in Section 4.

## 5.2 Methods

### 5.2.1 SST imagery selection

Since 1990 KNMI, the Dutch met office, collects NOAA AVHRR imagery at the raw data resolution of 1 km, processes it to SST and maps it for the North Sea (Roozekrans & Prangma, 1992; Roozekrans, 1997). The 1 km resolution is just sufficient to capture coastal ROFI features that have an internal Rossby Radius up to 10 km. From this long-term data set we selected a remarkable sequence of plume images in May 1990, see Fig. 5.3. This sequence meets three criteria that we adopted. The selected SST series has to exhibit a distinctly recognizable plume patch. As discussed in de De Kok *et al.* (2001), Arentz (2005) and Pietrzak *et al.* (2008b), this criterion practically limits us to stratified plumes. Generally the surface temperatures in well-mixed plumes do not differ sufficiently from the surrounding North Sea temperatures to delineate the river plume. The lateral temperature gradients are of the same order as background gradients due to differences in depth, and differences between Atlantic Channel waters and continental coastal waters (Lacriox *et al.*, 2004). In addition, temperature is not a useful conservative tracer to derive advective properties of the flow field in the Rhine plume (De Ruijter *et al.*, 1992). In contrast, in stratified plumes atmospheric and solar heat fluxes lead to an extra and fast SST contrast with surrounding waters that make it well recognizable. There are two explanations for this discerning signal. First, in the stratified area mixing of water between surface and bottom layers is reduced. The same applies to the properties of the water like heat content. The heat input in the surface layer is therefore confined to the upper layer, causing higher temperatures in the upper layer. In addition, in the case of low wind mixing the bottom-induced turbulent mixing is confined to the lower layer. Hence, in the absence of wind mixing, solar heat input will not be distributed evenly within the surface layer and a strong vertical temperature gradient can arise in the upper layer (De Kok *et al.*, 2001). The excess temperatures are confined to a very thin skin layer only. Local excess temperatures in SST images are therefore indicative of stratification, while the observed excess surface temperatures due to solar radiation cannot be

---

used explicitly to estimate the thickness of the surface layer. A fortunate fact is that the local density field is hardly affected by these temperature changes due to the strong haline stratification (De Ruijter *et al.*, 1992; De Kok *et al.*, 2001)). The full 15-year KNMI data set shows that clearly recognizable stratified plume images are scarce. Recognizable plumes occur mainly in May (warm plume, excess heating) and occasionally in November (cold plume, excess cooling), see also Arentz (2005) and Pietrzak *et al.* (2008b) in which an extensive analysis of SST and SeaWiFS data for 1998 are examined.

Second, a sufficient temporal resolution is also needed to be able to detect tidal straining from SST imagery. There were two NOAA satellites in orbit in 1990 with a 12 hour return time. This yields at most 4 images per day, which is just sufficient for capturing tidal processes. In May cloud cover is minimal in the southern North Sea. Our example in May 1990 (see Fig. 5.3) has an excellent data availability of 18 images/5 days in 1990. This yields on average 2 images per tidal cycle.

Third, the SST images need to coincide with a period of relatively low wind if we are to detect upwelling due to tidal straining. Strong winds are bound to mix up the plume (Visser *et al.*, 1994). Moreover, winds lead to plume displacements on top of the tidal displacements. Crossshore easterlies with velocities of about  $5 - 7 \text{ ms}^{-1}$  prevail in our 1990 example. We can estimate the effect of this wind before looking at the images. Fong *et al.* (1997) showed that river plumes are in approximate Ekman balance. They found that alongshore winds lead to up- and downwelling. Accordingly, the cross-shore wind in our case should lead to alongshore movements, which does not interact with any upwelling induced by cross-shore tidal straining that we are looking for. The amplitude of the plume movement can be estimated using the results from Fong & Geyer (2001). They found that  $0.1 \text{ Pa}$  upwelling favorable winds lead to offshore displacements of order  $20 \text{ km/day}$ . Accordingly the easterlies in 1990, with an associated shear stress of about  $0.05 \text{ Pa}$ , can be expected to cause a moderate northward alongshore displacement of about  $10 \text{ km/day}$ , about the same size as the alongshore tidal excursion. In order to support the notion of the independent responses of displacements induced by wind and tidal straining an idealized wind driven model run is also presented.

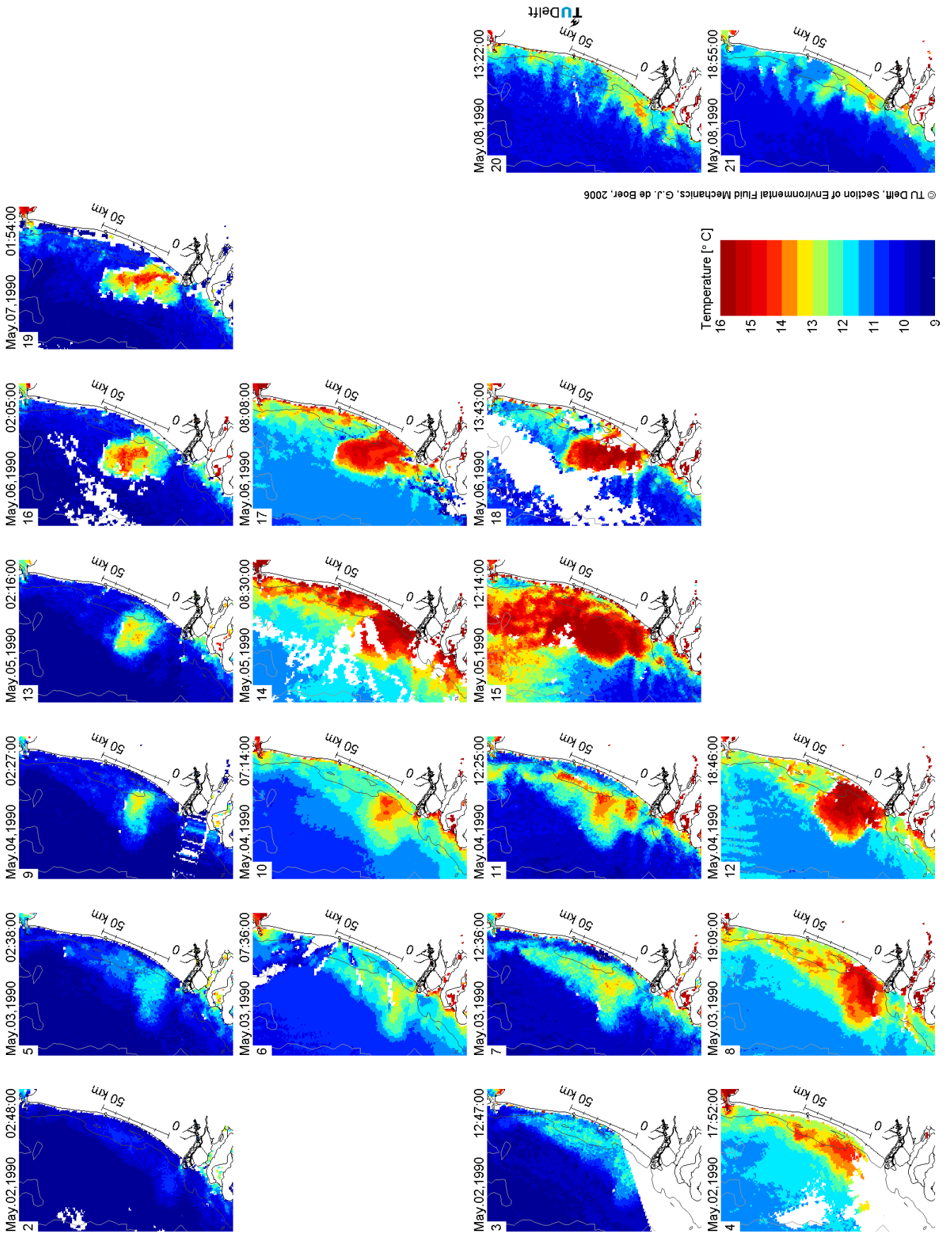
### 5.2.2 SST analyses

In the next sections, we attempt to extract information on tidal straining from the SST images. Due to the constraint of the coastal wall the surface waters are replenished by colder upwelling water, rather than by surrounding surface waters. Hence, in the spring the upwelling can be observed directly when looking at the temperature images. When there is a significant temperature difference between surface and bottom water, a cold patch near the coast in spring already indicates offshore displacement. We also analyzed spatial temperature gradients. When a stratified patch displaces, the convergence at the frontal side is expected to cause increased spatial temperature gradients. Strong spatial temperature gradients larger than  $1 \text{ }^\circ\text{C/km}$  (not shown) are indeed found to delineate the Rhine ROFI and show that the ROFI area is strat-

---

**Figure 5.3 (on the next page):** Plan view mosaic of plume SST in May 1990. The satellite images are numbered sequentially in the upper left corner of their panel. Image number 1 at May 1st 2:59 is not shown. The Rhine river source debouches in the North Sea between the smooth coastline in the north and the irregular coast of Zeeland in the south (Fig. 5.1). A small fresh water flux comes through the Texel inlet in the upper right hand corner where it joins the Rhine ROFI.





© TU Delft, Section of Environmental Fluid Mechanics, G.J. de Boer, 2006



ified and subject to movements. It should be noted that the largest gradients are flagged off as clouds by the spatial coherence cloud test in the atmospheric cloud detection mechanics (Roozkrans & Prangma, 1992). However, no correlation of the gradients with the phase of the tide was found; consequently, this method does not allow for any conclusions regarding tidal straining. Hence here we focus on an analysis of the individual SST images.

In order to be able to relate the plume displacements to tidal straining, the results from the direct analysis of the temperature evolution observed in the individual SST images outlined above, are analyzed together with the measured water level time series to assess whether the phasing indicates tidal straining. The tidal straining theory for the propagating Kelvin wave in the Rhine ROFI indicates that the plume moves offshore from LW to HW, and onshore from HW to LW. Hence the plume is located furthest offshore with maximal stratification around HW (Souza & Simpson, 1997; Fisher *et al.*, 2002). This implies that inshore of the plume a cold band of upwelling water is expected to be visible from slack before HW to slack after HW, but most clearly around HW.

### 5.2.3 Idealized numerical model

Besides analyzing SST images, a numerical simulation of an idealized river plume with atmospheric heat fluxes was analyzed. This numerical set-up allows us to test our assumptions and conclusions about the river plume regarding the SST imagery. We use the same model setup as adopted by De Boer *et al.* (2006), and add temperature as an extra constituent. Here we repeat only the relevant settings. We note that the idealized model is meant as a means to study the basic processes of the plume observed in May 1990. Although the parameters are chosen to mimic this plume, the model is not meant to be a true representation of the actual situation in May 1990. We do not present detailed wind simulations here because we focus on semi-diurnal upwelling. However, in order to support our conjecture above, about the role of the offshore winds, we include one wind simulation here.

The model used is the three-dimensional flow module of Delf3D with a third-order upwind scheme in the horizontal direction (Van Eijkeren *et al.*, 1993) and a second-order central scheme in the vertical for advection (Stelling, 1984; Stelling & Van Kester, 1994; Delft Hydraulics, 2006). Vertical mixing is resolved with a standard  $k - \epsilon$  model, including a buoyancy destruction term (Stelling, 1995). A background eddy viscosity of  $10^{-4} \text{ m}^2\text{s}^{-1}$  is adopted, which is small compared to the tidally induced eddy viscosity (order  $10^{-2} \text{ m}^2\text{s}^{-1}$ ).

The plume is modeled in a 20 m deep rectangular basin with a resolution of 500 m (Fig. 5.4). The vertical is resolved with 16 equidistant sigma-layers. At the West and north side stretched boundaries of the non-reflective Riemann type are used to avoid disturbances. On the southern boundary a Kelvin wave with a 12 hour (S2) period is imposed. On the eastern side a 45 km long estuary is located with a discharge of  $2500\text{m}^3\text{s}^{-1}$  0 PSU at its head which debouches into

the sea which has an initial salinity of 34.5 PSU (Suijlen & Duin, 2001). The SST images show that the river plume initially has a uniform temperature of  $11^\circ\text{C}$  (Fig. 5.3), indicating no significant temperature difference between sea and riverine water. Therefore the river discharge and initial sea water temperature are set to  $11^\circ\text{C}$ .

A barotropic spin-up period of 2.5 days was used. Then the river was switched on and the model was spun up baroclinically for another 15 days, after which time the river plume reached a distance of 100km downstream. In addition, it is almost fully cyclic; that is after every semidiurnal excursion the plume returned almost to the same state. After this 15-day simulation, temperature and atmospheric heat fluxes were switched on and the final 36 hour simulation covering three tidal periods was performed. The last 12 hour of the simulation, when there is a sufficient temperature contrast between the plume and the ambient water, is used for detecting upwelling induced by tidal straining. In agreement with the SST images the plume now starts with a uniform temperature. An excess temperature heat-flux model is used with a constant  $25^\circ\text{C}$  atmosphere temperature. This was the maximum measured temperature in a coastal meteorological station during our May 1990 SST imagery series. The heat flux to the surface layer of the model is calculated as an exchange coefficient times the temperature difference between air and sea surface. The exchange coefficient is a function of the surface temperature and wind speed. The heat is further transported by an advection-diffusion equation with the vertical eddy viscosity distribution calculated by the  $k - \epsilon$  model.

A detailed analysis of the role of winds is in preparation and will be presented elsewhere. Here we include the results of a model simulation forced with a steady  $7\text{ ms}^{-1}$  offshore wind. The model setup is identical to the unforced case except that an offshore wind is allowed to blow for 24 hour and the results are presented for a complete tidal cycle after this 24 hour period.

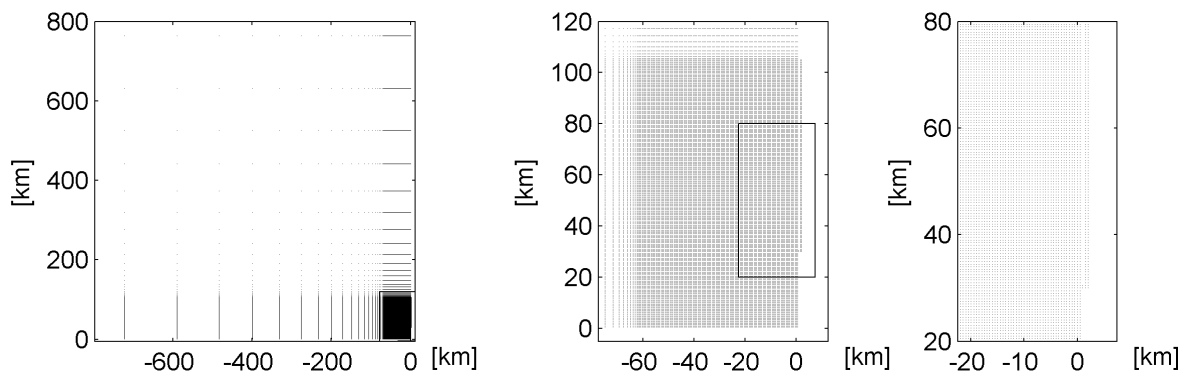


**Figure 5.4:** Plan view of the corner points of the numerical model grid dopted by De Boer *et al.* (2006). The northern and eastern boundary are located far away using a gradually increasing cell size from the inner  $65 \times 105\text{ km}^2$  domain outwards.

### 5.3 SST sequence

Fig. 5.3 shows the 18 snap shots of the plume in the 5-day period from May 2nd to May 7th. Every day the SST images are only available in one of four time slots. The first one is between 1:54 and 2:48 (1st row, from now on referred to as the 2 AM slot), the second is between 7:14 and 8:08 (2nd row, 8 AM slot), the third is between 12:14 and 13:43 (3rd row, 1 PM slot) and the last slot is between 17:52 and 19:09 (4th row, 6 PM slot). It is worth noting that the four fixed time slots are determined by the two satellites that both have a 12 h polar orbit. The 1.5 h spread is due to the fact that each spot can be covered by one pass, or by the next pass 1.5 h later.

Except for image number 2, the plume is visible as a clearly distinguishable region of higher temperatures. The offshore parts of the North Sea range from 9 to 11°C, while in the ROFI temperatures range from 10 to 16°C. The variation in the ROFI is much larger, indicating the presence of stratification. The ROFI region stretches almost 0 km offshore and over 100km alongshore. This area is quite patchy and exhibits a large difference in appearance between the four snap shots during the day. In comparison, images taken at the same time of the day show a smaller difference. During the course of the 5 days the plume slowly grows and warms up. Finally, on May 8th the plume patch has disintegrated into smaller filaments. This is probably due to increased mixing at the onset of springtide (neap is on May 4th, spring on May 11th) in accordance with the field data findings by Simpson *et al.* (1993) and Visser *et al.* (1994). Moreover, the direction of the wind suddenly changed from easterly to north-west.

The ROFI seems to consist of two independent superimposed shapes. This is most clearly visible in the image on May 4th 7:14 (Fig. 5.3). Here the ROFI looks very much like a classical river plume as modeled by Oey & Mellor (1993) and later authors. Just north of the Rhine mouth a patch with a diameter of 20 - 30 km is observed. This bears resemblance to the bulge region noted in river plume studies. To the north of that an almost coast parallel wedge-shaped region is observed. This looks like the coastal current found in all plume studies. The two shapes are now discussed separately.

#### 5.3.1 The bulge

The bulge just north of the river mouth is visible in all 18 images. During the day it warms up significantly, while during the night it cools down. This patch is visible in all 2 AM images, because the nighttime cooling does not compensate the daytime heating. The 2 AM images clearly show the gradual evolution of this patch. The bulge stretches north and slowly elongates until its northern front is 60 km from the river mouth. The net frontal displacement is about 25 km north. During this period the prevailing winds are from the east. Neglecting bottom friction, this suggests that the wind might be responsible for the northward elongation of the bulge. We can test whether the bulge movement is in stationary Ekman balance with the wind

by applying the simple conceptual frontal speed model by Fong & Geyer (2001). We apply this model for the cross-shore momentum balance of the front. A reasonable frontal depth of 4 - 7 m is then required to let the observed alongshore frontal velocity of  $5 \text{ cm s}^{-1}$  (25 km/5.5 days) balance the average 5-7  $\text{ms}^{-1}$  offshore wind, respectively (with a wind drag coefficient of  $C_d = 1e^{-3}$ ). A plume depth of 4 m is in accordance with a thickness of the upper layer of 3 - 5 m observed in transects cruises as reported in for instance Joordens *et al.* (2001). However, the bulge to which this scaling applies is probably deeper than the rest of ROFI judged by the persistence of the temperature in the patch. The required 4 - 7 m thickness is realistic for the bulge. This allows us to conclude that the patch is driven north by the wind and behaves independently of the rest of the ROFI. From now on we refer to this as the bulge.

Noteworthy is the wedge-shaped region of colder water that is found between the bulge and the coast on the 2 AM images. Due to the inclination of the coast this cold water wedge is formed between the coastline and the northward moving bulge. We can therefore assume that this marked region of cold water is not caused by upwelling, but is simply closed off by the wind-driven bulge movement.

### 5.3.2 Downstream coastal buoyancy current

The second ROFI shape is revealed by looking at the evolution of the SST pattern in the whole Dutch coastal zone during 1 day. A narrow and elongated almost classic downstream coastal plume shape is visible from 8 AM to 6 PM. It covers a  $50 \times 100 \text{ km}^2$  area to the north of the bulge. The shape bears resemblance to the extent of the near and far field stratified areas under average conditions defined in Van Alphen *et al.* (1988). This narrow area warms up during the day, but fully cools down again during the night. It is therefore hardly visible in the 2 AM images. From now on we refer to this shape as the coastal current.

On 4 consecutive days this second coastal current is clearly located offshore at midday, separated from the coast by a very long (100 km) but narrow ( $< 10 \text{ km}$ ) cold filament. In order to highlight the band of cooler upwelled waters and their scale, two detailed midday images are included, see Figs. 5.5 and 5.6. The timing and disappearance of this filament suggest a completely different origin than the cold wedge observed on the 2 AM images. What causes this midday cold water region? Is it due to upwelling and if so, what causes this upwelling? Our hypothesis is that it is upwelling caused by tidal straining.

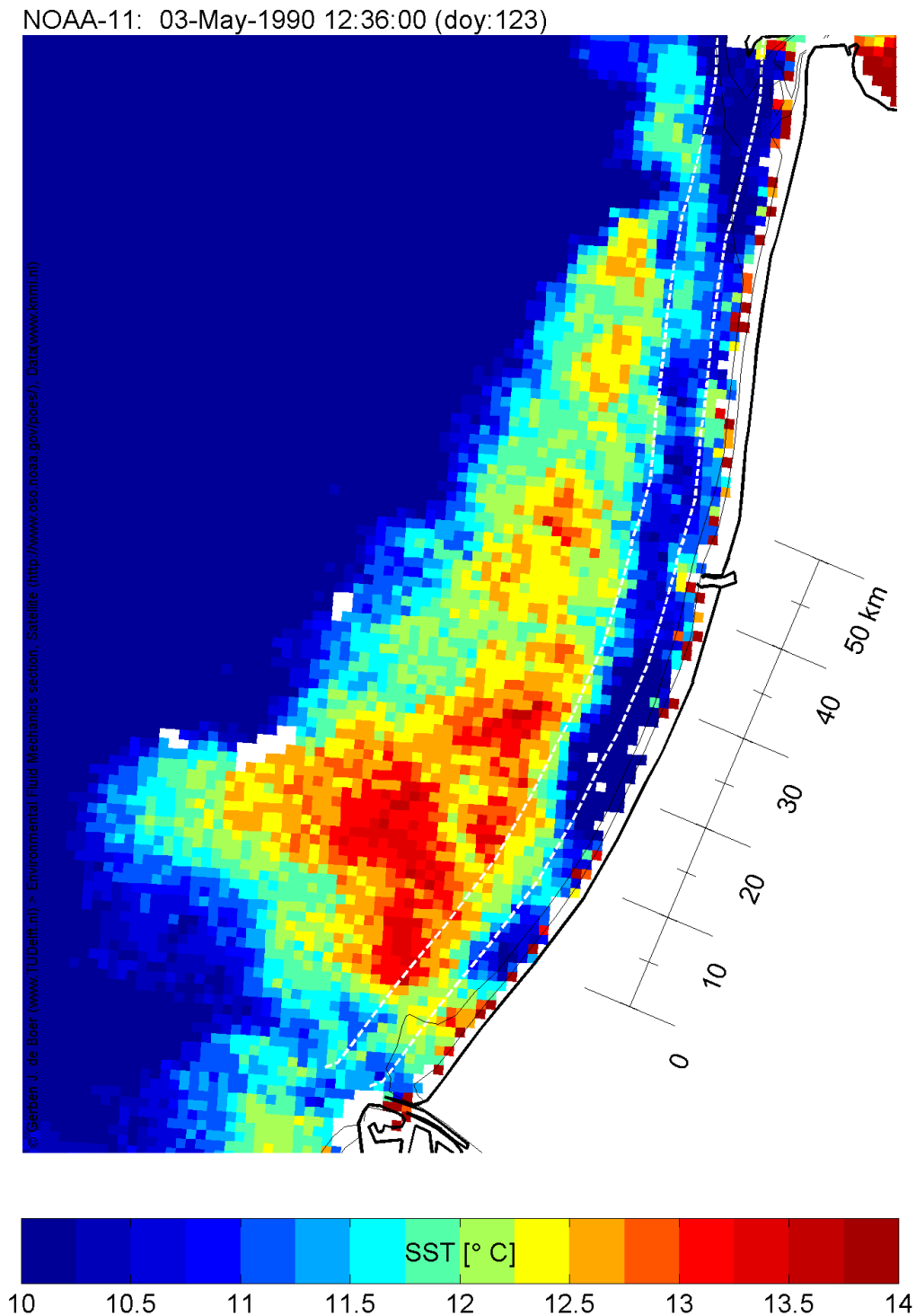


**Figure 5.5:** Enlargement of midday image 7 in Fig. 5.3 that clearly shows a 5 - 10 km wide upwelling band. The white dashed lines represent distances 5 and 10 km from the coast. They are included to be able to assess the width of the upwelling band. Note that the satellite pixels (that are individually visible) measure  $1 \times 1 \text{ km}^2$ . The thin black lines seawards of the coast are the 10 and 15 m isobaths.

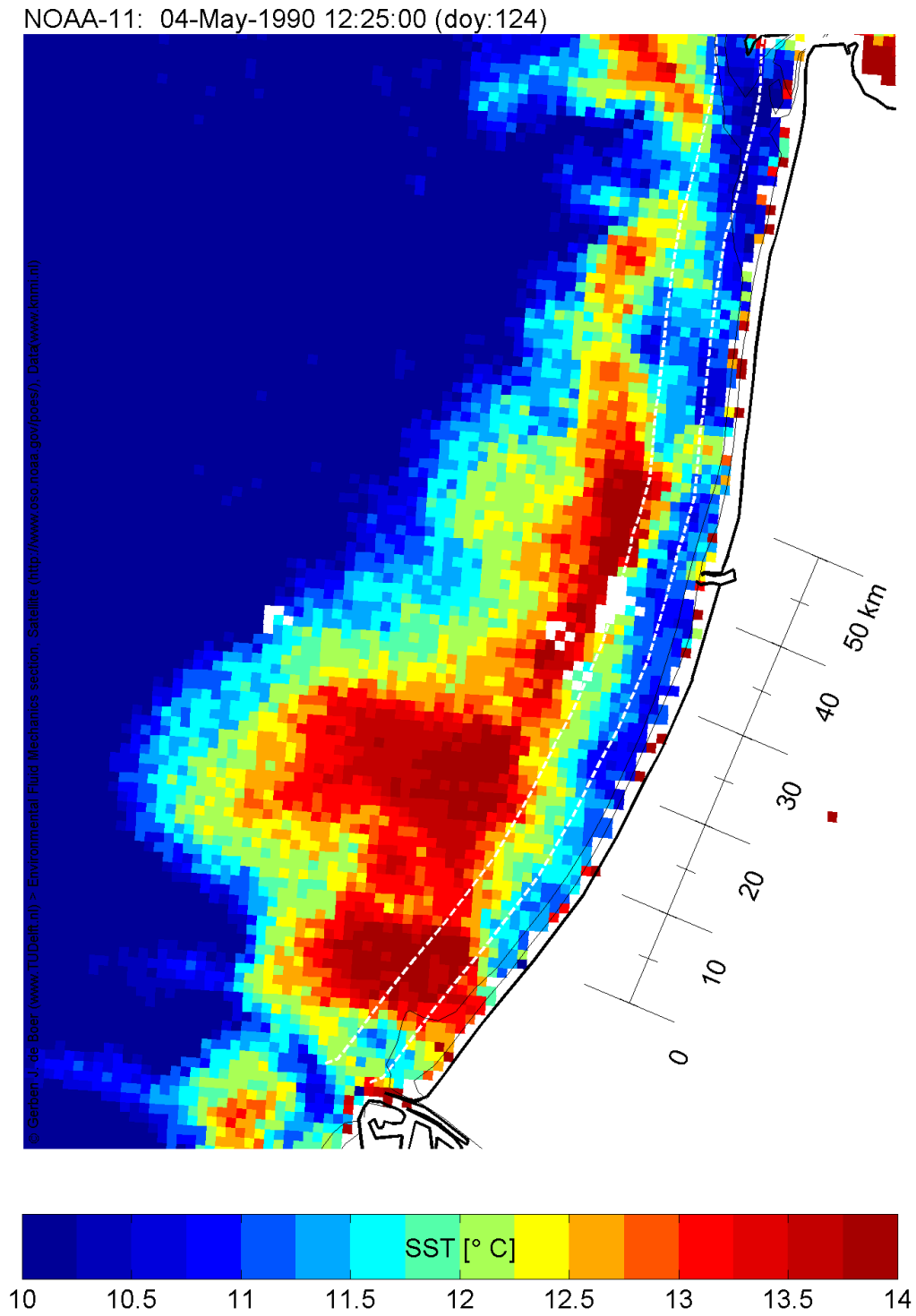


**Figure 5.6:** Enlargement of midday image 11 in Fig. 5.3, for explanation see caption Fig. 5.5.

In Fig. 5.7 the timing of these midday bands of cold water is shown in relation to the time series of the water level inside the ROFI. The bands occur between HW and the following slack. According to tidal straining theory for a progressive Kelvin wave, offshore surface currents occur from LW to HW. Accordingly, a plume would have reached its maximum offshore extent at HW. After HW surface velocities are onshore and the plume starts to move onshore again, so that the plume reattaches to the coast at LW. The observed presence of cold upwelled water between HW and the subsequent slack could therefore be caused by upwelling induced by tidal straining (as described above and summarized in Fig. 5.2).

Fig. 5.7 shows that the period under consideration shows a strong diurnal inequality. Only the larger HW at noon is captured with the SST data, the lower HW at midnight occurs

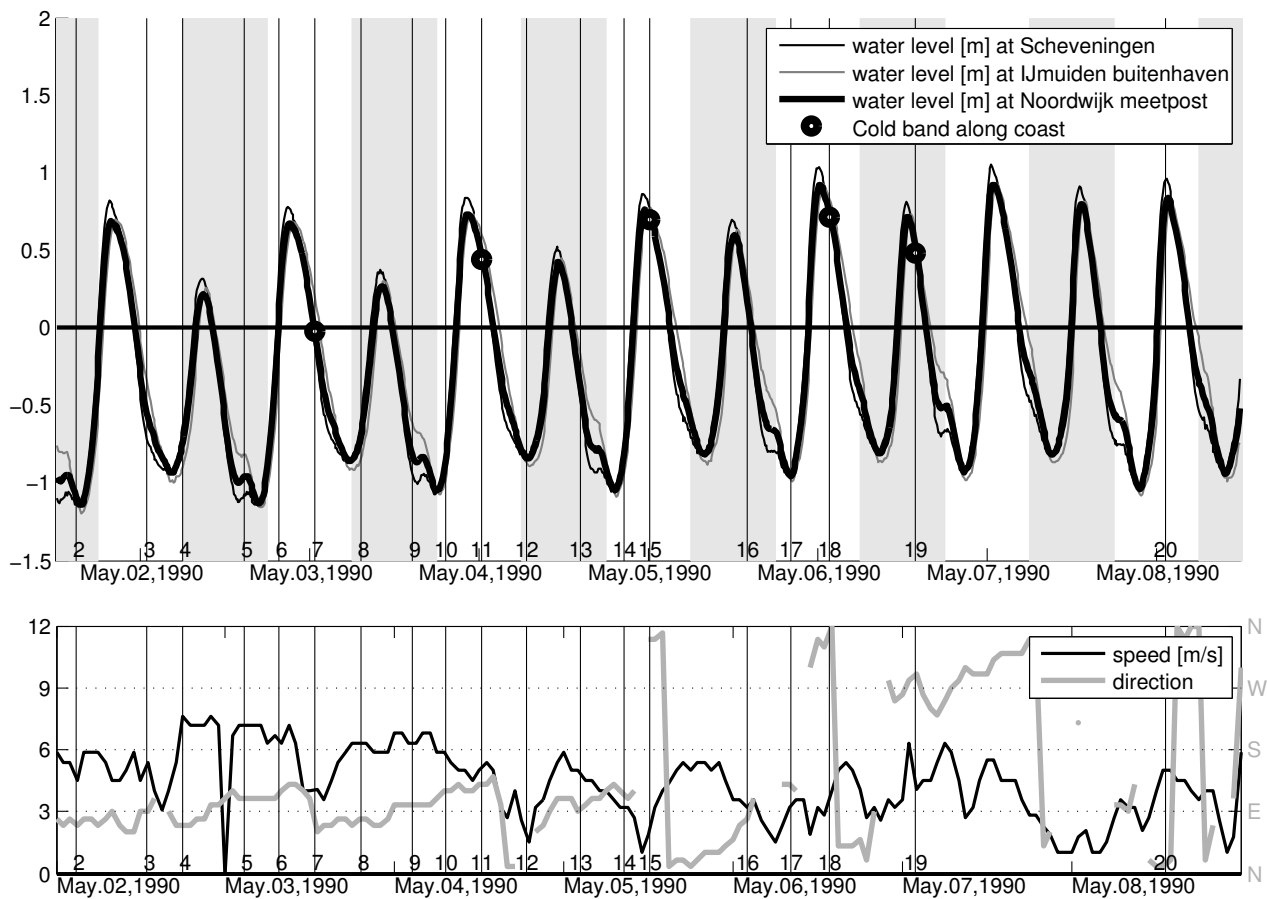


**Figure 5.7:** Upper panel: plume displacements and timing of tidal wave at the three water level stations the positions of which are shown in Fig. 5.1. The vertical lines indicate the times of the satellite passes, the numbers at their base correspond with the image numbers in Fig. 5.3. The light gray vertical bars indicate the nights (for clarity plotted from 6:00 to 18:00, while the actual night time was from 20:00 to 5:00). At the times of the five black dots a clear band of cold water is observed near the coast, indicating upwelling. Lower panel: wind in May 1990 in station Noordwijk meetpost (Fig. 5.1).



between two passes at night. Upon closer inspection the lower midnight HW on May 7th 1:54 also seems to have a long and small band of cold water near the coast. The presence of the cold water wedge between the bulge and the coast as discussed before obscures the presence of this upwelling filament. In addition, the southern part of this filament has been flagged off as cloud edge, probably due to the strong temperature gradients involved with this very upwelling event.<sup>1</sup> In contrast, the northern part of the filament extending to Texel inlet is clearly colder and is indicative of upwelling induced by tidal straining.

Finally, it should be noted that due to the 12.5 hour period of the dominant M2 tide, the moment of HW shifts gradually from early in the morning at May 2nd to past noon at May 8th. Therefore the image at noon May 2nd does not show a cold band, while the other images do show a cold band at noon.

The width of the observed upwelling band is 5 - 10 km. The upwelling band edge is everywhere less than 10 km from the coast. Inactive pixels directly along the coastline have to be subtracted from this distance. The first two to three pixels along the coastline are flagged off by atmospheric correction algorithm and due to the 2 km inaccuracy of the geometric correction. If the remaining 5 - 10 km band is caused by tidal straining, the band width should correspond with typical tidal straining velocities. A simple scaling analysis shows that this is indeed the case. The maximum cross-shore displacement can be calculated by integrating the cross-shore surface velocity over half a tidal cycle (from LW to HW). This gives the following expression for band width  $X$ :

$$X = \int_0^{T/2} U \sin\left(2\pi \frac{t}{T}\right) dt = \frac{UT}{\pi} \quad (5.1)$$

where  $U$  is the cross-shore surface velocity amplitude and  $T$  is the tidal period. With  $T = 12$  hour and an observed  $U = 0.4\text{ms}^{-1}$  (Visser *et al.* (1994), their Fig 2), this gives a surface displacement of 5.5 km. This value is within the 5 - 10 km range of the observed band width. The width of the upwelling band also corresponds to cross-shore differential displacements calculated with observed velocity data by Simpson & Souza (1995). They mention a relative displacement of the surface versus the bottom layer of 7 km.

### 5.3.3 Modeled downstream coastal buoyancy current

If the upwelling bands at HW in Figs. 5.5 and 5.6 are indeed caused by tidal straining, a numerical model of the Rhine ROFI should be able to reproduce them. The results from the numerical simulation (Fig. 5.8) indeed show the existence of a long and narrow coastal upwelling band induced by tidal straining. Furthermore, a cross-section of the crossshore velocities at slack water (Fig. 5.9), exhibits the characteristic cross-shore exchange current, in accordance with

---

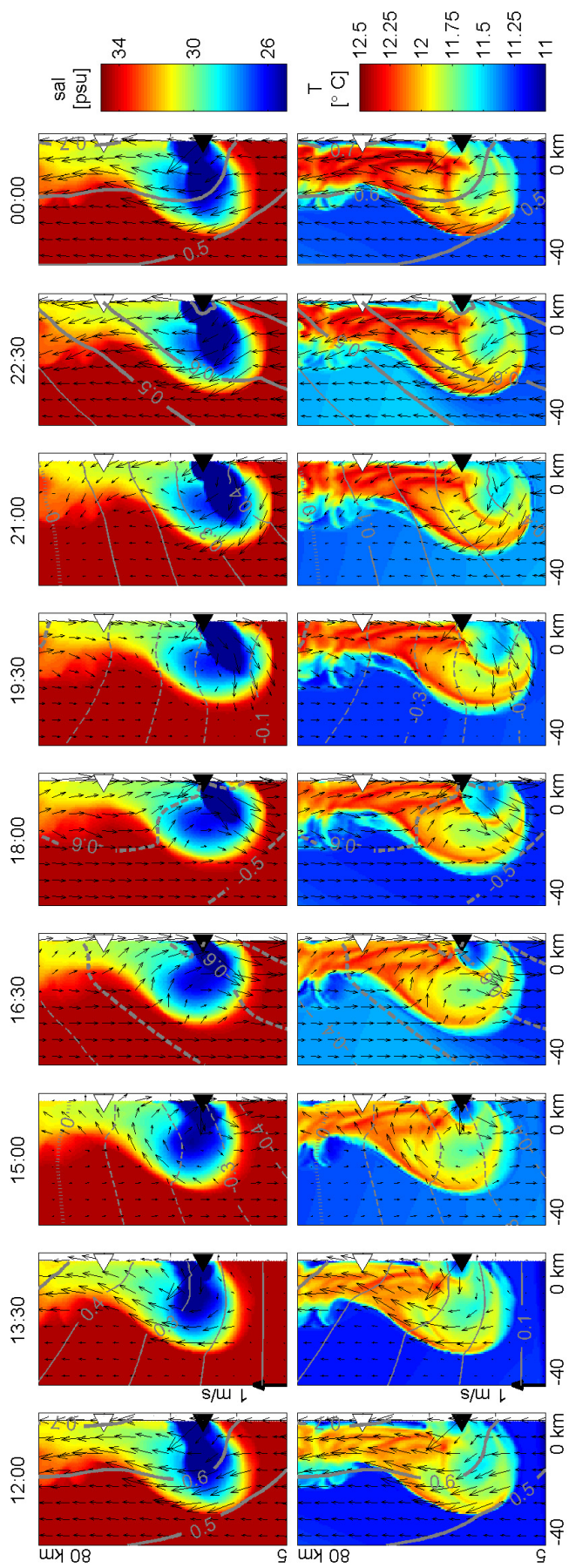
1. These pixels are along a satellite pixel scan line, the direction of which can also be seen in the erroneous pixels in image 9 of Fig. 5.3.

tidal straining theory. It is the upwelling induced by this exchange current that is responsible for the simulated band of cold water at HW. The model results also agree with the results that Souza & James (1996) obtained with a two-dimensional cross-shore slice model.

The timing of the modeled upwelling is also consistent with the SST observations according to tidal straining theory. The model shows a long and narrow band of upwelling at HW (12:00). Remnants of this band are still visible at slack before HW (21:00) and slack after HW (15:00). Subsequently, the band completely vanishes at LW (18:00), but appears again one tidal cycle later (00:00). However, it should be noted that the modeled width of the upwelling band is about 2 - 3 km, which is lower than the 5 - 10km band observed in the SST images. However, given the simplifications used in the idealized modeling of the Rhine ROFI, which neglects the actual bathymetry and tidal asymmetry present in the Dutch coastal zone, as well as the observed wind forcing, we believe the existence of an upwelling band in the model, as well as its timing, supports our contention that the upwelling band observed in the SST sequence is caused by tidal straining.

---

**Figure 5.8 (on the next page):** Plan view mosaic of modeled surface salinity and surface temperatures (T) with surface velocity vectors overlaid. The gray lines indicate water levels at 10 cm intervals. Solid lines are above mean water, dashed lines are below mean water. Levels of 50 cm and above are plotted with thicker lines. HW is at 12:00 and 0:00, LW is at 18:00. The black triangle indicates the river mouth, the white triangle indicates the position of the transect shown in Fig. 5.9.



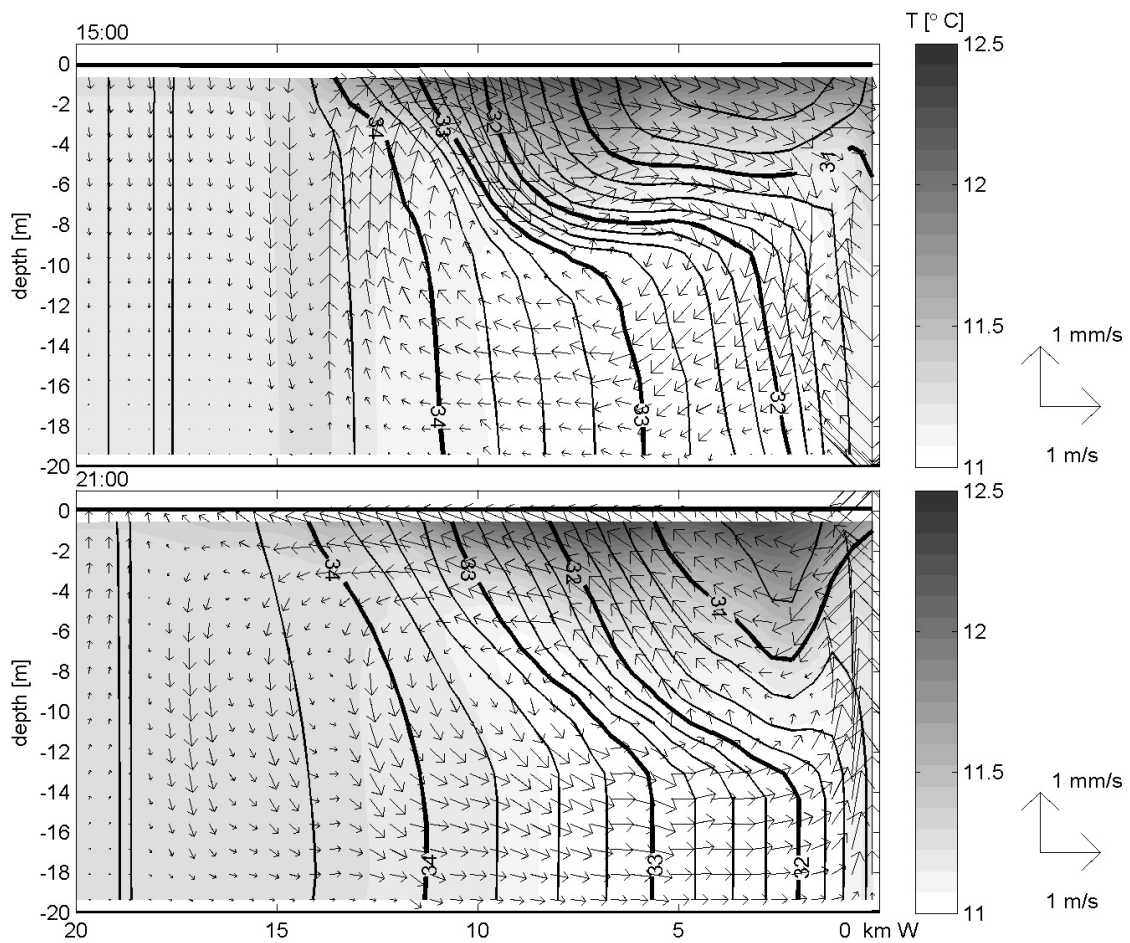


**Figure 5.9:** Cross-sections of model results in a transect 30 km north of the river mouth (see white triangle in Fig. 5.8) showing downwelling at slack between HW and LW (15:00) and upwelling at slack between LW and HW (21:00) (see also Fig. 5.8). The isolines depict levels of salinity.

### 5.3.4 Role of near shore mixing and offshore winds

Here consideration is given to the role of near shore mixing and offshore winds on the observed bands of colder coastal water. The cold band of water appears in the shallowest zone of the Rhine ROFI. However, it is unlikely that the semi-diurnal appearance of the cold band is due to the quarter-diurnal tidal variations in mixing. If mixing were indeed responsible for a cold band at HW, the cold band should also be present at or after maximal ebb mixing. However, images 10 and 14 (Fig. 5.3) do not show a cold band although their timing is directly after LW (Fig. 5.7). Furthermore, these shallow regions are continuously well mixed and are expected to show an increased response to surface heat fluxes due to their limited heat capacity. According to De Kok *et al.* (2001), this is the case for depths shallower than 7 m. Indeed, some of the most coastward pixels are actually warmer than the central plume water in the upwelling images (Figs. 5.5 and 5.6). This is not the case in the entire coastal zone because the two or three pixels closest to the coast are flagged off due to geopositioning inaccuracies and beach blinding. The 10 and 15 m isobaths included in Figs. 5.5 and 5.6 indicate that there are hardly any pixels at depths shallower than 10 m.

In order to investigate the role of wind a simulation was carried out in which the model was forced with a steady offshore easterly wind of  $7 \text{ ms}^{-1}$ . The results from this simulation, Fig. 5.10, indicate that offshore winds cause a response as suggested by Fong & Geyer (2001). The bulge and coastal current are both displaced northwards alongshore. However, the existence, timing and width of the upwelling band are only marginally altered by the easterly winds. These alongshore displacements caused by the wind are basically independent from the upwelling induced by cross-shore tidal straining. Hence the prevailing winds do not alter our conclusions regarding the upwelling induced by tidal straining. The easterly winds do lead to significantly higher plume temperatures though. This is due to the wind-dependent heat transfer coefficient and any change in the plume thickness.

Note also that the cold water band cannot be caused by upwelling favorable NE winds. Fig. 5.7 shows that the winds during this period were typically easterly to SE, with a small period of NE winds. It is unlikely that a short-term directional variation in the wind could cause the sudden upwelling event at noon, and then make it disappear again a few hours later. The bulge discussed previously shifts only 25 km north in 5.5 days due to the wind. The same applies to the modeled effect of wind on the plume (Fig. 5.10). Accordingly, short wind gusts with small changes in direction cannot cause a 10 km offshore movement in just 6 hours.

The timing of the observations, as well as the band width of the upwelling region and the consistent model results, lead us to conclude that the semi-diurnal appearance of a band of cold water in the SST imagery is caused by upwelling induced by tidal straining.



## 5.4 Discussion

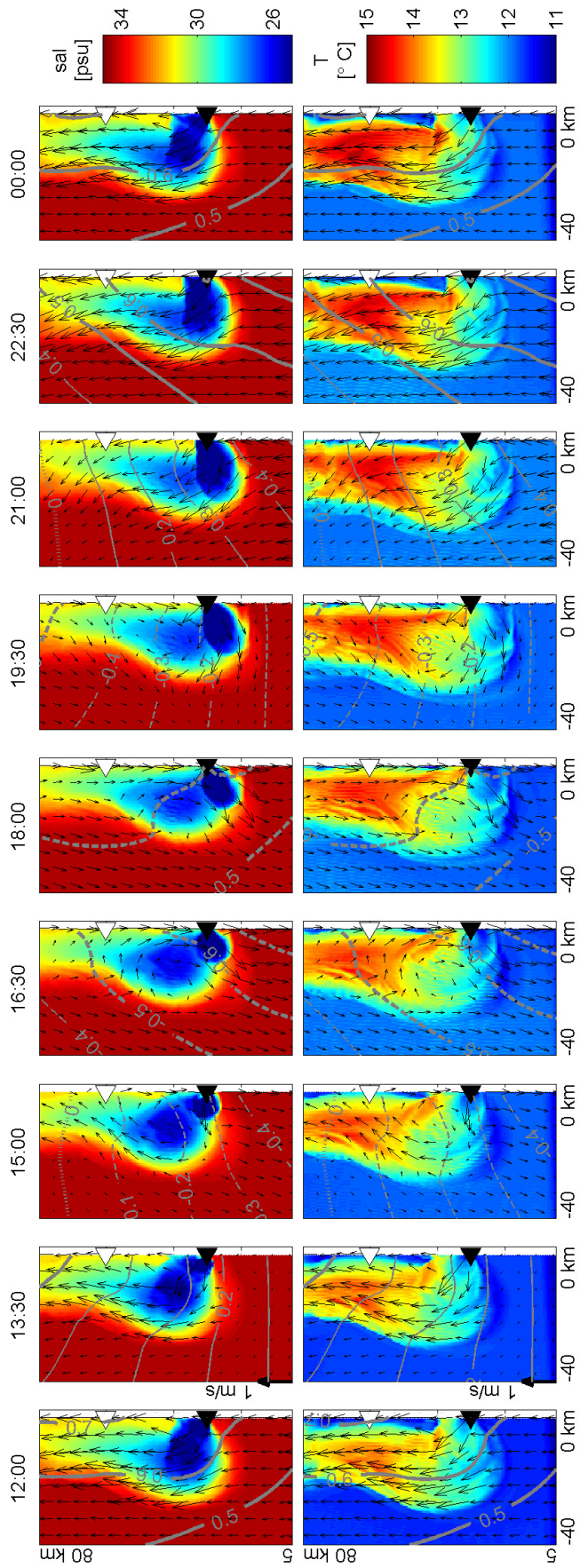
In this paper, we used a 6-day series of SST images with a high temporal resolution to detect a tidal straining signature in the Rhine ROFI. A unique sequence of SST images in May 1990 was found. It shows a ROFI that is much warmer than the surrounding water that exhibits a distinct and strong diurnal solar heating response and is clearly delineated by large spatial temperature gradients at the edges. These observations indicate that the whole ROFI area is stratified. In accordance with expectations, the series clearly reveals a semi-diurnal upwelling pattern. On 3 consecutive mid-days during neap tide, a 10 km wide and 100 km long band of water appeared between the coast and the ROFI. This water has the same temperatures as the surrounding well-mixed ambient water.

The band is observed between HW and the subsequent slack tide. This timing is in accordance with tidal straining theory as developed and treated by (Simpson & Souza, 1995; Simpson, 1997; Souza & Simpson, 1997; Fisher *et al.*, 2002) that allows for upwelled water at the surface from slack before HW to slack after HW. In addition, the cold water band was not present the morning before, and it has completely disappeared at the end of the afternoon. A similar narrow band was also observed once during HW at night. This example is less apparent though, due to the decreased temperature differences between the ROFI and the southern North Sea after the nightly cooling. The few nightly images with the correct timing do not show upwelling due to the absence of a temperature contrast. At the end of the SST series the ROFI is mixed up due to the onset of springs. Accordingly, the noon image does not show tidal straining any more. The same semidiurnal upwelling was also observed in an idealized river plume in a numerical model. This corroborates our conclusion that the upwelling is induced by tidal straining. To our knowledge this is the first time that the large spatial extension of tidal straining and associated upwelling has been observed. Until now evidence of tidal straining in the Rhine ROFI has only been observed directly with fixed arrays measuring over the water depth at a few locations and indirectly with spatial patterns of currents ellipses measured with HF Radar (Simpson *et al.*, 1993; Visser *et al.*, 1994; Simpson & Souza, 1995; Souza & Simpson, 1996, 1997; Simpson, 1997).

Typically, only cross-shore shear has been considered in tidal straining theories of the Rhine ROFI. This has helped to elucidate the dominant role of the tidal straining mechanism in the Rhine ROFI. Indeed, the long narrow upwelling region observed in the SST images indicates the dominance of this cross-shore mechanism. However, the analysis of the bulge region indicates that alongshore tidal straining and advection could also play an important role in the dynamics

---

**Figure 5.10 (on the next page):** Plan view mosaic of modeled surface salinity and surface temperatures ( $T$ ) with constant  $7 \text{ ms}^{-1}$  easterly winds. For explanation, see caption Fig. 5.8. Note the pronounced effect of the wind dependent heat adsorption coefficient, yielding much higher plume temperatures than in the case with no wind (Fig. 5.8).





of the Rhine ROFI, even though the average alongshore density gradients have been shown to be negligible (De Ruijter *et al.*, 1997). The pinched off bulge inside the ROFI persists for tens of kilometers from the river source. Similar long-lasting stratified fresh water pulses were observed in alongshore cruises (De Ruijter *et al.*, 1997). The patchy SST data therefore indicate the need for further research regarding the importance of alongshore tidal straining in ROFIs.

The wind and straining events captured nicely in the May 1990 Rhine plume sequence teach us to treat single coastal SST images with great precaution. Whenever possible, multiple images should be taken into account, preferably in combination with a three-dimensional numerical model. This is important, as an erroneous analysis of the origin of the cold water would also yield erroneous conclusions with respect to the (coastward) transport of nutrients, contaminants and fine sediments, to name a few. For example, the pinched off wedge of cold ambient water found in between the bulge and the coast is due to gradual northwards advection and stretching of the bulge at a small angle to the coast. When looking at the single SST image of May 7th 1:54, this pattern might be mistaken for upwelling. Similarly, when only looking at the image May 3rd 12:36, one might conclude that wind-driven upwelling takes place, whereas our analysis of multiple images shows that upwelling induced by tidal straining is the cause. The implications of upwelling induced by tidal straining are substantial. Upwelling induced by tidal straining is likely to have a significant influence on the local circulation. Upwelling affects not only the local stratification, but also brings nutrients and sediments to the surface every tidal cycle.

The SST data from the AVHRR instrument on board the NOAA satellites used in this paper were not designed for capturing tidal processes. The remote sensing system has been designed with the requirements to provide daily global coverage. The excess surface heating we use to infer information regarding stratification and tidal straining is actually only considered a nuisance for preparing composite SST images, and is generally removed (Roozkrans and Prangma, 1992). The fact that we showed its use in capturing an archetypical tidal straining event is a positive side-effect. Upwelling induced by tidal straining might also be visible with Ocean Color imagery. However, instruments like MODIS, MERIS and SeaWiFS have too low a temporal resolution to capture tidal processes. This can be remedied by using data from using multiple sensors, this has been attempted by Arentz (2005), Pietrzak *et al.* (2008b) for SeaWiFS and SST data.

Finally, it is recommended to use SST images to study ROFIs in areas with diurnal tides. This gives another incentive to extend the study to particular tropical ROFIs as suggested by Simpson (1997). The satellite revisit time is better suited to study their interesting features such as a marked seasonal discharge cycle with huge discharges and low Coriolis parameter. The SST images provide ample data for the calibration of three-dimensional numerical models of the coastal zone. Even if it would not be possible to reproduce these observations in detail, the present analysis of the Rhine ROFI has revealed a number of features such as tidal straining and associated coastal upwelling which should at least be reproduced qualitatively.

## Acknowledgements

The project is funded by the Dutch Organization for Scientific Research (NWO) in the ALW program within the framework of LOICZ-NL (ALW project number 014.27.006) whose support is gratefully acknowledged. We would like to thank the principal investigator, Dr. Herman Ridderinkhof from Royal Netherlands Institute for Sea Research (NIOZ), for a number of discussions. We thank Prof. John Simpson and one anonymous reviewer for their comments which substantially improved the manuscript. We would also like to thank Prof. Guus Stelling for valuable discussions on the numerical model. We are grateful to Loana Arentz and Walter Jacobs for the contribution they made during their MSc project on, respectively, the SST analyses and the numerical simulations. The tide and discharge data were made available on internet by the Dutch ministry of public works (RIKZ, the Hague, the Netherlands), the meteorological data by the Royal Dutch Met Office (KNMI, de Bilt, the Netherlands). Last but not least we are very grateful to KNMI setting up and maintaining an HRPT receiving station and Hans Roozkrans from KNMI in particular for providing the full archive of SST data.

## Appendix: warm upwelling band in autumn <sup>2</sup>

Due to the importance of the upwelling induced by tidal straining, we want to show here an additional, inverse example of UW induced by tidal straining. In autumn, stratified surface water cools down faster than well-mixed waters, such that the ROFI is visible on SST images as a region much cooler than the surrounding waters (Pietrzak *et al.*, 2008b). Under these circumstances upwelling induced by tidal straining should be visible as a warm band. In our example in Nov. 1993 (Figs. 5.11 and 5.12) a warm autumn UW band is visible around HW, just like the spring images (Figs. 5.3, 5.5, 5.6) that show a cold UW band. However, before concluding that this band is caused by tidal straining, any possible wind effects need to be excluded. The prevailing wind direction in this example is constantly South-Easterly (Fig. 5.13). In section 5.3.1 we showed that stratified plumes are in approximate Ekman balance with the Easterly winds using a simple balance from Fong & Geyer (2001). Hence Easterlies lead to a Northward movement of the ROFI, independent of any cross shore movements due to tidal straining. In section 5.3.1 the images indeed exhibited a Northward moving bulge moving North due to the Easterly winds. However, in this example no such bulge is present. Hence we cannot draw the conclusion that the plume would react similarly in this case. The plume might have a different stratified depth, due to which it might respond more frictional to the Easterly wind by moving offshore. However, if that were the case, it should exhibit a warm UW band in all the images. However, on image 6 and 9 (Fig. 5.11) the warm UW band is not present, so we can conclude that the Easterly winds are not causing any UW. Moreover, the Southerly wind components should lead to downwelling of the plume, whereas we see an UW band. Therefore we can conclude that this example also shows UW induced by tidal straining, and hence corroborates the tidal straining paradigm. In large scale ocean systems, upwelling is generally associated with a appearance of a cold band, due to the colder temperatures of deeper waters. However, this example shows that in coastal systems, upwelling is not necessarily linked to appearance of cold water masses.

---

2. This appendix was not part of De Boer *et al.* (2007).

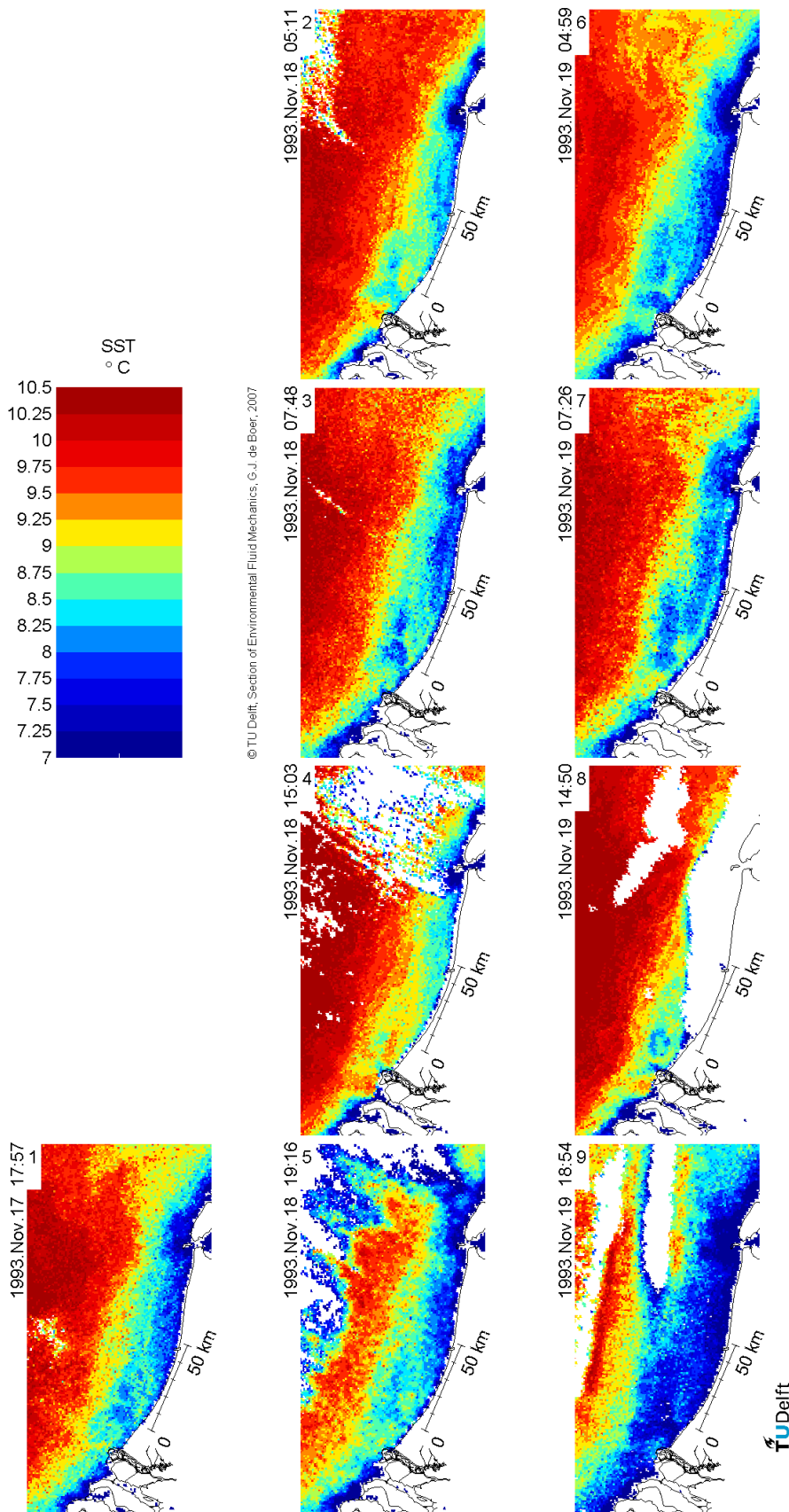


**Figure 5.11:** Plan view mosaic of plume SST in November 1993. The satellite images are numbered sequentially in the upper left corner of their panel. Image 2, 3 and 7 are approximately at HW (Fig. 5.13) and show a warm UW band, most clearly in image 7 (image 5 and 9 are also close to HW, but those are polluted by clouds).

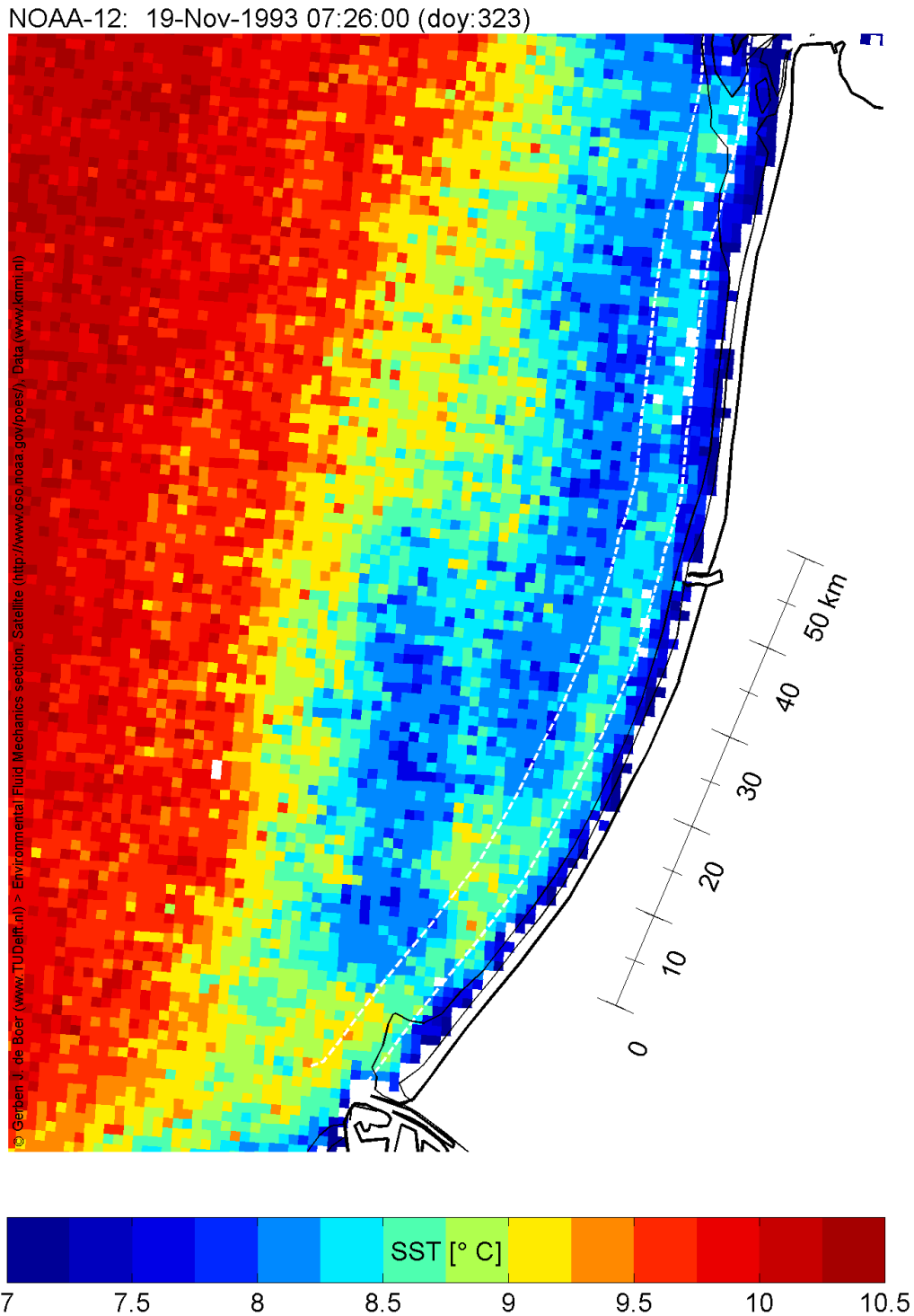


**Figure 5.12:** Enlargement of morning image 7 in Fig. 5.11 that clearly shows a 5 km wide upwelling band between 5 and 10 km offshore. The white dashed lines represent distances 5 and 10 km from the coast. They are included to be able to assess the width of the upwelling band. Note that the satellite pixels (that are individually visible) measure  $1 \times 1 \text{ km}^2$ . The thin black lines seawards of the coast are the 10 and 15 m isobaths.

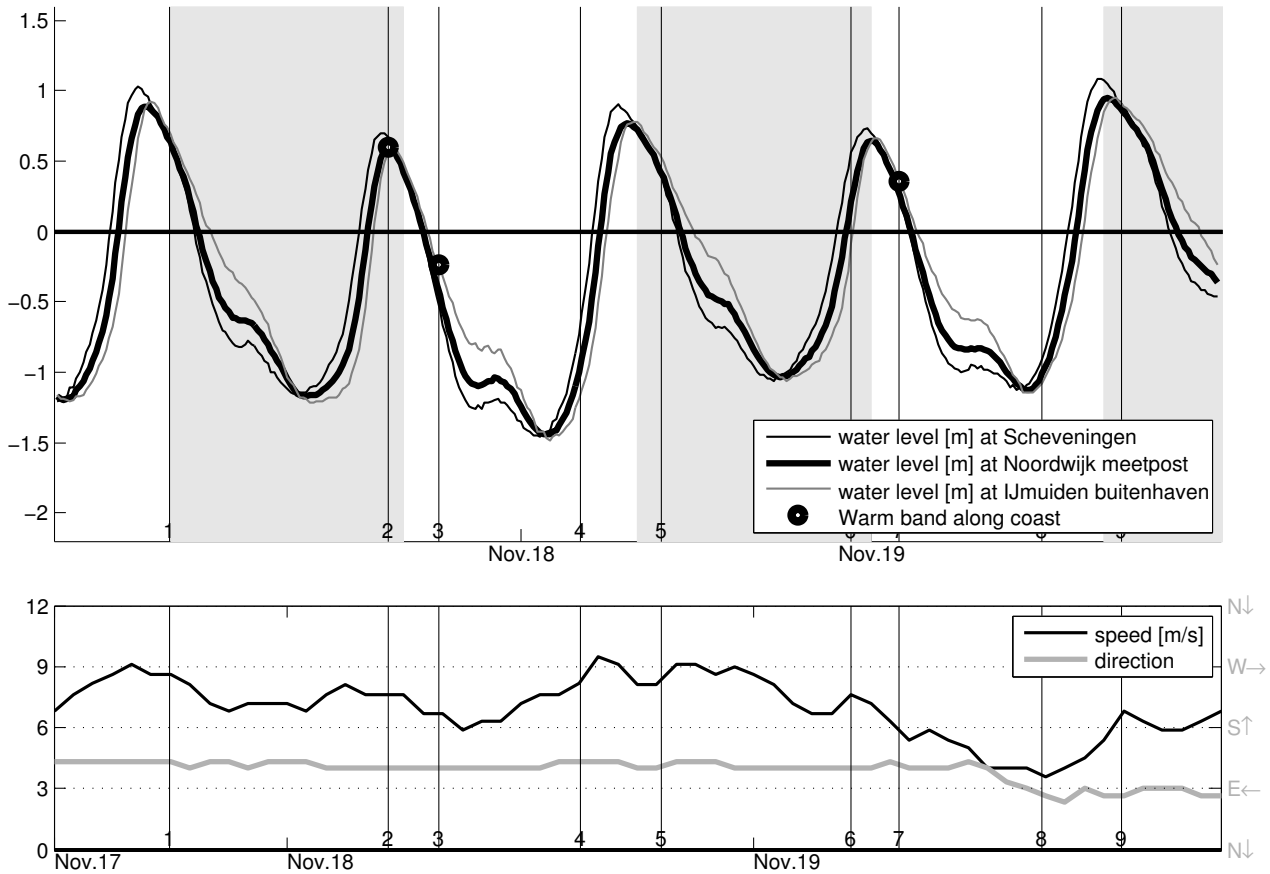


**Figure 5.13:** Upper panel: plume displacements and timing of tidal wave at the three water level stations the positions of which are shown in Fig. 5.1. The vertical lines indicate the times of the satellite passes, the numbers at their base correspond with the image numbers in Fig. 5.11. The light gray vertical bars indicate the nights (for clarity plotted from 6:00 to 18:00). At the times of the five black dots a clear band of warm water is observed near the coast, indicating upwelling. Lower panel: wind in November 1993 in station Noordwijk meetpost (Fig. 5.1) (Source: KNMI).





## Chapter 6

# The potential energy anomaly equation and ASIPS

This chapter has been published as : de Boer, G.J., Pietrzak, J.D., & Winterwerp, J.C. 2008. *Using the potential energy anomaly equation for tidal straining and advection of stratification in a ROFI. Ocean Modeling*, **22**(1-2), 1–86. doi:10.1016/j.ocemod.2007.12.003.

### Abstract

In this paper we derive the potential energy anomaly equation suitable for the analysis of three-dimensional numerical models. We apply this equation to the results of an idealised numerical model simulation of the Rhine River Plume and demonstrate how we can use the potential energy anomaly equation to analyse the physical processes affecting stratification, in this region of freshwater influence (ROFI). For this test case, we use the 10 terms from the potential energy anomaly equation that dominate the evolution of stratification in the Rhine ROFI. The principal terms are the cross-shore and along-shore straining and cross-shore and along-shore advection of horizontal density gradients. In addition non-linear shear dispersion terms representing correlations between density and velocity perturbations over the vertical control horizontal exchange and mixing in the cross-shore and along-shore directions. Moreover, in the vertical direction two terms dominate the vertical exchange processes: a term describing the effect of vertical mixing on the density profile, and a term related to up and downwelling. Analysis of the model results using the potential energy anomaly equation allows us to present a detailed overview of the spatial distribution of the terms affecting the evolution of stratification in the Rhine ROFI. The results highlight the important role of cross-shore tidal straining in the downstream coastal current region of the plume. In addition, the roles of alongshore straining, as well as along-shore and cross-shore advection in the Rhine ROFI, in particular in the region of the bulge near the river mouth, are also of importance. The results for the Rhine ROFI show that the potential energy anomaly equation provides a powerful tool with which to analyse the mechanisms contributing to mixing and stratification in coastal seas and estuaries.

## 6.1 Introduction

Coastal systems are dominated by regions of freshwater influence (ROFI); a term adopted by Simpson *et al.* (1993). The concept of tidal straining, introduced by Simpson *et al.* (1990), plays an important role in the dynamics and mixing of estuaries and ROFIs. Here, we are concerned with the competing influences that increase the stratification in coastal seas and estuaries and those that mix the water column, and in diagnosing the physical mechanisms contributing to this process.

Potential energy arguments have been found to be an excellent means with which to study the competing influences of stratification and mixing. Simpson & Hunter (1974) used them to investigate the position of fronts in the Irish Sea and in so doing, derived their widely used criterion to predict the occurrence of fronts and stratification in shelf seas. Following Simpson *et al.* (1978) and Simpson (1981), Simpson & Bowers (1981) considered changes in potential energy relative to the mixed condition and defined a scalar parameter  $\varphi$ , the potential energy anomaly,

$$\varphi = \frac{1}{H} \int_{-h}^{\eta} (\bar{\rho} - \rho)gzdz \quad (6.1)$$

where  $\rho$  is the vertical density profile over the water column of depth  $H$ , given by  $H = \eta + h$ ,  $\eta$  the free surface,  $h$  the location of the bed,  $\bar{\rho}$  the depth averaged density,  $z$  the vertical coordinate and  $g$  the gravitational acceleration. For a given density profile,  $\varphi$  ( $\text{Jm}^{-3}$ ) represents the amount of work required to bring about complete vertical mixing per unit of volume. In the absence of source and sink terms such as surface heating, stirring and rain, the time rate of change of  $\varphi$  has been described as

$$\varphi_t \equiv \frac{\partial \varphi}{\partial t} = \frac{g}{H} \int_{-h}^{\eta} \frac{\partial (\bar{\rho} - \rho)}{\partial t} z dz \quad (6.2)$$

where  $t$  is time. This is the well known and widely used potential energy anomaly equation. The only differences in its application come about from the assumptions made concerning the equations for density.

Initially density was considered to be a function of one dimension, the vertical. Simpson & Bowers (1981) effectively used their horizontally homogenous 1D-model to investigate the seasonal evolution of shelf sea structure. However, Van Aken (1986) was the first to incorporate effects of horizontal differential advection, as proposed by de De Ruijter (1983), into the potential energy anomaly equation. He showed the important role played by differential advection on the onset of seasonal stratification in shelf seas.

The effect of differential advection was further explored by Simpson *et al.* (1990) who derived the concept of tidal straining for estuarine-like sites. They substituted a simplified density equation in which they only considered advection in one horizontal direction ( $x$ ). They also assumed that the density gradient, in that direction, was independent of depth. This approach yields their classic tidal straining equation,

$$\frac{\partial \varphi}{\partial t} = \frac{g}{H} \frac{\partial \bar{\rho}}{\partial x} \int_{-h}^{\eta} (u - \bar{u}) z dz \quad (6.3)$$

in which the velocity  $u$  has been decomposed into a depth averaged value  $\bar{u}$  and a deviation from this value  $\tilde{u} = u - \bar{u}$ . The importance of this equation is that it describes the deformation of a vertically uniform, horizontal density gradient, by a velocity shear in one direction. The velocity shear acts upon the depth integrated horizontal density gradient to induce vertical stratification, as illustrated in Fig. 6.1. In Liverpool Bay the main tidal shear is in the same direction as the density gradient. This allowed ready application of the tidal straining paradigm to this semi-enclosed sea.

Simpson *et al.* (1990) elegantly show how differential advection by a vertical velocity shear act-

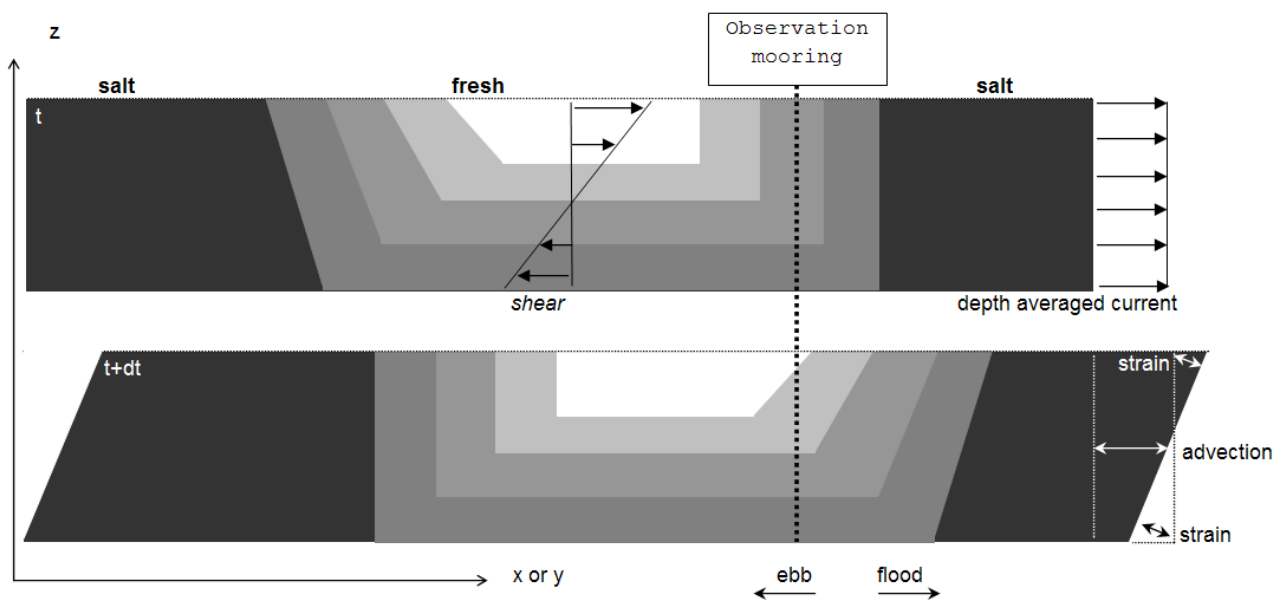


**Figure 6.1:** A sketch of the combined effects of tidal straining and advection. Tidal straining causes the deformation of a depth averaged horizontal density gradient by a velocity shear, whereas advection describes the displacement of a low salinity structure (implying a vertical variation of the horizontal density gradient) by the depth averaged current without deformation. At a fixed mooring an observed increase in stratification can thus be caused by both advection and straining, in either  $x$  or  $y$  direction. The two processes have opposite effects on the opposite sides of the ROFI.

ing upon a depth independent horizontal density gradient can be used to explain the oscillation of the stability of the water column. They demonstrated how tidal straining contributed to the semi-diurnal episodes of haline stratification observed within Liverpool Bay in the Irish Sea. In this way they demonstrated that strain induced periodic stratification (SIPS) was a dominant process in estuaries and coastal seas with large horizontal gradients of density. Since then tidal straining has been observed in a wide variety of estuarine and coastal systems, for example, the York River estuary (Sharples *et al.*, 1994), San Francisco Bay (Stacey *et al.*, 1999), the Columbia River (Jay & Smith, 1990) and the Hudson River (Nepf & Geyer, 1996).

Simpson & Souza (1995) applied the same concept to the Rhine ROFI where the situation is more complicated. Here, the tide has the nature of a propagating Kelvin wave, where the main tidal currents are along-shore whereas the main density gradient is cross-shore. Although semi-diurnal oscillations in the stratification were already observed here by Simpson *et al.* (1993), the configuration of the site did not allow for ready explanation of the oscillations with tidal straining. Subsequently, Visser *et al.* (1994) found that the Rhine ROFI can exhibit also a strong semi-diurnal cross-shore exchange current. During periods of stratification the surface tidal currents become anti-cyclonic with ellipticities of up to 40%, while bottom currents become cyclonic. Simpson & Souza (1995) were the first to realize that tidal straining in the Rhine ROFI consists of this periodic cross-shore velocity shear interacting with the average cross-shore density gradients. As such they were able to explain the semi-diurnal oscillations in stratification by applying the tidal straining concept in the cross-shore direction only. Consequently, from LW to HW the surface currents are directed offshore, due to horizontal differential advection the plume advects offshore and is maximally stratified at HW. From HW to LW the surface currents are onshore. Hence straining now causes the plume to be closest to the coast and nearly well-mixed at LW.

However, if one re-examines the Rhine ROFI observations of the semi-diurnal oscillation in stratification (Figs. 6 + 8 of Simpson & Souza (1995)), and simulations (Fig. 2 of Souza & James (1996)) there is evidence of along-shore processes. The data actually show a small phase lag of about one eighth of a tidal period between the time of maximum stratification and HW. Maximum stratification does not occur precisely at HW, as predicted by cross-shore tidal straining. Additionally, the maximum cross-shore displacements (Fig. 6 of Simpson & Souza (1995)) occur significantly earlier than the maximum stratification. If one imagines that the stratification were governed by alongshore straining alone, then maximum stratification would occur at slack tide, with a delay of a quarter of a wave period. The delay of one eighth of a wave period suggests almost equal contributions of along-shore and cross-shore effects.

Conversely, Van Alphen *et al.* (1988) attributed observed semi-diurnal oscillations to along-shore advection only, which has exactly the same timing as along-shore straining. However, re-examination of their velocity and stratification data (their Fig. 11) shows that maximum stratification does not occur at slack, as it would if only along-shore advection were present, but well before slack. In addition, at the next slack the water-column is not well-mixed, but already exhibits the onset of re-stratification, indicating the presence of cross-shore straining. Summarizing, the data set used to indicate cross-shore straining, exhibits along-shore effects, while the data set used to show along-shore processes, displays cross-shore effects. Therefore, it seems worthwhile to investigate other tidal straining configurations and tidal advection.

The importance of the  $\varphi_t$  equation for studies of stratification and mixing in shelf seas has been demonstrated over the past few decades; from simplifications that led to a criterion for the prediction of the location of fronts to the acknowledgement of the role of tidal straining in coastal seas. However, with the widespread use of numerical models in studies of coastal and ocean processes, there is a need to derive the complete potential energy anomaly equation suitable for the analysis of three-dimensional flows. Therefore, in this paper we derive this new  $\varphi_t$  equation. In order to achieve this, all of the terms arising from the three dimensional density equation and its respective depth integrated density equation are retained. We then use an idealised numerical model simulation of the Rhine ROFI and demonstrate the diagnostic powers of the  $\varphi_t$  equation. For this test case ten terms dominate the equation. We use the results of the analysis of the  $\varphi_t$  terms to gain further insight into the processes causing mixing and stratification in the Rhine ROFI. Finally, the advantages of applying the potential energy anomaly equation as an analysis tool for ocean modellers are discussed.

## 6.2 Derivation of the potential energy anomaly equation

In the spirit of Simpson *et al.* (1990), we derive the potential energy anomaly equation suitable for three-dimensional flows. Our starting point is the Reynolds averaged advection-diffusion equation for density with sources and sinks given by,

$$\frac{\partial \rho}{\partial t} = -u \frac{\partial \rho}{\partial x} - v \frac{\partial \rho}{\partial y} - w \frac{\partial \rho}{\partial z} - \frac{\partial \langle \rho' u' \rangle}{\partial x} - \frac{\partial \langle \rho' v' \rangle}{\partial y} - \frac{\partial \langle \rho' w' \rangle}{\partial z} + Q(x, y, z, t) \quad (6.4)$$

where  $x$  and  $y$  refer to the cross-shore and along-shore direction, respectively, and  $u$ ,  $v$  and  $w$  are the cross-shore, along-shore and vertical velocity. All other terms retain their previous definition. Here  $\langle \rho' u' \rangle$ ,  $\langle \rho' v' \rangle$  and  $\langle \rho' w' \rangle$  are the turbulent flux of mass in the  $x$ ,  $y$  and  $z$  directions and  $Q(x, y, z, t)$  represents the modification of density due to sources/sinks of temperature and/or salinity (e.g. O'Donnell (1993)). It should be noted that Burchard & Hofmeister (2008) independently derived a similar set of equations; their derivation contains a more rigorous derivation of the  $Q$  terms.

Integrating Eq. 6.4 over depth, the depth integrated density equation is given by,

$$\frac{\partial \bar{\rho} H}{\partial t} + \frac{\partial \bar{u} \bar{\rho} H}{\partial x} + \frac{\partial \bar{v} \bar{\rho} H}{\partial y} = -\frac{\partial \bar{\tilde{u}} \bar{\rho} H}{\partial x} - \frac{\partial \bar{\tilde{v}} \bar{\rho} H}{\partial y} - \langle \rho' w' \rangle|_s + \langle \rho' w' \rangle|_b + \bar{Q} \quad (6.5)$$

with  $\bar{\rho} = \frac{1}{H} \int_{-h}^{\eta} \rho dz$ ,  $\bar{u} = \frac{1}{H} \int_{-h}^{\eta} u dz$  and  $\bar{v} = \frac{1}{H} \int_{-h}^{\eta} v dz$  the depth averaged values. The first and second terms on the right hand side are shear dispersion terms,  $\langle \rho' w' \rangle|_s$  and  $\langle \rho' w' \rangle|_b$  are the surface and bottom density flux,  $\bar{Q}$  is the depth integrated source/sink term and  $\tilde{u} = u - \bar{u}$ ,  $\tilde{v} = v - \bar{v}$  and  $\tilde{\rho} = \rho - \bar{\rho}$  are the deviations from the depth mean values.

We substitute the density equations, Eqs. 6.4 and 6.5, into the following equation for the time rate of change of  $\varphi$ ,

$$\frac{\partial \varphi}{\partial t} = \frac{g}{H} \int_{-h}^{\eta} \frac{\partial (\bar{\rho} - \rho)}{\partial t} z dz - \frac{\varphi}{H} \frac{\partial H}{\partial t} - \left( \frac{g}{H} \right) \left( \tilde{\rho}(\eta) \eta \frac{\partial \eta}{\partial t} \right) \equiv \varphi_t \quad (6.6)$$

where  $\tilde{\rho}(\eta)$  is the perturbation density at the free surface. Retaining only the first term on the right hand side results in the well known potential energy anomaly equation, Eq. 6.2. However, in the differentiation of Eq. 6.1, we choose to retain two extra terms on the right hand side. Although typically small, we retain them for completeness. They represent barotropic effects due to depth and surface elevation changes with time, respectively. As such they would be important in the case of a lake filling, for example, and are consistent with retaining source and sink terms on the right hand side of Eqs. 6.4 and 6.5.

Substituting into Eq. 6.6 results in the potential energy anomaly equation suitable for the analysis of three-dimensional flows

$$\frac{\partial \varphi}{\partial t} = \frac{g}{H} \int_{-h}^{\eta} \left( \begin{array}{l} \tilde{u} \frac{\partial \bar{\rho}}{\partial x} + \bar{u} \frac{\partial \tilde{\rho}}{\partial x} + \tilde{u} \frac{\partial \tilde{\rho}}{\partial x} - \frac{1}{H} \frac{\partial \bar{\tilde{u}} \bar{\rho} H}{\partial x} + \frac{\partial \langle \rho' w' \rangle}{\partial x} + \dots \\ \tilde{v} \frac{\partial \bar{\rho}}{\partial y} + \bar{v} \frac{\partial \tilde{\rho}}{\partial y} + \tilde{v} \frac{\partial \tilde{\rho}}{\partial y} - \frac{1}{H} \frac{\partial \bar{\tilde{v}} \bar{\rho} H}{\partial y} + \frac{\partial \langle \rho' v' \rangle}{\partial y} + \dots \\ w \frac{\partial \rho}{\partial z} - \frac{1}{H} (\langle \rho' w' \rangle|_s - \langle \rho' w' \rangle|_b) + \frac{\partial \langle \rho' w' \rangle}{\partial z} \end{array} \right) z dz - \frac{\varphi}{H} \frac{\partial H}{\partial t} - \frac{g}{H} \left( \tilde{\rho}(\eta) \eta \frac{\partial \eta}{\partial t} \right) \quad (6.7)$$

### 6.2.1 Description of the terms in the $\varphi_t$ equation

For easy notational purposes, we assign a two letter symbol to each term, that refers to the depth integrated terms in Eq. 6.7.

$$\begin{aligned}
\frac{\partial \varphi}{\partial t} = \frac{g}{H} \int_{-h}^{\eta} & \left( \underbrace{\tilde{u} \frac{\partial \tilde{\rho}}{\partial x}}_{S_x} + \underbrace{\tilde{u} \frac{\partial \tilde{\rho}}{\partial x}}_{A_x} + \underbrace{\tilde{u} \frac{\partial \tilde{\rho}}{\partial x}}_{N_x} + \underbrace{-\frac{1}{H} \frac{\partial \tilde{u} \tilde{\rho} H}{\partial x}}_{C_x} + \underbrace{w \frac{\partial \rho}{\partial z}}_{W_z} + \dots \right) z dz + \dots \\
& \left( \underbrace{\tilde{v} \frac{\partial \tilde{\rho}}{\partial y}}_{S_y} + \underbrace{\tilde{v} \frac{\partial \tilde{\rho}}{\partial y}}_{A_y} + \underbrace{\tilde{v} \frac{\partial \tilde{\rho}}{\partial y}}_{N_y} + \underbrace{-\frac{1}{H} \frac{\partial \tilde{v} \tilde{\rho} H}{\partial y}}_{C_y} + \underbrace{\frac{\partial \langle \rho' w' \rangle}{\partial z}}_{M_z} \right) z dz + \dots \quad (6.8) \\
& \int_{-h}^{\eta} \left( \underbrace{\frac{\partial \langle \rho' u' \rangle}{\partial x}}_{D_x} + \underbrace{\frac{\partial \langle \rho' v' \rangle}{\partial y}}_{D_y} - \frac{1}{H} \left( \underbrace{\langle \rho' w' \rangle|_s}_{D_s} - \underbrace{\langle \rho' w' \rangle|_b}_{D_b} \right) \right) z dz - \underbrace{\frac{\varphi}{H} \frac{\partial H}{\partial t}}_{B_H} - \underbrace{\left( \frac{g}{H} \right) \left( \tilde{\rho}(\eta) \eta \frac{\partial \eta}{\partial t} \right)}_{B_\eta}
\end{aligned}$$

$S_x$  and  $S_y$  are the cross-shore and along-shore straining terms; note  $S_x$  is the well known tidal straining term of Simpson *et al.* (1990), see Eq. 6.3. The terms  $A_x$  and  $A_y$  are referred to as advection terms. They describe the effect of advection of a vertical density structure by a depth mean current. For example, these terms account for a lens of fresh water displacing with the depth averaged current, without being deformed. The joint action of the  $A$  and  $S$  terms is illustrated in Fig. 6.1.

The third set of terms,  $N_x$  and  $N_y$ , describe the non-linear interaction between the deviation of both density and velocity over the vertical. These terms originate from the advection-diffusion equation for the density. Although they look similar to the  $A$  and  $S$  terms, we propose to consider them together with the fourth set of terms,  $C_x$  and  $C_y$ , that are dispersion terms, describing the effect of correlations over the vertical, between the velocity shear and the vertical variation of the horizontal gradient. These terms originate from the advection-diffusion equation for the depth averaged density. The terms  $C_x$  and  $C_y$  are just the depth averaged counterparts of  $N_x$  and  $N_y$ . The term  $M_z$  describes the effect of vertical mixing on the density profile,  $W_z$  is related to up and downwelling (UW/DW). The  $D_x$  and  $D_y$  terms are the horizontal depth averaged dispersion terms. The terms  $D_s$  and  $D_b$  are the surface density and bed density fluxes, respectively. The last two terms  $B_H$  and  $B_\eta$  are due to changes in the water depth or the surface elevation in time.

### 6.2.2 Method of analysis

The power of the potential energy anomaly analysis is that it can be applied both to the model output from a three-dimensional numerical model and to measured data, if available. We adopt two methods of analysis. The first is the time series method in which we simply calculate the instantaneous terms in Eq. 6.8, at a selected location and time step, and plot them. This tells us how the individual terms contributing to  $\varphi_t$  evolve within a selected time period. The second method is the covariance method. In this method the covariance between a term  $\alpha$  and  $\varphi_t$  is calculated as



$$\begin{aligned}
xcov(\alpha, \varphi_t) &= \sum_{i=0}^{N-1} [(\alpha(i) - avg(\alpha))(\varphi_t(i) - avg(\varphi_t))] \\
avg(\alpha) &= \frac{1}{N} \sum_{i=0}^{N-1} \alpha(i)
\end{aligned} \tag{6.9}$$

where  $\alpha$  represents the term in Eq. 6.8 under consideration,  $i$  is a time step counter and  $N$  the number of time steps. If one applies this method to model output, one can calculate the covariance at each grid point in the model and hence generate a time-invariant map showing the spatial distribution of the covariance terms. In contrast to plotting instantaneous values, the covariance method allows us to understand the processes contributing to the longer term evolution of the plume. One simply has to select the period and sampling frequency over which the covariance is calculated. In addition one can calculate correlations between terms and present them in the same way as the covariance.

### 6.3 Numerical model set-up and calculation of terms in $\varphi$ equation

In order to test the power of Eq. 6.8 as an analysis tool for ocean models, we re-examine the numerical model setup of de De Boer *et al.* (2006). This test case focuses on the evolution of the ROFI due to tides and river discharge; the effect of wind forcing is not considered here. The plume is modelled in a 20 m deep rectangular basin with a resolution of 500 m. The vertical is resolved with 16 equidistant sigma-layers. On the Southern boundary a Kelvin wave with a 12 h (S2) period is imposed with a 75 cm amplitude representative of neap tide.

A barotropic spin-up period of 2.5 days was used. Then the river was switched on and the model was spun up baroclinically for another 15 days, after which time the river plume reached a distance of 100 km downstream. In addition it is almost fully cyclic; that is after every semi-diurnal excursion the plume returned almost to the same state. After this 15 day simulation, the final 36 h simulation covering three tidal periods was performed. The results from this 36 h simulation were stored for subsequent analysis every 20 min and used to evaluate the terms in Eq. 6.8.

For the settings, results and detailed validation of the model set-up, refer to de De Boer *et al.* (2006). In Fig. 6.2 the order of events during one tidal cycle is shown. The river plume bulge displaces more than 10 km North-South, while the East-West movement is almost 5 km. Fronts are visible at all edges of the bulge, as well as around the fresher water blobs released from the river. The gradients are strongest at the side where the currents flow out of the river plume. The maximum gradients are about 2 PSU/km, whereas inside the plume the gradients are lower, 0.5 PSU/km, in agreement with the cruise data in van Van Alphen *et al.* (1988) and De Ruijter *et al.* (1997), respectively.

### 6.3.1 Description of terms in the Rhine ROFI test case

Here we consider which terms are important for our test case; the surface and bed density flux is zero. Furthermore we neglect horizontal diffusion, source and sink and barotropic terms, as they are negligible for the test case presented here. Hence in the following we only evaluate the remaining ten terms, as these are the terms that dominate, in our test example.

$$\varphi_t = \left( \begin{array}{cccccc} S_x & +A_x & +N_x & +C_x & +W_z & +\dots \\ S_y & +A_y & +N_y & +C_y & +M_z & \\ \underbrace{\hspace{1.5cm}}_{AS} & & & & & \end{array} \right) \equiv RHS \quad (6.10)$$

$$(S_x + A_x + S_y + A_y) \equiv AS$$

Eq. 6.10 comprises four terms that operate in the crossshore plane, four similar terms that operate in the alongshore plane and two terms that operate in the vertical. The symbol *RHS* is used to denote all terms on the right hand side, while the symbol *AS* is used to denote the subset of the four terms related to straining and advection only. Note, that  $\varphi_t$  is only approximately equal to the *RHS* for our test case due to the neglect of some small terms.

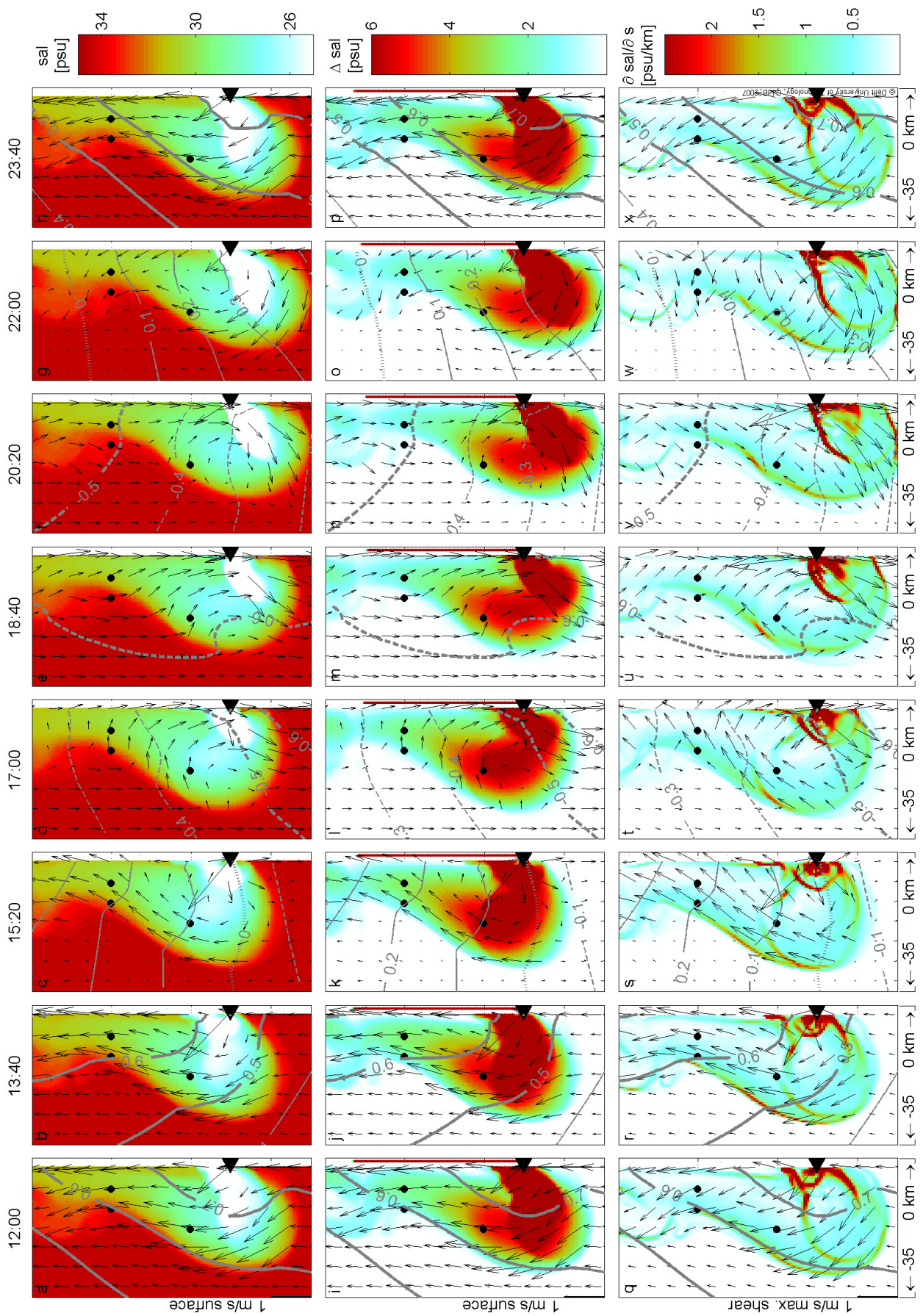
## 6.4 Results of the potential energy anomaly equation budget

### 6.4.1 Covariance distribution $\varphi_t$ and $\varphi_t$ predictors

The covariance between the individual terms or sums of terms in Eq. 6.10 and the  $\varphi_t$  signal is presented in Fig. 6.3. For this case  $N = 109$  in Eq. 6.9, equivalent to three tidal cycles sampled

---

**Figure 6.2 (on the next page):** Plan view showing the evolution of the river plume modelled by De Boer *et al.* (2006) during one tidal cycle. The black dots indicate the positions of the stations from which model time series have been extracted, as shown in Figs. 6.4-6.6. The gray lines indicate water levels at 10 cm intervals. Solid lines are above mean water, dashed lines are below mean water. Amplitudes of 50 cm and above are plotted with thicker lines. HW is at 12:00 and 0:00, LW is at 18:00. The black triangle ( $\blacktriangleleft$ ) indicates the river mouth ( $2000 \text{ m}^3 \text{ s}^{-1}$ ). The upper row (panels a to h) shows salinities in the surface model layer, the middle row (panels i to p) shows the difference between the surface and bottom salinities, the third row (panels q to x) shows the absolute value of the horizontal density gradient in the surface layer. Each column represents a snapshot every 1 h 40 min. Note a lens of fresh water being released from the river mouth at 13:40 (panel r). It grows concentrically with one side attached to the southern bulge edge (panel s-x, q-t) until it has finally merged with the NW bulge edge more than one tidal cycle later at 17:00 (panel t). Until 20:20 it is responsible for a patch with increased spatial salinity gradients at the seaward side of the coastal current (panel v).



every 20 min. Note that the magnitude of the covariance depends on the product of  $\varphi_t$  and the term under consideration. This implies that in regions where the covariance is negligibly small (white), either  $\varphi_t$  anomalies are small or the term under consideration does not contribute to  $\varphi_t$ . Therefore, the autovariance of  $\varphi_t$  ( $\propto \varphi_t^2$ ) can serve as a means for comparison. It shows that in the NE quadrant of the bulge and the (shoreward half of the) coastal current, directly adjacent to the coastal wall, variations in  $\varphi_t$  are relatively small. The largest  $\varphi_t$  variations are confined to the SSE bulge edge and NW bulge edge, at the transition between the bulge and the coastal current. The SW quadrant of the bulge, and the downstream part of the coastal current, have intermediate values of  $\varphi_t$ .



The covariance between the  $RHS$  ( $\sum_{RHS}$ ) and  $\varphi_t$  is nearly identical to the autovariance of  $\varphi_t$ . This allows us to conclude that the  $RHS$  gives a good representation of  $\varphi_t$ . This is further supported by the plot of the covariance of the residual ( $\epsilon_{RHS}$ ) which is calculated from  $\varphi_t - RHS$ . This term is negligible, except for some scatter in the near field, at the mouth of the estuary.  $AS$  has a similar covariance performance as the sum of the  $RHS$ . While there is a residual of  $AS$  ( $\epsilon_{AS}$ ) in the bulge region, it is relatively small compared to the amplitude of  $\varphi_t$ . Notably, in the coastal current the performance of  $AS$  is as good as that of the  $RHS$ . The similar performance of  $RHS$  and  $AS$  indicates that the sum of the other six terms largely cancels out. However, Fig. 6.3 shows that the other terms do matter because the covariances between these terms and  $\varphi_t$  are significant throughout the plume.

The single term with the most similar covariance to the  $\varphi_t$  signal is  $A_y$  (Fig. 6.3). The same maxima in the SSE and NW bulge region are apparent. However, the amplitude of  $A_y$  is too small to explain the full  $\varphi_t$  variation.  $S_y$  exhibits the same spatial pattern as  $A_y$ , albeit with a much smaller amplitude. Together with  $A_y$  it almost fully describes the  $\varphi_t$  signal.  $S_x$  is much smaller, except in one region located between 20 and 30 km North of the river mouth, the very region where the isohalines are coast parallel.

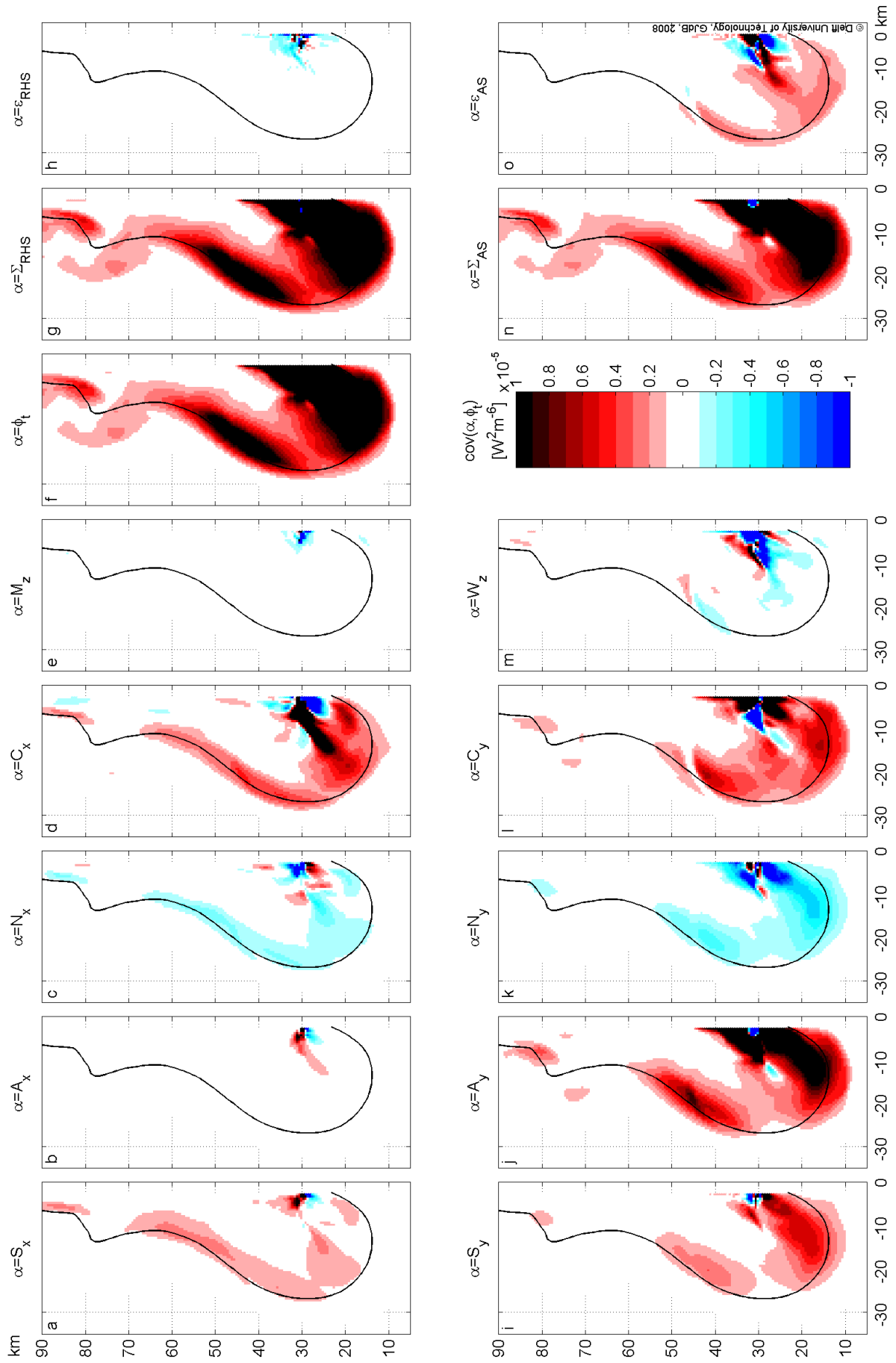
#### 6.4.2 $\varphi_t$ terms in the bulge and downstream locations

In this section we discuss the contribution of the individual terms in Eq. 6.10 to  $\varphi_t$ . In order to do this, time series of the individual terms have been calculated at three stations (see dots in Fig. 6.2); Station 1 in the NE bulge where  $A_y$  is dominant and Stations 2 and 3 30 km North of the river mouth in the region where  $S_x$  is dominant (Fig. 6.3). The latter two stations are located 6 and 11 km from the coast along a cross-shore transect. Despite their close proximity to one another, the three stations show distinctly different behaviour.

The time series from Station 1 in the NE bulge (Fig. 6.4) exhibits a strong semi-diurnal sinusoidal response, with a spike due to the advection of a lens of fresher water through the station. The trajectory of this discharge lens can clearly be observed in Fig. 6.2. While the terms  $C_y$ ,  $N_y$  and  $W_z$  are also large at this location, the full signal is well described by  $AS$ . At Station 2 the  $\varphi_t$  signal is dominated by a smooth semi-diurnal variation (Fig. 6.5). The biggest term is now the classic cross-shore straining term  $S_x$ . However, at Station 3 (Fig. 6.6) the terms contributing to  $\varphi_t$  are remarkably different. While  $S_x$  is large, it no longer explains the  $\varphi_t$  signal.

---

**Figure 6.3 (on the next page):** The covariance between the various terms in Eq. 6.10 and  $\varphi_t$  as calculated from Eq. 6.9. Panel f shows the (auto)variance of  $\varphi_t$  which is proportional to the squared amplitude.  $\sum_{RHS}$  indicates the  $RHS$  in Eq. 6.10,  $\epsilon_{RHS}$  indicates the unexplained residual  $\varphi_t - \sum_{RHS}$ ,  $\sum_{AS}$  indicates  $AS$  in Eq. 6.10 and  $\epsilon_{AS}$  indicates the unexplained residual  $\varphi_t - \sum_{AS}$ . The black line indicates the tidally averaged 32.5 PSU isohaline at the surface (averaged over the three 12 h tides of our simulation).



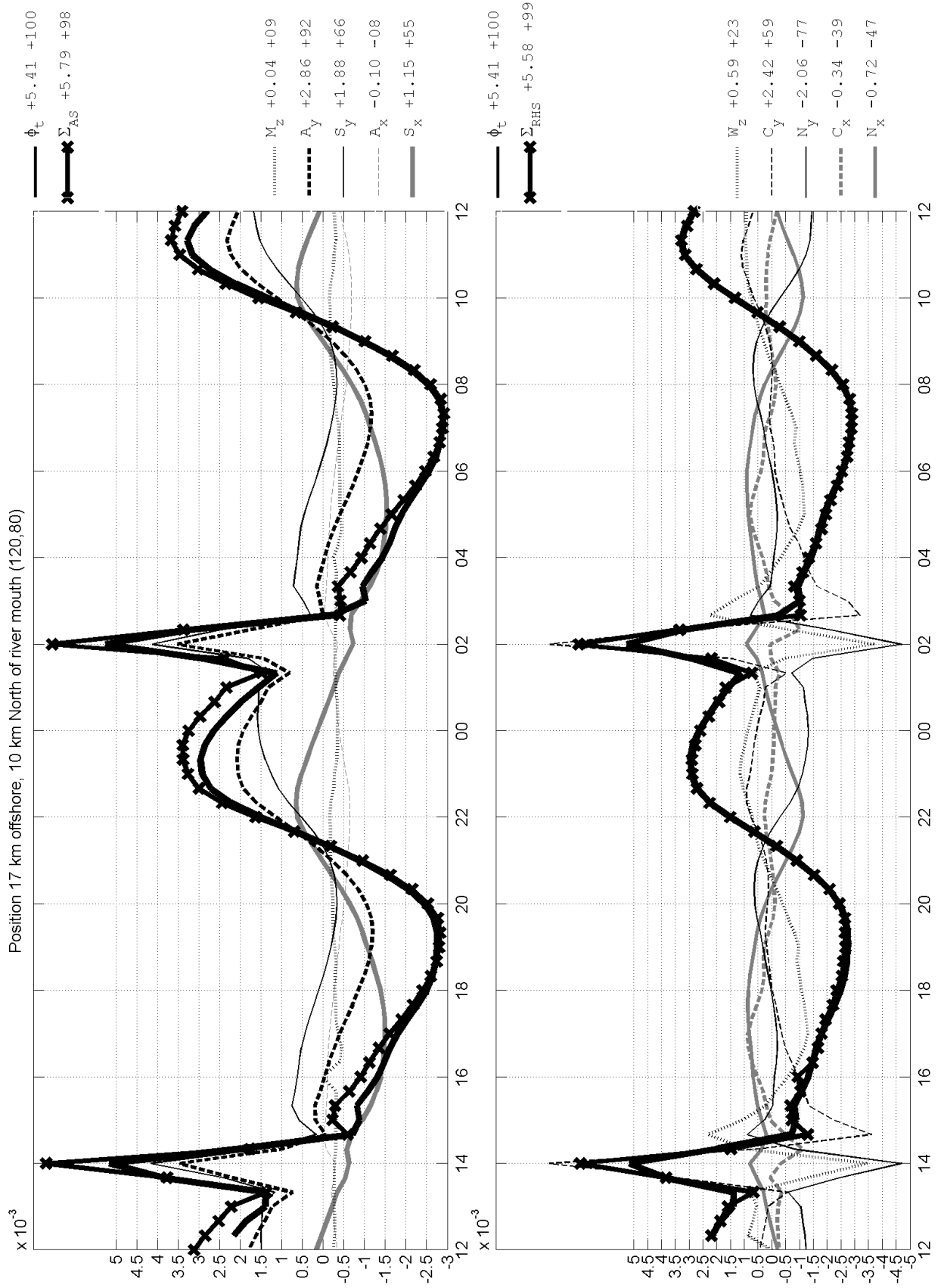
© Deft University of Technology, GdR, 2008

The biggest term  $C_x$  is partly balanced by  $N_x$ . The along-shore terms  $C_y$ ,  $S_y$  and  $A_y$  are also large. This along-shore effect is probably due to the position of this station at the transition from the bulge to the coastal current. The times when the along-shore terms are large coincide with the most Northward position of the bulge (at 15:20 in Fig. 6.2).

---

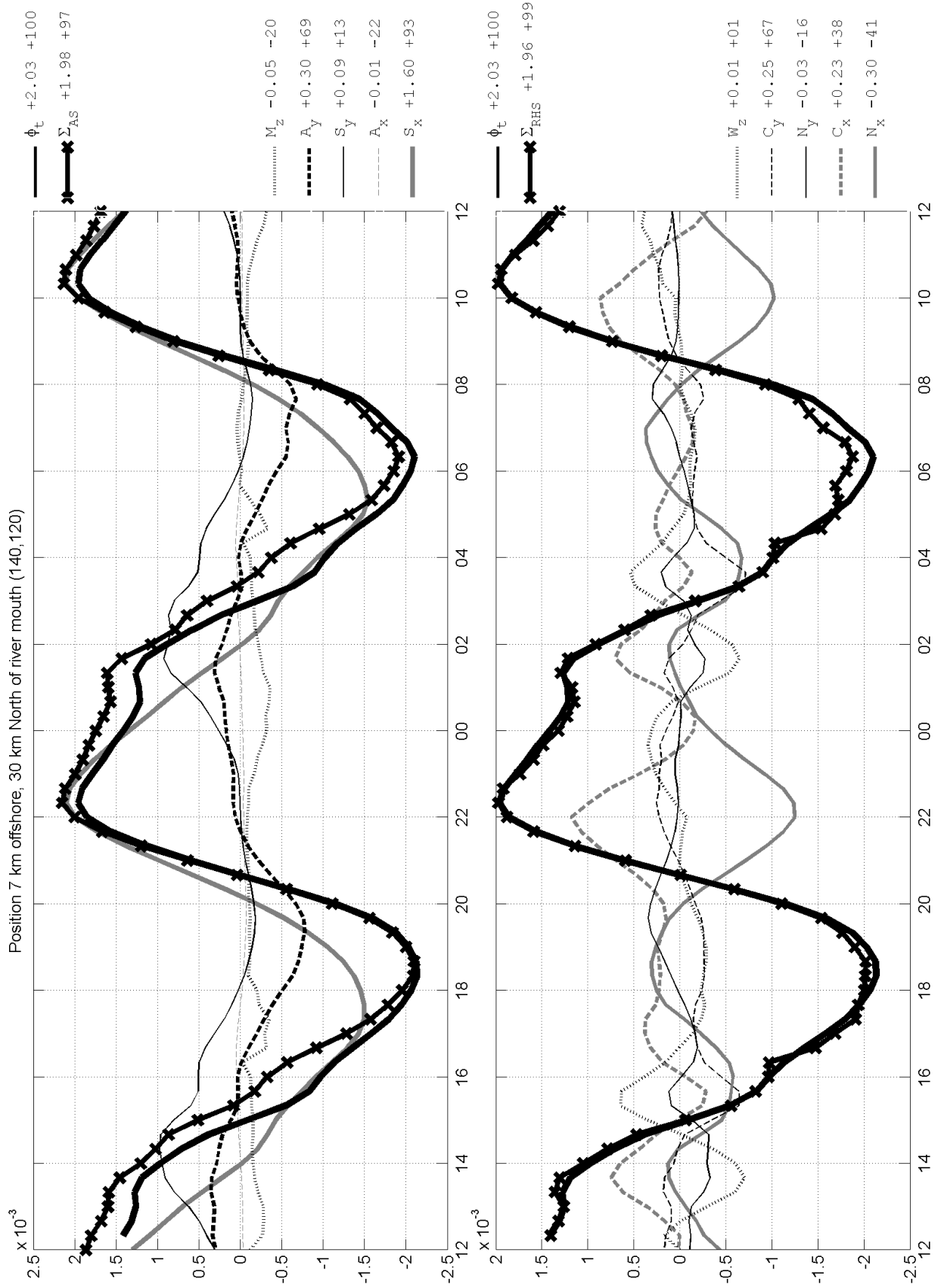
**Figure 6.4 (on the next page):** The evolution of the individual terms in Eq. 6.10 in  $Wm^{-3}$  over time (h) at Station 1 in the NE bulge (located 15 km offshore, 10 km North of the river mouth, see dot in Fig. 6.2). The first number in the legend on the right of the term label indicates the covariance with  $\varphi_t$  in  $10^6 ((Wm^{-3})^2)$ . The second number indicates the correlation in % (ranging from -100 to 100) between a given term and  $\varphi_t$  obtained by normalizing with the auto-variances. Horizontal  $\varphi_t$  grid lines are drawn every  $0.0005 Wm^{-3}$  step, to allow for quick comparison between the time series Figs. 6.4 to 6.6.  $\sum_{RHS}$  indicates the *RHS* in Eq. 6.10,  $\epsilon_{RHS}$  indicates the unexplained residual  $\varphi_t - \sum_{RHS}$ ,  $\sum_{AS}$  indicates *AS* in Eq. 6.10 and  $\epsilon_{AS}$  indicates the unexplained residual  $\varphi_t - \sum_{AS}$ . This location is sufficiently far away from the plume edge for stratification to be present during the entire period, the  $\varphi_t$  signal is non-zero. The time series shows a strong semi-diurnal sinusoidal curve, with a short-lived spike occurring around 14:00 and 02:00. It should be noted that the central difference method used to calculate the time rate of change of  $\varphi_t$  with a 20 min data availability has its limitations in describing the 1 h spike at two o'clock. The positive part of the sinusoidal term is mainly caused by  $A_y$  and  $S_y$ . After 03:00 the lens has passed the station, so the station is inside the remnant of the lens. This spike is well described by along-shore advection and straining. However, the  $C_y$ ,  $N_y$  and  $W_z$  terms are larger when the spike passes. Otherwise the *AS* terms describe the  $\varphi_t$  signal fairly well.





---

**Figure 6.5 (on the next page):** The evolution of the individual terms in Eq. 6.10 in  $\text{Wm}^{-3}$  over time (h) for Station 2 (located 6 km offshore, 30 km N of the river mouth, see dot in Fig. 6.2). The caption is the same as for Fig. 6.4. The signal is close to sinusoidal. It is dominated by cross-shore straining with a contribution from alongshore straining. The deviation from the sinusoidal shape between 1:00 and 3:00 is correlated with the advection of a fresh water lens through the station (Fig. 6.2). Conversely, the larger values of  $A_y$  between 6:00 and 8:00 are due to the barotropic ebb current moving the bulge back toward the south again (Fig. 6.2). The amplitudes of the cross-shore terms  $N_x$  and  $C_x$  are also large, but tend to cancel with  $W_z$ .



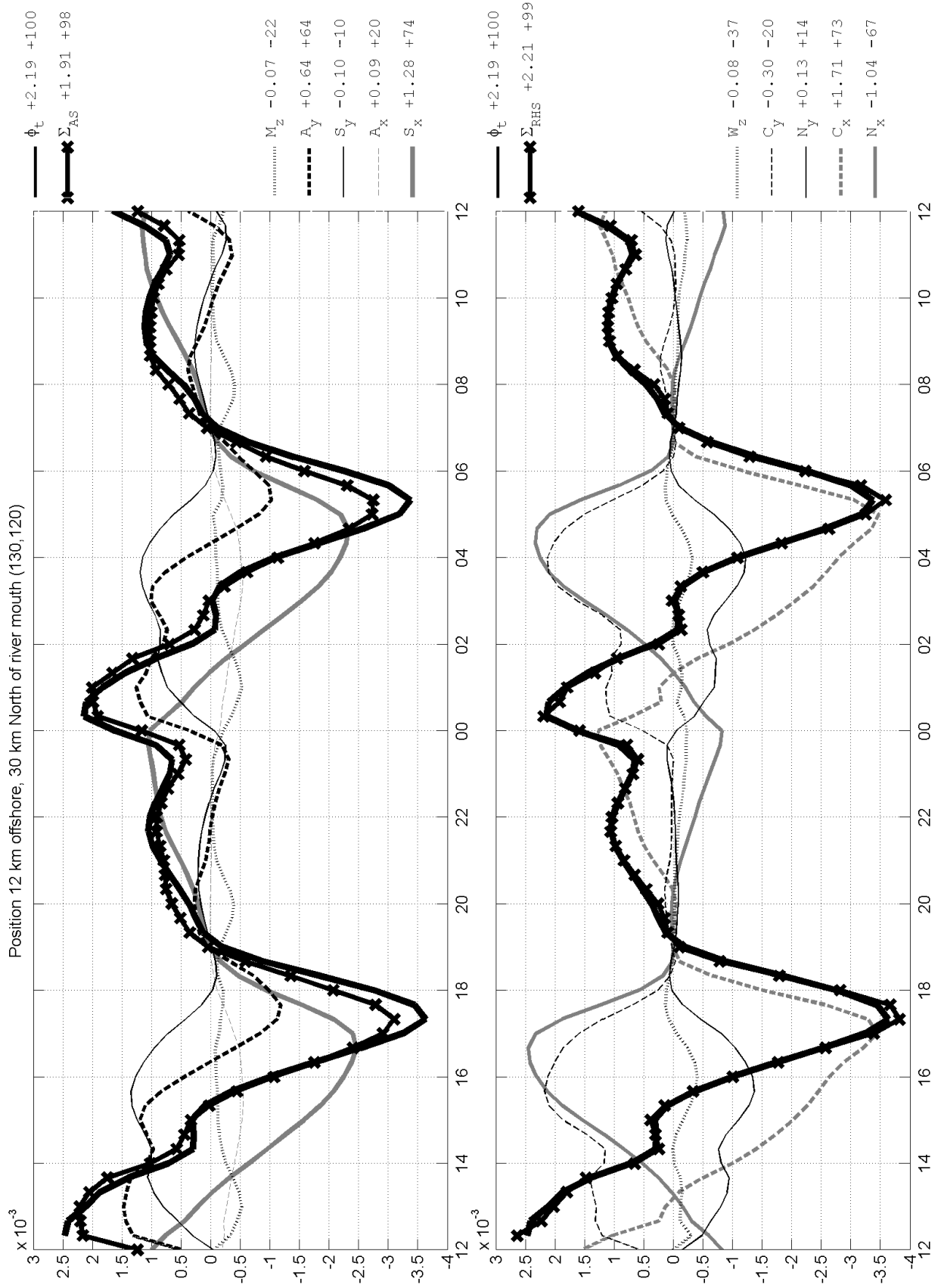
### 6.4.3 Synthesis of results

The above results suggest that the four terms accounting for cross-shore and along-shore straining and advection, can serve as a simple explanation of the evolution of stratification in the Rhine ROFI. While the other six terms are not negligible, they typically add up to zero. Hence advection and strain/shear induced period stratification (ASIPS) rather than just SIPS alone, may be important in controlling the stratification in the Rhine ROFI (Fig. 6.7).

However, the presence of fronts is clearly observed in the  $\varphi_t$  signal. Here the ASIPS concept performs less satisfactorily (see Fig. 6.3  $\epsilon_{AS}$ ), while the full  $\varphi_t$  equation does capture the variability in fronts (see Fig. 6.3  $\epsilon_{RHS}$ ). This means that although the ASIPS concept can be used to explain most of the variability in the river plume, the full  $\varphi_t$  is required to describe the general case.

---

**Figure 6.6 (on the next page):** The evolution of the individual terms in Eq. 6.10 in  $\text{Wm}^{-3}$  over time (h) for Station 3 (located 11 km offshore, 30 km N of the river mouth, see dot Fig. 6.2). The caption is the same as for Fig. 6.4. In this station the same increase of  $\varphi_t$  due to a fresh water lens is observed between 0:00 and 2:00. Note that while the  $S_x$  term still has a smooth sinusoidal course, it is not close to the  $\varphi_t$  signal. Its contribution is comparable to the  $A_y$  and  $S_y$  terms.



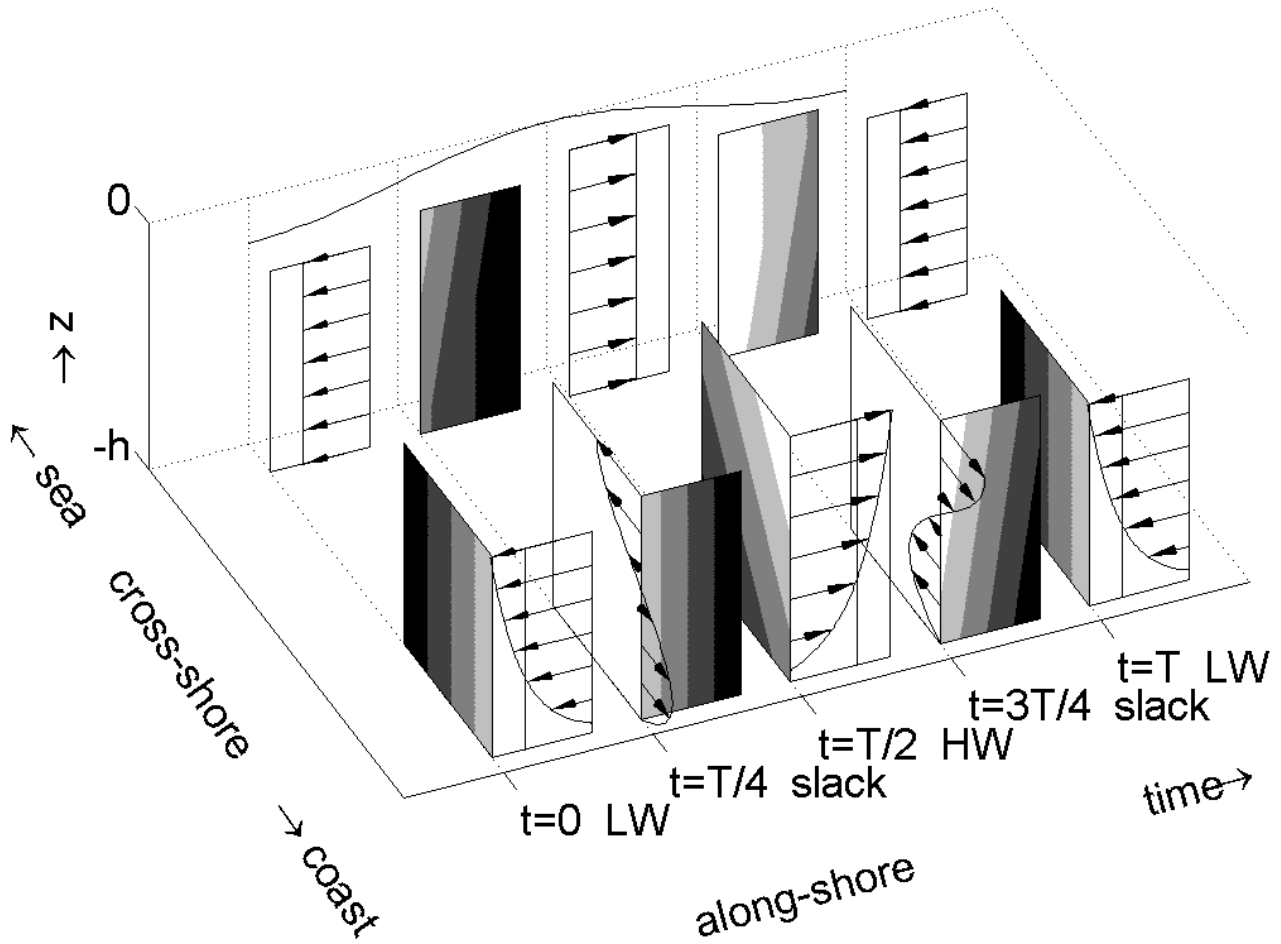


**Figure 6.7:** A sketch of the combined effect of along-shore advection (behind), along-shore shear and cross-shore shear acting in the downstream area of the Rhine ROFI (with  $T$  the tidal period). While Fig. 6.1 showed the joint action of the advection and straining terms in a general case, this sketch shows their joint action for the specific site configuration of the Rhine ROFI. Maximum stratification is governed by cross-shore tidal straining that operates to establish maximum stratification at HW (at  $T/2$ ), see Simpson & Souza (1995) and along-shore straining (log profile in the foreground) and advection (depth averaged flow behind) that operate together to establish maximum stratification at the subsequent slack ( $3T/4$ ). In the special case when the sum of the two along-shore processes and the cross-shore straining are equal, maximum stratification occurs exactly at  $5T/8$  and minimum stratification at  $T/8$ .

#### 6.4.4 Discussion

The potential energy anomaly equation is a powerful analysis tool demonstrating that the dominant terms contributing to the stratification signal can vary over short distances and that the behaviour of the  $\varphi_t$  signal can be markedly different. Fig. 6.8 summarises the contribution of the individual terms to the potential energy anomaly budget in the Rhine ROFI. The classic tidal straining mechanism dominates in the downstream coastal current region. This is indeed the configuration where cross-shore tidal straining for the Rhine ROFI was proposed by Simpson & Souza (1995). This is also the region for which upwelling observed in SST images can be explained by cross-shore straining alone in De Boer *et al.* (2007) (Chapter 5).

In the bulge region along-shore advection also dominates, hence in this region ASIPS controls the evolution of the stratification. The contribution of along-shore straining is small compared to along-shore advection, but is required to describe the evolution of the stratification signal in the numerical model. Returning to the data in the papers of Simpson & Souza (1995) and Van Alphen *et al.* (1988), it appears that ASIPS can account for the observed timing of maximum stratification. The frequent presence of fresh water pulses in the Rhine ROFI, as observed in cruise data, van Van Alphen *et al.* (1988), De Ruijter *et al.* (1997), can be examined in terms of the four terms contributing to ASIPS. An analysis of SST data, De Boer *et al.* (2007) and Pietrzak *et al.* (2008a), showed that wind also plays an important role in the evolution of stratification in this region. However, an analysis of the  $\varphi_t$  terms, in recent wind driven simulations by Pietrzak *et al.* (2008a), shows that winds typically act to increase vertical mixing and/or differential advection.

The effect of vertical mixing can only be dealt with properly by performing turbulence measurements, as done by Simpson *et al.* (2002), Fisher *et al.* (2002) and Souza *et al.* (2008). However, our results presented above have implications for the interpretation of such 1D-measurements, not only in ROFI. It is fundamentally difficult to distinguish between horizontal advective and vertical mixing processes as measured for example by ADCP and CTD profiles. Yet this is typically the only data available to us. Ideally, these data should be combined with data that allows one to distinguish mixing from horizontal advection and straining. For example, in order to be able to distinguish between the four ASIPS terms, proper estimates of density gradients in both horizontal directions are required. Fixed moorings consisting of an array would address this situation. However, the configuration of such an array should match the ratio between cross-shore and along-shore plume displacements. Based on the model results presented here, such an array for the Rhine ROFI should measure about 10 km along-shore and 5 km crossshore (Fig. 6.9). Unfortunately, the exact determination for a given site is non-trivial. The average position of a plume may alter with season, wind forcing, river discharge and so forth.

We have shown that the  $\varphi_t$  equation allows us to analyse the mechanisms contributing to mixing and stratification in the Rhine ROFI. We believe the  $\varphi_t$  analysis described here can be applied to a wider range of coastal systems and estuaries, as well as inland bodies of water such



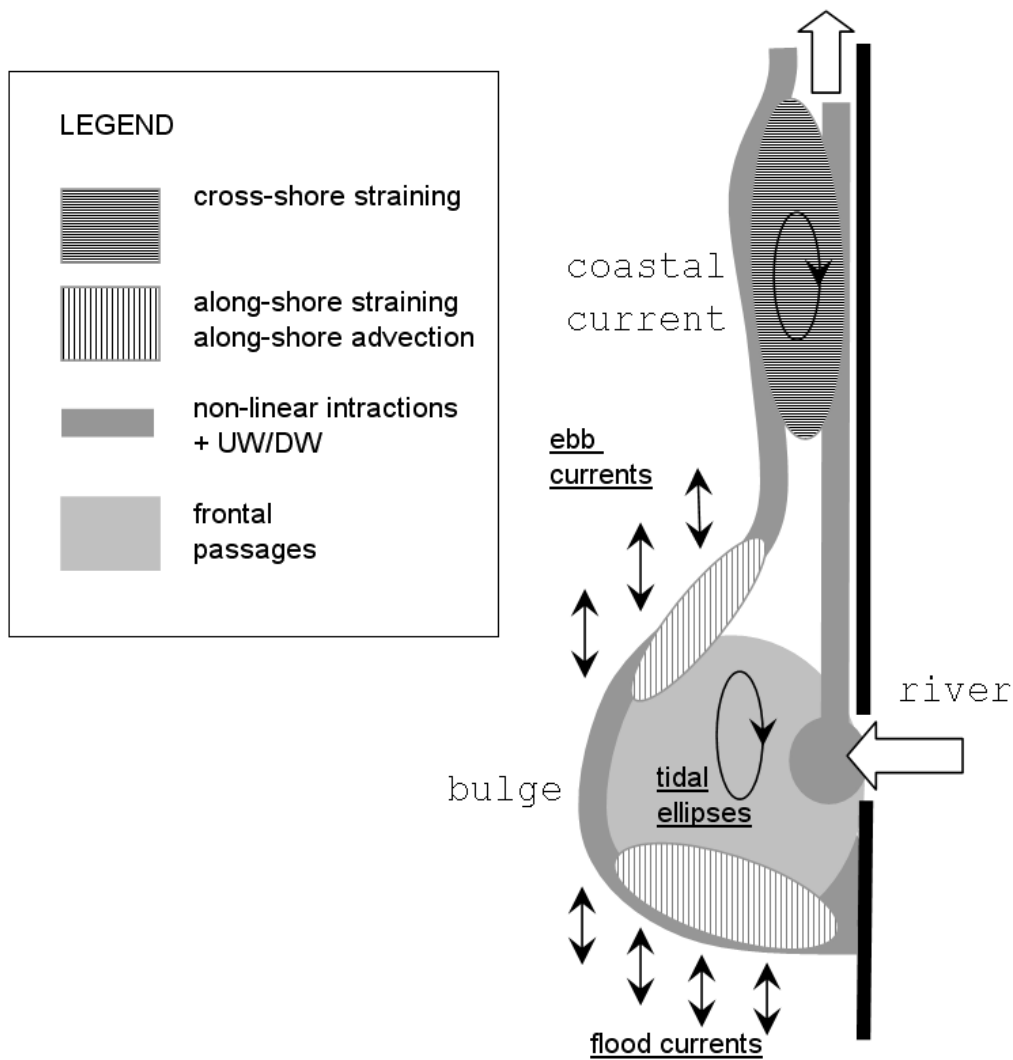


**Figure 6.8:** A sketch summarising the dominant terms controlling stratification and mixing within the Rhine ROFI. It is based on a synthesis of the covariance results presented in Fig. 6.3 from three semi-diurnal tidal cycles. Hence this provides us with a picture of the tidally averaged processes contributing to stratification and mixing. Note the difference between the bulge region and the downstream coastal current. The classic tidal straining mechanism dominates in the downstream coastal current region, in the area of the coastal current where isohalines are coast parallel. Along-shore advection also dominates the ROFI. Its effect is largest where barotropic along-shore tidal currents interact with the ROFI. This occurs at the South side of the bulge when flood currents meet the out-flowing plume, and in the NE part of the bulge when ebb currents intersect the plume. Along-shore straining is important in the same region, when baroclinic tidal currents are directed out of the bulge. This happens during ebb at the South edge of the bulge, and during flood at the NE side of the bulge. A north-south transect of the ROFI therefore, behaves as the fresh water lens sketched in Fig. 6.1 with opposite effects on opposite sides of the ROFI. In the central ROFI there is a pronounced effect of fresh water blobs released from the estuary as shown by the spikes in Figs. 6.4 to 6.6. The edges of the ROFI are dominated by fronts.

as lakes. In addition, in the spirit of the Simpson & Hunter (1974) criterion it can be used to investigate frontal processes, and the role of vertical mixing versus horizontal shear dispersion, for example. Hence we want to stress the power of the  $\varphi_t$  analysis as a diagnostic ocean modelling tool. It can be used to study the instantaneous evolution of the terms contributing to mixing and stratification. Moreover, we show that by a suitable choice of convolution period, in the covariance method presented here, one can assess which terms contribute to mixing and stratification at different time scales. One could foresee that, if we were investigating the long term evolution of the plume, the potential energy anomaly analysis presented here could help us determine how the plume evolves on a weekly, monthly, seasonal and annual time scale.

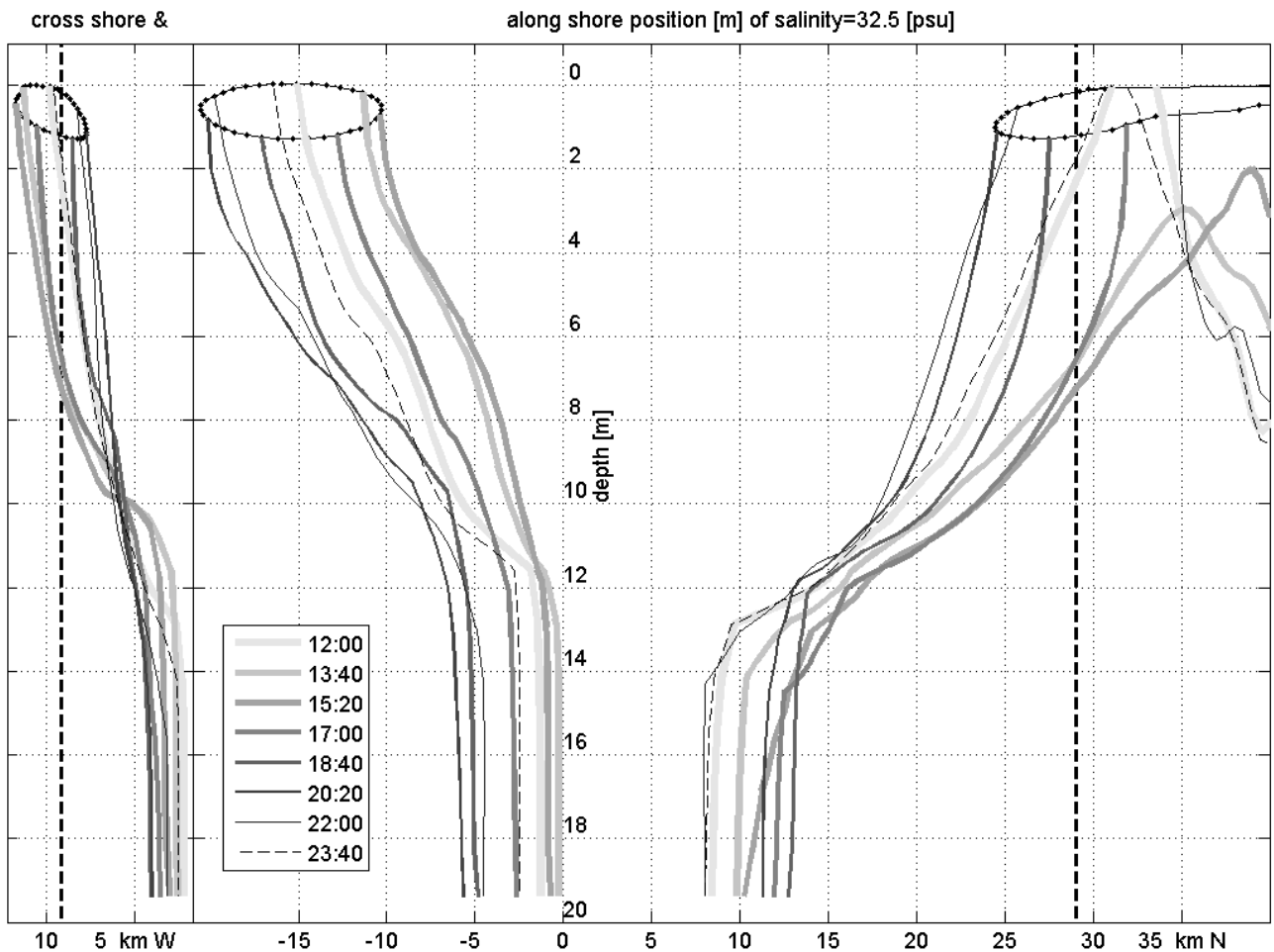


**Figure 6.9:** Cross-shore and along-shore positions of the simulated 32.5 PSU isohaline; left in a cross-shore transect and right in an along-shore transect. Note that this isohaline value is the same as used for the tidally averaged isohaline plotted in Fig. 6.3. The vertical dashed line indicates where the two transects cross. The surface position of the isohaline ( $\frac{1}{2}\Delta z$  below the water surface) is plotted every 20 min with connected dots. In the left panel the horizontal axis indicates the cross-shore distance westward off the coastal wall, in the right panel the horizontal axis indicates the along-shore distance northward of the river mouth, that is located at the origin. The vertical axis represents depth.

## 6.5 Conclusions

We conclude that the potential energy anomaly equation provides a powerful framework to analyse mechanisms contributing to mixing and stratification. While we have presented the results for a stratified, shallow shelf sea plume, we believe the analysis carried out here can be applied to a wider range of estuarine, coastal ocean systems, and lakes. The potential energy anomaly concept introduced by Simpson and co-workers is an invaluable tool with which to analyse numerical models. The simple extension to three-dimensions presented here has further highlighted the important role of cross-shore tidal straining in the Rhine ROFI. However, it also suggests that along-shore straining as well as cross-shore and along-shore advection should be considered.

We also demonstrate the importance of idealised numerical model studies in furthering our knowledge of coastal ocean systems. Many river plume studies have concentrated on the role of along-shore advection, whereas shallow shelf sea studies have tended to focus on tidal straining. Here we stress the important role played by both mechanisms in maintaining and controlling the stratification in coastal seas. The combination of straining and advection is of key importance to an accurate numerical reproduction of the observed stratification. Finally we conclude that it is important to include tides in coastal ocean models in order to reproduce the stratification.

## Acknowledgements

The project is funded by the Dutch Organization for Scientific Research (NWO) in the ALW programme within the framework of LOICZ-NL (ALW project number 014.27.006) whose support is gratefully acknowledged. We would like to thank the principal investigator, Prof. dr.ir. Herman Ridderinkhof from Royal Netherlands Institute for Sea Research (NIOZ), for a number of discussions. We would like to thank ir. Michel de Nijs for many useful discussions on the potential energy anomaly equation and the ASIPS model. We would also like to thank Prof. Hans Burchard for a number of discussions on the equation, and the Rhine ROFI, as depicted by Fig. 6.8. We would also like to thank Dr. Susan Allen for her comments on the equations. We would like to thank both Prof. John Simpson and an anonymous reviewer for their detailed comments, which substantially improved the paper.

## Chapter 7

### Synthesis

In this chapter we synthesize the key processes governing the physical behaviour of the Rhine Region of Freshwater Influence (ROFI, Simpson *et al.* (1993). Tides, the rotation of the Earth, bottom friction and stratification are the principal elements in controlling the river plume behaviour (Fig. 7.1).

The rotation of the Earth governs the Rhine ROFI by imposing the basic shape of the ROFI for the tide to interact with. Upon entering the North Sea, the rotation of the Earth deflects the fresh water plume to the right to form a narrow coastal current; a feature shared with most of the world's other river plumes. This coastal current controls the advection and dispersal of sediments, pollutants, biota and nutrients. Coastal currents can maintain their cross-shore structure for hundreds of kilometres due to a balance between the rotation of the Earth and alongshore baroclinic residual currents. As in an estuary, initially the fresher coastal water has a tendency to flow offshore in the surface layer, whereas the saltier offshore waters have a tendency to flow coastward near the bottom. However, the surface current of this gravitational circulation is immediately deflected to the right due to the rotation of the Earth. The freshwater flows alongshore to the North, such that the onshore Coriolis force generated by the alongshore velocity balances the cross-shore baroclinic pressure gradient, a balance which is known as thermal wind from meteorology. The predominantly SW winds add to this baroclinic residual current (Van Alphen *et al.*, 1988; Van der Giessen *et al.*, 1990; De Ruijter *et al.*, 1992). However, due to the effect of bottom friction, a cross-shore estuary-line circulation component remains. The superposition of the resulting alongshore and cross shore residual components in a shallow frictional system with a cross shore density gradient has been described by Heaps (1972).

Within the seemingly constrained shape set by freshwater and the rotation of the Earth, the ROFI is known to exhibit a plethora of phenomena due to tidal influences. The semi-diurnal tides are the most energetic phenomenon in the Southern North Sea (Zimmerman, 1986). The interaction between the tide and the stratification field under the influence of the rotation of the Earth is dominated by two processes: tidal mixing and tidal straining. Simpson (1997) noted that these two terms provide a powerful concept for a first order understanding of the ROFI.

The work in this thesis builds upon these key concepts derived by Simpson and co-workers which include the slow, fortnightly modulation of stratification by tidal mixing levels and the fast, semi-diurnal variations in stratification due to tidal straining. The objective of this thesis is to gain a further understanding into these two complex flow-density interactions.

Our objectives have been achieved by adding two simple, yet powerful concepts to the Rhine ROFI body of literature. First we identified upwelling induced by tidal straining as a new key mechanism operating in the Rhine ROFI. Second, in chapter 6 we formulated advection and strain induced periodic stratification (ASIPS) as the main agent in controlling intra-tidal variations in stratification. ASIPS is a natural extension of the SIPS terminology of Simpson *et al.* (1990) and can be written as a subset of the full potential energy anomaly definition of (Simpson *et al.*, 1978; Simpson & Bowers, 1981; Simpson, 1981).

## 7.1 Tidal mixing and straining

The primary appearance of the ROFI is controlled by tidal mixing, which governs its basic bi-modal nature in competition with buoyancy forcing (Simpson *et al.*, 1993). The ROFI is either

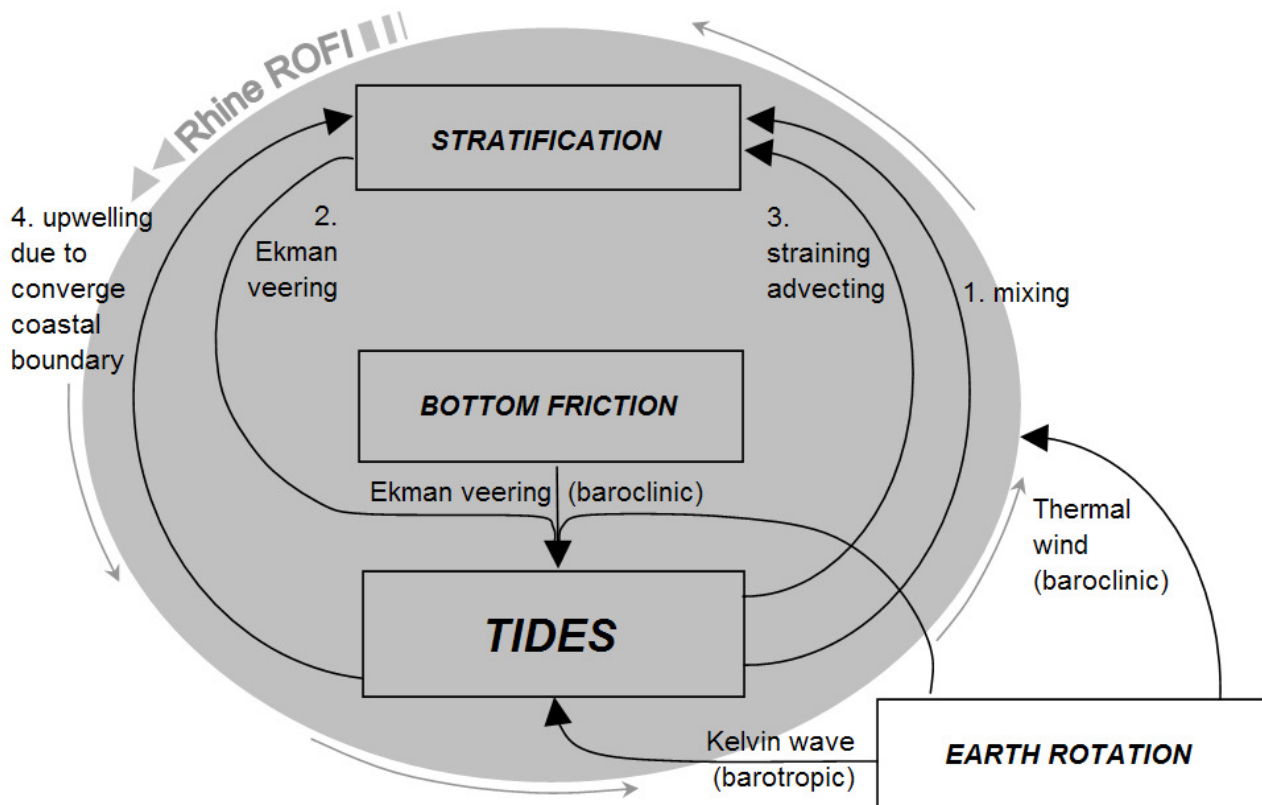


**Figure 7.1:** The dominant processes controlling the complex stratification structure in the Rhine ROFI, with Earth rotation and stratification as important moderators for the tide.

forced in a vertically well-mixed state during spring tide, also known as bottom-advected, or is allowed to stratify during reduced neap tide mixing levels, also known as surface-advected Yankovsky & Chapman (1997). Wind mixing further affects this basic state (Simpson *et al.*, 1993) (Fig. 1.3). The main time scale of the system is set by the spring-neap mixing cycle, with an irregular component due to wind mixing.

In this thesis we investigated the basic physical processes governing the Rhine ROFI with an idealized model approach. We created a numerical model set-up that allows us to study the interaction between the tides and the stratification field in isolation, without being diverted by ‘noise’ due to complex variations in discharge, wind, bathymetry etc. First we validated the important effect of stratification on damping of turbulence by comparison with field measurements of dissipation. Subsequently, in chapter 4 we employed this 3D numerical model to simulate this basic time scale of the ROFI as an extension of the 1D point model simulations of Simpson & Souza (1995). We simulated separate neap and spring tide situations, as well as a successive alternation between neap and spring tides. The model also showed a well-mixed ROFI during spring tide and a stratified system during neap tide. This allows us to conclude that, with the given numerical settings, tidal mixing alone is sufficient to cause the transition between bottom-trapped and surface trapped. The successful reproduction of this dominant fortnightly time scale can be considered an essential validation step of the numerical model. After this step, the model can be confidently applied for further study of the ROFI, notably for tidal straining, the second dominant process in governing the Rhine ROFI physics.

The basic complexity of the ROFI system is thus governed by tidal mixing operating on the available buoyancy to set the level of stratification. A second level of complexity is introduced by a feed-back mechanism in which the level of stratification operates on the tidal properties, instead of the other way around (Fig. 7.1). Initially stratification is only an emergent property, dictated by the tidal mixing. However, once it exists, it becomes an important force on its own in controlling the ROFI. Stratification is known to have a significant influence on the tidal velocity profiles (e.g. Sverdrup (1927) and Maas & Van Haren (1987)). During well-mixed periods, the tidal currents are rectilinear alongshore over the entire depth, which can be described with degenerated rectilinear current ellipses .

In contrast, when the ROFI is stratified, pronounced tidal ellipses emerge with eccentricities up to 40%, rotating anti-cyclonically in the surface layer and cyclonically in the bottom layer (Visser *et al.*, 1994; Simpson *et al.*, 1996)(Fig. 1.5). The rotation of the Earth and bottom friction are responsible for this veering of the ellipse rotation sense over depth. This phenomenon is known as Ekman dynamics, which includes time variation due to tides as the main characteristic distinguishing it from classic stationary Ekman mechanics. Due to its dynamic nature, Ekman dynamics involves two boundary layers instead of just one. The cyclonic tidal component rotating in the same direction as the Earth has the smallest boundary layer thickness and is trapped below the pycnocline during periods of stratification. This leaves the upper layer to

be dominated by the other, anti-cyclonic, tidal component which has a three times larger layer boundary layer thickness. The resulting surface layer vector is therefore continuously deflected to the right by the rotation of the Earth, unimpeded by bottom friction from which it is shielded by the pycnocline. Meanwhile, the bottom current rotates in opposite direction, in the same direction as the Earth. The velocity profiles in this stratified ROFI situation deviate strongly from the rectilinear Kelvin wave velocities during well-mixed periods.

Insight into the onset and nature of the tidal ellipses is provided by the analytical model of Prandle (1982a,b). In his 1D point model only the three essential processes are present: local acceleration, the rotation of the Earth and friction. The model solves the local velocity profile by decomposition into two counter rotating components that are conveniently uncoupled in mathematical sense which can, accordingly, be solved separately. However, in the Rhine ROFI these components are coupled physically by the proximity of the coastal wall, yielding a zero depth averaged flow in cross shore direction at any time, in line with the very definition of the Kelvin wave. Prandle employed simple analytical expressions for the eddy viscosity profile for barotropic waters to obtain an expression for the velocity profile. Maas & Van Haren (1987) and Howarth (1998) extended this model to deep, seasonally stratified waters by employing separate analytic formulations for the three distinct water layers above, within and below the pycnocline. However, we show in Chapter 4 that in the Rhine ROFI the analytic expressions of Prandle (1982a,b) may already be sufficient for a basic understanding by simply employing one depth-averaged bulk eddy viscosity. A tenfold reduction of the bulk eddy viscosity already results in a significant increase of the ellipticity veering. A two-layer model has also been used earlier to understand the onset of periods with increased ellipticity (Visser *et al.*, 1994) albeit at the cost of reduced simplicity. However, an exact description of the ellipticity veering in the Rhine ROFI requires a detailed description of the vertical mixing profile with a numerical turbulence model. Such vertical turbulence model can be employed either as a separate 1D point model (e.g. GOTM, POLCOMS) or incorporated as a sub-process into a full 3D model (e.g. DELFT3D-FLOW) as employed in this thesis.

The veering in ellipse properties during stratified periods due to the rotation of the Earth generates a strong tidal shear in the cross-shore direction, up to  $70 \text{ cms}^{-1}$  over the depth (Visser *et al.*, 1994). This further increases the level of complexity by providing a third feed-back link (Fig. 7.1). Through a process known as tidal straining (Simpson *et al.*, 1990) the shear interacts with the dominant cross-shore density structure (Van Alphen *et al.*, 1988; De Ruijter *et al.*, 1992; Simpson *et al.*, 1993; De Ruijter *et al.*, 1997; Suijlen & Duin, 2002). This imposes a second, semi-diurnal cycle on the stratification level, known as Strain Induced Periodic Stratification, in short SIPS (Simpson *et al.*, 1990). In the Rhine ROFI case, the reversing semi-diurnal cross-shore surface currents in turns advect fresher coastal waters offshore to enhance stratification, or advect fresher water back onshore to diminish stratification (Fig. 6.7). The amplitude of the resulting semi-diurnal modulation can be so strong with respect to the mean stratifi-



cation, that the system can switch from fully well-mixed to stratified within one tidal cycle. Thus the semi-diurnal SIPS stratification signal is indirectly, yet inextricably linked to the fortnightly tidal mixing cycle through two intriguing interaction mechanisms (Fig. 7.1): the effect of stratification on tidal ellipse veering which is known as Ekman dynamics and the subsequent effect of tidal ellipse veering in combination with horizontal density gradients on stratification which is known as tidal straining.

## 7.2 Tidal upwelling

In chapter 5 we presented upwelling and downwelling induced by tidal straining as a new key mechanism operating in the Rhine ROFI. This is our first contribution to the Rhine ROFI body of literature. We show that the cross-shore tidal straining mechanism interacts with the coastal boundary to induce a tidal upwelling signal. Any offshore surface current associated with the tidal ellipses, needs to be replenished instantaneously near the coast in order to fulfil continuity requirements. Due to the large alongshore extent and uniformity of the ROFI, this water cannot be supplied by the surrounding ambient surface waters. Therefore an onshore bottom water flux compensates the offshore flux of the surface currents, and vice versa. Hence, the cross shore SIPS process should lead to upwelling at the tidal frequency.

Observing upwelling is known to be difficult in general due to the small vertical velocities involved. Therefore upwelling is usually observed only indirectly by exploiting the different properties of surface and bottom water masses. For instance, through the indirect effect of stratification trapping solar heating into the surface layer, this phenomenon can be observed with SST satellite imagery. Whereas in the world's large wind driven upwelling regions the surface and bottom water masses already have a different temperature before they arrive into the upwelling system, in the smaller Rhine ROFI system the different temperature properties develop in the water masses locally. Any solar heating trapped in the stratified surface layer creates a temperature difference with the surrounding well-mixed ambient waters, where solar energy is distributed over the entire water depth. This process allows for detection of upwelling induced by tidal straining in spring and summer time. Thus stratification is responsible for both the upwelling mechanism as well as the temperature difference that allows for its observation.

An excellent SST example of upwelling induced by tidal straining has been found in May 1990 as shown in chapter 5. The sequence of SST images shows a ROFI much warmer than the surrounding waters, indicating that the whole ROFI area is stratified. A marked 5-10 km wide and 100 km alongshore band of cold upwelling is observed along the coastline at HW, while this upwelling band is not present in images later or earlier that day. The timing of this upwelling indicates that it is caused by tidal straining. An additional, yet reversed example was found for an autumn case. Here the temperature contrast is inversed with respect to the spring situation with a warm semi-diurnal upwelling band appearing in a cold ROFI area. The upwelling and

downwelling induced by the tide are similar to the frequent outcropping of isopycnals at the surface of lakes due to reversing wind conditions.

The upwelling induced by tidal straining supports the important role known to be played by SIPS (Simpson & Souza, 1995). Furthermore, the dimensions indicate the large spatial scale of cross shore tidal straining in the Rhine ROFI. In addition, we believe that the observed tidal coastal upwelling mechanism is sufficiently important to be considered as a separate new key feature of the Rhine ROFI. Although from a physical point of view it is only an emergent property whose existence is dictated by tidal straining, the tidal upwelling phenomenon in the Rhine ROFI can have large consequences on non-physical properties such as the advection and dispersal of sediment, nutrients, pollutants and biota. Therefore we advocate further research into this phenomenon in specific.

### 7.3 Advection of stratification

In chapter 6 we presented advection and strain induced periodic stratification (ASIPS) as the main agent in controlling intra-tidal variations in stratification. This is our second contribution to the Rhine ROFI body of literature. The Rhine ROFI has primarily been studied through observations, and with 1D and 2D models. These methods are sufficient to capture the nature of the two key processes operating in the Rhine ROFI, viz. the vertical nature of tidal mixing (1D models) and the cross-shore nature of tidal straining (2D models) effectively. However, in chapter 6 we show that application of a full 3D numerical model to an idealized Rhine ROFI reveals that additional mechanisms are active in governing the stratification field. In fact, in chapter 6 we could only describe the local stratification signals observed in the 3D numerical model results sufficiently well when considering both advection and strain induced periodic stratification (ASIPS), in both the alongshore and cross shore directions (Fig. 6.8). The classic SIPS and tidal mixing mechanisms alone are not sufficient to describe the stratification signals.

The role of ASIPS was then supported by reanalysis of previously published observations. Observations that were employed to indicate tidal straining (Simpson & Souza, 1995), exhibit advection tendencies. Conversely, observations used to indicate alongshore tidal advection, show tidal straining effects (Van Alphen *et al.*, 1988). Furthermore, the Rhine ROFI density field is known to be horizontally inhomogeneous due to the presence of fresher baroclinic eddies (De Kok, 1997) and water lenses (Van Alphen *et al.*, 1988; De Ruijter *et al.*, 1992; Simpson *et al.*, 1993) originating from tidal pulsing for example (De Ruijter *et al.*, 1997). Only a conceptual description in terms of ASIPS can capture the dominant physics of such a heterogeneous system in sufficient detail, uniting the important, classic cross shore tidal straining SIPS mechanism with the alongshore tidal excursion of stratified patches. In addition to tidally induced movements, fresher water displacements due to wind can be described with ASIPS as well, although this has not been dealt with in this thesis. These events may include the alongshore displacement

of fresher water lenses by cross-shore wind as shown in chapter 5, as well as any cross-shore displacements due to alongshore winds (Fong & Geyer, 2001).

## 7.4 Potential energy anomaly analysis

Despite their fundamental difference in character, ASIPS and mixing can be united into one overall framework. The tidal straining concept has originally been derived by Simpson *et al.* (1990) as a subset of the potential energy anomaly approach of (Simpson *et al.* (1978); Simpson & Bowers (1981); Simpson (1981)). A thorough re-analysis of this derivation (Chapter 6, and Burchard & Hofmeister (2008) yielded an equation for the evolution of the stratification, in which we identified ASIPS as an important subset among multiple other terms. However, vertical mixing is part of this very same equation as well. Hence, the classic potential energy anomaly approach can naturally combine both the direct and the indirect processes controlling stratification of the ROFI. The potential energy anomaly approach encompasses all direct (tidal mixing) and indirect processes (ASIPS) interacting with stratification as presented in Fig. 7.1. It should be stressed though, that once stratified for a prolonged period as dictated by tidal mixing, time series of stratification are dominated by large-amplitude ASIPS effects. This was shown in our correlation analysis in Chapter 6, where the ASIPS terms emerged as a powerful predictor of stratification, while tidal mixing had only a negligible correlation on the tidal time scale. Nevertheless, only the mixing aspects dictate the primary state of the ROFI, which determines whether ASIPS occurs at all. The efficiency of tidal mixing therefore deserves special attention, as was already noted by Simpson (1997).

## 7.5 Dealing with tidal mixing and straining

The importance of tidal mixing can only be dealt with properly by employing sophisticated numerical turbulence models with include buoyancy effects. However, before these models can be applied to ROFIs with confidence, they have to be assessed against measurements. Excellent measurements for this goal are the vertical dissipation profile measurements as introduced by (Rippeth *et al.*, 2001). This approach has first been performed for Liverpool Bay by Simpson *et al.* (2002) using measurements performed by Rippeth *et al.* (2001). In chapter 3 we validated our 3D numerical model against the same data. More recently, Fisher *et al.* (2002) performed dissipation measurements for the Rhine ROFI which were subsequently reproduced with a 1D numerical turbulence model by Souza *et al.* (2007). Unfortunately, this fruitful scientific approach of both measuring and modelling tidal velocity, density and mixing profiles is not deployed in the present Dutch operational monitoring practise in the Rhine ROFI. However, despite the success of Simpson *et al.* (2002); Souza *et al.* (2007) in reproducing dissipation profiles with a 1D vertical numerical model, 1D vertical models an sich are not sufficient to fully

capture the essential properties of the Rhine ROFI. Advection and straining dominate stratification signals, and thus 1D vertical models only work as long as the time and depth dependent density field is prescribed. This conclusion has also been drawn for a site in the central North Sea, where horizontal advection is responsible for a significant part of the variations (Bolding *et al.*, 2002). 1D vertical turbulence models are essential, but not sufficient to describe the Rhine ROFI. The same applies to horizontal circulation models of course. These are essential, but not sufficient without a sophisticated turbulence model.

Nevertheless, despite the paramount importance of tidal mixing, it is not widely accounted for in all river plume models yet. The primary sources of mixing are wind mixing, partly indirectly due to waves, and tidal mixing. The turbulence input due to wind originates from the water surface and penetrates downward. In contrast, the mixing by tides originates from the shear stresses at the bottom and penetrates upward. In deep water, the two sources of turbulence can be confined to either end of the water column, separated by a layer of water with low turbulence levels in between (Simpson & Tinker, 2007). In contrast, in the shallow Rhine ROFI, both the Ekman surface and bottom boundary layers (BBL) can extend over the entire water column, only limited by the level of stratification. Hence the mixing of the ROFI is governed by both turbulence sources. Wind mixing entrains saltier bottom water into the surface layer, while tidal mixing entrains fresher surface water into the bottom layer. Many river plume studies concerned with deeper water do not include the tide, because its direct impact on mixing is thought to be negligible. However, the results of Simpson & Tinker (2007) show that the effect of the tidal turbulence generated at the bed may penetrate upward in the water column in the order of 100 m. The stratified surface layer is not only eroded by wind mixing from above, but also by tidal mixing from below, albeit more slowly in deeper waters. Hence, the common use in many numerical plume studies of specifying only a residual background current and wind forcing (for example Kourafalou *et al.* (1996a); Fong & Geyer (2001) does not yield the required mixing levels paramount for determining the fate of fresh water.

Apart from the portion of tidal mixing that might reach the pycnocline upwards from the bottom, the tide affects deeper plumes in yet another manner. Due to the rotation of the Earth, the velocities in the surface layer may deviate substantially from the tidal plug flow normally present above the BBL. This phenomenon has been shown to occur during thermal stratification on the central North Sea by Maas & Van Haren (1987). The same applies to haline stratification in fresh water plumes in deeper water. Here, tidal velocities in the stratified surface layer may substantially deviate from the tidal velocities in the ambient water below. Due to the rotation of the Earth, the stratified surface layer may gain a surplus of anti-cyclonic rotation compared to the well-mixed case. The water below the surface layer will gain a small surplus of cyclonic rotation to keep a zero depth-averaged cross shore velocity. This difference causes differential advection of the stratified surface layer over the vertical. In addition, the associated shear may enhance mixing in the pycnocline. Neglecting tides altogether in numerical plume

studies does not capture this straining phenomenon and the associated mixing sufficiently well. The consequences of neglecting both the direct and the indirect effects of the tide on the river plume may be substantial.

## 7.6 Concluding remarks

In this thesis we highlighted the paramount importance of the role of tides in governing the Rhine ROFI. Tides not only control the primary appearance of the ROFI through direct mixing, but also control the long-term fate of its transport paths for its constituents through an intricate web of interactions, involving the rotation of the Earth, the coastal boundary, bottom friction, stratification and the residual currents as important moderators. The employment of 3D numerical models can teach us about the profound impacts of tidal mixing, straining and advection mechanism involved on these interactions. Herein the role of tides is of crucial importance for understanding the 3D density structure in the Rhine ROFI through a multitude of intriguing interactions.

We show that the method employed here of applying a 3D numerical model to an idealized numerical domain of a coastal ROFI constitutes a powerful method. Therefore we recommend further application of this approach, that can serve as a bridge between mathematical scaling analyses and application of full 3D numerical models to realistic domains. These three methods provide different insights and should preferably be employed in combination with in situ data and remote sensing data.



## REFERENCES

- Arakawa, Akio, & Lamb, Vivian R. 1977. Computational Design of the basic dynamical processes of the UCLA General Circulation Model. *Pages 173–265 of: Chang, Julius (ed), General circulations models of the atmosphere*. Methods in computational physics; advances in research and applications, vol. 17. New York: Academic Press.
- Arentz, Loana. 2005 (Jan). *Remote sensing of the Rhine river plume*. MSc. thesis, Delft University of Technology, Stevinweg 1;2628 CN Delft; The Netherlands.
- Battjes, J.A. 1998. *Stroming in waterlopen*. Lecture notes 3310. Delft University of Technology, Stevinweg 1;2628 CN Delft; The Netherlands. In Dutch.
- Blanton, Jackson O., Amft, Julie, & Tisue, Tom. 1997. Response of a small-scale bottom-attached estuarine plume to wind and tidal dissipation. *Journal of Coastal Research*, **13**(2).
- Bolding, Karsten, Burchard, Hans, Pohlmann, Thomas, & Stips, Adolf. 2002. Turbulent mixing in the Northern North Sea: a numerical model study. *Continental Shelf Research*, **22**(18-19), 2707–2724.
- Broomans, Peterjan. 2003 (February). *Numerical accuracy in solutions of the shallow-water equations*. MSc. thesis TU Delft, Delft Hydraulics, Rotterdamseweg 185; P.O. Box 177; 2600 MH; Delft; The Netherlands.
- Burchard, H. 2002. *Applied turbulence modelling in marine waters*. Warnemünde: Springer.
- Burchard, Hans, & Hofmeister, Richard. 2008. A dynamic equation for the potential energy anomaly for analysing mixing and stratification in estuaries and coastal seas. *Estuarine, Coastal and Shelf Science*, **77**(4), 679–687.
- Chao, S.-Y. 1987. River-forced estuarine plumes. *Journal of Physical Oceanography*, **18**(1), 72–88.
- Chao, S.-Y. 1988. Wind-driven motion of estuarine plumes. *Journal of Physical Oceanography*, **18**(8), 1144–1166.
- Chao, S.-Y. 1990. Tidal modulation of estuarine plumes. *Journal of Physical Oceanography*, **20**(7), 1115–1123.
- Davies, A.M., & Xing, J. 1999. Sensitivity of plume dynamics to the parameterisation of vertical mixing. *Journal for Numerical Methods in Fluids*, **30**, 357–405.
- De Boer, G. J., Pietrzak, J. D., & Winterwerp, J. C. 2008. Using the potential energy anomaly equation to investigate tidal straining and advection of stratification in a region of freshwater influence. *Ocean Modelling*, **22**(1-2), 1–11.



- De Boer, G.J., Pietrzak, J.D., & Winterwerp, J.C. 2006. On the vertical structure of the Rhine region of freshwater influence. *Ocean Dynamics*, **56**(3-4), 198–216. Special issue PECS 2004.
- De Boer, G.J., Pietrzak, J.D., & Winterwerp, J.C. 2007. SST observations of upwelling induced by tidal straining in the Rhine ROFI. *Continental Shelf Research*. In press, special issue PECS 2006.
- De Kok, J.M. 1996. A two-layer model of the Rhine plume. *Journal of marine Systems*, **8**, 269–284.
- De Kok, J.M. 1997. Baroclinic eddy formation in a Rhine plume model. *Journal of marine Systems*, **12**, 35–52.
- De Kok, J.M., De Valk, C., Van Kester, J.H.Th. M., De Goede, E., & Uittenbogaard, R.E. 2001. Salinity and temperature stratification in the Rhine plume. *Estuarine, Coastal and Shelf Science*, **53**, 467–475.
- De Ruijter, W.P.M. 1983. Effects of velocity shear in advective mixed-layer models. *Journal of Physical Oceanography*, **13**(9), 1589–1599.
- De Ruijter, W.P.M., Postma, L., & De Kok, J.M. 1987. *Transport atlas of the Southern North Sea*. Tech. rept. Rijkswaterstaat tidal waters division and Delft Hydraulics.
- De Ruijter, W.P.M., Van der Giessen, A., & Groenendijk, F.C. 1992. Current and density structure in the Netherlands coastal zone. *Chap. 26, pages 529–550 of: Prandle, D. (ed), Dynamics and exchanges in estuaries and the Coastal Zone*. Coastal and Estuarine Studies, vol. 40. Washington DC: AGU.
- De Ruijter, W.P.M., Visser, A.W., & Bos, W.G. 1997. The Rhine outflow: A prototypical pulsed plume in a high energy shallow sea. *Journal of marine Systems*, **12**, 263–276.
- Delft Hydraulics. 2006. *Delft3D-FLOW, version 3.13, user manual*. Delft Hydraulics, Rotterdamseweg 185; P.O. Box 177; 2600 MH; Delft; The Netherlands.
- Dewey, Richard, Crawford, William R., Gargett, Ann E., & Oakey, Neil S. 1987. A microstructure instrument for profiling oceanic turbulence in coastal bottom boundary layers. *Journal of Atmospheric and Oceanic Technology*, **4**(June), 288–297.
- Eckart, Carl Henry. 1958. Properties of sea water, part II: The equation of state of water and sea water at low temperatures and pressures. *American journal of science*, **256**(April), 225–240.
- Fisher, N.R., Simpson, J.H., & Howarth, M.J. 2002. Turbulent dissipation in the Rhine ROFI forced by tidal flow and wind stress. *Journal of Sea Research*, **48**, 249–258.
- Fong, D.A., & Geyer, W.R. 2001. Response of a river plume during an upwelling favorable wind event. *Journal of Geophysical Research*, **106**(C1), 1067–1084.
- Fong, D.A., & Geyer, W.R. 2002. The alongshore transport of freshwater in a surface-trapped river plume. *Journal of Physical Oceanography*, **32**(3), 957–972.
- Fong, D.A., Geyer, W.R., & Signell, R.P. 1997. The wind-forced response on a buoyant coastal current: Observations of the western Gulf of Maine plume. *Journal of marine Systems*, **12**, 69–81.

- Garcia Berdéal, I., Hickey, B.M., & Kawase, M. 2002. Influence of wind stress and ambient flow on a high discharge river plume. *Journal of Geophysical Research*, **107**(C9), 3130.
- Garvine, R.W. 2001. The impact of model configuration in studies of buoyant coastal discharge. *Journal of Marine Research*, **59**, 193–225.
- Godin, Gabriel. 1972. *The analysis of tides*. Liverpool: Liverpool University Press.
- Gonella, Joseph. 1972. A rotary-component method for analysing meteorological and oceanographic vector time series. *Deep Sea Research*, **19**, 833–846.
- Heaps, N.S. 1972. Estimation of density currents in the Liverpool Bay Area of the Irish Sea. *Geophysical J. R. astr. Soc.*, **30**, 415–432.
- Hetland, Robert D. 2005. Relating river plume structure to vertical mixing. *Journal of Physical Oceanography*, **35**(9), 1667–1688.
- Hickey, B., Geier, S., Kachel, N., & MacFayden, A. 2005. A bi-directional river plume: The Columbia in summer. *Continental Shelf Research*, **25**, 1631–1656.
- Horner-Devine, Alexander R., Fong, Derek A., Monismith, Stephen G., & Maxworthy, Tony. 2006. Laboratory experiments simulating a coastal river inflow. *Journal of Fluid Mechanics*, **555**, 203–232.
- Howarth, M.J. 1998. The effect of stratification on tidal current profiles. *Continental Shelf Research*, **18**, 1235–1254.
- Howarth, M.J., Simpson, J.H., Sündermann, J., & Van Haren, H. 2002. Processes of vertical exchange in shelf seas PROVESS. *Journal of Sea Research*, **47**, 199–208.
- Hulscher, Suzanne J.M.H. 1996. Tidal-induced large-scale regular bed form patterns in a three-dimensional shallow water model. *Journal of Geophysical Research*, **101**(C9), 20727–20744.
- Huthnance, J.M. 1997. The PROFILE project: an overview. *Journal of marine Systems*, **12**, 249–261.
- Hyatt, J., & Signell, R.P. 2000. Modeling surface trapped river plumes: a sensitivity study. In: Spaulding, M.L., & Blumberg, A.F. (eds), *Estuarine and Coastal Modeling, 6<sup>th</sup> International Conference*. New Orleans, LA, USA: ASCE.
- IPCC. 2001. *Climate Change 2001: Working Group I: The Scientific Basis. Technical Summary*. Tech. rept. IPCC.
- Jacobs, Walter. 2004 (June). *Modelling the Rhine River Plume*. MSc. thesis, Delft University of Technology, Stevinweg 1;2628 CN Delft; The Netherlands.
- Jay, David A., & Smith, J.Dungan. 1990. Circulation, density distribution and neap-spring transitions in the Columbia River Estuary. *Progress in Oceanography*, **25**, 81–112.
- Joordens, J.C.A., Souza, A.J., & Visser, A. 2001. The influence of tidal straining and wind on suspended matter and phytoplankton distribution in the Rhine outflow region. *Continental Shelf Research*, **21**, 301–325.
- Kao, T.W. 1981. The dynamics of oceanic fronts. Part II: shelf water structure due to freshwater discharge. *Journal of Physical Oceanography*, **11**(9), 1215–1223.
- Klamer, J.C., Hull, R.N., Laane, R.W.P.M., & Eisma, D. 1990. The distribution of heavy

- metals and polycyclic aromatic hydrocarbons in the sediments of the Oyster Grounds (North sea). *Netherlands Journal of Sea Research*, **26**(1), 83–87.
- Kourafalou, V. H., Lee, T.N., Oey, L.-Y., & Wang, J.D. 1996a. The fate of river discharge on the continental shelf. 1. Modelling the river plume and the inner shelf coastal current. *Journal of Geophysical Research*, **101**(C2), 3415–3434.
- Kourafalou, V. H., Lee, T.N., Oey, L.-Y., & Wang, J.D. 1996b. The fate of river discharge on the continental shelf. 2. Transport of coastal low-salinity waters under realistic wind and tidal forcing. *Journal of Geophysical Research*, **101**(C2), 3435–3455.
- Lacroix, G., Ruddick, K., Ozer, J., & Lancelot, C. 2004. Modelling the impact of the Scheldt and Rhine/Meuse plumes on the salinity distribution in Belgian waters (southern North Sea). *Journal of Sea Research*, **52**, 149–163.
- Lee, A.J. 1980. *The North-West European shelf seas: the sea bed and the sea in motion. II. Physical and chemical oceanography, and physical resources*. Elsevier Oceanography series, vol. 24B. Amsterdam: Elsevier. Chap. 14: North Sea: Physical Oceanography, pages 467–493.
- Lesser, G.R., Roelvink, J.A., Van Kester, J.A.T.M., & Stelling, G.S. 2004. Development and validation of a three-dimensional morphological model. *Coastal Engineering*, **51**, 883–915.
- Luyten, Patrick J. 1996. An analytical and numerical study of surface and bottom boundary layers with variable forcing and application to the North Sea. *Journal of marine Systems*, **8**, 171–189.
- Maas, L.R.M., & Van Haren, J.J.M. 1987. Observations on the vertical structure of tidal and inertial currents in the central North Sea. *Journal of Marine Research*, **45**, 293–318.
- McClimans, Th. A., Pietrzak, J.D., Huess, V., Kliem, N., Nilsen, J.H., & Johannessen, B.O. 2000. Laboratory and numerical simulation of the Skagerrak circulation. *Continental Shelf Research*, **20**, 941–974.
- Mestres, M., Sierra, J.P., & Sanchez-Arcilla, A. 2007. Factors influencing the spreading of a low-discharge river plume. *Continental Shelf Research*. Published online.
- Nepf, H.M., & Geyer, W.R. 1996. Intratidal variations in stratification and mixing in the Hudson estuary. *Journal of Geophysical Research*, **101**(C5), 12079–12086.
- Nihoul, Jacques, & Ronday, Francois C. 1975. The influence of the "tidal stress" on the residual current. *Tellus*, **27**(5), 484–490.
- Nof, D., & Pichevin, T. 2001. The ballooning of outflows. *Journal of Physical Oceanography*, **31**(10), 3045–3058.
- O'Donnell, J. 1993. Surface fronts in estuaries: a review. *Estuaries*, **16**(1), 12–39.
- Oey, L.-Y., & Mellor, G.L. 1993. Subtidal variability of estuarine outflow, plume and coastal current: a model study. *Journal of Physical Oceanography*, **23**(1), 164–171.
- OSPAR Commission. 2007a. *2006/2007 CEMP Assessment: Trends and concentrations of selected hazardous substances in the marine environment*. Tech. rept. 330. OSPAR Commission, London.

- OSPAR Commission. 2007b. *Annual Report of the OSPAR Commission 2006/07*. Tech. rept. 345. OSPAR Commission, London.
- Otto, L., Zimmerman, J.T.F., Furnes, G.K., Mork, M., Seatre, R., & Bekker, G. 1990. Review of the physical oceanography of the North Sea. *Netherlands Journal of Sea Research*, **26**(2–4), 161–238.
- Peperzak, L., Colijn, F., Koeman, R., Gieskess, W.W.C., & Joordens, J.C.A. 2003. Phytoplankton sinking rates in the Rhine region of freshwater influence. *Journal of Plankton Research*, **25**(4), 365–383.
- Phillips, N.A. 1958. A coordinate system having some advantages for numerical forecasting. *Journal of Meteorology*, **14**(April), 184–185.
- Pietrzak, J.D., & Bolding, K. 1999. Towards a coastal ocean prediction system for the Danish domestic waters. *Coastal and estuarine studies*, **56**, 19522.
- Pietrzak, J.D., Jakobson, Jan B., Burchard, Hans, Vested, Hans Jacob, & Petersen, Ole. 2002. A three-dimensional hydrostatic model for coastal and ocean modelling using a generalised topography following co-ordinate system. *Ocean Modelling*, **4**, 173–205.
- Pietrzak, J.D., De Boer, G.J., & Arentz, L. 2008a. On upwelling due to tidal straining and winds in the Rhine ROFI as observed in SST data from May 1998. In prep.
- Pietrzak, J.D., De Boer, G.J., & Arentz, L. 2008b. The variability of the Rhine River Plume observed from SST and nLw Remote Sensing Images. Submitted.
- Prandle, D. 1978. Residual flows and elevations in the southern North Sea. *Proceedings of the Royal Society of London A*, **359**, 189–228.
- Prandle, D. 1982a. The vertical structure of tidal currents. *Geophys. Astrophys. Fluid Dynamics*, **22**, 29–49.
- Prandle, D. 1982b. The vertical structure of tidal currents and other oscillatory flows. *Continental Shelf Research*, **1**(2), 191–207.
- Prandle, D. 1984. A modelling study of the mixing of  $^{137}\text{Cs}$  in the seas of the European continental shelf. *Philosophical transactions of the Royal Society of London A*, **310**, 407–436.
- Proudman, J., & Doodson, T. 1924. V. The principal constituent of the tides of the North Sea. *Phil. Trans. R. Soc. Lond. A*, **CCXXIV**, 185–219.
- Rasmussen, Erland, Pietrzak, Julie, & Brandt, Rune. 1999. A coupled ice-ocean model for the Greenland, Iceland and Norwegian Seas. *Deep Sea Research part II*, **46**, 1169–1198.
- Rippeth, Tom P., Fisher, Neil R., & Simpson, John S. 2001. The cycle of turbulent dissipation in the presence of tidal straining. *Journal of Physical Oceanography*, **31**(8), 2458–2471.
- Roelvink, J.A., Van der Kaaij, Th., & Reussink, B.G. 2001 (May). *Calibration and validation of large-scale 2D/3D flow models*. Tech. rept. Z3029.11. WL — Delft Hydraulics in MARE consortium, Rotterdamseweg 185; P.O. Box 177; 2600 MH; Delft; The Netherlands.
- Roozkrans, J.N. 1997. Operational use of NOAA AVHRR imagery in the marine environ-

- ment. In: Stel, J.H., Behrens, H.W.A., Borst, J.C., Droppert, L.J., & v.d. Meulen, J. (eds), *Operational Oceanography: The challenge for European Co-operation*. Elsevier Science B.V.
- Roozkrans, J.N., & Prangma, G.J. 1992. *Observatie van het aard-atmosfeer systeem door de NOAA-satellieten (ontvangst, productie, toepassing en gebruik van de NOAA-data*. Tech. rept. BCRS report 92-02. BeleidsComissie Remote Sensing = Netherlands remote Sensing Board. (BCRS projects IS-3.5 and OP-1.12, In Dutch).
- Ruddick, K.G., Deleersnijder, E., De Mulder, T., & Luyten, P.J. 1994. A model study of the Rhine discharge front and downwelling circulation. *Tellus*, **46A**, 149–159.
- Ruddick, K.G., Deleersnijder, E., Luyten, P.J., & Ozer, J. 1995. Haline stratification in the Rhine-Meuse freshwater plume: a three-dimensional model sensitivity analysis. *Continental Shelf Research*, **15**(13), 1597–1630.
- Shao, S.-Y., & Boicourt, W.C. 1986. Onset of estuarine plumes. *Journal of Physical Oceanography*, **16**(12), 2137–2149.
- Sharples, J., Simpson, John H., & Brubaker, J.M. 1994. Observations and modelling of periodic stratification in the upper York river estuary, Virginia. *Estuarine, Coastal and Shelf Science*, **38**, 301–312.
- Simpson, J.H. 1981. The shelf-sea fronts: implications of their existence and behaviour. *Phil. Trans. R. Soc. Lond. A*, **302**, 531–546.
- Simpson, J.H. 1997. Physical processes in the ROFI regime. *Journal of marine Systems*, **12**, 3–15.
- Simpson, J.H., & Bowers, D. 1981. Models of stratification and frontal movement in shelf seas. *Deep Sea Research*, **28A**(7), 727–728.
- Simpson, J.H., & Hunter, J.R. 1974. Fronts in the Irish Sea. *Nature*, **250**(Aug), 404–406.
- Simpson, J.H., & Souza, A.J. 1995. Semidiurnal switching of stratification in the region of freshwater influence of the Rhine. *Journal of Geophysical Research*, **100**(C4), 7037–7044.
- Simpson, J.H., & Tinker, J.P. 2007. A test of the influence of tidal stream polarity on the structure of turbulent dissipation. *Continental Shelf Research*. In press, special issue PECS 2006.
- Simpson, J.H., Allen, C.M., & Morris, N.C.G. 1978. Fronts on the continental shelf. *Journal of Geophysical Research*, **83**(C9), 4607–4614.
- Simpson, J.H., Brown, J., Matthews, J., & Allen, G. 1990. Tidal straining, density currents, and stirring in the control of estuarine stratification. *Estuaries*, **13**(2), 125–132.
- Simpson, J.H., Bos, W.G., Schirmer, F., Souza, A.J., Rippeth, T.P., Jones, S.E., & Hydes, D. 1993. Periodic stratification in the Rhine ROFI in the North Sea. *Oceanologica Acta*, **16**(1), 23–32.
- Simpson, J.H., Crawford, William R., Rippeth, Tom P., Campbell, Andrew R., & Cheok, Joseph V.S. 1996. The vertical structure of turbulent dissipation in shelf seas. *Journal of Physical Oceanography*, **26**(8), 1579–1590.
- Simpson, J.H., Burchard, H., Fisher, N.R., & Rippeth, T.P. 2002. The semi-diurnal cycle of



- dissipation in a ROFI: model-measurement comparisons. *Continental Shelf Research*, **22**, 1615–1628.
- Simpson, J.H., Williams, E., Brasseur, L.H., & Brubaker, J.M. 2005. The impact of tidal straining on the cycle of turbulence in a partially stratified estuary. *Continental Shelf Research*, **25**, 51–64.
- Soulsby, R.L. 1983. *Physical Oceanography of coastal and shelf seas*. Elsevier Oceanography Series, vol. 35. Amsterdam: Elsevier. Chap. 5: The bottom boundary layer of shelf seas, pages 189–266.
- Soulsby, R.L. 1990. *The Sea*. Ocean Engineering Science, vol. 9A. New York: Wiley InterScience. Chap. 15: Tidal current boundary layers, pages 523–567.
- Souza, A.J., & James, I.D. 1996. A two-dimensional (x-z) model of tidal straining in the Rhine ROFI. *Continental Shelf Research*, **16**(7), 949–966.
- Souza, A.J., & Simpson, J.H. 1996. The modification of tidal ellipses by stratification in the Rhine ROFI. *Continental Shelf Research*, **16**(8), 997–1007.
- Souza, A.J., & Simpson, J.H. 1997. Controls on stratification in the Rhine ROFI system. *Journal of marine Systems*, **12**, 311–323.
- Souza, A.J., Fisher, N. R., Simpson, J.H., & Howarth, M.J. 2008. The effects of tidal straining on the semi-diurnal cycle of dissipation in the Rhine ROFI: model-measurement comparisons. *Journal of Geophysical Research*, **113**(C01011).
- Souza, Alejandro J., Holt, Jason T., & Proctor, Roger. 2007. Modelling SPM on the NW European shelf seas. *Pages 147–158 of: Balson, P. S., & Collins, M. B. (eds), Coastal and Shelf Sediment Transport*. Special Publications, vol. 274. The Geological Society of London.
- Souza, A.S. 1994 (Sept.). *Controls on stratification in the Rhine ROFI system*. Ph.D. thesis, University College of North Wales, School of Ocean Sciences, Menai Bridge, Gwynedd LL59 5EY, U.K.
- Stacey, Mark T., Monismith, Stephen G., & Burau, Jon R. 1999. Observations of Turbulence in a Partially Stratified Estuary. *Journal of Physical Oceanography*, **25**(8), 1950–1970.
- Stelling, G.S. 1984. *On the construction of computational methods for shallow water flow problems*. Rijkswaterstaat Communications 35, Rijkswaterstaat, Government Printing Office, The Hague, The Netherlands.
- Stelling, G.S., & Leendertse, J.J. 1991. Approximation of convective processes by cyclic AOI methods. *Pages 771–782 of: Proceeding of the 2nd ASCE Conference on Estuarine and Coastal Modelling*. ASCE, New York.
- Stelling, G.S., & Van Kester, J.A.Th. M. 1994. On the approximation of horizontal gradients in sigma co-ordinates for bathymetry with steep bottom slopes. *International Journal for Numerical Methods in Fluids*, **18**(18), 915–935.
- Stelling, Guus S. 1995. Compact differencing for stratified free surface flow. *Pages 378–386 of: CHES, & IRTCES (eds), Advances in Hydro-Science and -Engineering*, vol. II, part A. Beijing: Tsinghua University Press.

- Suijlen, J.M., & Duin, R.N.M. 2001. *Variability of near-surface total suspended matter concentrations in the Dutch coastal zone of the North Sea*. Werkdocument RIKZ/OS/2001.150X. National Institute for Coastal and Marine Management/RIKZ. In Dutch.
- Suijlen, J.M., & Duin, R.N.M. 2002 (December). *Atlas of near-surface Total Suspended Matter concentrations in the Dutch coastal zone of the North Sea*. Tech. rept. RIKZ/2002.059. National Institute for Coastal and Marine Management/RIKZ.
- Sverdrup, H.U. 1927. Dynamic of tides on the northern siberian shelf. Results from the Maud Expedition. *Geofysiske publikasjoner Norske Videns, Acad. Oslo*, **4**, 2–75.
- Taylor, Geoffrey Ingram. 1921. Tidal Oscillations in gulfs and rectangular basins. *Proceedings of the London Mathematical Society*, **XX**(2). Reprinted in: The scientific papers of Sir Geoffrey Ingram Taylor, Volume II, meteorology, oceanography and turbulent flow, Cambridge University press, 1960.
- Tee, K.T. 1979. Structure of 3-dimensional tide-generating currents .1. oscillating currents. *Journal of Physical Oceanography*, **9**(5), 930–944.
- Tee, K.T. 1980. The structure of 3-dimensional tide-induced current .2. residual currents. *Journal of Physical Oceanography*, **10**(12), 2035–2057.
- TriWaq. 1999. *TriWaq - Three dimensional shallow water flow model; technical documentation*. Simona report 99-01, version 1.1. National Institute for Coastal and Marine Management/RIKZ, EDS, Leidschendam.
- Uittenbogaard, R.E., & Imberger, J. 1993 (Nov.). *The importance of internal waves for mixing in a stratified estuarine tidal flow. Part one: text and appendix*. Tech. rept. Z694. Delft Hydraulics, Rotterdamseweg 185; P.O. Box 177; 2600 MH; Delft; The Netherlands. prepared for: Dutch ministry of Transport, Public Works and Water management, Tidal waters division.
- Uittenbogaard, R.E., Van Kester, J.A. Th. M., & Stelling, G.S. 1994 (May). *Implementation of three turbulence models in TRISULA for rectangular horizontal grids*. Tech. rept. Z162. Delft Hydraulics, Rotterdamseweg 185; P.O. Box 177; 2600 MH; Delft; The Netherlands. Prepared for Dutch Ministry of public works and water management, tidal waters division.
- Van Aken, Hendrik. 1986. The onset of seasonal stratification in shelf seas due to differential advection in the presence of a salinity gradient. *Continental Shelf Research*, **5**(4), 475–485.
- Van Alphen, J.S.L.J., De Ruijter, W.P.M., & Borst, J.C. 1988. Outflow and three-dimensional spreading of Rhine river water in the Netherlands coastal zone. *Pages 70–92 of: Dronkers, J., & Van Leussen, W. (eds), Physical processes in estuaries*. Berlin: Springer-Verlag.
- Van der Giessen, A., De Ruijter, W.P.M., & Borst, J.C. 1990. Three-dimensional current structure in the Dutch coastal zone. *Netherlands Journal of Sea Research*, **25** 1/2, 45–55.
- Van Eijkeren, J.C.H., De Haan, B.J., Stelling, G.S., & Van Stijn, Th.L. 1993. Linear upwind biased methods. *Pages 55–91 of: Vreugdenhil, Cornelius B., & Koren, Barry (eds), Numerical methods for advection-diffusion problems*. Notes on numerical fluid mechanics (NNFM), vol. 45. Braunschweig/Wiesbaden: Friedrich Vieweg & Sohn Verlag.
- Van Kester, J.A.Th., Uittenbogaard, R.E., & Stelling, G.S. 1994 (Mar.). *Gevoeligheidson-*



- derzoek 3D-NOORDWIJKRAAI-model. Variaties in roosterafstand, turbulentiemodel, bodemruwheid en windschuifspanning.* Verslag onderzoek Z691. Delft Hydraulics, Rotterdamseweg 185; P.O. Box 177; 2600 MH; Delft; The Netherlands. In Dutch, prepared for: RWS/RIKZ.
- Visser, A.W., Souza, A.S., Hessner, K., & Simpson, J.H. 1994. The effect of stratification on tidal current profiles in a region of freshwater influence. *Oceanologica Acta*, **17**(4), 369–381.
- Visser, Marijke. 1993. *On the transport of fine sediment in the Netherlands coastal zone.* Ph.D. thesis, Universiteit Utrecht, faculty of physics and astronomy.
- Xing, J., & Davies, A.M. 1999. The effect of wind direction and mixing upon the spreading of a buoyant plume in a non-tidal regime. *Continental Shelf Research*, **19**, 1437–1483.
- Yankovsky, A.E., & Chapman, D.C. 1997. A simple theory for the fate of buoyant coastal discharges. *Journal of Physical Oceanography*, **27**(7), 1386–1401.
- Yankovsky, Alexander E., Hickey, Barbara M., & Munchow, Andreas K. 2001. Impact of variable inflow on the dynamics of a coastal buoyant plume. *Journal of Geophysical Research*, **106**(C9), 19809–19824.
- Yasuda, Hidekazu. 1987. Vertical Structure of the Tidal Current Ellipse in a Rotating Basin. *Journal of the Oceanographical Society of Japan*, **43**, 309–318.
- Ye, Jianhuan, & Garvine, Richard W. 1998. A model study of estuary and shelf tidally driven circulation. *Continental Shelf Research*, **18**, 1125–1155.
- Zimmerman, J.T.F. (ed). 1978. "Texel 1978"; *waterbeweging en menging in het Zuidelijk gedeelte van de Noordzee.* in Dutch.
- Zimmerman, J.T.F. 1986. The tidal whirlpool: A review of horizontal dispersion by tidal and residual currents. *Netherlands Journal of Sea Research*, **20**(2/3), 133–154.



REM island (Noordwijk meetpost Figs. 1.2 and 5.1) in the middle of Rhine ROFI before removal.  
(image credit: J.A. van Duin).

## List of Figures

1.1	Overview map Southern North Sea. . . . .	2
1.2	Overview map Rhine ROFI. . . . .	3
1.3	Sketch well-stratified vs. well-mixed Rhine ROFI. . . . .	4
1.4	Conceptual 3D sketch of velocity and density profiles in Rhine ROFI. . . . .	6
1.5	Sketch vertical variation of horizontal tidal velocities. . . . .	7
1.6	Three synoptic views on the North Sea.. . . .	8
2.1	Block cartoon: study area. . . . .	14
2.2	Southern North Sea: water masses. . . . .	15
2.3	Southern North Sea: depth averaged residual current. . . . .	16
2.4	Southern North Sea: Average surface average salinity. . . . .	18
2.5	Block cartoon: 2D density and current structure. . . . .	19
2.6	Block cartoon: force balance 3D density and current. . . . .	20
2.7	Block cartoon: 3D residual current. . . . .	22
2.8	Southern North Sea: extent of stratification. . . . .	23
2.9	Southern North Sea: position fronts. . . . .	24
2.10	Block cartoon: 3D density structure ‘thermal wind’. . . . .	25
2.11	Cartoon: Sketch defining river plume. . . . .	26
2.12	Block cartoon: upwelling favorable wind. . . . .	27
2.13	Southern North Sea: amphidromic system. . . . .	30
2.14	Block cartoon: idealized Kelvin wave. . . . .	31
2.15	Cartoon: 3D time series well-mixed. . . . .	32
2.16	Measurements: near-surface tidal ellipses. . . . .	34
2.17	Block cartoon: well-mixed condition. . . . .	36
2.18	Cartoon: example phasors. . . . .	39
2.19	Cartoon: vertical variation of horizontal tidal velocities. . . . .	40
2.20	Cartoon: synthetic time-series 2 time scales. . . . .	41
2.21	Measurements: time-series tidal straining and mixing. . . . .	41
2.22	Cartoon: concept of tidal straining. . . . .	43
2.23	Cartoon: 3D time series stratified condition. . . . .	44
2.24	Measurements: progressive vectors diagrams. . . . .	45

3.1	Numerical model grid. . . . .	53
3.2	Numerical grid schematization. . . . .	54
3.3	Force balance in a Kelvin wav. . . . .	56
3.4	Imposed tide at model boundary. . . . .	58
3.5	Measured ROFI profiles. . . . .	60
3.6	Modelled ROFI profiles layers. . . . .	61
3.7	Modelled ROFI profiles 16 layers. . . . .	62
3.8	Monthly number of SST pixels SST 1998. . . . .	64
3.9	Monthly mean SST 1998. . . . .	65
3.10	Monthly standard deviation SST 1998. . . . .	66
4.1	Schematic overview numerical model grid. . . . .	71
4.2	Vertical profiles of ellipse properties (neap). . . . .	76
4.3	Vertical profiles of ellipse properties (spring). . . . .	77
4.4	Time averaged values of salinity during (neap). . . . .	78
4.5	Time averaged values of salinity (spring). . . . .	79
4.6	Vertical profiles of residual velocities (neap). . . . .	80
4.7	Vertical profiles of residual velocities (spring). . . . .	81
4.8	Vertical profiles of ellipse properties (neap). . . . .	84
4.9	Vertical profiles of ellipse properties (spring). . . . .	85
4.10	Time series of vertical profiles (neap). . . . .	86
4.11	Time series of vertical profiles (spring). . . . .	87
4.12	Spatial distribution of ellipse properties (neap). . . . .	89
4.13	Spatial distribution of ellipse properties (spring). . . . .	91
4.14	Richardson number vs. ellipticity (neap). . . . .	92
4.15	Richardson number vs. ellipticity (spring). . . . .	93
4.16	Vertical distribution of ellipticity and salinity (spring-neap cycle). . . . .	95
4.17	Scheme of ellipticity vs. bulk eddy viscosity according to Prandle. . . . .	97
5.1	Location Rhine ROFI. . . . .	103
5.2	Conceptual sketch of tidal straining Rhine ROFI. . . . .	104
5.3	Plan view mosaic of plume SST in May 1990. . . . .	108
5.4	Schematic overview numerical model grid. . . . .	111
5.5	SST image of UW band on May 3 <sup>rd</sup> 1990 12:36. . . . .	114
5.6	SST image of UW band on May 4 <sup>th</sup> 1990 12:25. . . . .	115
5.7	Time series water levels, wind and SST images May 1990. . . . .	116
5.8	Plan view mosaic of modeled SST (no wind). . . . .	118
5.9	Modeled cross-sections in coastal current. . . . .	120
5.10	Plan view mosaic of modeled SST (easterly wind). . . . .	122
5.11	Plan view mosaic of plume SST in November 1993. . . . .	127

---

5.12	SST image of UW band on November 19 <sup>th</sup> 1993 07:26. . . . .	128
5.13	Time series water levels, wind and SST images November 1993. . . . .	129
6.1	Combined effects of tidal straining and advection. . . . .	133
6.2	Evolution of the river plume. . . . .	139
6.3	Plan view covariance $\varphi_t$ terms. . . . .	142
6.4	Time series covariance $\varphi_t$ terms station 1. . . . .	144
6.5	Time series covariance $\varphi_t$ terms station 2. . . . .	146
6.6	Time series covariance $\varphi_t$ terms station 3. . . . .	148
6.7	Sketch of combined effect of along-shore/cross-shore shear/advection. . . . .	150
6.8	A sketch of dominant terms controlling stratification and mixing in ROFI. . . . .	152
6.9	Cross-shore and along-shore positions of isohalines. . . . .	153
7.1	Feed-back loop Rhine ROFI processes. . . . .	156



REM island (Noordwijk meetpost Figs. 1.2 and 5.1) in middle of the Rhine ROFI during removal. (image credit: J.A. van Duin).

## List of Tables

4.1	Overview of tides imposed at boundaries. . . . .	73
4.2	Overview of time frame in simulations. . . . .	73
4.3	Overview of vertical eddy viscosity in simulations. . . . .	74





Red algae in the Rhine ROFI.  
(image credit: J.A. van Duin).

# List of Symbols

## Roman Symbols

$A_{major}$	major axis of tidal ellipse ( $A_{major} =  R^+  +  R^- $ )	$\text{m s}^{-1}$
$A_{minor}$	minor axis of tidal ellipse ( $A_{minor} =  R^+  -  R^- $ )	$\text{m s}^{-1}$
$D$	total derivative operator	
.	position of the bed ( $D = -h$ )	$\text{m}$
$E$	ellipticity of tidal ellipse ( $E = A_{major}/A_{minor}$ )	-
$E_H, E_z$	horizontal, vertical eddy viscosity	$\text{m}^2 \text{s}^{-1}$
$G$	water level gradient (complex)	$\text{m m}^{-1}$
$H$	water depth ( $H = \eta + h$ )	$\text{m}$
$Q$	source	
$R^-$	(anti-)cyclonic phasor (complex)	$\text{m s}^{-1}$
$R^+$	(anti-)cyclonic phasor (complex)	$\text{m s}^{-1}$
$R_o$	Rossby radius	$\text{m}$
$S$	salinity	PSU
$T$	temperature	$^{\circ}\text{C} / ^{\circ}\text{K}$
.	tidal period	$\text{s}$
$U, V$	depth averaged $u, v$ -velocity	$\text{m s}^{-1}$
$a, b, c, d$	coefficients in $(u, v)$ velocity decomposition	$\text{m s}^{-1}$
$c$	concentration of dissolved substance	$\text{kg m}^{-3}$
.	wave celerity	$\text{m s}^{-1}$
$f$	Coriolis acceleration	$\text{m s}^{-2}$
$g$	gravitational acceleration	$\text{m s}^{-2}$
$h$	position of the bed ( $h = -D$ )	$\text{m}$
$i$	complex unit	-
$k$	bed friction factor of Prandle	-
.	turbulent kinetic energy	$\text{m}^2 \text{s}^{-2}$
.	wave number	$\text{rad m}^{-1}$
$p$	pressure	Pa
$s$	linearised bottom friction	$\text{m}^{-1}$
$t$	time	$\text{s}$
$u, v, w$	velocity in $x, y, z$ -direction	$\text{m s}^{-1}$
$x, y, z$	$x, y, z$ -co-ordinate (cross shore, alongshore, vertical (positive up))	$\text{m}$

## Greek symbols

$\alpha$	inverse boundary layer height ( $\alpha = \delta^{-1}$ )	$\text{m}^{-1}$
$\delta$	boundary layer height	m
$\epsilon$	turbulent kinetic energy dissipation	$\text{m}^2 \text{s}^{-3}$
$\eta$	the free water surface	m
$\kappa$	friction coefficient	-
$\lambda$	quadratic bottom friction coefficient	-
$\rho$	density	$\text{kg m}^{-3}$
$\sigma$	relative position of within water depth	-
$\tau$	bed friction	Pa
$\phi$	phase of tidal ellipse	rad
$\varphi$	potential energy anomaly	$\text{J m}^{-3}$
$\psi$	inclination of tidal ellipse	rad
$\omega$	vertical velocity relative to $\sigma$ -layers	$\text{m s}^{-1}$
.	angular frequency	$\text{rad s}^{-1}$

## Abbreviations

ADCP	Acoustic Doppler Current Profiler
ADI	Alternating Direction Implicit
ASIPS	Advection and Strain Induced Periodic Stratification
AVHRR	Advanced Very High Resolution Radiometer
CTD	Conductivity, Temperature, Depth
DW	downwelling
HW	High Water
GOTM	General Ocean Turbulence Model ( <a href="http://www.gotm.net">www.gotm.net</a> )
KNMI	Koninklijk Nederlands Meteorologisch Instituut ( <a href="http://www.knmi.nl">www.knmi.nl</a> )
LAC	Local Area Coverage
LW	Low Water
NOAA	National Oceanic and Atmospheric Administration ( <a href="http://www.noaa.gov">www.noaa.gov</a> )
NH	Northern Hemisphere
PROFILE	Processes in regions of freshwater influence (EU MAST II project)
PROVESH	Processes of Vertical Exchange in Shelf Seas (EU MAST III project)
ROFI	Region of Freshwater Influence (Simpson <i>et al.</i> ,1993)
SIPS	Strain Induced Periodic Stratification (Simpson <i>et al.</i> ,1990)
SST	Sea Surface Temperature
UW	upwelling

## Acknowledgements

During my PhD research in the Fluid Mechanics Section, I was privileged to work with and get support from a number of colleagues. First of all, I would like to thank my direct supervisor Julie Pietrzak. As an MSc. student her Physical oceanography and Density currents courses inspired me to start this PhD. Subsequently, as a PhD student, I am grateful for the many challenging scientific discussions we have had. She also served as an enthusiastic sparring partner during many long distance calls from Calgary where she spent her sabbatical, and where she proved an excellent host for me when I visited her. Furthermore, she patiently taught me how to write scientific papers. Secondly, I would like to thank Han Winterwerp for being an enthusiastic mentor at my part-time Delft Hydraulics job, where we did challenging work on wave-fluid mud interaction, together with MSc. student Wouter Kranenburg. Thirdly, I would like to thank my promotor Guus Stelling for teaching me the intricate numerics behind the DELFT3D model, larded with many entertaining stories.

In addition to my supervisors, I would like to thank two MSc. students who assisted me right after I started my research. First I am grateful to Walter Jacobs for helping me to set up an idealized model of the Rhine ROFI, with open boundary input from Dano Roelvink. Second I would like to thank Loana Arentz for helping with the processing of ocean color images after directions from Sharon Tatman, and in lasting collaboration with Marieke Eleveld from VU-IVM. From my fellow PhD students I am indebted to Michel de Nijs, and also my roommate Alexander Breugem. I had some powerful discussions with them on the application of the potential energy anomaly equations to Michels Rotterdam WaterWay and my Rhine ROFI that stood at the basis of Chapter 6.

Furthermore, I am grateful to Herman Ridderinkhof and the ALW LOICZ-NL program from NWO for the funding of this project. In addition Herman allowed me to join to two NIOZ Navicula cruises; one relaxing in spring, the other in a nasty autumn weather where I was the only support to Lucas Merckelbach, my fellow NWO grant researcher. These cruises actually allowed me to see the Rhine ROFI in real life, in addition to the digital ones that I studied for this thesis.

I would like to thank KNMI, and Hans Roozkrans in particular, for providing all their NOAA SST data, and Rijkswaterstaat, with Erik Marsman in particular, who co-financed the associated expenses. In addition, I am indebted to John Simpson and three anonymous reviewers for their critical reviews that helped to improve the papers in this thesis significantly.

Returning back to our lab, I would like to thank my fellow PhD students and other staff in the tight-knit Stevin III group: Andre; Andre and Simon for our linux clusters and trusting me as joint root; Arie; Bas (3x); Bianca; Bram for his boxes; Claire; David for his debates and computer support;

Federico for his music; Francesca for her Italian tastes; Hans for assembling me a powerful, lasting desktop PC; Harry; Harmen; Jaap for his informal chats; Jaap and Ruben as mates during the rise and fall of our TU Delft hockey team; Jasper; John; Kees; Maarten; Marcel; Marcel Stive for asking me to join in many MSc. projects; Mark; Martijn (2x); Marije for organizing many socials; Mohammed; Olga; Otti for all informal chats; Petra as determined tour guide in Japan; Rob; Robert-Jan; Sander; Shadid; Stephan; Tim; and the 2 Wims.

During my PhD period I also worked on related topics at Delft Hydraulics, now Deltares, for one day per week. I am grateful Delft Hydraulics for granting me this contract, which allowed me to discuss my research with colleagues who already studied the Rhine ROFI with different methods. There are too many Delft Hydraulics colleagues to mention them all, so I limit myself to mentioning the fruitful collaboration with Thijs van Kessel, Bas Borsje and Mindert de Vries. In addition I would like to thank Bert Jagers for his elaborate DELFT3D Matlab toolboxes, which saved me lots of time and motivated me to elaborate on Matlab functions myself as well, and Mark van Koningsveld for launching a local Matlab community.

For my research I have really benefited from the EU-funded Rhine ROFI projects that were performed in the early 90s (PROFILE and PROVISS) by the key researchers John Simpson and Alex Souza. The findings from these field campaigns were very stimulating and provided key foundations on which I could build my research. I am also grateful for the people who invest energy in organizing the PECS, NCK, ESA, EGU and INTERCOH conferences and summer schools, which provided me with an inspiring community in which to perform and share science.

In my personal life I am grateful to friends and family who, perhaps unknowingly, provided their support, sometimes by inquiring about my research progress and sometimes by wisely not mentioning it at all. In particular I would like to thank Guido Kuiper for discussing Delft research at length during his excellent dinners, and for being paranymph together with Bram. I am very grateful to my parents Gerda and Ytzen and my brother Bram, for the inspiring and supporting atmosphere in which I grew up, and for the many discussions and debates we still enjoy. Last but not least I would like to thank my Caroline for all her patience and loving support, especially during the stage of finishing, and for just being there for me.

## Curriculum Vitae

Gerben de Boer was born on January 10<sup>th</sup> 1978 in Amsterdam. He grew up in Hoofddorp, an Amsterdam 'suburb', where he completed gymnasium-beta cum laude at the Katholieke Scholengemeenschap Hoofddorp (KSH) in 1996. He started his study Civil Engineering in 1996 at TU Delft. From 1999 to 2002 he was employed as student assistant at the section of Structural Mechanics, providing assistance for the B.Sc. 'Dynamics of systems' course. During an internship at WL|Delft Hydraulics and a visit of HydroQual Inc. (New York) he wrote his M.Sc. thesis on the consolidation and erosion of cohesive sediments. In 2002 he obtained his M.Sc. cum laude, after which he immediately started as junior advisor at WL|Delft Hydraulics. Subsequently in February 2003 he started his PhD research at TU Delft at the Section of Environmental Fluid Mechanics which resulted in this thesis. He worked on his PhD research for 4 days per week until February 2008. Meanwhile he was still employed by at WL|Delft Hydraulics 1 day per week where he worked on various other topics. He attended three PECS, three InterCoh, one EGU and one Bangor conference, and participated in the NCK summer-school on Texel in 2005 and the ESA Envschool in Frascati in 2006. Since February 2008 he is nearly full-time employed at Deltares, the institute into which WL|Delft Hydraulics merged on Januari 2008, but is still part-time employed by TU Delft as well.





## List of author's publications

### Journal papers:

- de Boer, G.J., Pietrzak, J.D., & Winterwerp, J.C. 2008. Using the potential energy anomaly equation to investigate tidal straining and advection of stratification in a region of freshwater influence, *Ocean Modeling*, 22(1-2), 1-8 (this thesis, Chapter 6).
- de Boer, G.J., Pietrzak, J.D., & Winterwerp, J.C. 2007. SST observations of upwelling induced by tidal straining in the Rhine ROFI, *Continental Shelf Research*, in press, special issue PECS 2006 (this thesis, Chapter 5).
- de Boer, G.J., Pietrzak, J.D., & Winterwerp, J.C. 2006. On the vertical structure of the Rhine region of freshwater influence, *Ocean Dynamics*, Vol. 56, 3-4, 198-216, special issue PECS 2004 (this thesis, Chapter 4).
- Borsje, B.W., de Vries, M.B., Hulscher, S.J.M.H. & G.J. de Boer, 2008. Modeling large scale cohesive sediment transport affected by small scale biological activity, *Estuarine, Coastal and Shelf Science*, 78(3), 468-480.
- Vinzon, S.B. , Winterwerp, J.C., de Boer, G.J., & Nogueira, R. 2008. Mud deposit formation on the open coast of the larger Patos Lagoon-Cassino Beach system, *Continental Shelf Research*, accepted.
- Pietrzak, J.D., de Boer, G.J., Eleveld, M. A., Arentz, L. & Winterwerp, J.C.. The variability of the southern North Sea observed from SST and SPM Remote Sensing Images, *Continental Shelf Research*, submitted.

### Manuscripts in preparation:

- Pietrzak, J.D., de Boer, G.J., Eleveld, M. & Arentz, L.. The high frequency variability of the Rhine ROFI observed from SST and SPM Remote Sensing Images (in preparation).
- Kranenburg, W.M., Winterwerp, J.C., de Boer, G.J. & Cornelisse, J.M.. Viscous wave damping in a two-layer fluid mud schematization. I: dispersion relations and comparison of models (in preparation).
- Kranenburg, W.M., Winterwerp, J.C., de Boer, G.J. & Zijlema, M.. Viscous wave damping in a two-layer fluid mud schematization. II: implementation in SWAN and applications (in preparation).
- Pietrzak, J.D. & de Boer, G.J.. On the role of upwelling due to tidal straining and winds in the Rhine ROFI as observed in SST data from May 1998 (in preparation).

## Reports:

- de Boer, G.J. 2007. A note on Open Boundary Conditions (including Neumann) for nested idealized coastal tidal models in Delft3D. TU Delft, Civil Engineering and Geosciences Faculty, Environmental Fluid Mechanics Section, report no. 2007-1.

## Conference proceedings / (published) abstracts / presentations:

- 2008, de Boer, G.J., Winterwerp, J.C. & A.R. van Dongeren. Flume experiments of wave damping by fluid mud. 10th InterCoh, 2009, Rio de Janeiro / Paraty, Brazil (Submitted).
- 2008, Eleveld, M.A., van der Woerd, H.J., Blaas, M., El Serafy, G.Y.H., van Kessel, Th. & de Boer, G.J. 2008. Assimilation of Remotely Sensed Observations in a Sediment Transport Model: Interpretation of results. Ocean Optics OOXIX (OO080477). Halifax: Lewis Conf. Services Int. Inc.
- 2008, de Boer, G.J. & Pietrzak, J.D. 2008. Relating river plume structure to vertical mixing using potential energy anomaly budgets and salinity coordinates. 14th PECS, 25-29 Aug. 2008, POL, Liverpool, UK (presentation).
- 2008, Pietrzak, J.D. & de Boer, G.J. 2008. Using the potential energy anomaly equations as a new diagnostic tool for coastal ocean modeling. EGU Meeting, Vienna.
- 2008, de Boer, G.J., Pietrzak, J.D., & Winterwerp, J.C. 2008. The Rhine region of freshwater influence. NCK days 2008, 26-27 Mar 2008, Deltares, Delft, the Netherlands (presentation).
- 2007, Borsje, B.W., Hulscher, S.J.M.H., de Vries, M.B., G.J. de Boer, 2007. Modeling large scale cohesive sediment transport by including biological activity, Eds. Dohmen-Janssen and Hulscher, Proceedings fifth IAHR Symposium on River, Coastal and Estuarine Morphodynamics, 255-262.
- 2007, Blaas, M., El Serafy, G.Y.H., van Kessel, Th., de Boer, G.J., Eleveld, M.A. & van der Woerd, H.J., 2007. Data Model Integration of SPM transport in the Dutch coastal zone. Proceedings Joint 2007. EUMETSAT Meteorological Satellite Conference and the 15th American Meteorological Society (AMS) Satellite Meteorology & Oceanography Conference, CD ISBN 992-9110-079-X. Publisher: EUMETSAT, Darmstadt. (<http://www.eumetsat.int/>).
- 2007, de Boer, G.J., Pietrzak, J.D., Arentz, L. & Winterwerp, J.C. 2007. The appearance of SPM in the Rhine plume on colour satellite images. 9th InterCoh, 25-28 Sep 2007, Ifremer, Brest, France (presentation).
- 2007, de Boer, G.J., Pietrzak, J.D., & Winterwerp, J.C. 2007. Tidal straining induced upwelling in the Rhine ROFI, EGU Meeting, Vienna (poster).
- 2006, de Boer, G.J., Pietrzak, J.D., & Winterwerp 2007. The effect of tidal straining on plume displacements in the Rhine ROFI. 13th PECS, 18-22 Sep 2006, Astoria, USA (presentation).
- 2006, de Boer, G.J. 2006. Density effects on transport paths in the Rhine region of freshwater influence. Coastal and Shelf Seas - Present Understanding and and Future Challenges, conference to mark the retirement of Professor John Simpson, 10 - 12 Apr 2006, Bangor, Wales (presentation).
- 2006, de Boer, G.J. 2006. Remote sensing of the Rhine plume. NCK days 2006, 23-24 Mar 2006, Unesco IHE / the Hague, the Netherlands (presentation).
- 2005, de Boer, G.J., van Beek, J.K.L., van Kessel, Th., van Loon, A.F. & J.C. Winterwerp.

On the long-term balance of fine sediment in the Wadden Sea. 8th InterCoh, 20-23 Sep 2005, IIT, Saga, Japan (presentation).

- 2005, de Boer, G.J., Pietrzak, J.D., & Winterwerp, J.C. 2005. On the vertical structure of the Rhine region of freshwater influence. NCK days 2005, 10-11 Mar 2005, TU Twente, the Netherlands (poster).
- 2005, de Boer, G.J., Pietrzak, J.D., & Winterwerp, J.C. 2005. The Rhine river plume. 12th PECS, 19-22 Oct 2004, Merida, Mexico (presentation).
- 2004, de Boer, G.J., Pietrzak, J.D., & Winterwerp, J.C. 2004. The transport of fine sediment in the Dutch coastal zone. NCK days 2004, 18-19 Mar 2004, NIOO, Yerseke, Netherlands (presentation).
- 2003, de Boer, G.J., Merckelbach, L.M., & Winterwerp, J.C. 2007. A parameterized consolidation model for cohesive sediments. pp 243-262 of: Maa, Sanford & Schoellhamer (eds), Estuarine and coastal fine sediment dynamics. Proceedings in Marine Science, Vol. 8. Elsevier (InterCoh-2003, VIMS, USA). 7th InterCoh 2003, 1-4 Oct 2003, VIMS, Virginia, USA (presentation).
- 2003, de Boer, G.J., Pietrzak, J.D., & Winterwerp, 2003. The transport of SPM in the Dutch coastal Zone. NWO-VLANEZO meeting Antwerp (presentation).
- 2003, de Boer, G.J., Merckelbach, L.M., & Winterwerp, J.C. 2003. A parameterized consolidation model for mud. NCK days 2003, NIOZ, Texel, the Netherlands (presentation).



61A 201

057